Motion induced unsteady aerodynamics at high angles-of-attack

Pilkington, David J.

Award date:
1996

Awarding institution:
University of Bath

MOTION INDUCED UNSTEADY AERODYNAMICS AT HIGH ANGLES-OF-ATTACK

Submitted by David J. Pilkington
for the degree of PhD
of the University of Bath
1995.

ProQuest LLC
789 East Eisenhower Parkway
P.O. Box 1346
Ann Arbor, MI 48106-1346

ABSTRACT

The aim of this programme of work was to determine the low speed, unsteady, trailing edge control effects on a 55° leading edge sweep, delta wing model, to angles-of-attack beyond the stall point and to frequencies of control oscillation equivalent to a typical first wing bending mode of a combat aircraft configuration. Hence, the level of structural excitation of a wing bending mode to rapid control surface motion could be established.

The steady and unsteady surface pressures for steady elevon angles and control oscillations were measured using a rigidly mounted half-model. The pressures were measured using a dynamically calibrated tubing/scanivalve system. A flexible root mounting was used to model a first wing bending mode and to obtain the structural response to various elevon oscillation frequencies throughout the angle-of-attack range.

The change in the attached flow with steady elevon angle was constant with incidence, whilst the separated, vortex flow response reduced with increasing incidence. The steady changes for both surfaces were non-linear with mean elevon angle. The level of vortex response to elevon oscillations reduced rapidly with frequency and angle-of-attack. The response of the attached flow on the upper surface increased with frequency of oscillation. The lower surface amplitude and phase characteristics did not change with angle-of-attack, and had a large effect on the unsteady control derivatives for the complete model. The amplitudes of the unsteady pressures changed with the mean angle about which the elevon was oscillated. For the model with a flexible root mounting, the wing motion was greatest at zero angle-of-attack and reduced as incidence was increased. There was a large damping associated with the root bending mode.

ACKNOWLEDGEMENTS

This programme was jointly funded by British Aerospace Defence Ltd, Warton and The Science and Engineering Research Council (now EPSRC). The author is extremely grateful for their financial support, and the guidance and constructive criticism offered by various members of the Aerodynamics department at Warton, in particular, Tom Kelly, Martin Burtt and Chris Degen (for the original impetus and supervision).

I would like to thank Dr. Norman Wood for supervising the work, offering encouragement when required, and for helping me get a job and two trips to conferences in California!

My colleagues in the office, both past (Doug, Dave, Bill, Uwe and others) and present (Tony, Jon, Mike, Fraser, Mark, Paddy), deserve something for putting up with me (and especially my northern humour). With the help of the rest of the coffee club (Anna, Beccy, Rhona and Mike Seel) they were just about able to keep me sane, or weren't quite able to send me mad, I'm too crazy to work out which.

This thesis is dedicated to my parents, brothers and their families, without whose love and support it may not have been possible.

CONTENTS

NOMENCLATURE

A	half wing area (m^2)
A_η	outboard elevon area (m^2)
C_h	hinge moment coefficient
$C_{m\ a.c}$	pitching moment coefficient, about the aerodynamic centre
C_n	normal force coefficient
$C_p(t)$	pressure coefficient, time history
$C_p(\nu)$	complex pressure coefficient in frequency domain at ν
C_r	root bending moment coefficient
c	chord (m)
$\overline{c}$	mean geometric chord (m)
c_η	elevon chord (m)
d	unsupported width of flexible mounting plate (m)
$h(\nu)$	hinge moment coefficient, transfer function, in frequency domain, at ν (rad^{-1})
i	$\sqrt{-1}$ for complex Fourier Transform notation
$k(t)$	accelerometer acceleration time history (m/s^2)
$k(\nu)$	accelerometer acceleration transfer function, in frequency domain, at ν ($m/s^2 rad$)
$m(\nu)$	pitching moment coefficient transfer function, in frequency domain, at ν (rad^{-1})
$n(\nu)$	normal force coefficient, transfer function, in frequency domain, at ν (rad^{-1})
P_s	Static pressure (N/m^2)
$r(\nu)$	root bending moment coefficient transfer function, in frequency domain, at ν (rad^{-1})
s	semispan (m)
t	time (s)
V_∞	freestream velocity (m/s)
x	chordwise coordinate from apex (m)
y	spanwise coordinate from wing root (m)
$z(t)$	accelerometer displacement time history (m)
$z(\nu)$	accelerometer displacement transfer function, in frequency domain, at ν (m/rad)

α	angle-of-attack, (°)
η	elevon angle (rad)
$\overline{\eta}$	mean elevon angle (rad)
$\eta(t)$	elevon angle time history, (rad)
$\eta(\nu)$	complex elevon angle in frequency domain, at ν (rad)
ν	frequency parameter, $\omega s/V_\infty$ (rad)
ρ	freestream air density (kg/m^3)
ϕ	phase angle (°)
ω	angular velocity (rad/s)

Subscripts

a.c.	about the aerodynamic centre
h	hinge moment
h.l.	hinge line
local	local value
l.e.	leading edge
m	pitching moment
n	normal force
o	amplitude
r	root bending moment
root	root of wing
tip	tip of wing

η	transfer function component in phase with elevon angle
$\dot{\eta}$	transfer function component out of phase with elevon angle

Superscripts

'	real part of complex Fourier transform
"	imaginary part of Fourier transform
®	registered trademark

1. INTRODUCTION.

This chapter gives a general introduction into the area of this research. A detailed literature survey covering the more technical background is presented in Chapter Two.

1.1 Background.

Despite the introduction of stand-off weapon systems and long range air-to-air missiles, the manoeuvrability of combat aircraft is still of vital importance in the within-visual-range (WVR) combat situation. Recent advances in computerised Flight Control Systems (FCS), structural materials and flight control effectors (e.g. thrust vectoring) has led to attempts to produce supermanoeuvrable combat aircraft capable of operating at extreme angles-of-attack, α (i.e. α beyond the stall point) in combination with roll and yaw. Within this region of the flight envelope, however, the flow can be highly unsteady and complex.

1.2 Supermanoeuvrability.

The term "supermanoeuvrability" (also referred to as post-stall manoeuvrability) was introduced by Herbst [1983] following computer simulations of an aircraft with thrust vectoring. The purpose of supermanoeuvrability is to produce a combat aircraft with an enhanced flight envelope, thus giving it an advantage both in beyond-visual-range encounters (BVR) for missile locking, but especially in WVR dog-fight situations. Although the pilots who flew the Herbst computer simulator only used the aircraft's extra manoeuvrability under certain limited situations, it was found to give an important advantage. Fig. 1.1 shows a typical supermanoeuvre, which is now commonly referred to as the Herbst manoeuvre. Here, an aircraft uses its high kinetic energy on entry (Mach No. approx. 0.4, point 1 on figure) to effect a rapid pitch-up to high-α (around 70 degs., point 4) before coning to a new heading (point 5), reducing α (point 6) and rapidly accelerating in the reverse direction to that at entry.

Other standard manoeuvres have been defined to enable different aircraft control concepts to be evaluated, such as those described by Foster et al [1993] and given in fig. 1.2.

1.3 Current Aircraft Programmes Investigating Post-Stall Manoeuvres.

Various aircraft programmes are currently considering the practical aspects of supermanoeuvrability, namely the X-29, F-18 HARV, X-31 and F-16 MATV. The results of the flight trials have been compared by Norris [1992]. Each aircraft has a different configuration : the X-29 has a forward swept wing and a foreplane, and was originally built for high speed testing of this configuration; the F-18 HARV (High-Alpha Research Vehicle) is fitted with thrust vectoring vanes and is also being used to test flow separation control techniques such as forebody blowing; the X-31 (fig. 1.3) has a double delta wing with foreplane and thrust vectoring, and was designed specifically to evaluate high-α flight in a combat scenario; the F-16 Multi-Axis Thrust Vectoring (MATV) has been flown against standard F-16s to determine the combat advantage available from thrust vectoring and relaxed static stability. Although all the above aircraft have been flown in controlled manoeuvres at high-α (typically α=70-80°, and transiently to 115° in the case of MATV (Flight International [1993])), all have experienced problems of "nose-slicing" (yawing of aircraft) and wing rock (a mainly rolling oscillation) due to the large scale separations and non-linear flow over the aircraft under these conditions. Although the above aircraft all employ novel control effectors such as thrust vectoring, they still rely extensively on traditional control surfaces for manoeuvring, e.g. on the X-31, the wing trailing edge elevons are used exclusively to control the aircraft in roll and extensively for control in pitch (Ross [1991]).

1.4 Implications of supermanoeuvrability on Flight Control Systems.

Lang et al [1985] have described the importance of an FCS in dealing with the short time constants associated with the complex sequence of dynamical events experienced by aircraft flying at high-α, in order to reduce the work load experienced by the pilot, allowing him to concentrate on the combat situation. To achieve this, the FCS designer must have sufficient knowledge of the dynamic effects present in such a complex system.

Foster et al [1993] have highlighted the increase in the required number of controls

present on combat aircraft to provide control power throughout the flight envelope (fig. 1.4). They suggest it will be necessary to integrate twenty or more controls on future configurations. The interactions between each control and the aircraft must be investigated to determine the best control combinations and resulting dynamic effects. This has a direct effect on the complexity of the multi-input, multi-output, FCS. This problem may be further exacerbated in the future with the use of adaptive structures. The processing power of parallel computers may well be necessary to control such systems, with localised autonomous control within each deformable area. Integration of such systems into a coherent FCS will pose a significant challenge.

1.5 Aeroservoelasticity.

As new materials and construction techniques have been introduced, the structure of combat aircraft has become more flexible (Felt et al [1978]). This has increased the potential for interactions/feedback between the structural modes of the aircraft, the unsteady aerodynamics resulting from these vibration modes, and the natural unsteadiness within the flow, i.e. the aeroelastic stability labelled in fig. 1.5.

The use of FCSs has further increased the potential for adverse interactions by providing a feedback path between the structural dynamics, the control effectors and the sensors, and by introducing further natural modes into the system. When the unsteady aerodynamic effects are added, the potential for aeroservoelastic/structural coupling instabilities is great. This complete feedback system is shown schematically in fig. 1.6.

On a modern "flexible" combat aircraft, a lot of time is spent determining the stability of this system, as has been demonstrated recently with the delays to the Eurofighter 2000 first flight. To accurately mathematically model the complete aircraft system, and hence determine its stability, it is necessary to have a detailed knowledge of the structural, sensor, actuator and aerodynamic steady and unsteady responses throughout the flight envelope.

1.6 Historical Aspects of Aeroservoelasticity.

Various American aircraft have suffered from some form of aeroservoelastic (ASE) stability problem, as detailed by Felt et al [1978]. As early as 1948, the B-36 bomber was found to suffer from an ASE instability resulting from fuselage bending being fed back through the sensors mounted in the tail to the autopilot. Similarly, a ride control system tested on a B-52 was unstable when crew members walking inside caused oscillations of accelerometers mounted to the structure.

The difficulties in trying to anticipate and analyse every potential instability was demonstrated by experiences with a modified F-4, where with the gear and flaps down, buffeting of the flaps at 23 Hz caused excitation of the pitch rate gyro that powered the stabilisers, thus feeding the excitation back. More recently, an equally unexpected sequence of events on the YF-22, namely the retraction of the landing gear and ignition of the afterburners, caused the gains scheduled within the FCS to allow a pilot induced oscillation to occur. The YF-16 experienced two antisymmetric ASE instabilities (one with, one without tip missiles fitted). An ASE analysis had been carried out for transonic Mach Numbers, but the two instabilities occurred at much lower speeds, again highlighting the need for full analysis throughout the flight envelope. Similarly, the YF-17 had two potential ASE instabilities, although in this case they were predicted and prevented by the inclusion of notch filters in the FCS to remove the excitation frequencies from the feedback loop.

From the above experiences (and no doubt other unreported problems), the Americans have determined the need for a unified approach to the problems of ASE. The ability to accurately predict the structural dynamics of a complex structure has been identified as being of vital importance, as has the need to update the mathematical models used based on correlation with static, dynamic, aeroelastic and aeroservoelastic wind tunnel model test data taken throughout the likely flight envelope.

British aircraft programmes have experienced similar ASE problems (Caldwell [1994]). In 1964, TRS2 was known to have a fin structural coupling problem. At high speed, the aircraft was directionally unstable. High gains were introduced into the feedback of lateral acceleration to the all-moving fin to produce a stable system. To prevent excitation of the structural modes due to the high gains, it was necessary to introduce 8 notch filters into the system. Following ground dynamic testing on the Panavia Tornado, a notch filter was introduced into each axis, and the gyros were relocated to achieve the required level of

stability. When the Jaguar Fly-by-Wire demonstrator was produced, digitisation effects within the sampling system meant anti-aliasing filters had to be used along with various notch filters. Finally, the Experimental Aircraft Programme (EAP) combined a flexible carbon fibre airframe with a powerful FCS on an aircraft unstable in pitch and yaw. Numerous notch filters were required to prevent structural coupling problems, as given in Table One.

1.7 Aims/Objectives of the Research.

During the development of an FCS, the designer often has to use the aerodynamic terms measured/computed at low α in the ASE analysis at all speeds and α, as a complete matrix of aerodynamic terms is often not available. At high-α, this approach can lead to a reduction in the manoeuvrability of the aircraft by defining conservative gains within the system. For example, the reduction in control power at high-α requires a greater gain to be used in the FCS compared to that predicted using low-α results. Without an improved knowledge of both the steady and unsteady aerodynamics in this extreme region of α, software designers may not be able to obtain the potential manoeuvrability for which the aircraft configuration was chosen.

Although often necessary, the introduction of notch filters into an FCS increases the complexity of the system and further complicates the flight clearance procedures/software checks required. Notch filters also introduce phase lags into the system and hence degrade the flight performance. Such effects can be considerable, especially in the supermanoeuvre part of the flight envelope. Again, notch filters often have to be defined following analysis using unrepresentative aerodynamic terms. Lang et al [1985] described how traditional stability derivatives were unable to represent the highly unsteady, separated flow characteristics experienced at high-α. Given a better understanding of the unsteady aerodynamics and structural interactions at high-α, notch filter design could be improved, thus reducing the negative effect on manoeuvrability.

The main aims of the research reported in this thesis were:

(i) to obtain an understanding of the steady and unsteady flow characteristics at high-α resulting from trailing edge control surface motion, and its likely effect on the wing first bending mode,

(ii) to determine the levels of structural coupling and potential for low speed flutter between the two modes (wing bending and elevon rotation) at high-angles-of-attack.
The importance of this work was highlighted by Caldwell [1994]. This knowledge will help FCS designers produce more effective control systems, with fewer notch filters for the supermanoeuvrable combat aircraft of the future.

The research was conducted on a 55° leading edge sweep, delta wing configuration typical of current and proposed combat aircraft. The trailing edge control surface effects were investigated for two main reasons. Firstly, they are one of the main control effectors used on current configurations and will continue to be of vital importance for supermanoeuvrable aircraft. Secondly, the elevon rotation mode is known to be one of the main potential causes for excitation of the wing first bending mode, often the lowest natural frequency for the aircraft. Various researchers (Ross [1989], Orlik-Rückemann [1982], Lang et al [1985]) have suggested the control actuators within the FCS would need to operate to higher frequencies and gains to provide a stable platform at high-α, thus increasing the potential for structural interactions between the structural modes.

The following objectives were set in order to achieve the above aims :

- Measure the steady surface pressures resulting from steady elevon deflections, at high-α

- Measure the unsteady surface pressures resulting from elevon oscillations, at high-α, up to a frequency equivalent to the frequency of a typical first wing bending mode

- Compare the steady and unsteady results to determine the relationship between the two forms of response and hence obtain an understanding of the form of the unsteady response

- Predict the likely effect of the elevon rotation mode on the wing bending mode

- Determine the structural response of the wing to elevon oscillations in the presence of a wing bending mode, to examine the likelihood of low speed flutter occurring.

1.8 Outline of Test Techniques

A brief description of the tests conducted is now given. A rigid wind tunnel half-model was constructed with 157 pressure tappings in the upper surface. A half-span trailing edge elevon was operated through a closed loop control system, allowing small amplitude sinusoidal oscillations to be produced. The unsteady pressures at various α, mean elevon angle, η, and elevon amplitude, η_0, were measured.

The model was altered to allow a flexible root mounting system to be employed. This introduced a root bending mode into the wing. The structural response resulting from elevon oscillations were measured to determine the level of aerodynamic/ structural interaction.

All tests were carried out at low speeds for α=0° to 40°.

1.9 Outline of rest of thesis.

Chapter 2 - summary of existing work covering delta wing aerodynamics, unsteadiness associated with vortex flow and their response to forcing, steady and unsteady control effects, problems associated with aeroservoelasticity, and steady and unsteady computational prediction techniques. The areas where information is lacking are highlighted.

Chapter 3 - desriptions of the wind tunnel apparatus, including the closed loop elevon control system, the unsteady pressure tappings and flexible root mounting system. The data acquisition system is also detailed.

Chapter 4 - the calibration of the tunnel centreline pressure and model pressure tubing system are presented. The wind tunnel test procedure is discussed.

Chapter 5 - the analysis techniques for both steady and unsteady pressures are detailed as are

the integration routines to obtain the overall forces and moments. The software routines created to implement these equations are described.

Chapter 6 - pressure results for steady elevon deflections are presented. The changes with incidence and elevon angle are discussed.

Chapter 7 - unsteady pressure results for elevon oscillations are presented. The effect of oscillation frequency, angle-of-attack and mean elevon angle are discussed for the upper and lower surfaces to determine the form of the unsteady responses. The results are compared to the steady derivative values.

Chapter 8 - results of the flexible root mounting tests showing the structural response to elevon oscillations at various frequencies and incidences.

Chapter 9 - conclusions are drawn from the previous three chapters for the steady and unsteady responses of the flow to elevon motion, and the likely excitation of a root bending mode.

Chapter 10 - areas requiring further work are highlighted in Chapter 10.

Table1 - Notch Filter solutions, Caldwell [1994]

Aircraft	Feedback	Solution
TSR-2	Pitch Roll Yaw N_z A_y	1 NF 2 NFs, 1 2nd O Lag, 1 Lag / Lead 2 NFs 1 NF, 1 1st O Lag 2 NFs
Jaguar	All Axes	1 1st Order lag (4Hz), 1 NF (10Hz)
Tornado	Pitch Roll Yaw	1 NF (11.5Hz) 1 NF (11Hz) 1 NF (5Hz skew notch)
Jaguar FBW	Pitch Roll Yaw N_z A_y	1 AAF (12.5Hz), 1 an.(25Hz), 2 dig.NF (11Hz,12Hz) 1 AAF (12.5Hz), 1 an.(8Hz), 1 dig.NF (12Hz) 1 AAF (12.5Hz), 1 dig.NF (12Hz) 1 AAF (12.5Hz) 1 AAF (12.5Hz)
EAP	Pitch Roll Yaw N_z A_y	0 AAF (AMSU gives AAF), 1 'analogue', 6 dig.NF 0 AAF, 2 'analogue', 1 dig.NF 0 AAF, 2 'analogue', 1 dig.NF 0 AAF, 2 'analogue', 1 dig.NF 0 AAF, 2 'analogue', 1 dig.NF

AAF - Anti-Aliasing Filter
NF - Notch Filter

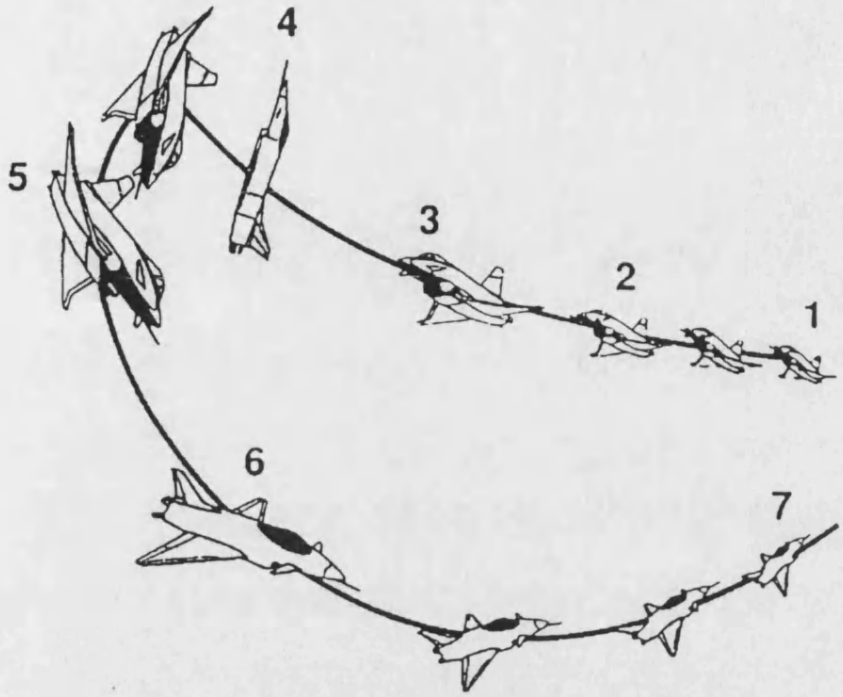

1. X-31 enters maneuver at high speed (Mach 0.4 or greater)
2. X-31 decelerates rapidly while increasing angle of attack
3. Exceeds conventional aerodynamic limit (stall) - needs thrust vectoring for control
4. Angle of attack increases to maximum of 70 degrees
5. X-31 rapidly "cones" to new flight direction
6. X-31 lowers nose and accelerates to high speed
7. X-31 now flying in opposite direction

Fig. 1.1 - Herbst Manoeuvre, Weeks and Nagaraja [1993]

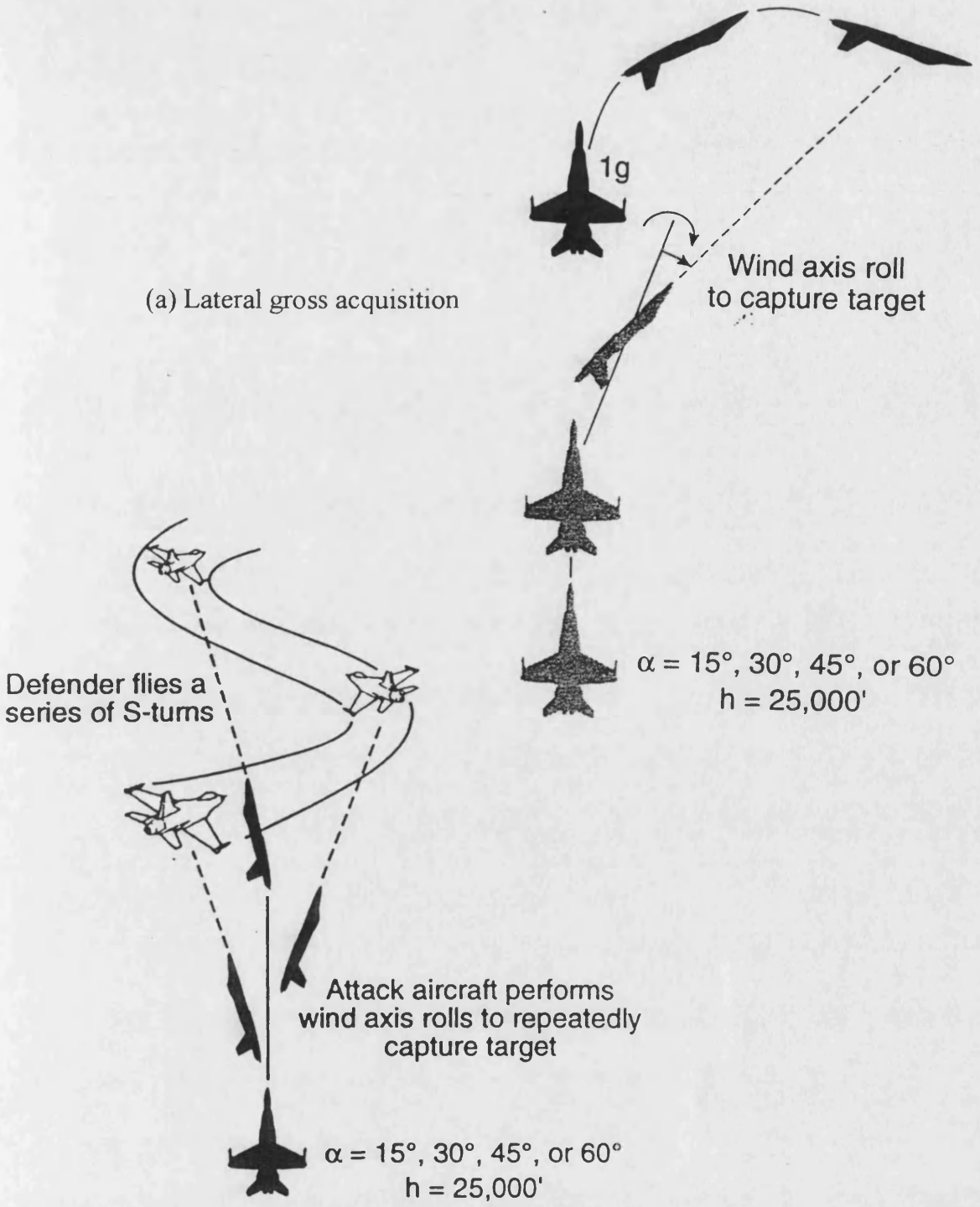

Fig. 1.2 - Illustration of evaluation manoeuvres, Foster et al [1993]

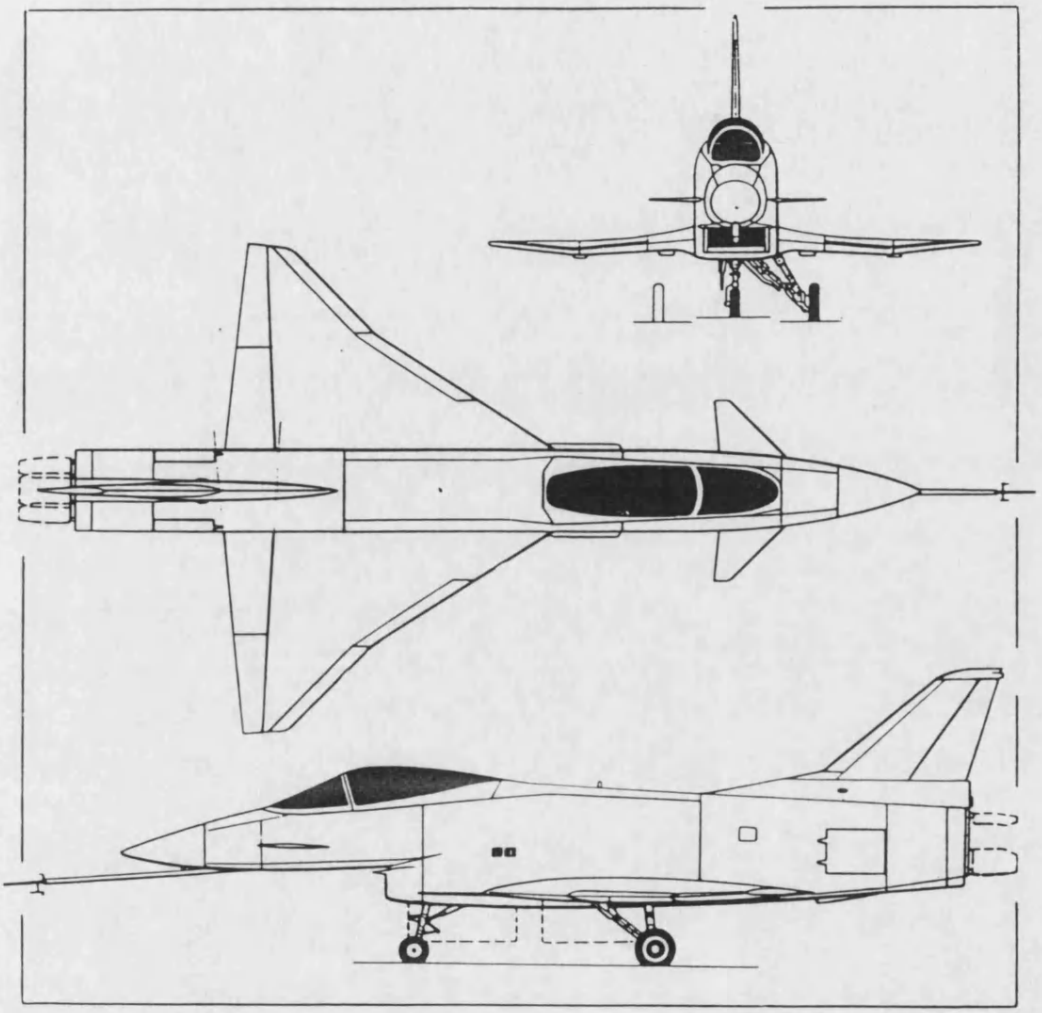

Fig. 1.3 - X-31 experimental aircraft, Braybrook [1990]

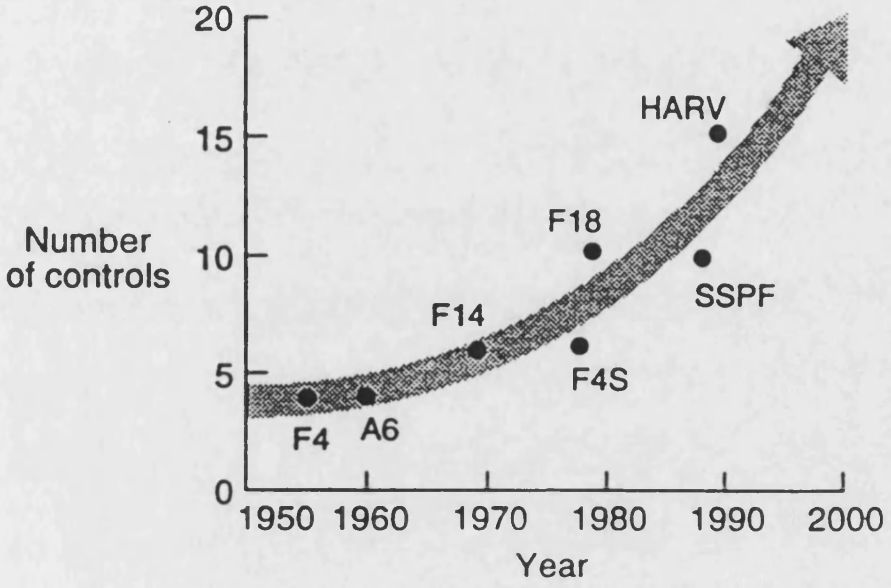

Fig. 1.4 - Trend in number of control effectors, Foster et al [1993]

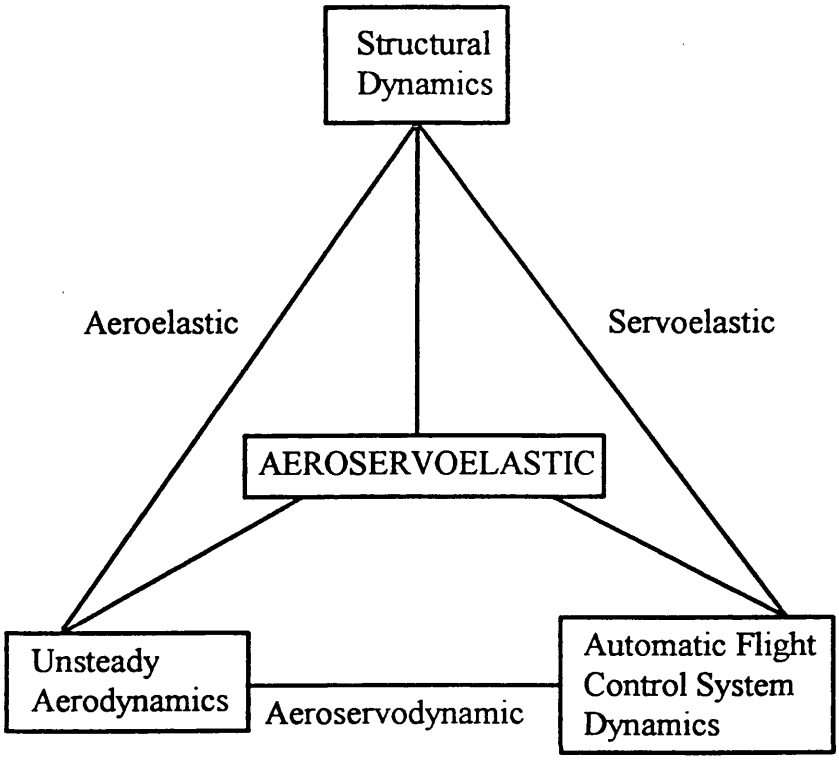

Fig. 1.5 - Aeroservoelasticity Interaction Triangle

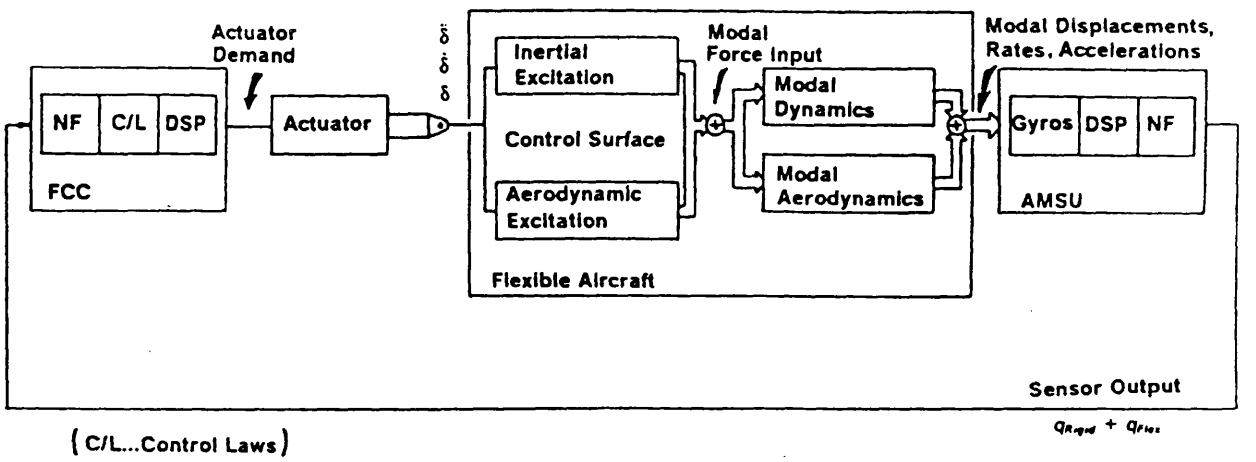

AMSU - Aircraft Motion Sensor Unit
DSP - Digital Signal Processing
NF - Notch Filter
δ- Trailing Edge Flaperon Deflection

Fig. 1.6 - Structural coupling loop, Caldwell [1994]

2. LITERATURE SURVEY.

Little work on the unsteady aerodynamics at high-α resulting from structural modes has been reported within the public domain. There are, however, various areas of related research of importance to this thesis. The following sections in this chapter are put into context by re-emphasising the main features of this research :

- o The tests deal with low speed aerodynamics at high-angles-of-attack.
- o A delta wing planform was tested, typical of combat aircraft configurations.
- o The main investigations centred around the unsteady pressures resulting from oscillation of a half-span trailing edge elevon at frequencies matching a typical first wing bending mode, in order to predict the likely structural interaction between the two modes.
- o The actual response of a rigid wing, with root flexibility in roll, to elevon oscillations was measured.

2.1 General Delta Wing Aerodynamics.

Delta wing aerodynamics are dominated by the presence of leading edge vortices on the upper surface of the wing. At incidence, the upper and lower surface boundary layers separate from the surface at the leading edges, forming shear layers. The shear layers roll up to form a pair of contrarotating vortices above and inboard of the leading edges, fig. 2.1. Inboard of the vortex core, the flow reattaches to the surface. The adverse pressure gradient on the wing outboard of the primary core causes the boundary layer to again separate from the surface forming another shear layer. This rolls up and forms a secondary vortex outboard and below the primary vortex. It is thought this process continues forming further vortices, but these have only been observed occasionally at low Reynolds numbers (Hummel [1967]). The Reynolds number of the tests also affects the balance between, and size of both the primary and secondary vortices and hence the surface pressure distributions (fig. 2.2). As the

Reynolds number reduces, the size of the secondary vortex increases, whilst the primary reduces and moves inboard. However, there is no net effect on the force or moment coefficient values. A schematic of a typical surface flow visualisation result is given in fig. 2.3, showing the separation and reattachment points.

As the angle-of-attack is increased, the strength of the shear layer and hence vortices increases. At a fixed incidence, increasing the sweep angle reduces the strength of the vortex structures (Zohar and Er-El [1988], tested leading edge sweeps between 55° and 74°).

At some point in the flow, the vortices burst and although rotation is still present in the burst portion of the vortex (but with reduced circulation compared to the unburst portion of the vortex, Visser and Nelson [1993]), the structure is less distinct and has a greater turbulence level than the unburst vortex. At the core of the burst vortex, the axial velocity is greatly reduced, and can even be reversed, giving a region of stagnated flow. As α increases, the burst or breakdown point moves forward onto the wing until at some incidence, dependent on wing geometry, the leading edge vortices are fully burst from the apex. Typical variation of the angle-of-attack for which the breakdown first occurs over the wing, for various sweep angles is presented in fig. 2.4. For the wing geometry tested in the research (leading edge sweep of 55°), the figure suggests the vortex burst will be above the wing for $\alpha>12°$.

The mechanism of vortex breakdown is not yet fully understood. Two forms of breakdown have been observed in wind tunnel experiments on delta wings, termed bubble and spiral modes, as shown in fig. 2.5. Payne et al [1985] observed that the type of breakdown observed would sometimes change between the two types, each having a different burst location on the wing. Lambourn and Bryer [1962] discussed the main features leading to vortex burst. They found that disturbing the shear layer had no effect on the burst location and concluded the burst was not the result of amplification of small upstream disturbances. They determined the main factor to be the longitudinal pressure gradient outside the vortex, the effect of which is amplified inside the core. The pressure gradient inside the viscous core results from the following items:

- increasing vorticity with distance from the apex causes a reducing axial pressure with distance from the apex
- diffusion of vorticity within the viscous core results in rising axial pressure
- deceleration of the longitudinal velocity component outside the vortex, associated

with the presence of the trailing edge causes a positive external pressure gradient which is amplified within the core.

The low total pressure at the axis of the vortex means any change in this balance could easily cause stagnation of the flow at the core and hence vortex breakdown.

The deflection of a trailing edge control surface alters the external pressure gradient and hence burst point, a downward deflection reducing the pressure gradient towards the trailing edge causing the burst point to move aft.

Several attempts have been made to determine the parameter that will allow the prediction of vortex breakdown, e.g. Hall [1972] and more recently by Jumper et al [1993]. As yet no single parameter applicable to all situations has been determined/validated, thus making the prediction of breakdown point very difficult.

2.2 Natural Unsteadiness in Vortical Flows.

As was discussed in Chapter One, the vortical structures formed above delta wings have a natural unsteadiness associated with them, dependent on whether the vortex is burst or unburst. The frequency content of the unsteadiness is of interest for two main reasons:

- any structural modes with a frequency close to that of the natural unsteadiness could be excited by the flow (as in the case of fin or wing buffeting)

- control oscillations (or more correctly, the ability of an actuator to move the control at this frequency) could cause a resonance to be set up between the aerodynamics, the structure and the FCS.

The unsteadiness present within the burst portion of a vortex appears to be different than for an unburst vortex, hence they will be treated separately.

2.2.1 Unsteadiness within an unburst vortex.

Squire [1961] noted the presence of discrete streamwise vortices in the leading edge shear layers, as shown in fig. 2.6. Gad-el-Hak and Blackwelder [1985] (and various other researchers) documented similar unsteady vortices. Lowson [1988] concluded these structures were the result of classical two-dimensional Kelvin-Helmholtz shear layer instabilities. Navier-Stokes numerical simulations by Gordnier and Visbal [1994] also predicted the existence of these unsteady structures. Other researchers, however, have found these vortices to be stationary, as in fig. 2.7. Reynolds and Abtahi [1989] have been able to produce both steady and unsteady forms and found them to be very sensitive to any external disturbances. Turbulence within the flow could well cause shedding of these discrete vortex structures.

Gursul [1994] has investigated the unsteady variations within burst and unburst vortices above wings by measuring wing unsteady pressures and using hot wire probes within the vortex. He did not observe coherent pressure fluctuations within an unburst vortex, suggesting that even if there are discrete vortices within the shear layer, they do not result in significant unsteady pressures.

Becker and Gravelle [1985] measured the unsteady pressures on a rigid half-wing at various steady incidences and Mach numbers to determine the frequency content within separated flow. The Power Spectral Densities (PSDs) of the surface pressures were found to be very broadband from 0-100 Hz, with no particular peak frequency. The amplitudes increased greatly between α=6 and 8° (as separation from the leading edge became fully developed) but then only increased slightly with incidence. The modulus of the PSDs was similar for Mach numbers between 0.3 and 0.6, but reduced as Mach number approached 0.9. The coherence of the unsteady pressures (even neighbouring ones) was low suggesting little structure to the unsteady pressures and was more typical of general turbulence rather than from periodic, discrete vortical structures.

2.2.2 Unsteadiness within a burst vortex.

As already mentioned, Gursul [1994] could only measure coherent pressure fluctuations within the burst portion of the vortex and found them to be in the form

of helical waves resulting from instability of swirling breakdown wake flow. The frequency of the pressure fluctuations, when multiplied by (x/U_∞), where x is the distance from the apex, was found to be constant at each α, but to decrease as α increased. Because the frequency changes with distance from the apex, it is unlikely to cause significant excitation of a flexible structural mode as the excitation would be very localised and countered elsewhere. Also, the unsteady frequency within the burst vortex at high-α is equivalent to twice the first wing natural mode frequency for a typical combat aircraft in this situation, and is even greater at lower incidence.

2.3 Characteristic Response of Leading Edge Vortices to Forcing.

The review paper of Greenwell and Wood [1994] concentrated the great volume of data published relating to vortex response on pitching delta wings to produce a transfer function modelling the response of vortex breakdown location for changing angle-of-attack. They produced a second order fit to the experimental data, with a damping ratio of 1.67 and natural frequency 2.0, giving the amplitude ratio (ratio of the range of movement of unsteady burst location during the oscillation cycle, to the difference in burst location as measured in steady tests at the maximum and minimum α experienced during an oscillation) and phase angle (between α and incidence for breakdown) shown in fig. 2.8. Within the context of the present work, this figure suggests that if the elevon motion causes a similar vortex response as a change in α, the breakdown motion will be significantly attenuated with a large phase lag.

Huang and Hanff [1993] have also produced a prediction technique for the dynamic motion of the breakdown location based on measurements from steady results and pitching motions. The method allows for the steady location of the breakdown, the quasi-steady (camber) effects (e.g. during pitching, the actual angle-of-attack on each part of the wing varies along the chord, causing a camber effect) and the changing range of positions (x) at which breakdown occurs over the wing, as the mean α increases. These results, however, were based on tests at low frequency parameters compared to those needed to predict the effect on structural modes.

Tests involving changing the freestream velocity of flow over a delta wing (Gursul and

Ho [1993]) suggested that if no breakdown was present, the vortex would respond in a quasi-steady manner over the range of frequencies of interest in this current research. However, with a burst present, Gursul and Ho observed a large time lag for the change of breakdown location after a step change in freestream velocity.

Unfortunately, much of the work on forced motions has been for large amplitude oscillations (especially in pitch) where the breakdown position has varied over at least half the root chord. Since aerodynamics at high-α tend not to be linear, the response of the vortex breakdown location to small amplitude motions (such as wing vibration mode) may not obey the same apparent rules.

2.4 Control Effects - Experimental results and Comparison with Predictions.

Very little work has been published for unsteady control effects on delta wings, and even less for high-α effects. This was highlighted as a deficiency in the literature by Ross and Thomas [1979] in their "Survey of Experimental Data on the Aerodynamics of Controls in the Light of Future Needs". As a result, this section of the chapter deals mainly with experimental data (and comparisons with theoretical predictions) for 2-d sections, high aspect ratio wings and delta wings at low-α. Although comparisons with theory are described, the details of the prediction techniques are only summarised, greater detail being given in section 2.7.

2.4.1 Early tests.

Early attempts to determine unsteady control effects were limited by the instrumentation and transducer technology available at the time. This is typified by Bergh [1955] who used a variable spring suspension system to determine the various control derivatives necessary for flutter analysis, i.e. at high subsonic Mach numbers. Comparisons against an unidentified inviscid analysis code showed similar trends but magnitudes were in error by 50-100%.

A similar experimental technique was developed by Bratt et al [1957] who used the change in system natural frequency between wind-on and wind-off tests to determine the hinge moment stiffness and damping terms for a full span control on a

60.5° delta wing. However, all the tests were conducted for α=0°, the main interest being in the effect of Mach number on the hinge moments. This highlights the reason for development of swept wings at the time, i.e. to reduce the wave drag at high speed, and hence the need to determine the flutter speed characteristics. Although of interest, these tests are of little relevance to the present work as they are for low-α where no leading edge vortices are present, and high subsonic Mach numbers where compressibility and 'speed of transmission' of unsteady effects are important. Unusual control surface geometries were also investigated to determine their effectiveness at higher Mach numbers (Guyett and Curran [1961]).

2.4.2 Scale effects.

A review of published data on 2-d and 3-d models was carried out by Moore [1969] to determine the scale effects on unsteady control surface derivatives. He concluded that it was better not to fix transition on the model as fixing it produces a boundary layer on the control that is too thick relative to the chord. The effect of Reynolds number, for free transition, on aerodynamic stiffness values is small, and the effect on damping is even lower. A later report by Försching [1981] contradicts Moores report, stating that unsteady hinge moments are "decisively dependent upon Reynolds number". Försching draws this conclusion from a report by Kienappel and Round [1980]. Kienappel and Round, however, state that changing the test velocity (between 20m/s and 50m/s - Re number = 1.36 to 3.4 million based on chord) "produced similar changes [to pressures and aerodynamic coefficients] to varying the frequency". Unfortunately, the results are not plotted for constant frequency parameter at different Reynolds numbers and hence it is not possible to quantify any scale effects from these results. The lack of data (at the same α, same mean flap angle etc.) also makes it impossible for this author to produce the necessary plots.

It does not appear that the problem of scale effects has been fully resolved. Due to the limitations of the wind tunnel used for the investigations of this thesis, it was not possible to perform tests over a sufficiently large Reynolds number range to add anything to the discussion on scale effects.

2.4.3 Other parameter effects.

Kienappel and Round [1980] also conducted other parameter tests on the 2-d section, as described below. As the frequency of oscillation was increased, the real (in phase) unsteady pressure component decreased while the imaginary (out of phase) component increased, i.e. the phase angle between the unsteady pressures and flap increased. The change in the real component was mainly at the leading edge of the section, the smallest change being at the slot between the wing and the flap (see fig. 2.9). The largest change in imaginary component occurred on the flap itself. As can be seen from fig. 2.9, the unsteady pressures on the control lead the flap motion[1]. This reduces to a lag at the leading edge of the main section. The rest of the findings can be summarised as follows :

- the unsteady pressures were affected by the mean flap angle, due to flow separation over the flap
- the unsteady pressure components were not greatly affected by the mean incidence of the wing
- the size of the slot between wing and flap significantly affected the unsteady pressures, especially as α increased.

Due to the detailed nature of the results presented by Kienappel and Round, the report will form a good basis for comparison with the results presented later in the thesis.

Mabey et al [1979] tested a part span control on a 36.7° sweep aspect ratio 6, half model of a typical transport aircraft. Again, the measurements were primarily concerned with variation of the aerodynamic coefficients with Mach number. A comparison was made with the inviscid linearised theory for 3-d flow developed by Marchbank [1978]. Again, the comparison was poor. The authors suggest the boundary layer thickness is the main cause of error, however, the model was also known to flex during the tests causing further error.

Geissler [1981] compared his results for a 2-d section with flap to a source/doublet surface panel method. The code considered the system as two elements, each with their own modelled wake and 2 Kutta conditions. During the experiments, the flow was seen to separate in the gap between wing and flap causing a reduction in the peak suction and real pressure component. This separation also caused additional unsteady pressures and interacted with the flow response to flap oscillation.

1 - Additional notes on fig. 2.9 are given on the following page.

Additional notes on fig. 2.9.

The modulus of the unsteady pressures given on fig. 2.9 (labelled 'MOD (DCP)') show that the pressure response near the leading edge of the section decreases as the frequency increases, whilst the reverse is true over the elevon itself. This suggests there are two different mechanisms by which the elevon motion affects the aerodynamics. The flow over the elevon is influenced greatly by the induced angle due to the angular velocity of the elevon. As the frequency increases, so the amplitude of this induced incidence increases. The angular velocity also leads the elevon angle by 90°, hence the phase angle (labelled 'ARG(DCP)' on fig. 2.9) of the pressures on the elevon increase with frequency as the influence of the velocity induced incidence also increases.

The section upstream of the elevon is influenced more by changes in the overal flow field. The speed and amplitude of response of the overal flow is such that the unsteady pressures towards the leading edge show a reducing amplitude and increasing phase lag with increasing frequency. These concepts are discussed further in Chapter 7.

Since the theory could not predict either of these effects, the comparison was not good.

No literature has been found relating to the unsteady effects of trailing edge control surface motion on a swept wing at high angles-of-attack. This was one of the main reasons for the instigation of this research.

2.5 Aeroelasticity/Aeroservoelasticity.

An excellent introduction to aeroelasticity is given by Broadbent [1954], starting from static aeroelastic stability to two mode systems and beyond. An outline of aeroservoelasticity was given in section 1.5, herein.

As was explained earlier, aeroservoelastic stability depends on the interactions between the flexible structure, the unsteady aerodynamics resulting from control and structural motion, and the Flight Control System (FCS), including the natural frequencies within the software model and the response of the sensors and control actuators.

2.5.1 Natural modes of the structure.

The first four wing structural modes for an F-16 with no underwing stores are shown in fig. 2.10. These are typical for a combat aircraft. Becker [1991] shows the lowest frequency modes for a modern combat aircraft of carbon fibre construction. The structural model includes the wing, fuselage, engine and wing stores etc.. It is interesting to note the effect of adding an underwing fuel tank to the aircraft, the first three modes all involving significant tank motion as well as wing bending (modes 2 and 3). As a result, the structural modes and resulting aeroservoelastic stability for each configuration must be investigated, e.g. with and without underwing stores and even for differing fuel loads. The aerodynamic and structural terms within the FCS would also be different for each case. The fourth mode is the result of engine pitch freedom and flexible forward fuselage - a common problem on modern canard aircraft.

2.5.2 Unsteady Aerodynamics resulting from Structural Motion.

The most applicable results are those of Becker [1991] [1985]. Becker was able to measure the unsteady pressures resulting from small amplitude, harmonic wing roll oscillations on a rigid half model. Some typical results, in terms of real and imaginary components, for M=0.3, α=12.5° and 25° at two different frequency parameters are shown in fig. 2.11. At α=12.5° there is an unburst vortex above the wing, whilst at α=25°, the vortex is likely to be burst from near the apex. The difference in the upper surface (vortex side) response can be seen in the results, even allowing for the difference in frequency parameter of the two sets of data, the unsteady response of the unburst vortex being greater than of the burst vortex, particularly under the core. From the results, Becker was able to conclude that aerodynamic damping of the elastic modes would be present at least up to α=40°. He warns, however, that greater mode excitation may result from trailing edge flap rotation modes than was measured from the rolling oscillations due to the increase of trailing edge real and imaginary pressures found at high-α. Becker also states that high-α effects must be considered in aeroservoelastic stability predictions under these conditions.

Becker also describes a technique for improving theoretical predictions for all structural modes using experimental results from just one mode (e.g. in this case from the rolling mode).

2.5.3 Importance of Actuator and Sensor Models at high-α.

Another aspect of aeroservoelastic stability is the need to model the characteristic responses of actuators/sensors and their coupling to the structure. Brenner [1993] conducted a study of these effects using a numerical model of the F/A-18. By altering the order of the actuator/sensor models, he determined that the complex situation at high-α requires a detailed model of actuator/structural coupling to accurately predict the stability of the aeroservoelastic system. He also states, however, that the unsteady aerodynamics associated with the modal responses are relatively insignificant due to the low dynamic pressure where high-α manoeuvres can be used, contradicting the findings of Becker [1991]. It is not known, however, whether the aerodynamic terms within the numerical model used by Brenner were

based on high-α results (numerical or experimental) or from low-α results as is often the case. Beckers conclusions were definitely based on model measurements and subsequent aeroservoelastic stability calculations. This may explain their difference of opinion on the importance of modal aerodynamics.

2.5.4 Aeroservoelastic Investigations.

Various aeroservoelastic investigations have been conducted for fighter aircraft configurations. Abel [1992] has recently detailed the various programmes being conducted by NASA Langley, as follows :

- Active Flexible Wing Program - a wing/fuselage configuration mounted onto a free-to-roll sting. By using a deliberately flexible wing, it is intended to increase the control power available, and hence manoeuvrability and to reduce the structural weight. The system was also developed to allow suppression of flutter and to reduce the manoeuvring loads. A 50% reduction in wing torsional loading experienced during a typical roll manoeuvre has been achieved. A block diagram of the flutter suppression system is shown in fig. 2.12. For such systems to be effective, a knowledge of the active structure, actuator responses and resulting aerodynamics is essential. Further details of this programme have been given by Noll et al [1989].

- Rigid, unswept, half wings have been mounted to a structure with flexibility in pitch and plunge (heave). This apparatus has been used primarily to compare the aerodynamics resulting from such motions with computational predictions, and hence to compare transonic flutter speed characteristics.

- Investigations into the use of adaptive structures - flutter suppression using piezoelectric materials. The above flexible mount, fitted with piezoelectric actuators has been used to investigate the control systems necessary for such adaptive structures.

The idea of an active aeroelastic control system has been applied to the F-16 aircraft. Medina et al [1992] conducted an analytical investigation into the concept whilst Pendleton and Lee [1992] have constructed and structurally tested a fifth scale, composite wing which will be tested in a wind tunnel to determine the aerodynamic coefficients needed for the complete flight control system.

2.6 Prediction Techniques for Steady Aerodynamics of Delta Wings at High-α.

Although it is not the purpose of this research to carry out comparisons with numerical predictions, the industrial sponsor may well use the results to compare with the aeroservoelastic techniques they currently use. Hence, it is important to have at least a knowledge of the various techniques employed. The flow separation at the leading edge of delta wings at high-α immediately discounts results from many of the traditional computational techniques, e.g. source/doublet or vortex panel methods, as they can not deal with separated flow.

One prediction technique that has been used and developed by various researchers is the Leading Edge Suction Analogy (LESA) of Polhamus [1966] [1971]. The lift produced by a delta wing is broken down into the attached flow and vortex contributions. The analogy assumes that with reattached flow, the normal force on the upper surface required to maintain the flow about the vortex is the same as the leading edge suction force required to maintain attached flow about the leading edge. A typical example of C_L vs α, predicted by this technique is shown in fig. 2.13. The apparent accuracy of the technique (as shown for example by Er-El and Yitzhak [1988]), despite the lack of a firm analytical foundation for the technique (Coe [1974]) has led various researchers to develop the basic analogy to deal with more complex configurations and even to predict the unsteady derivatives for rigid body motion (see following section).

Coe [1974] has developed a model using line vortices of varying strength to represent the primary vortices above a delta wing. Entrainment of flow into the cores is allowed for by sinks distributed along the axes of the cores. The result of the analysis is an expression similar to the LESA. Unfortunately, for Coe's technique, it is necessary to know the location

of the cores to perform the calculations! Other similar methods, employing for example a line vortex with feeding sheet linked to the leading edge have also been produced.

All the above methods suffer from the same main problem - their inability to predict the breakdown of the vortices. Unless a parameter to determine when breakdown will occur (see section 2.1) can be found, further use of these 'preliminary design' type techniques will be limited and will have to be corrected using semi-empirical approaches where breakdown is estimated using existing data.

Euler codes have been used to predict the leading edge vortex flows at high-α. However, as pointed out by Fujii and Kutler [1980], the Euler equations can not actually describe flow separation mathematically; instead the separation at the leading edge results from numerical dissipation within the solution algorithm. For the same reason, Euler codes do not predict the presence of secondary vortices, causing significant discrepancies with experimentally measured flow fields and pressure distributions. Euler codes also can not allow for the reduction in total pressure associated with the rotational vortex flow.

Instead, Navier-Stokes (NS) codes are seen as the way to predict accurately the separated flow over delta wings. Although many researchers have worked (and continue to work) on NS solvers, only two groups will be highlighted here.

Thomas et al [1987] used the thin layer approximations to the 3-d, time-dependent, compressible, Navier-Stokes equations for laminar flow (i.e. no turbulence model was employed). The grid topology for solution of the low speed flow over an aspect ratio one, delta wing is shown in fig. 2.14. The predictions were compared with the results of Hummel [1973] (see fig. 2.15). It has been suggested that the Hummel results show a transition from laminar to turbulent flow resulting in the change in relative size of primary and secondary vortices towards the trailing edge. The predictions, which assume laminar flow, are hence less accurate in this region. Otherwise, the comparison is good, with both primary and secondary vortices being predicted. Fig. 2.16 shows the presence within the computational solutions of a bubble type vortex breakdown (where U/U_∞ is negative showing a region of recirculating flow within the core). The solution gives the breakdown location at 0.6 of the root chord back from the apex (0.6c), whilst experimental results by Payne et al [1986] give the breakdown at 0.4c under the same conditions.

Fujii and Kutler [1980] also solved the thin-layer, Navier-Stokes equations, but with

the inclusion of a two-layer algebraic viscosity model developed by Baldwin and Lomax [1978]. The example solutions in the paper are for the same planform as the results of Hummel, but for a rounded rather than sharp leading edge. Hence, the comparisons reproduced in fig. 2.17 are not as good as those in fig. 2.16 (Thomas et al) where no turbulence model was used. The large negative pressure peak in the computational solution in fig. 2.17 is a consequence of the rapid expansion of the flow round the leading edge.

2.7 Prediction of Unsteady Aerodynamics.

This section details prediction techniques of relevance to the current work, though none directly relate to the unsteady aerodynamics resulting from control surface motion on a delta wing at high-α.

2.7.1 Prediction of unsteady aerodynamics resulting from wing pitch and roll modes.

As mentioned in section 2.6, researchers have developed the Leading Edge Suction Analogy of Polhamus to predict the unsteady aerodynamic effects of mainly rigid aircraft modes. This implies relatively low frequencies compared to any structural modes. The analysis of Boyden [1971] is typical. He extended the LESA to predict the roll damping on slender wings using a subsonic lifting-surface solution to compute the distribution of the leading edge suction force due to rolling and the suction analogy to determine the resulting vortex effect on roll damping.

Ericsson and Reding [1975][1977][1978] similarly started from the LESA results for steady trends and used an altered slender wing theory based on experimental results to predict the unsteady components.

The above techniques are only useful within a preliminary design stage, both being semi-empirical in nature.

One of the most detailed techniques of this type is that of Huang and Hanff

[1993] for the prediction of normal force on a delta wing rolling at high incidence. Using the breakdown location equation already described in section 2.3 (based on experimentally measured results of steady and unsteady locations on pitching wings), the technique again uses the LESA. Comparisons with measured normal force on a rolling 65° delta wing are reasonable, but show significant differences at higher frequency parameters, suggesting the dynamic breakdown location model may not be completely satisfactory.

Strganac and Mook [1986][1990] have used an unsteady vortex lattice method to predict the unsteady aerodynamics on various configurations due to motion. By combining the code with a structural solution algorithm, it has been possible to determine the motion response of a wing to changes in external conditions, e.g. a sudden gust. The combination of aerodynamic and structural solvers into a single code can, however, increase the solution time for complex situations, compared with the technique of determining the aerodynamic response for known modes and combining this with structural characteristics in a matrix solution. In this way, the aerodynamics and structural modes need only be calculated once.

Work is currently underway to produce suitable solution algorithms for the unsteady Navier-Stokes equations. The use of supercomputers and parallel processing has made the solution of such complex equations, in an economic manner, possible. Another aspect of this work is the need to deal with a solution grid which must be able to cope with a moving body. This is usually acheived by deforming the grid as the geometry oscillates. This further complicates the equations, mainly within the grid generation algorithm.

2.7.2 Prediction of control surface induced unsteady aerodynamics.

As early as 1938, Von Kármán and Sears [1938] detailed the mechanisms behind the aerodynamic response to wing motion. Beginning with statements that the total circulation in the flow must be zero and that wake vortices are translated at the freestream velocity, they were able to determine the characteristic aerodynamic response of a 2-d wing to motion. The expressions for unsteady lift and moment were composed of three terms : the 'apparent mass' of the fluid due to acceleration of the

fluid present in a flow without circulation; the quasi-steady contribution of the aerodynamics resulting from the instantaneous angle-of-attack etc, and the contribution of the wake vortices to the build up of lift as they are translated downstream. Fig. 2.18 shows the vorticity distributions induced on an aerofoil by a wake vortex at various locations from the trailing edge. This analysis forms a useful tool in the later interpretation of the results of this thesis, as control motion causes a similar change in circulation.

A solution to Laplace's equations for incompressible, 2-d flow for a complex perturbation in velocity potential was produced by Theodorsen [1935]. By using the boundary condition of flow fixed to the flat plate aerofoil and employing the Kutta condition at the trailing edge, a loading equation involving mathematical functions, now commonly referred to as the Theodorsen function, was created. Küssner and Schwarz [1940] extended the theory to deal with a moving hinged flap. The accuracy was further improved by Zwaan [1968] who used new loading functions to deal with the discontinuity in downwash at the leading edge of the deflected flap. The development of the technique to 3-d geometries was conducted by Küssner [1940].

A similar analysis technique was developed by Jones [1943][1948]. Steady experimental results gave the loading functions which were then used to produce an equivalent profile. This was used for solutions on oscillating aerofoils. Sinnott [1953] extended the method to deal with oscillating control surfaces.

All these techniques assume attached, linear, and in most cases, incompressible flow, making their use at high-α, for delta wings limited.

Various panel methods have been extended to unsteady flow, as typified by Lan [1974][1979] who used an unsteady vortex lattice method. This suffers the same problems as above.

In general, the results of all these forms of solution do not compare well against experimental results - see section 2.4.

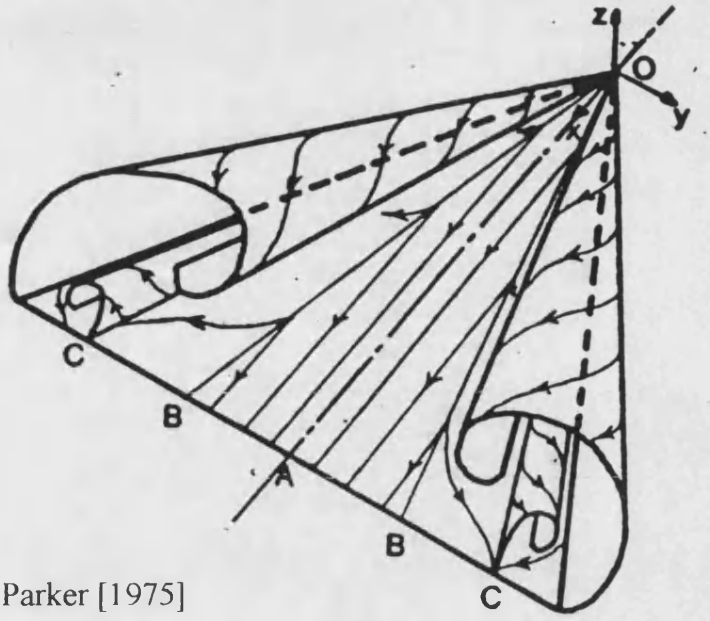

Parker [1975]

B - primary attachment C - secondary separation

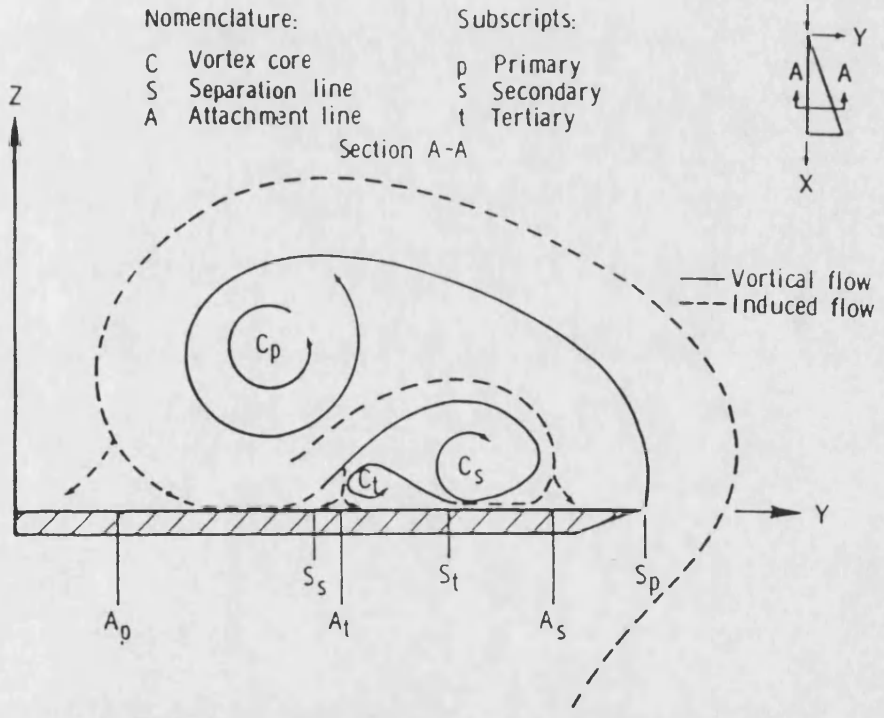

Thomas et al [1987]

Fig. 2.1 - General vortical flow structure

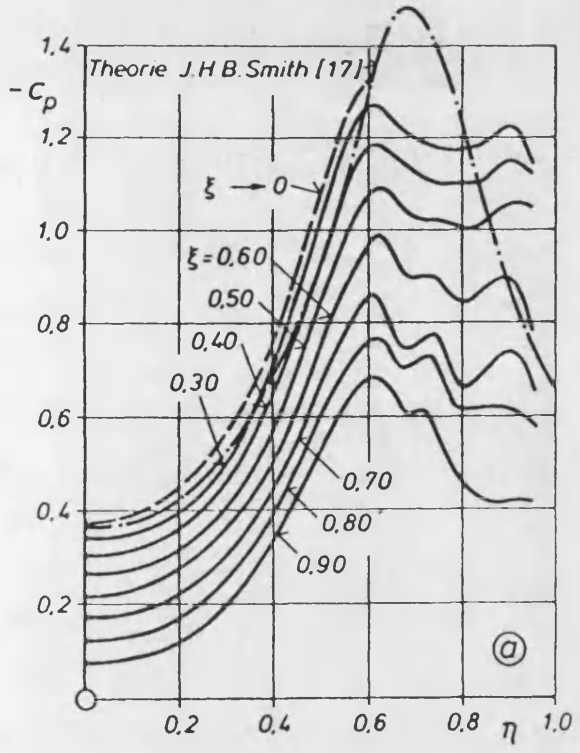

Re = $9*10^5$

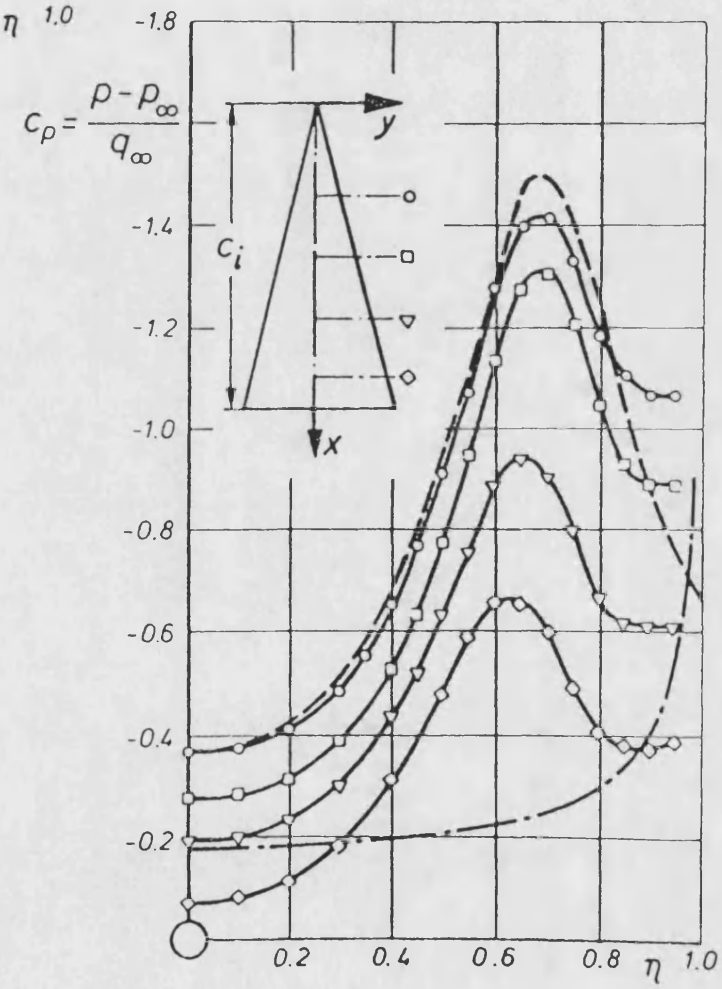

Turbulent boundary layer

Fig. 2.2 - Pressure distributions for two Reynolds Numbers, Aspect ratio 1.0 delta wing, α=20.5°. Hummel [1988]

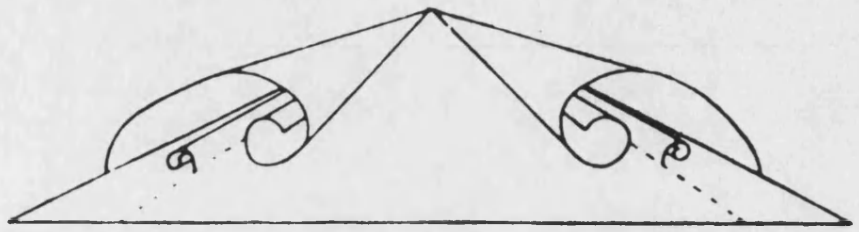

(a) VORTEX SHEETS FORMED ABOVE THE WING

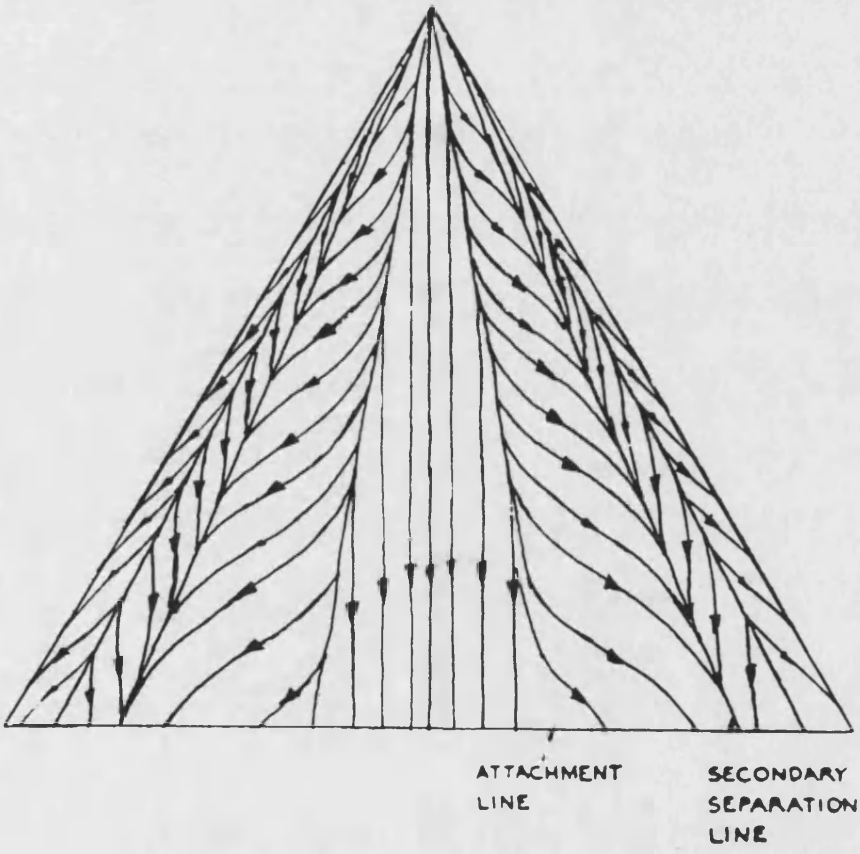

(b) SURFACE FLOW PATTERN

Fig. 2.3 - Typical flow over a delta wing at moderate incidence, Earnshaw and Lawford [1964]

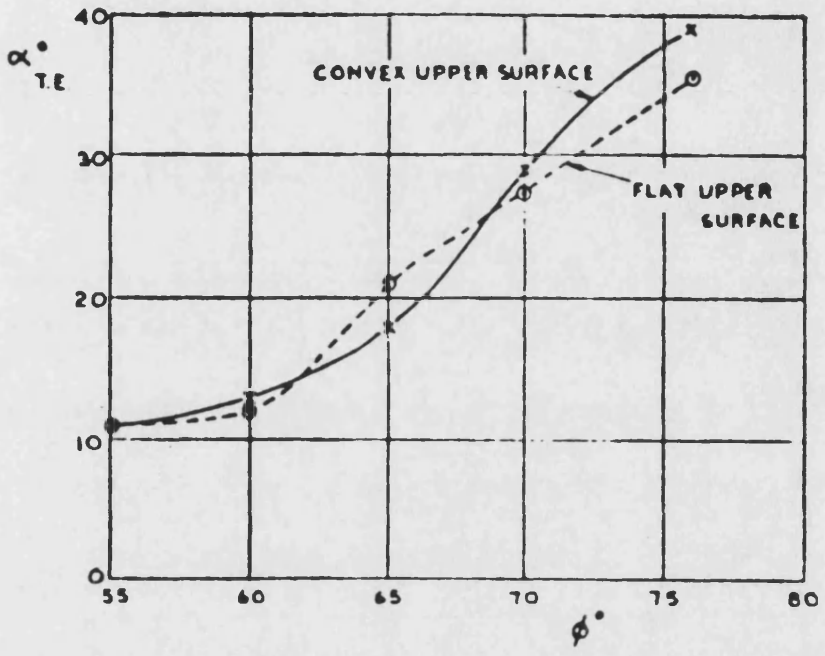

$\alpha_{T.E.}$: INCIDENCE FOR VORTEX BREAKDOWN IN THE PLANE OF THE TRAILING EDGE.

ϕ : LEADING-EDGE SWEEPBACK ANGLE.

Fig. 2.4 - Incidence for vortex breakdown at trailing edge, Earnshaw and Lawford [1964]

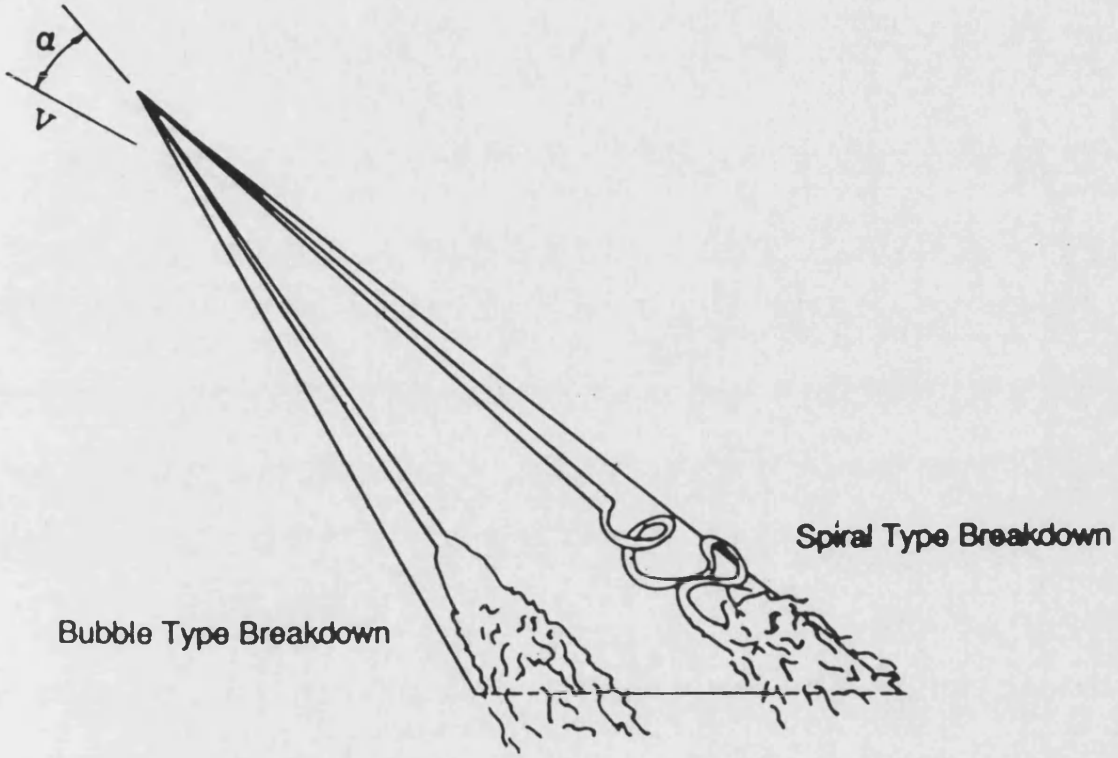

Fig. 2.5 - Bubble and spiral types of vortex breakdown,
Payne et al [1986]

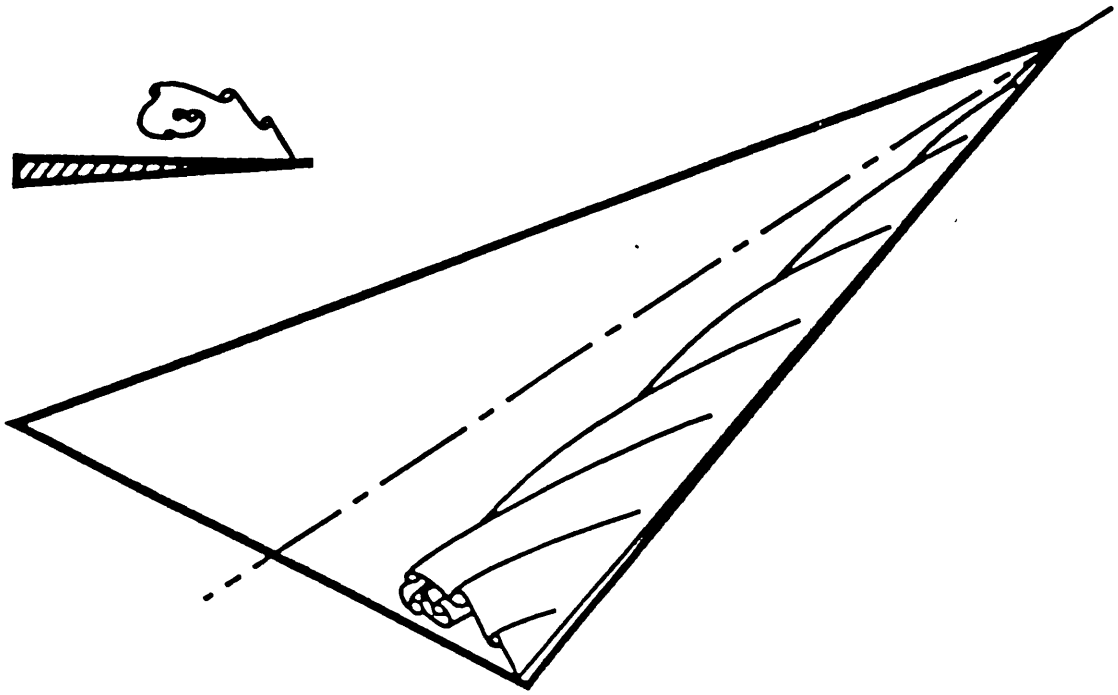

Fig. 2.6 - Schematic of streamwise vortices, Squire [1961]

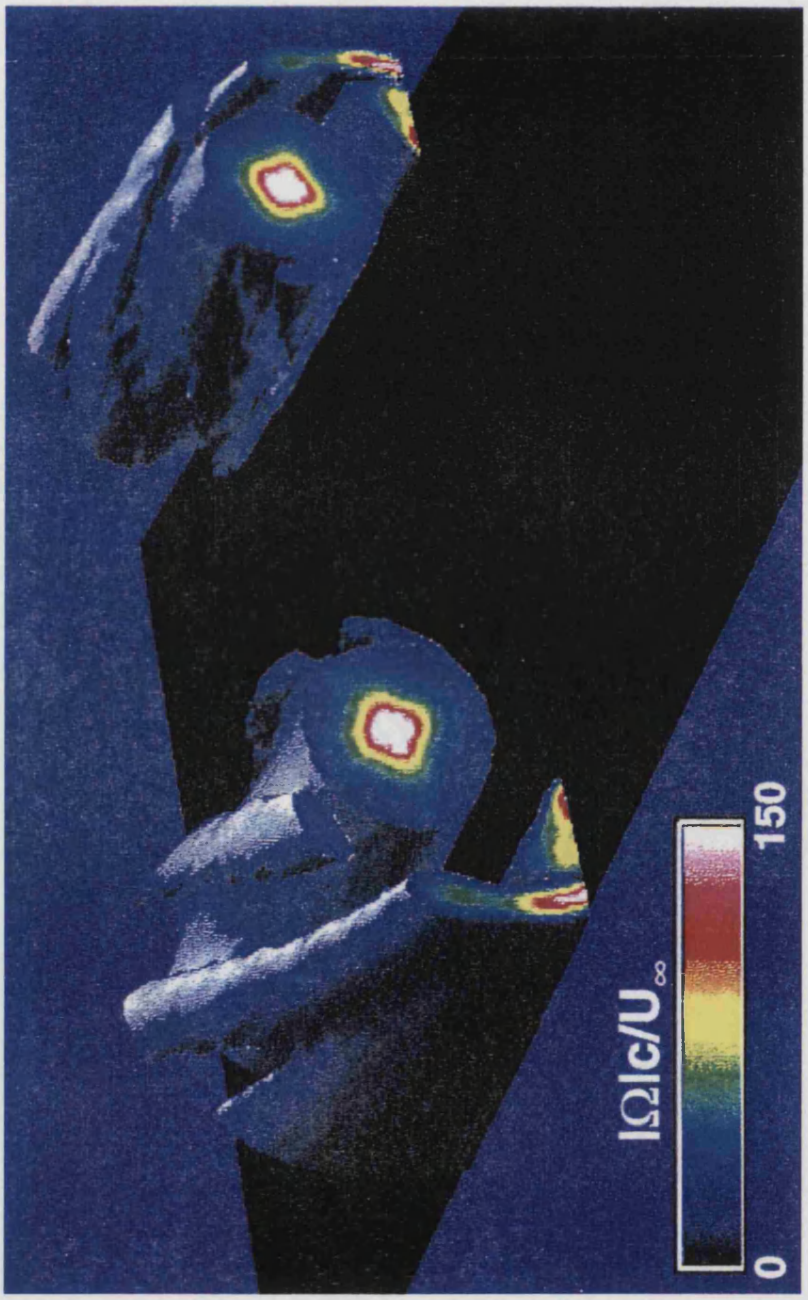

Fig. 2.7 - Experimental surfaces of vorticity magnitude, Washburn et al [1994]

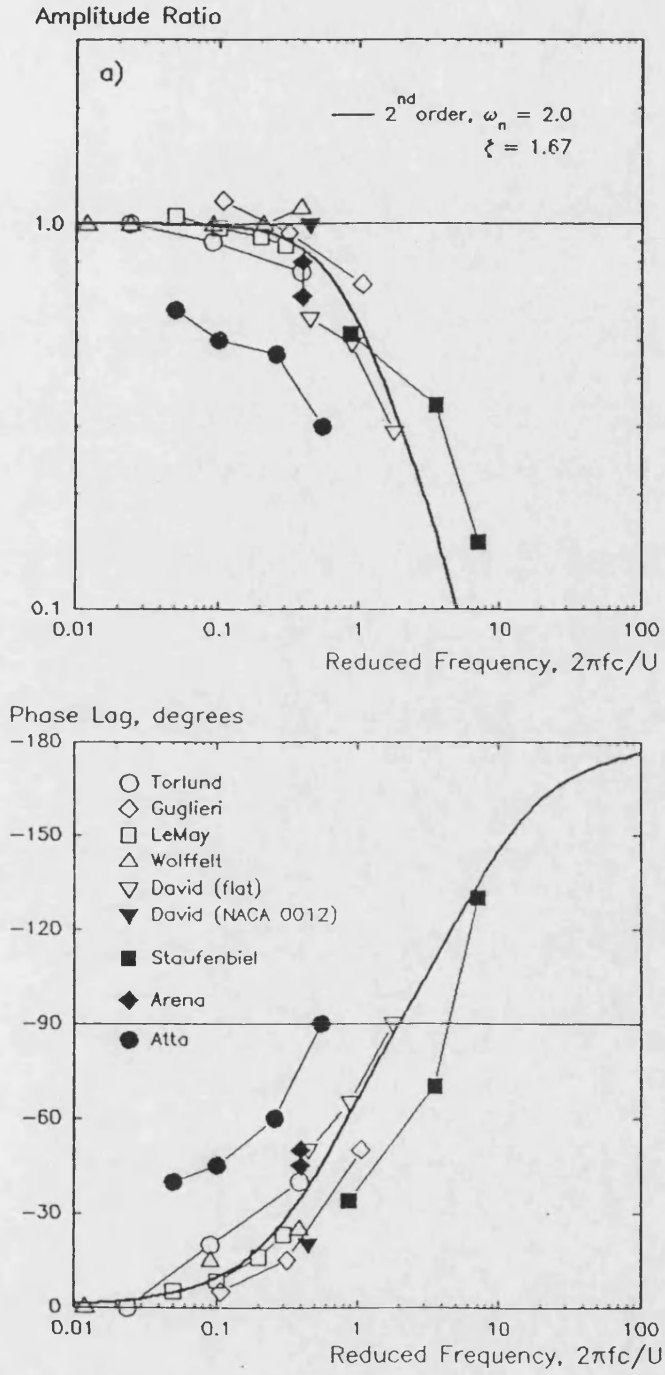

Fig. 2.8 - Bode plot representation of published 'periodic' burst response data, Greenwell and Wood [1994]

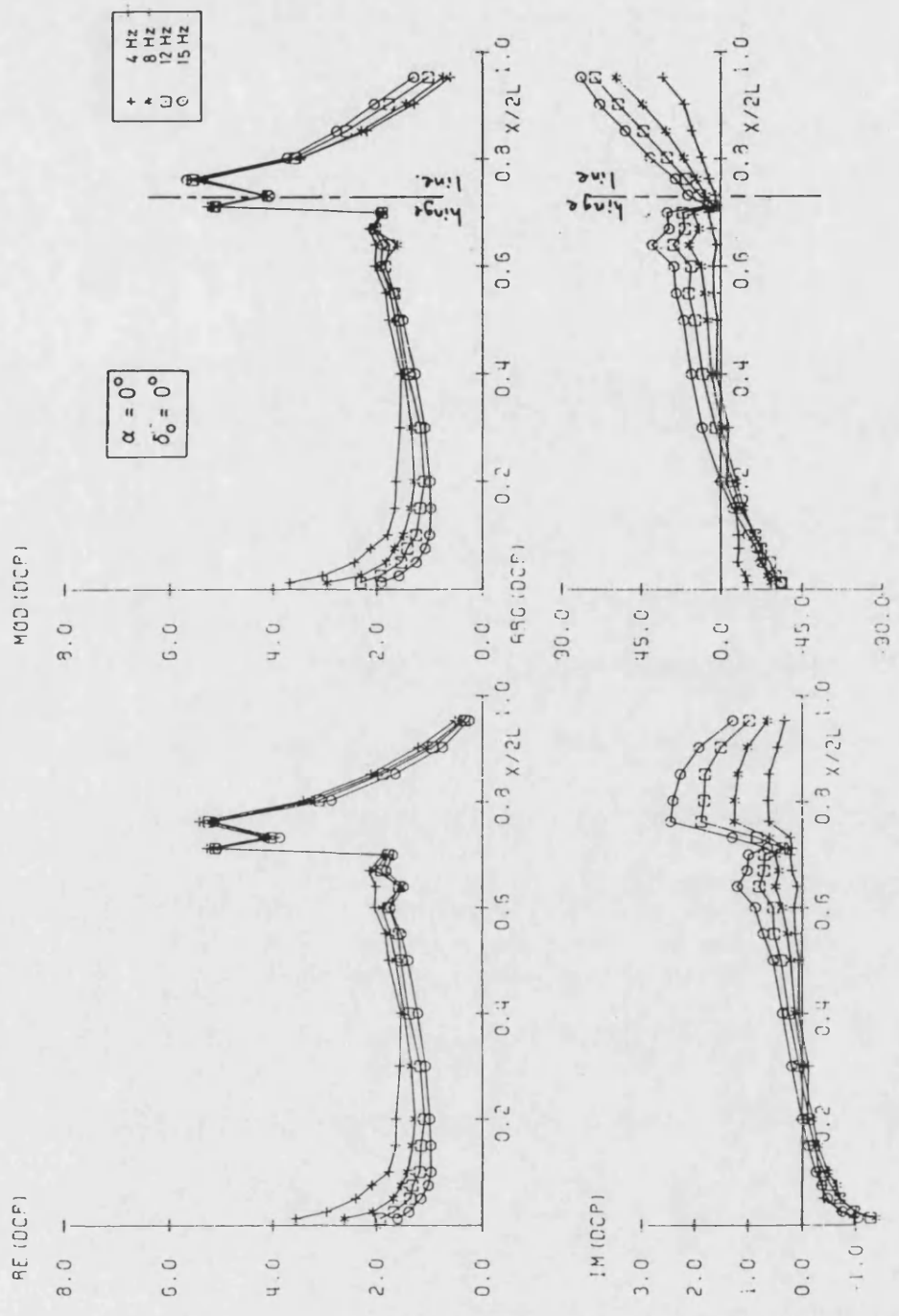

Frequency (Hz)	Frequency parameter
4	0.43
8	0.85
12	1.32
15	1.64

Fig. 2.9 - Unsteady pressure distributions,
Kienappel and Round [1980]

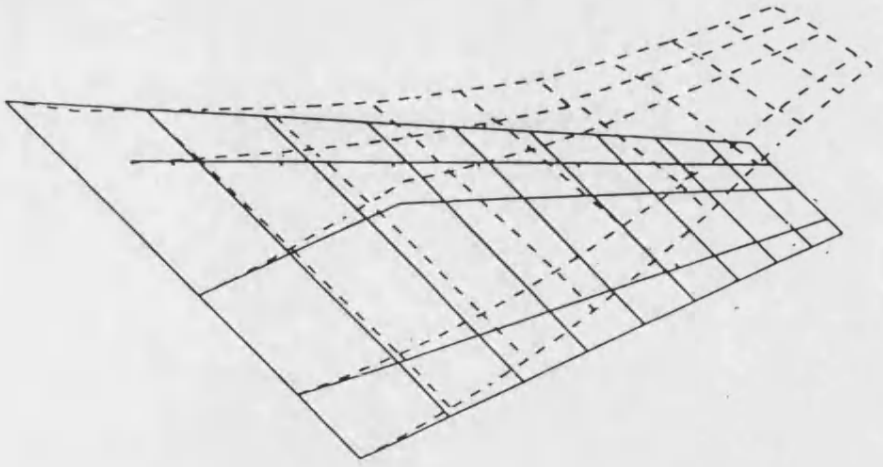

Baseline wing—1st bending mode.

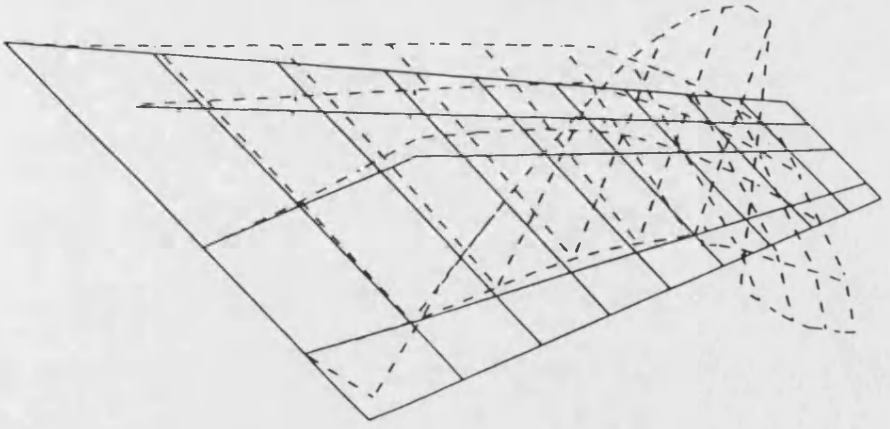

Baseline wing—1st flaperon mode.

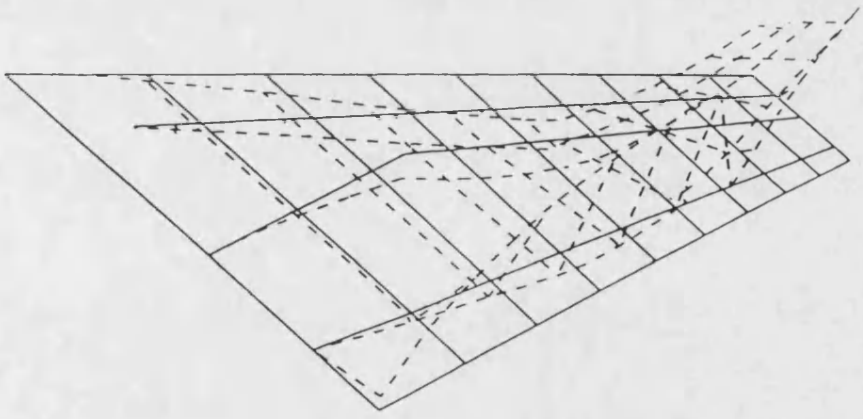

Baseline wing—2nd bending mode.

Fig. 2.10 - Typical combat aircraft wing modes, Pendleton and Lee [1992]

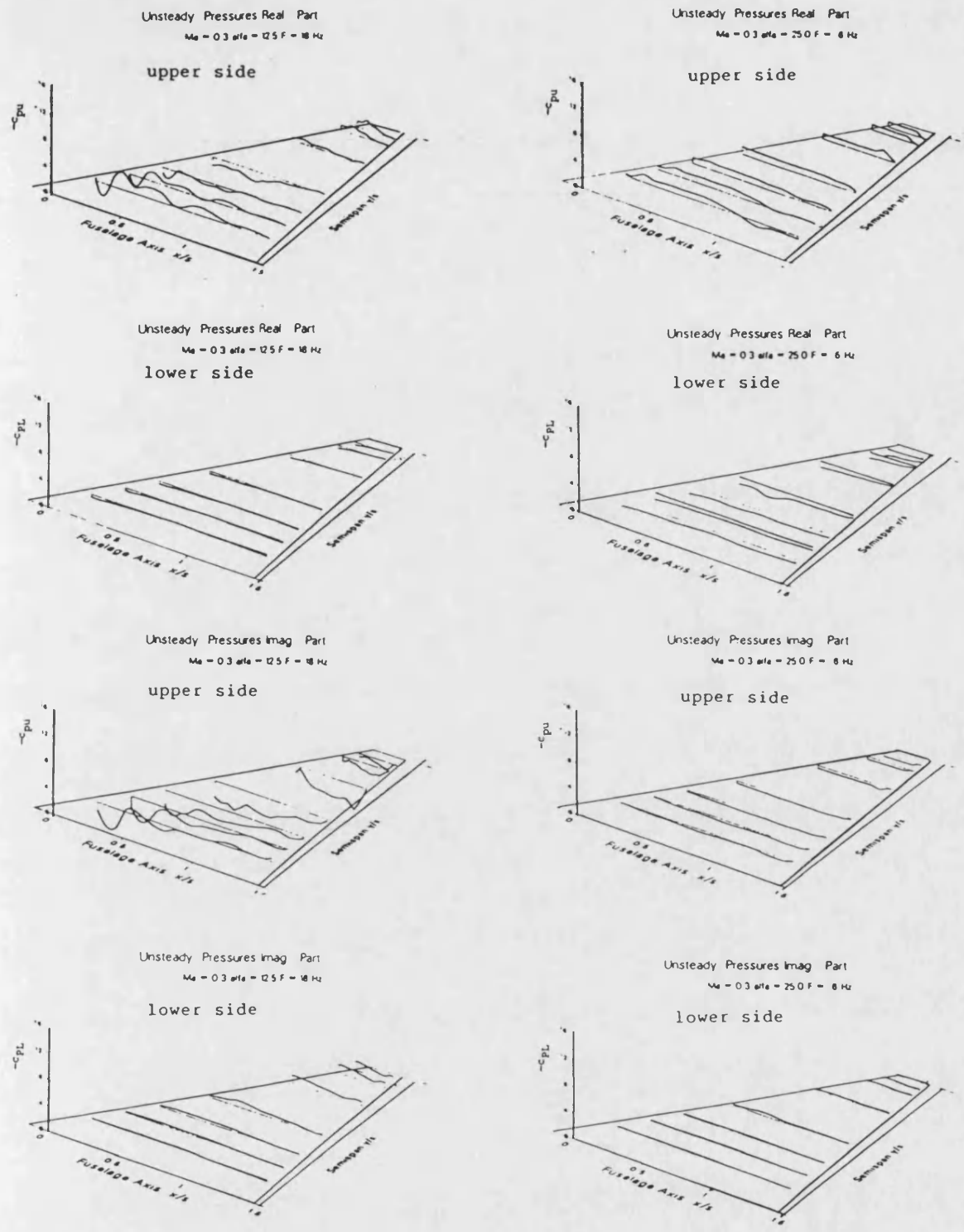

UNSTEADY PRESSURES DUE TO HARMONIC WING ROLL MOTION AT UPPER AND LOWER SIDE, MACH 0.3, α = 12.5 DEG., REDUCED FREQUENCY k = 0.94

UNSTEADY PRESSURES DUE TO HARMONIC WING ROLL MOTION AT UPPER AND LOWER SIDE, MACH = 0.3, α = 25 DEG., REDUCED FREQUENCY k = 0.31

Fig. 2.11 - Unsteady pressures resulting from wing roll oscillations, Becker [1991]

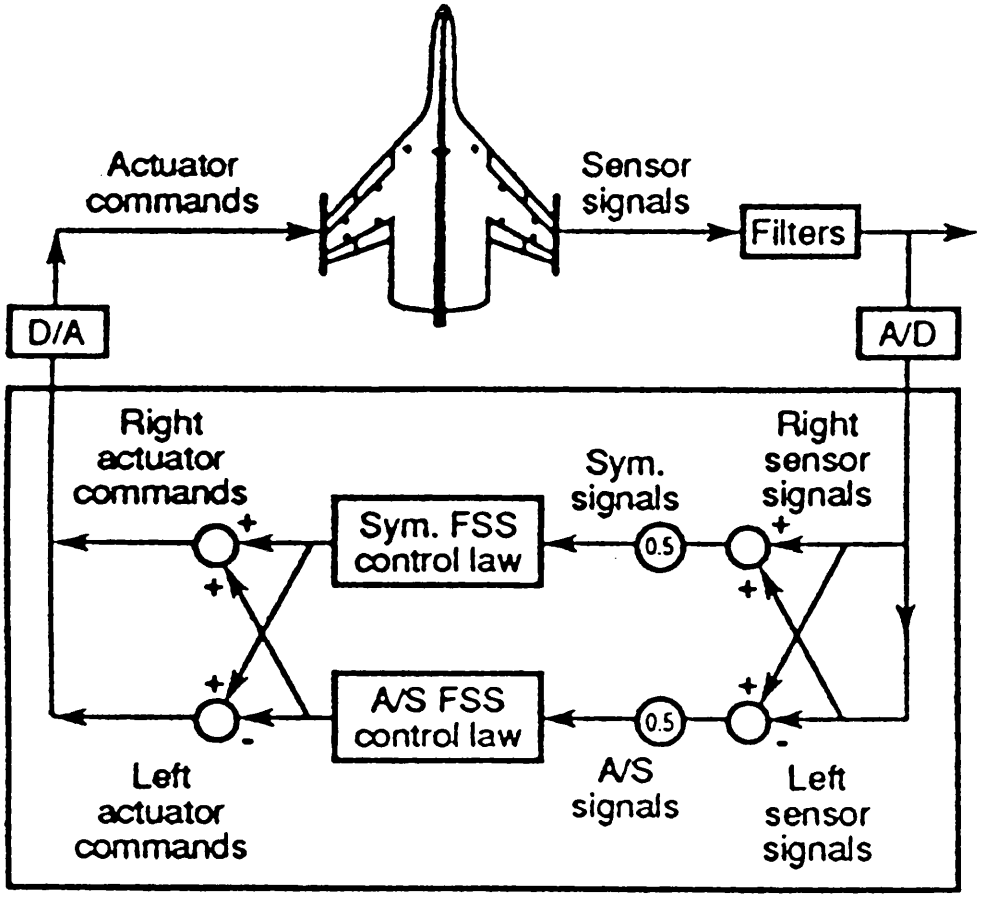

Fig. 2.12 - Flutter supression block diagram, Abel [1992]

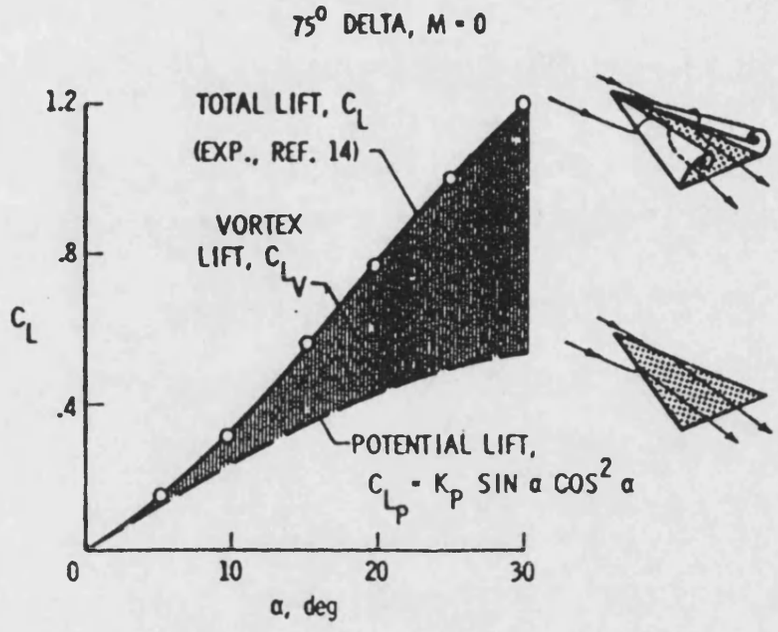

Fig. 2.13 - Illustration of the vortex lift for a 75° delta wing, Polhamus [1971]

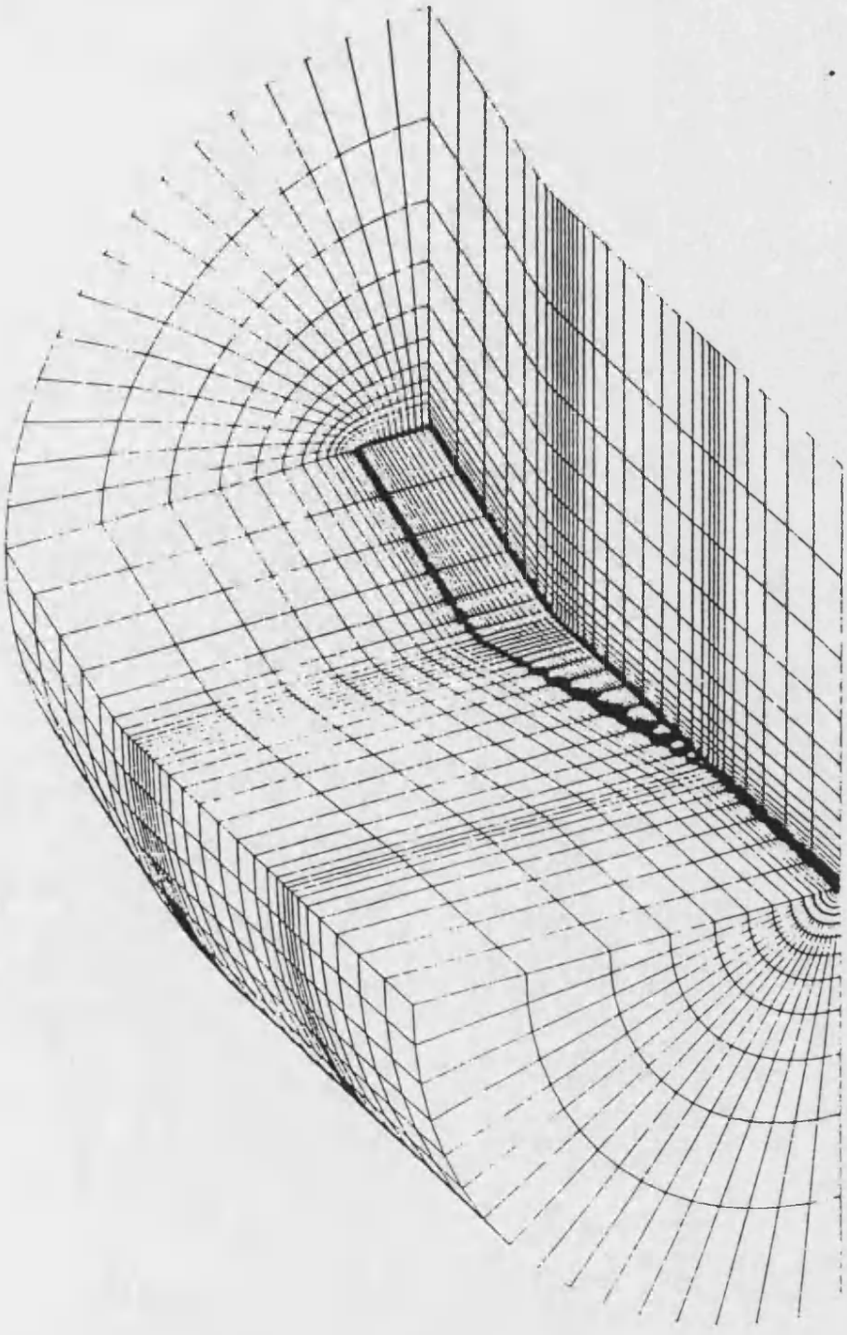

Fig. 2.14 - Three-dimensional grid for delta wing solution,
Thomas et al [1987]

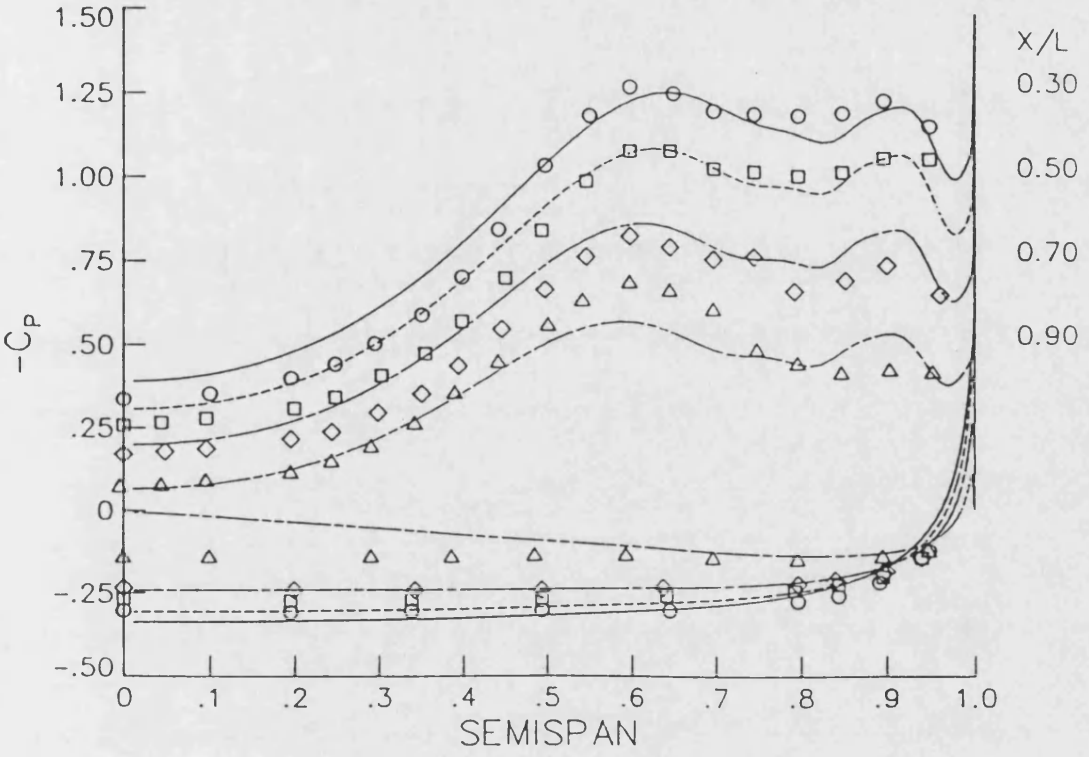

Fig 2.15 - Surface pressurte comparisons between experiment (symbols), Hummel [1973] and computations, Thomas et al [1987]

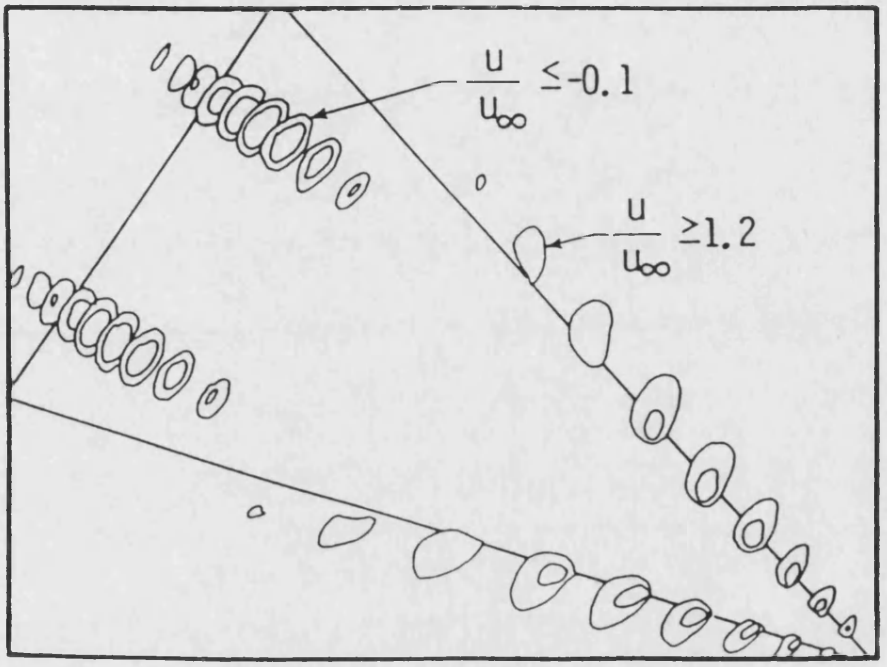

Fig. 2.16 - Streamwise velocity contours, α=40°, Thomas et al [1987]

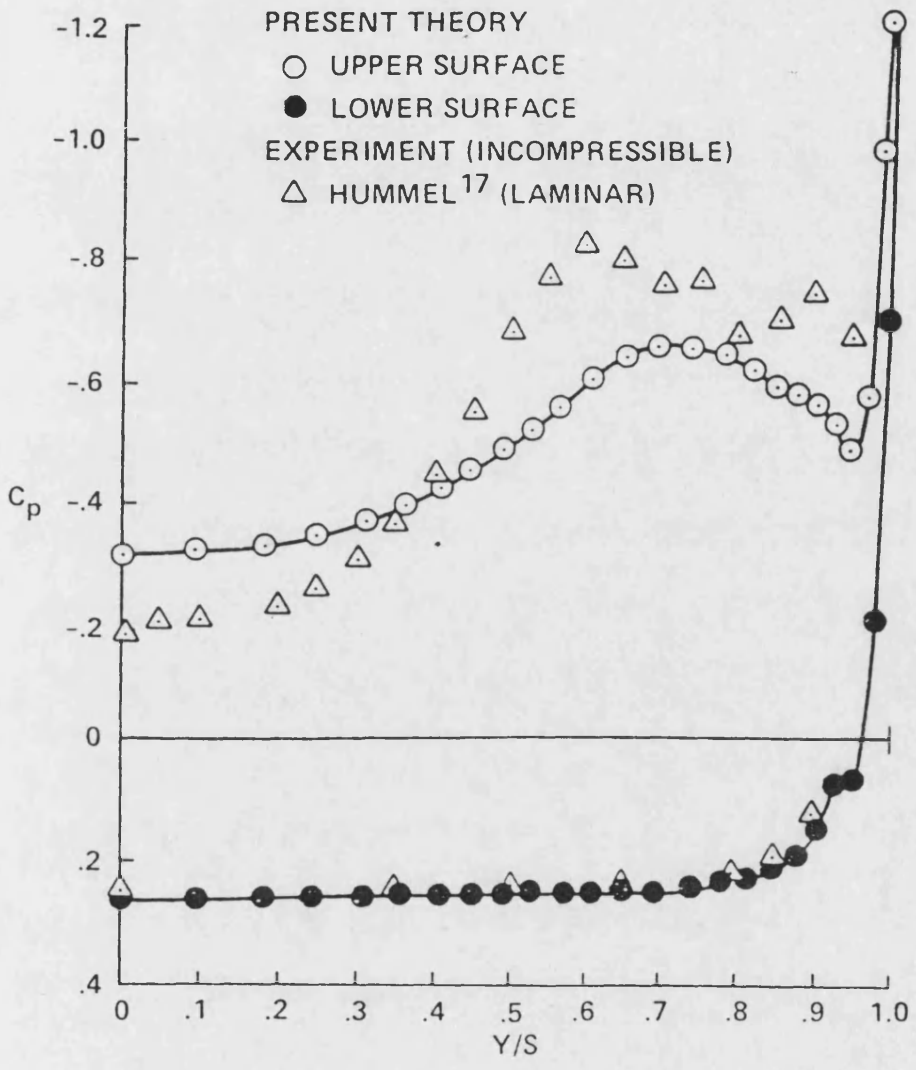

Fig. 2.17 - Computed and experimental results for laminar flow conditions, Fujii and Kutler [1980]

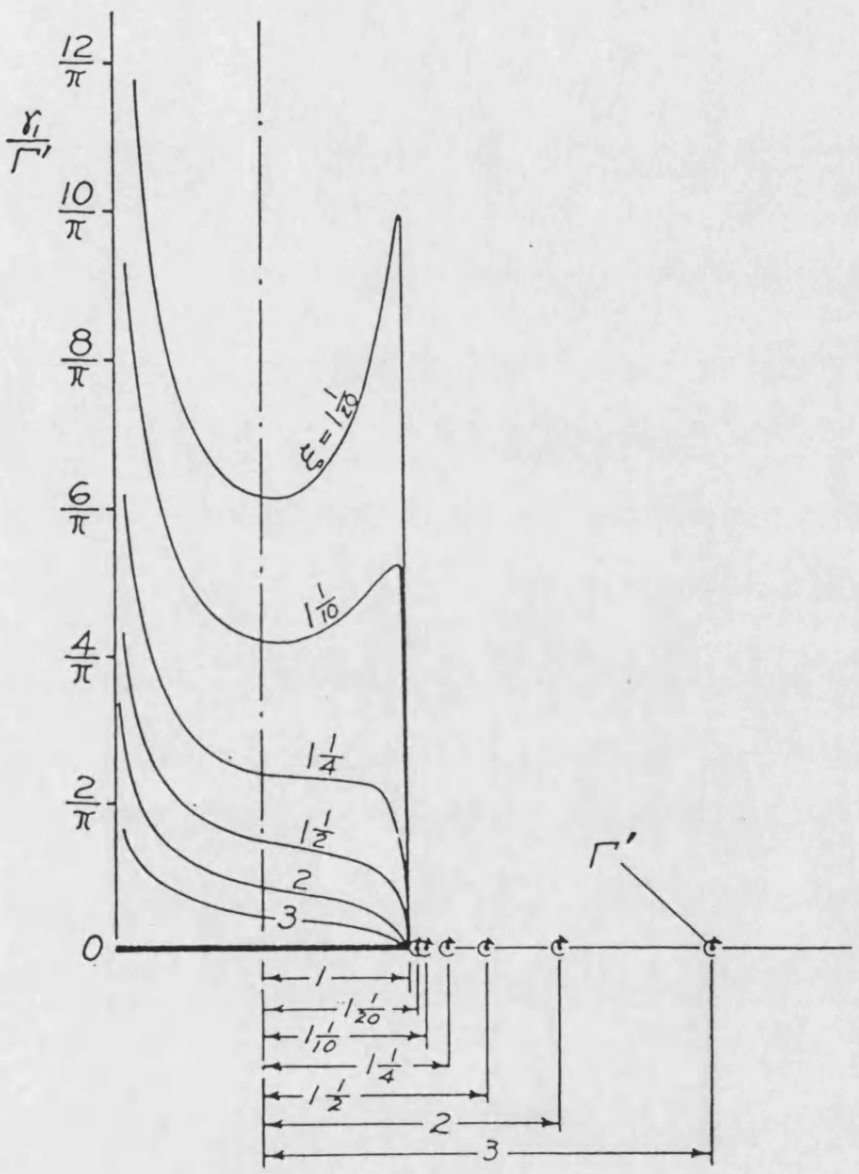

Fig. 2.18 - Vorticity distributions induced by a wake vortex at various distances from the midpoint of the airfoil, Von Kàrmàn and Sears [1938]

3. TEST APPARATUS.

All the tests reported here were carried out in the University of Bath, 2.13m by 1.52m (7 ft. by 5ft.), low speed wind tunnel facility, fig. 3.1. The closed loop tunnel has two working sections. For this project, the higher speed section was used. Before carrying out any unsteady tests, the overall steady forces and moments were measured using the 6-component balance mounted above the wind tunnel. Although the balance had been designed to isolate each of the degrees of freedom, cross-coupling effects still had to be allowed for as detailed in the manufacturers report (Aerotech [1970]). The overall steady forces and moments were used as a reference for comparison with the unsteady results. They also enabled the general flow characteristics throughout the angle-of-attack range to be determined.

3.1 Model Mounting Arrangement.

The wing was mounted to the 6-component mechanical balance situated above the wind tunnel. Due to the presence of a boundary layer at the tunnel walls (previously measured at 0.15m), it was necessary to mount the model away from the ceiling and employ a circular splitter plate to aerodynamically isolate the wing from the support structure and actuation system (fig. 3.2). The splitter plate was also structurally separate from the model, and had a rounded edge. Initial tests with an existing splitter plate revealed the existence of a large separation bubble at its sharp leading edge. This separation bubble interfered with the formation of the vortex over the wing and showed evidence of Reynolds Number effects in the normal force curves. This problem was not present for the rounded leading edge splitter plate. The balance frame could be rotated to allow the model and mount to be rotated to any angle-of-attack, α, from -90° to +90°.

3.2 Wind Tunnel Model.

The geometry of the rigid, 55° leading edge sweep, half model is given in fig. 3.3. It was manufactured from 6mm thick aluminium plate, with a semi-span of 300mm and root chord of 528mm, thus giving a wing tip chord of 100mm. The upper surface of the wing was

completely flat, whilst the lower surface had a leading edge bevel of 22° normal to the leading edge, and a trailing edge taper angle of 6°.

The trailing edge control surfaces consisted of two separate, half span elevons, thus allowing each control angle to be set separately. Each control surface had a constant chord of 50mm, and a linear thickness taper of 6mm to 1mm at the trailing edge. The leading edge of the outboard elevon was rounded to maintain a constant gap between the main wing and the control surface. The inboard elevon was held at the zero angle position by two brackets on the lower surface (fig.3.3), the outboard elevon being driven through a closed loop control system, as detailed below.

3.2.1 Moveable Outboard Elevon.

The complete elevon control system is shown in fig. 3.4. In order to prevent any dangerous levels of structural excitation of the elevon, it was necessary for the moveable elevon to have a low inertia yet high natural frequency compared with the frequency of oscillation required during the unsteady tests. To achieve this, the control surface was constructed using a carbon fibre skin, foam core, sandwich technique. The foam core was accurately cut using a hot wire cutter. A single layer of 150 gm/m^2 woven carbon fibre matting, bonded with cold curing, two part epoxy resin was used. In order to obtain the maximum torsional stiffness for the control, the weave was orientated at 45° to the trailing edge.

An actuation rod of length 170 mm was secured to the root of the elevon and directly to the position control motor. The elevon was supported between bearings mounted at the root and tip of the elevon.

The required elevon angle, η, was calculated in near real time by a PC and communicated to a closed loop control system. The controlling software was written specifically for this programme of work and used ATLAB® subroutines supplied with the Data Translation DT2821® analogue input/output board. This software (see Appendix I) produced steady elevon positioning, sinusoidal oscillations and step changes in elevon position. Due to the requirement within the programme to calculate the next angle for the elevon to move to, it was necessary to calibrate the oscillation routine for the speed of the particular computer processor being used. This resulted in

a rate of 2000 requested elevon angles per second when producing a sinusoidal motion. The actual motor response to this form of requested angle was checked and found to produce an excellent oscillatory motion, as shown in fig. 3.5(a).

The motor used was a Pitman 5112 WDG4®, 3 phase brushless motor with LoCog®, 12-step drive. This form of motor can be positioned accurately and supplies near constant torque throughout the speed range. The Pitman® motor had a low mechanical time constant due to its high torque to inertia ratio, and exhibited minimal torque ripple due to its LoCog® 12-step drive. These features produced a smooth motor operation and accurate motor positioning.

The angle feedback to the motor driver was provided by an encoder mounted on the end of the motor shaft. This effectively removed the structural flexibility from the control loop. Had the elevon angle been used as feedback, background electrical noise would have produced the potential for a resonance to occur within the system due to the flexibility of the actuation rod and the inertia of the elevon. The brushless motor also used 3 Hall sensors mounted within its case to provide the timing for current changes in the absence of a commutator. This function was provided by a Pitman 304-014-222® motor servo amplifier. The difference between the requested and actual positions was sent to the motor driver which then produced the required power signal to the motor.

Since the feedback encoder mounted on the motor shaft did not measure the actual elevon angle, a Hall effect sensor was attached to the root of the control surface, as shown in fig. 3.4. This sensor reading was used as the elevon reference angle throughout the analysis. The Hall effect sensor produced a voltage related to the magnetic field passing through it. A permanent magnet was secured to the main wing, close to the sensor such that the voltage variation with elevon angle was as large as possible, typically 1 Volt difference for a 40° change in angle, hence, no further amplification was required. The quadratic fit of fig. 3.6 was used for the Hall sensor calibration with elevon angle.

Comparing the requested elevon angle signal with the Hall effect sensor angle (as given in fig. 3.7), the actuation system as shown was found to have a lowest natural frequency of over 150 Hz., more than 5 times the frequency to which the elevon would be oscillated during the tests, thus producing an effectively rigid elevon actuation

system.

3.2.2 Upper Surface Pressure Tappings.

All steady force and moment measurements were made before the model was fitted with any pressure tappings.

In total, 168 pressure tappings were used, 144 arranged in 12 spanwise rows on the main wing, 13 in 2 rows on the inboard elevon, and 11 in 3 rows on the outboard elevon (fig. 3.8). The pressure measurements on the moveable elevon were recorded using 3 miniature barrel transducers (Kulite® XCS-093-5D) mounted through the elevon, with the screen mounted flush to the surface. To obtain sufficient unsteady pressure results on the elevon, these transducers were repositioned as necessary and the test point repeated.

All other pressure tappings were constructed by laying groups of individual stainless steel tubes (one per tapping) into grooves machined into the upper surface of the wing. The surface of the wing was reformed by filling the grooves with laminating epoxy and smoothing to a level finish when set. Finally, the tappings were formed by drilling 0.5mm diameter holes perpendicularly into each tube. Pressure tappings were only formed in the upper surface of the model. To record lower surface pressures, the model was tested at negative angles of attack.

Each stainless steel tube was connected, via a 1m length of Scanivalve VYL-040® tubing, to one of 5 'J' type Scanivalve® units, thus allowing 5 pressures to be recorded at a time. Each Scanivalve® had a separate pressure transducer, and 48 individual ports, thus allowing up to 240 pressures to be recorded. The port was selected by sending a digital signal to the Scanivalve drive controller which then powered a solenoid to step the port. Port 0 of each unit was used to measure the wind-off zeros for the transducers by leaving it open to atmosphere, outside the tunnel.

The length of vinyl tubing was kept as short as possible by mounting the Scanivalve units directly above the model, just outside the tunnel. This kept the amplitude of the unsteady pressures transmitted to the transducers to a maximum. Also, to reduce the level of electrical noise introduced into the pressure signals, the amplifiers for the transducers were mounted close to the Scanivalve® units.

3.2.3 Flexible Root Mounting System.

The rigid mounting system was altered to allow a wing root bending mode to be introduced into the model. The portion of wing extending inboard of the splitter plate, previously used to supply the necessary rigidity to the interface between the tunnel mount and the model, was removed. Instead, a 1.5mm thick, ground stock steel plate was used to connect the model to the rigid mount, fig. 3.9. Ground stock steel was used as it had low energy loss characteristics, thus keeping the structural damping as low as possible. By altering the length, d, of the unsupported portion of the flexible plate, it was possible to change the natural frequency of the resulting flexible mode.

Three miniature accelerometers (Entran EGA-125F-100D®) were mounted to the lower surface of the model at the locations given below :

Acc. A	x= 441 mm	y= 277mm
Acc. B	x= 425mm	y= 134mm
Acc. C	x= 255mm	y= 134mm

By using 3 accelerometers, any bending or twisting of the wing could be monitored, to determine whether the structural mode was pure root bending. The ratio of the amplitude of motion of accelerometer A to B and C should be equal to the ratio of distance from the flexible root support at all frequencies for no model bending to be present.

3.3 Data Acquisition System for Unsteady Pressure Measurements.

A schematic representation of the complete acquisition system is shown in fig. 3.10. All data acquisition was performed by a PC based system using a Data Translation®, DT2821 acquisition board, controlled by specially written software that was able to both manipulate the large buffers needed to store the unsteady pressure data, and produce control signals to the Scanivalve® units and elevon control PC. This software was constructed using the ATLAB® subroutines. The program listing is given in Appendix II. The board used Direct Memory Access (DMA) to areas in the memory, thus allowing the acquisition to proceed at the required frequency without any interaction with the rest of the program. A flowchart showing the logic

for the acquisition process is given in fig. 3.11.

As well as setting up and controlling the data acquisition, the program used two bits of an 8 bit digital output port to control the selection of the required Scanivalve port. Having stepped to the required port, a 0.3s delay was invoked to allow each pressure transducer to respond to the new pressure level before beginning to acquire a block of data.

To prevent the acquisition of data being compromised in any way, the control of the elevon position was controlled by a separate PC from that acquiring data. The two PCs communicated via 2 bits of an 8 bit digital port, in order to allow for correct timing and positioning of the elevon.

Each transducer signal, except for the Hall effect sensor measuring the elevon angle, was amplified using d.c. amplifier cards produced by Bath University. The gain of each board was set to suit both the transducer being used as well as the expected measurement range required. Although analog filters were fitted to the amplifier boards, no filter was applied to the data before being acquired by the acquisition board.

3.4 Data Acquisition System for Flexible Wing Mounting.

A signal generator was used to generate the oscillatory command signal of requested elevon angle sent to the Pitman servo amplifier, rather than the analogue output from a PC as in the unsteady pressure measurement tests. Each accelerometer signal was amplified using instrumentation produced by the University of Bath. No filtering was applied to the signals. The elevon angle (from the Hall effect sensor) and the accelerometer signals were sampled through a Data Translation DT2821® analogue to digital board using GLOBALAB® data acquisition and analysis software. The acquisition system is shown schematically in fig. 3.12.

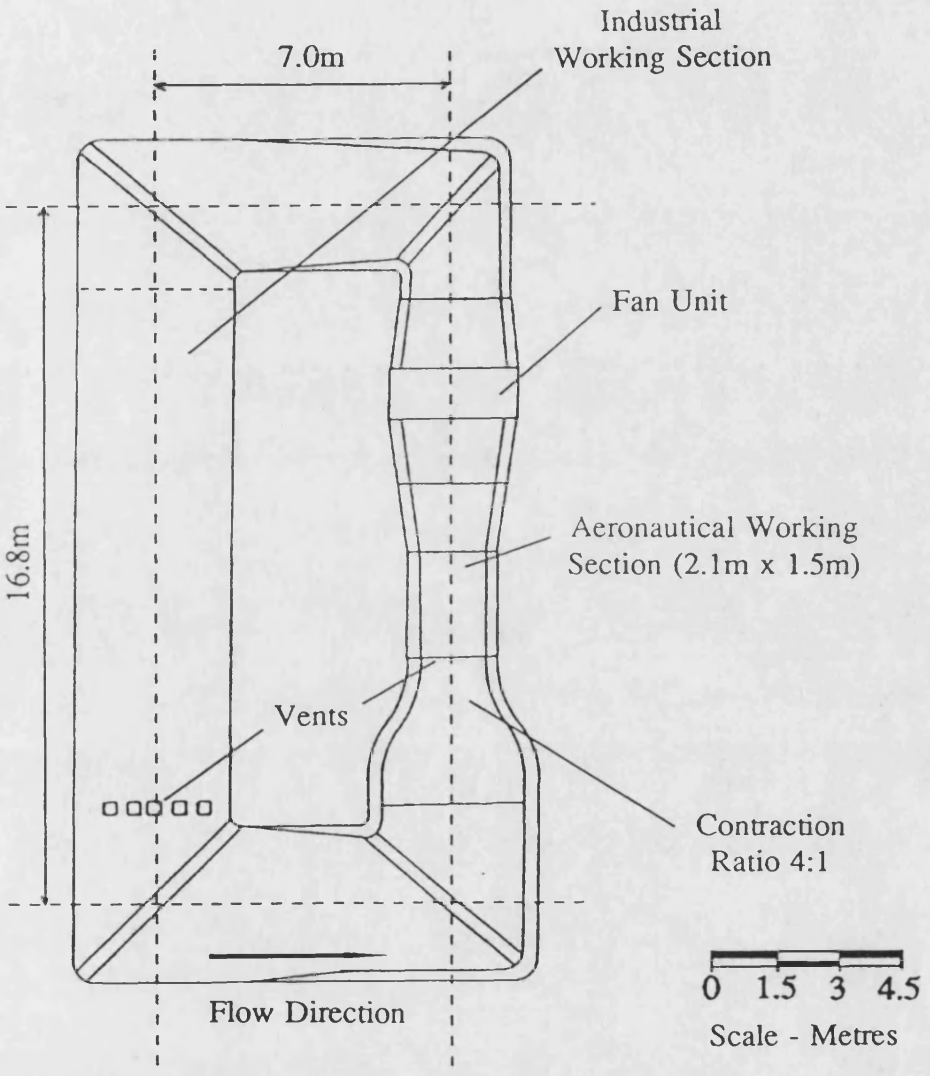

Fig. 3.1 - University of Bath, Low Speed Wind Tunnel

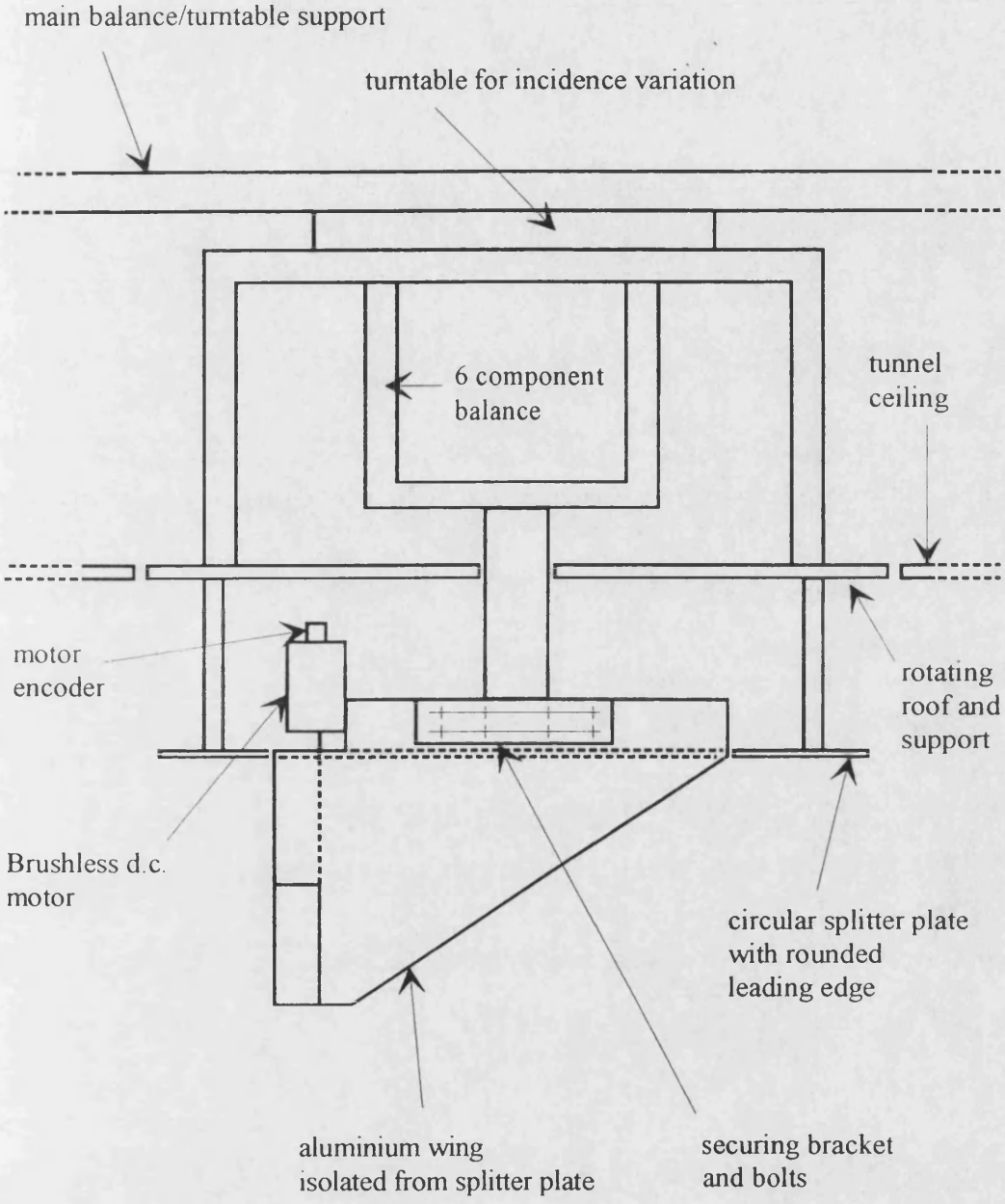

Fig. 3.2 - Half model mounting arrangement.

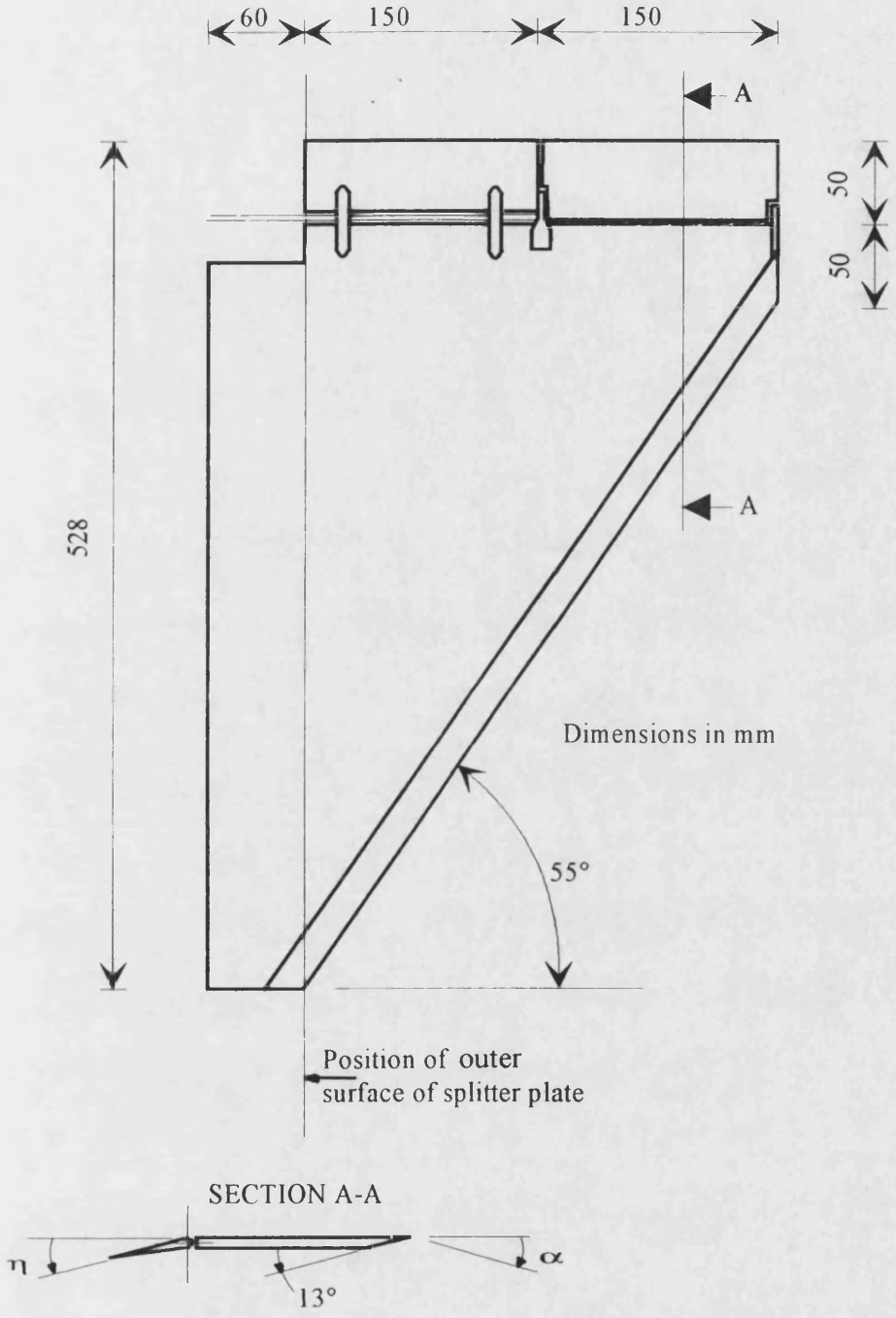

Fig. 3.3 - Geometry of Half Model.
- view from underside.

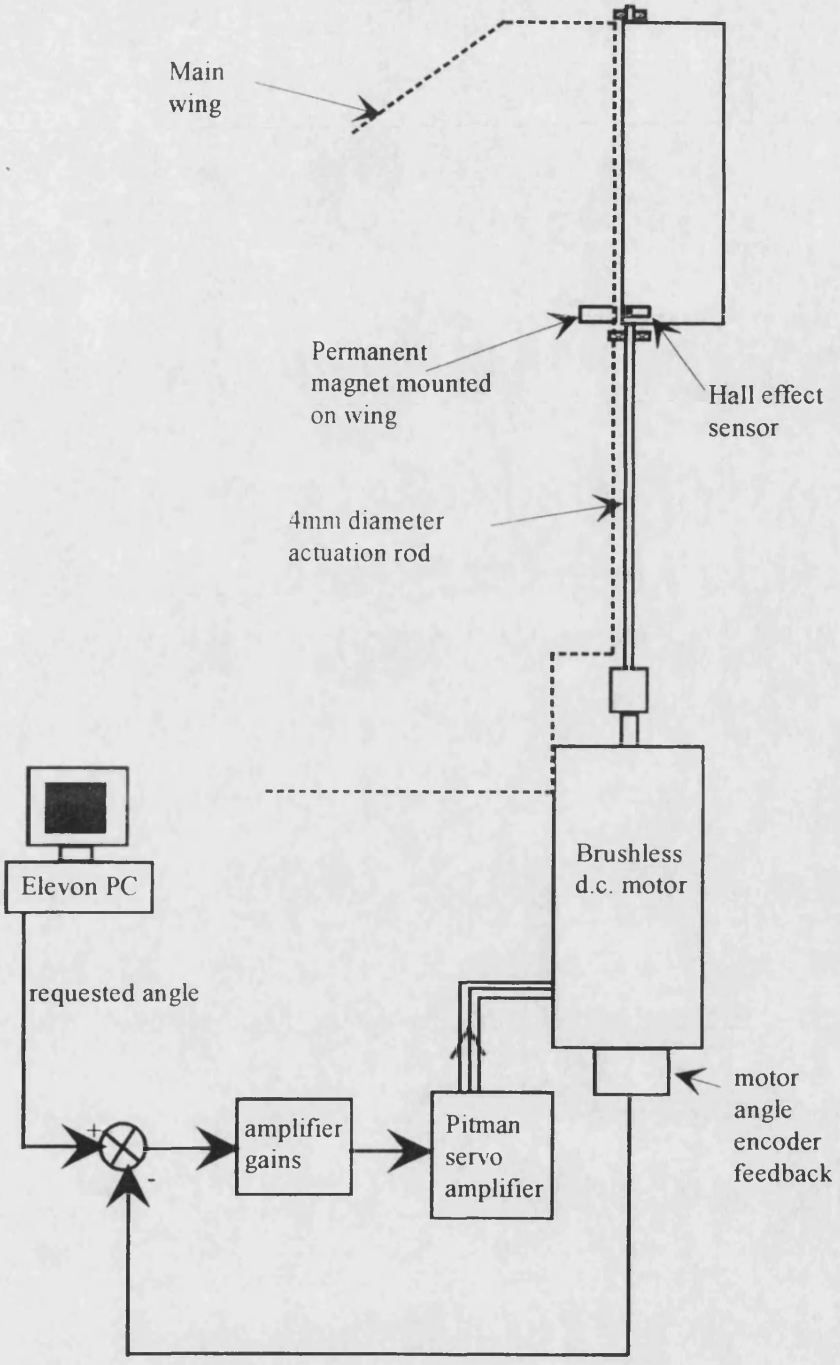

Fig. 3.4 - Elevon Actuation System.

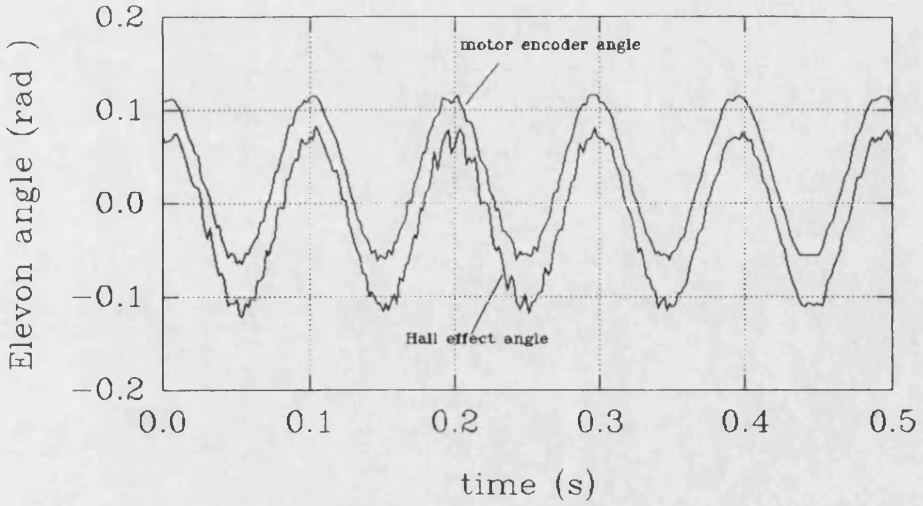

Note : angles separated for clarity

(a) Comparison of elevon angles – requested and actual.

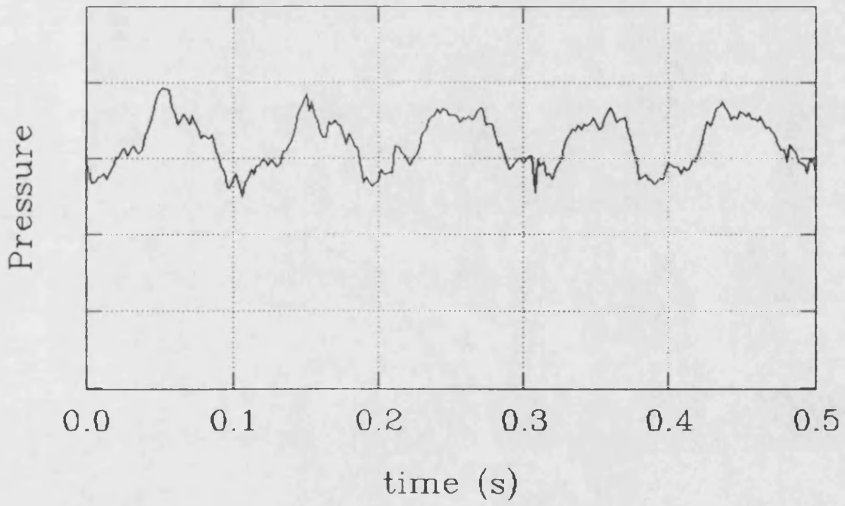

(b) corresponding uncalibrated pressure signal

Fig. 3.5 - Example elevon angles and pressure signals

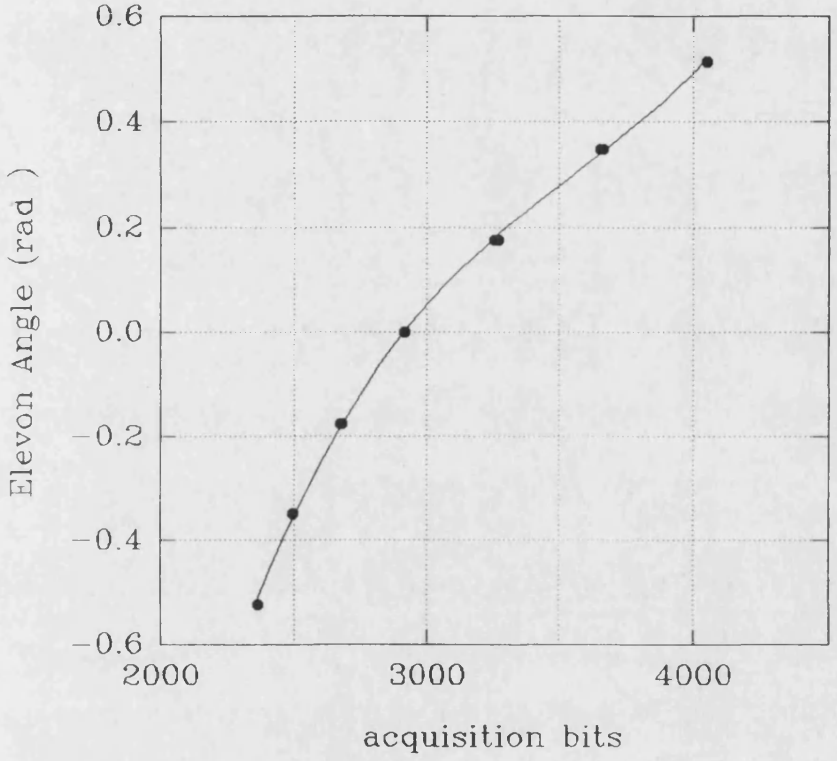

Fig. 3.6 - Hall effect sensor calibration

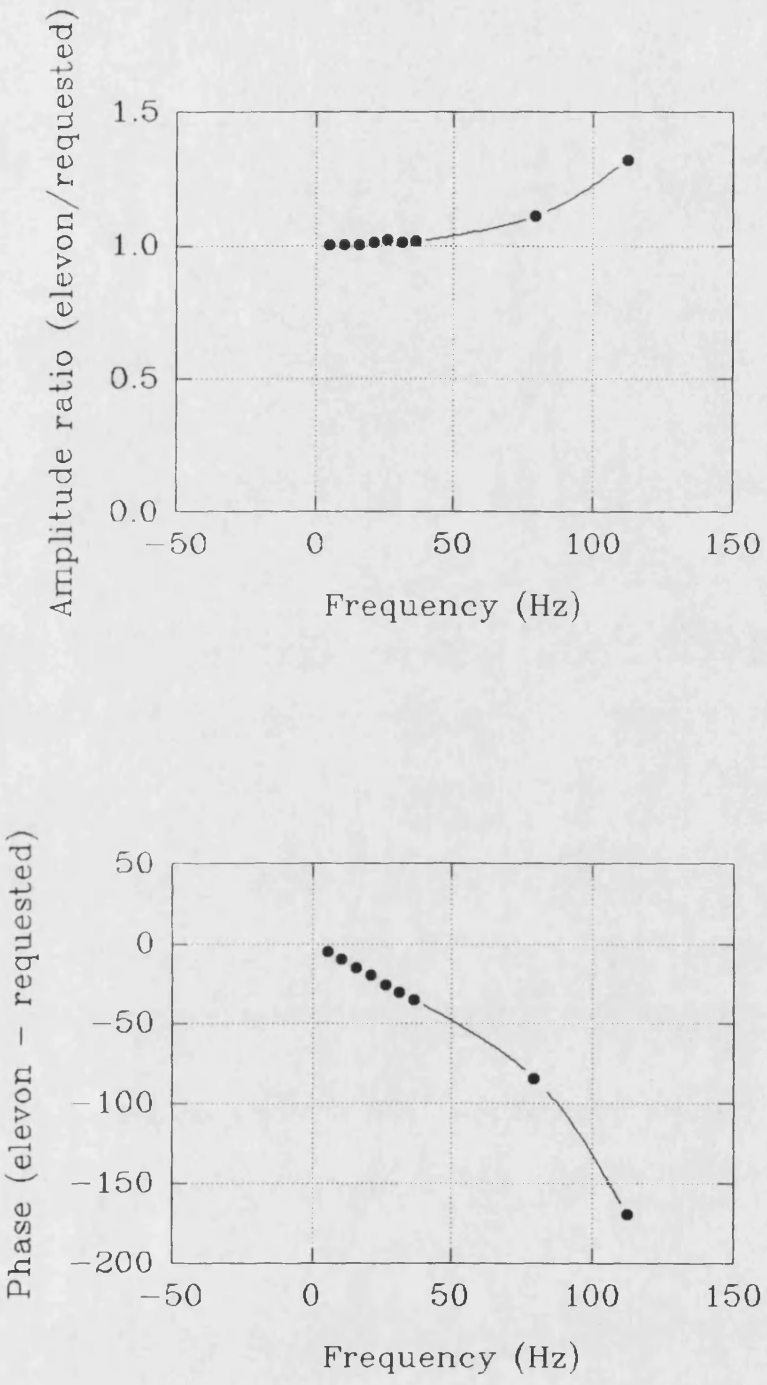

Fig. 3.7 - Actuation system performance

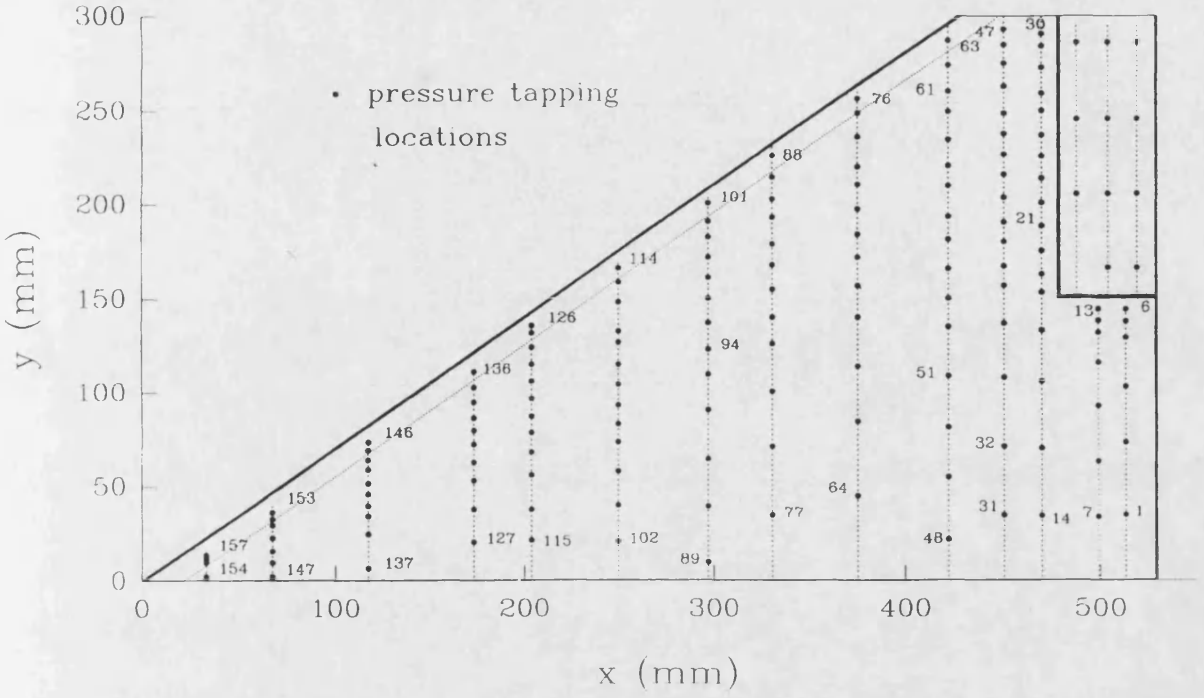

(a) Pressure tapping locations

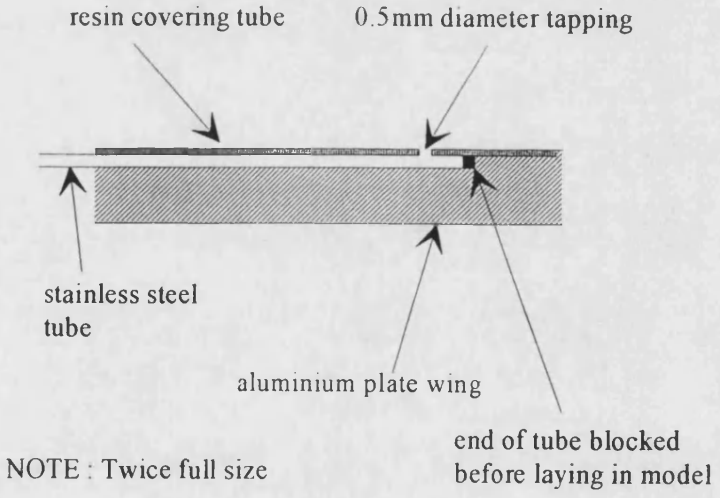

(b) Formation of individual tappings

Fig. 3.8 - Pressure tappings.

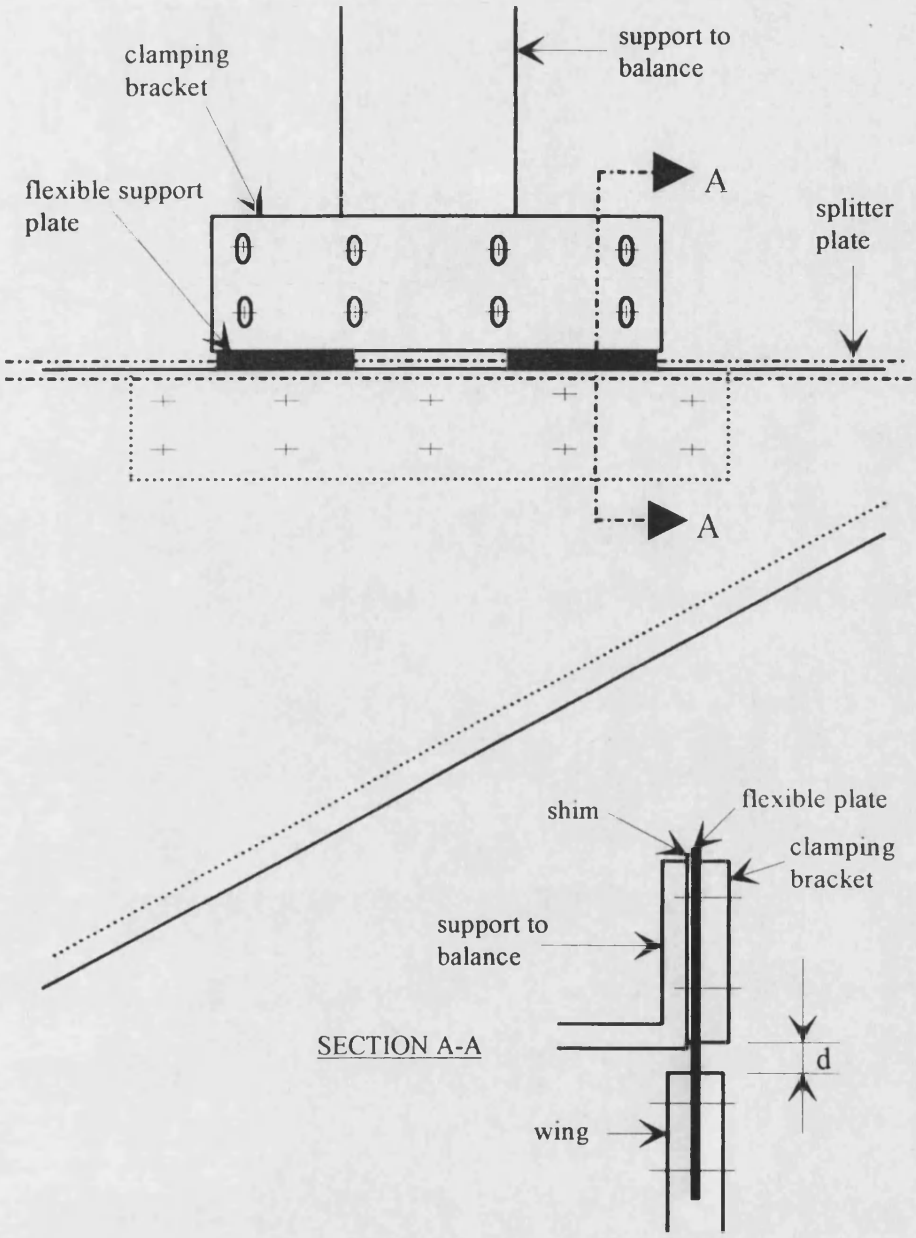

Fig. 3.9 - Flexible Mounting System

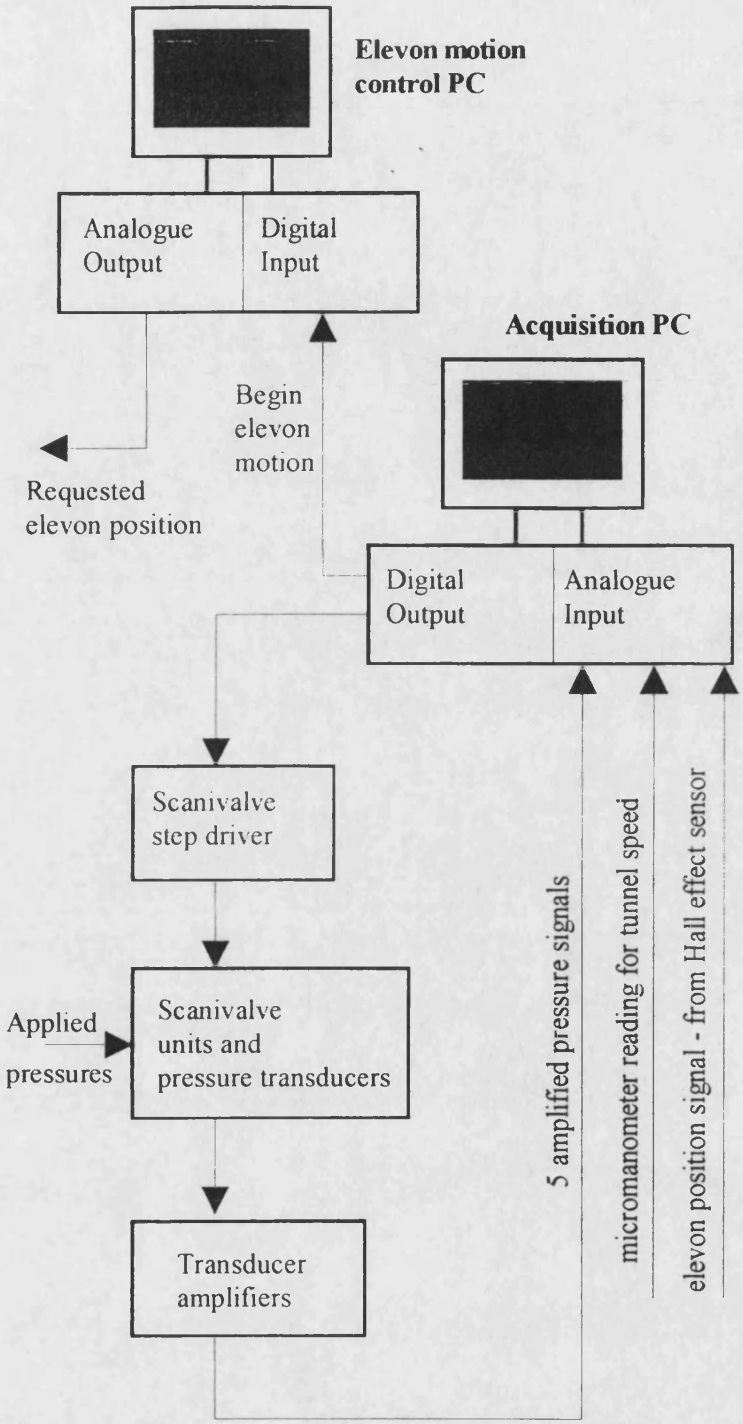

Fig. 3.10 - Acquisition system.

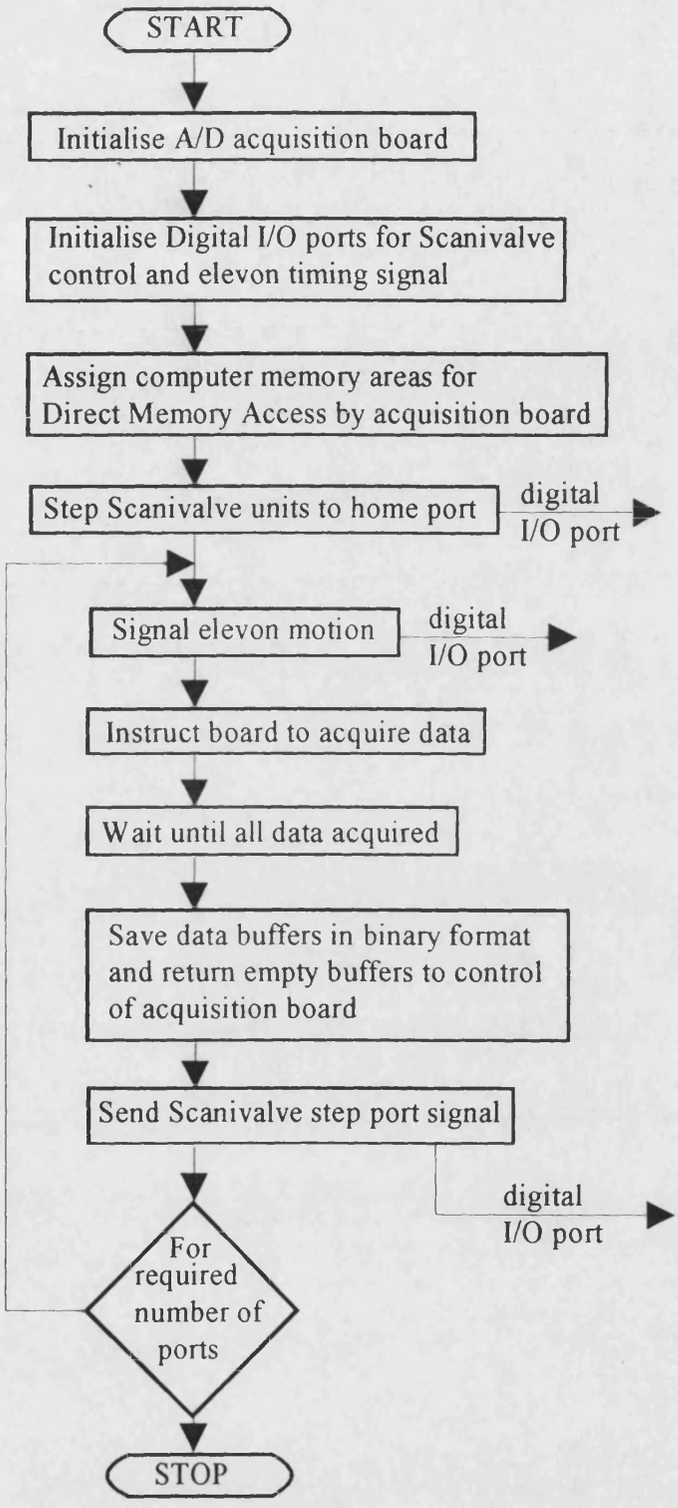

Fig. 3.11 - Acquisition program flowchart.

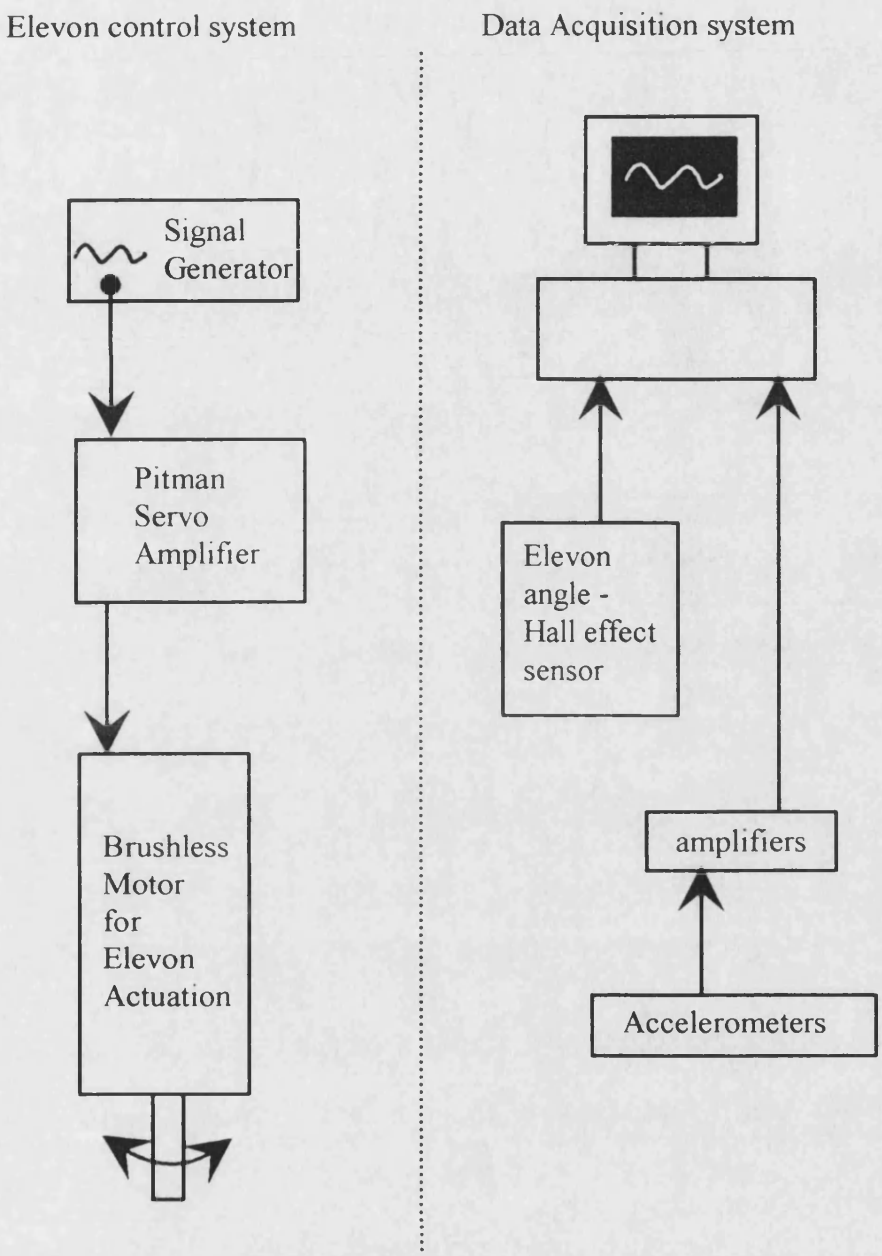

Fig. 3.12 - Data Acquisition and Elevon control System for Flexible Mounted Wing.

4. TEST PROCEDURES.

4.1 Calibration of Tunnel Centreline Pressure.

The tunnel speed was monitored during testing by measuring the pressure difference between two upstream tappings on the contraction section using a digital micromanometer. The calibration between this reading and the centreline dynamic and static pressure was obtained by mounting a Pitot-static tube upstream of the model installation, as in fig. 4.1. These tests were performed with the model installed and positioned at various angles-of-attack. The centreline dynamic pressure was 10.3 times the manometer reading (fig. 4.2). The centreline static pressure was found to be lower than the ambient pressure outside the tunnel by 0.399 times the centreline dynamic pressure†, despite the use of two wall vents at the start of the tunnel working section. Both this correction factor and the dynamic pressure calibration were found to be insensitive to changes in model angle-of-attack, i.e. to model blockage effect. Previous investigations (Greenwell et al [1992,A]) have shown the variation of dynamic pressure across the working section to be +4% to -1% horizontally and -1% to +0.5% vertically, with a turbulence level of 0.6% at 30 m/s.

4.2 Measurement of Steady Forces and Moments.

Since part of the model support structure was mounted inside the tunnel, it was necessary to measure its aerodynamic effect so that the results with the half model installed could be corrected. This was carried out by first measuring the forces and moments on a dummy plate which represented only that part of the wing that would be protected behind the splitter plate during the tests (including the elevon actuation motor). The results from these tests, and the appropriate wind-off values, could then be subtracted from those for the full wing at test conditions.

For all steady force/moment tests, the gap between the splitter plate and the model was sealed using grease, thus allowing for movement of the model while preventing any leakage of air through the gap.

All 6-components of force and moment were measured for α= -45° to +45°, in increments of 2.5°, as a function of tunnel speed and mean elevon position. Any cross-

† i.e. (Tunnel Static Pressure) = (External Static Pressure) - 0.399*(Centreline Dynamic Pressure)

couplings within the mechanical balance were applied prior to transforming the data into normal force and pitching moment coefficients in model axes. These tests were carried out at Reynolds Numbers of 2.02×10^6 per metre and 1.35×10^6 per metre.

At various α, the elevon angle, η, was altered in order to determine the steady control derivatives, $C_{n\eta}$ and $C_{m\eta}$.

To determine the type of flow present over the model at various angles-of-attack and elevon angle, extensive surface flow visualisation was performed using a solution formed from approximately equal parts of Oleic acid, Titanium Dioxide and Paraffin. The surface of the model was coated with the fluid before starting the wind tunnel. The wind tunnel was then run for a sufficient period for the paraffin to evaporate leaving the flow patterns as traces of Titanium Dioxide.

Off-surface flow visualisation was performed using a laser light sheet to illuminate smoke entrained into the flow so as to highlight the flow structures, as shown in fig. 4.3.

4.3 Measurement of Surface Pressures.

Each of the barrel transducers used to measure the pressures on the elevon, and the 5 transducers within the Scanivalve unit were statically calibrated over the expected range of applied pressures and were found to have a linear response (fig. 4.4). For each of the tappings connected to a transducer through a tubing system, however, it was also necessary to obtain a dynamic calibration in order to correct the amplitude and phase of measured unsteady pressures.

4.3.1 Dynamic Calibration of Pressure Tubing System.

Initially, it was planned to use the corrections developed by Bergh and Tijdeman [1965] [1972], whose technique allows for various diameters and lengths of tubes, for the mean pressure and temperature at the tapping, and for variations of local flow velocity. When these predictions were checked against the results from tests where oscillatory pressures were applied to various tappings, it was discovered that, for this particular tubing system, the corrections were not sufficiently accurate.

The tubing system used can be simplified into three lengths of tubes of different diameters, as shown in fig. 4.5. The complex internal geometry of a Scanivalve unit was modelled by a tube of constant diameter, with the length determined by matching predictions with the results from an oscillatory pressure applied to the end of the unit. The vinyl tubes all had a length of 1m, whilst the stainless steel tube lengths varied from 0.05m to 0.4m. This caused large variations in the dynamic calibrations of the set of tubing runs.

Starting from the Navier-Stokes equations, the continuity equation, the equation of state and the energy equation, Bergh and Tijdeman [1965] [1972] produced equations to predict the complex transfer characteristics for a tube. This then forms a recursive equation for a complete tubing system. The equations were greatly simplified by assuming small sinusoidal disturbances, small ratio of internal tube diameter to length and laminar flow in the tube. The resulting equations were coded into a 'C' program as given in Appendix III. Results from this program were checked against predictions calculated by other researchers (Bergh and Tijdeman [1972], Förscher [1976], Mabey [1983], Warsop [1987]).

The calibration apparatus shown in fig. 4.6 was constructed to allow a sinusoidal pressure to be applied to any tapping. The piston was operated by a d.c. electric motor, allowing the frequency to be altered as a function of the applied voltage. A miniature pressure transducer was mounted in the side of the piston to provide a reference pressure. The reading from this transducer was checked against a similar sensor mounted at the bottom of the piston to ensure that the reference reading was the same as would be applied to a tapping under test, which was found to be the case. This equipment was used whenever it was necessary to determine the dynamic calibration of a tubing system.

Tappings 21 and 94 represented typical lengths of tubing (l_1 = 0.2m) and were intended to be physically identical. However, as can be seen in fig. 4.7, not only are the numerical predictions in error but the calibration results for the two tappings are also significantly different from each other. Comparing the results for a much shorter tube system as in tapping 14 (l_1 = 0.05m), the predictions do not adequately predict the dynamic calibration, fig. 4.8.

An investigation was conducted into the cause of the above differences. A 1m

length of vinyl tubing was tested, without any steel tube connected. As can be seen from fig. 4.9, there was a significant phase difference between the actual and predicted phase angles. This difference is most likely the result of the inconsistent internal diameter of the tubing used. To further investigate these variations, a model of tapping 14 was constructed, the only difference being that rather than drilling down into the steel tube, the tapping was formed by drilling a hole down through a test plate into which the steel tube was secured, fig. 4.10(a). The comparison of the dynamic calibrations and prediction is given in fig. 4.8. There is a large difference in the amplitude ratios. Upon closer inspection of tapping 14, a large burr was found on the hole drilled into the steel tube, as shown in fig. 4.10(b). It is felt that this is the most likely cause for the difference between the calibrations for tappings which have the same tube geometry.

As a result of these findings, the dynamic calibration for each tapping was determined using the apparatus of fig. 4.6. A cubic fit was applied to each curve and the regression coefficients were used to correct for the dynamic effect of the tubing during analysis of the data. This implied that no account could be taken of the effect of the local static pressure or velocity of the flow at the tapping as was possible using the theoretical predictions. To estimate the likely error, a simple parametric study was conducted using the prediction technique for a steel tube of length 0.2m and vinyl length of 1m (i.e. tappings 21 and 94).

The static pressure would typically be 2000 N/m^2 below atmospheric. Fig. 4.11 shows the effect of a 5000 N/m^2 variation in pressure at the tapping. These results predict only a small effect. At a test speed of 30 m/s, a C_p value of -2 means a local tapping cross-flow velocity of 50 m/s. Fig. 4.12 shows the effect of both a 25m/s and 50m/s cross-flow. This effect is quite large, producing a difference of 4° in phase, at a frequency of 20Hz., between V=0 (i.e. the test condition under which the dynamic calibrations were conducted) and V=50m/s.

In an attempt to quantify the actual errors, rather than the predicted values, the dynamic calibrations of three tappings were tested wind-on, using the elevon to produce an oscillating pressure. A barrel transducer was mounted through the wing, next to each tapping, to act as the reference sensor. The model was set at α=0°, and V=30m/s. The tappings were specifically chosen as follows : tapping 32 - a short length of steel tube;

tapping 61 - long steel tube; tapping 51 - tapping with a large burr effect.Unfortunately, scatter in the results masked any difference due to velocity etc.. However, from the results of this investigation, it is felt that the accuracy of the tubing corrections were within ±5° in phase and ±7% in amplitude.

During the unsteady tests, the 6-component mechanical balance was locked to improve the stiffness of the mounting system. In this form, the most obvious balance natural mode was at 2 Hz. However, due to the large inertia of the balance, this was not considered to be a problem in terms of structural excitation of the model. The lowest model mode was at 65 Hz. and was a wing bending mode. The very low structural damping, however, meant that the tests could be carried out to 25 Hz. elevon oscillation without excessive model excitation. The gap between the splitter plate and the model was sealed with insulation tape for the pressure tests.

For each test point, the 5 pressures measured from the Scanivalve unit were recorded along with the tunnel velocity, the signal from the Hall effect sensor (elevon angle) and the feedback angle from the actuation motor (as previously shown in fig. 3.4). No calibrations or filtering were applied to the data at this point. The chosen acquisition frequency was 500 Hz. per channel to allow for good definition of the oscillation and an acceptable Fourier Analysis frequency resolution. A total of 2048 samples per channel were recorded for each unsteady test. This value was determined following an investigation into the effect of various sample lengths and averaging techniques, as detailed below.

4.3.2 Effect on Fourier Analysis of sample size and sample overlapping techniques.

By subdividing a sample of 4096 data points taken during a wind-on elevon oscillation test, it was possible to investigate the effect of sample lengths of 512, 1024, 2048 and 4096 points on the FFT results. This was done for two different elevon oscillation frequencies, namely 4 and 26 Hz. The results for 26Hz. are given in fig. 4.13. The Fourier analysis results from each sample length were compared in two ways - the peak amplitude at the elevon oscillation frequency and the full spectrum results. Using only 512 samples tended to reduce definition of the frequency peak.

Averaging of Fourier spectrums, both without any data overlapping and for an

overlap of 50%, did not significantly improve the accuracy of the results. The peak in the spectrum associated with the elevon oscillation was very clean and hence averaging was not able to improve upon the accuracy of the results, see fig. 4.14.

Each test point consisted of the following : recording of the transducer zeros from port zero of the Scanivalves; measurement of the required number of points for the 5 pressures; block saving of this data in binary format; stepping to next Scanivalve port; recording of next set of data. The elevon pressures were recorded during separate tests and involved several runs since only three barrel transducers could be mounted into the elevon at any one time. By using the elevon position as the reference for the pressures it was possible to compare the results from each of these runs.

No calibrations were applied or analysis performed during the acquisition of the data.

Steady pressure measurements were carried out, for a steady elevon position of zero, at α = -35° to + 40°, in steps of 2.5°. At α = 10°, 12.5°, 15°, 20°, 27.5° and 35° (both positive and negative), tests were made for $\eta = \pm 20°, \pm 10°, \pm 5°$, and 0°.

Unsteady pressure tests were also carried out for the above α values, for a frequency range of 5 - 25 Hz., in increments of 5Hz., at a test speed of 30 m/s, giving a frequency parameter range of ν=0.3 to 1.6, based on semi-span, with an amplitude of 5° and mean angle of 0°. In addition, some similar tests were carried out for mean elevon angles of ±15°.

4.4 Test Procedure for Flexibly Mounted Wing.

Within the GLOBALAB® acquisition software, the sample frequency was set to 500 Hz with 2048 samples being recorded for each channel, namely, the three accelerometers and the elevon angle. The natural frequency of the wing was determined by performing a Fourier Analysis on the accelerometer responses recorded when the wing tip was released from a displaced position.

The signals were recorded for various discrete elevon oscillation frequencies, both wind-off and wind-on. The model was tested at α=0°, 10°, 12.5°, 15°, 20°, 25°, 35°. The

length, d, of the unsupported region of the flexible plate was altered to produce three different natural frequencies of 17.1, 21.5 and 24 Hz. All tests were conducted with a freestream velocity of 30m/s. The wing mode frequencies corresponded to ν=1.07, 1.35, 1.51, and hence were in the range expected for a typical first wing bending mode.

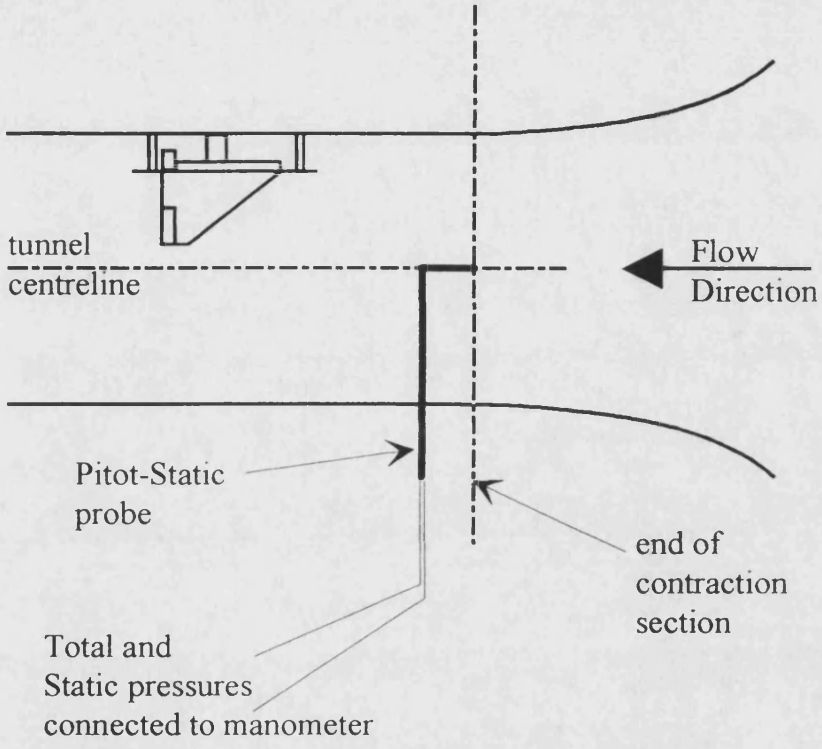

Fig. 4.1 - Section through tunnel working section showing calibration of dynamic and static pressure.

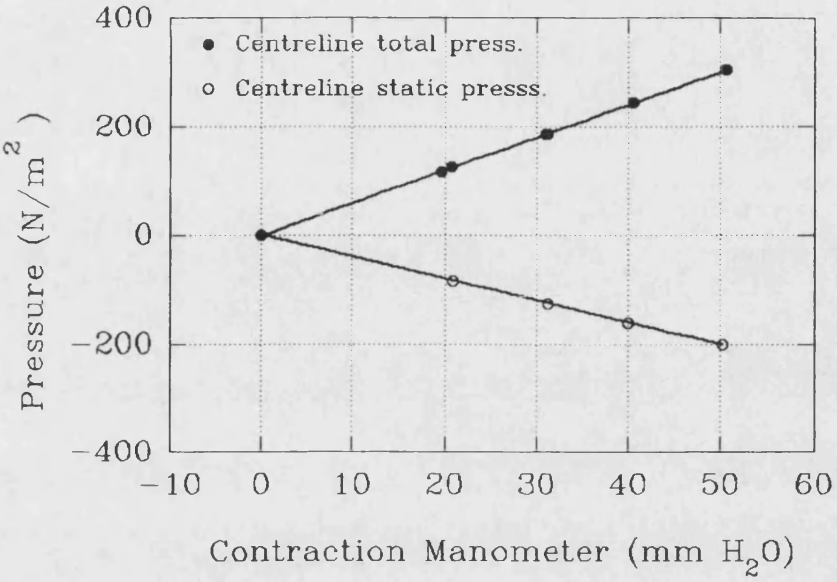

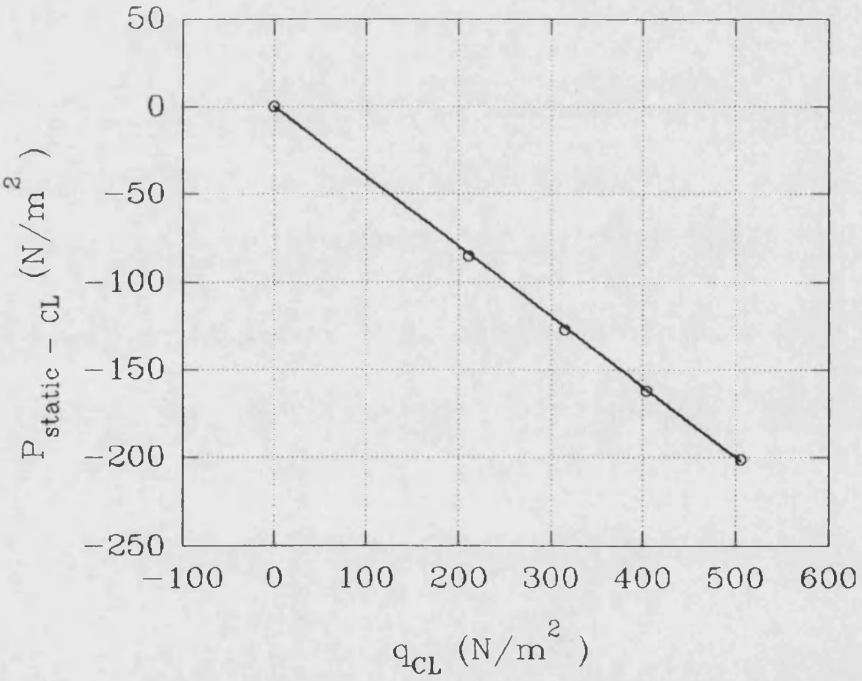

Fig. 4.2 - Windtunnel calibration curves

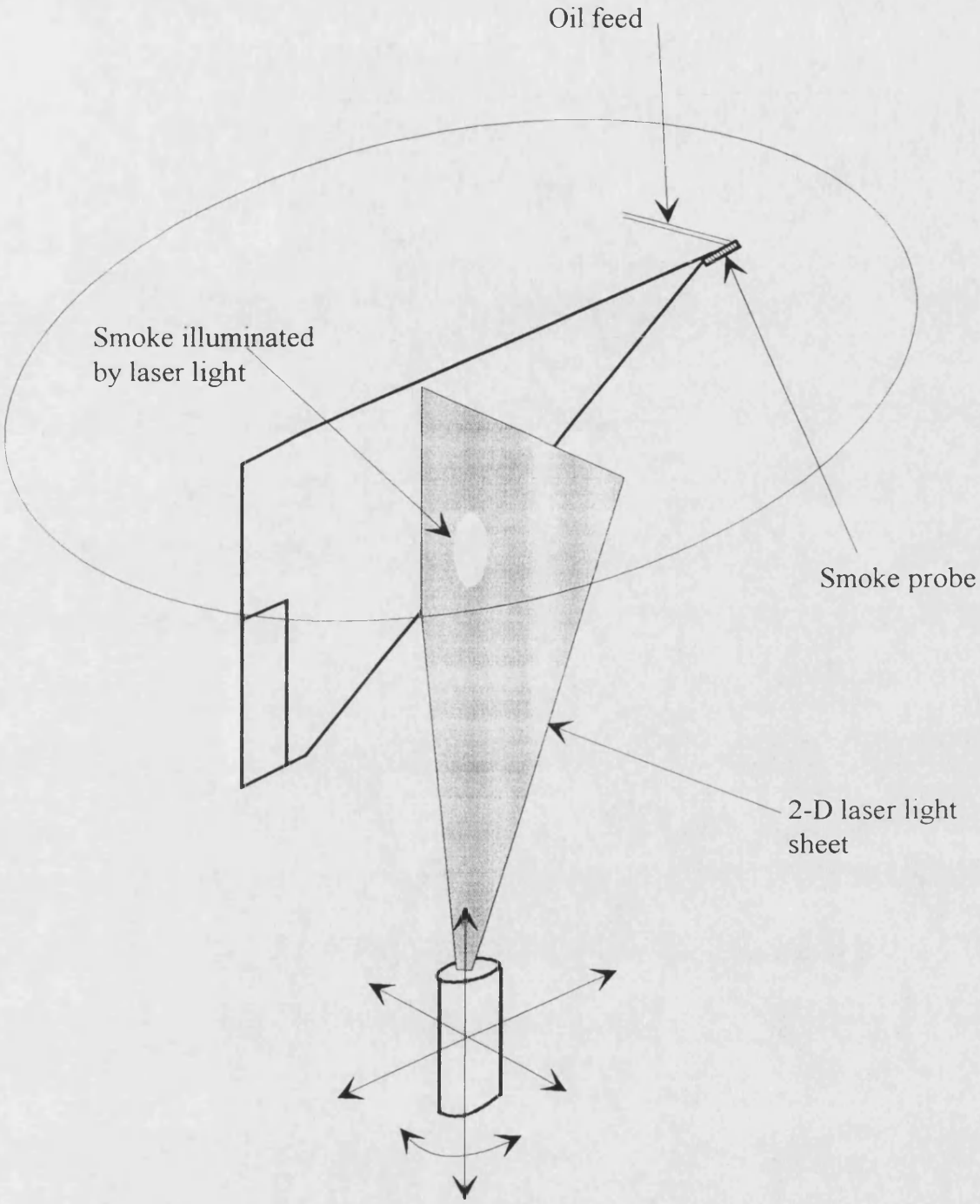

Fig. 4.3 - Off-Surface Flow Visualisation using a Laser-Light-Sheet.

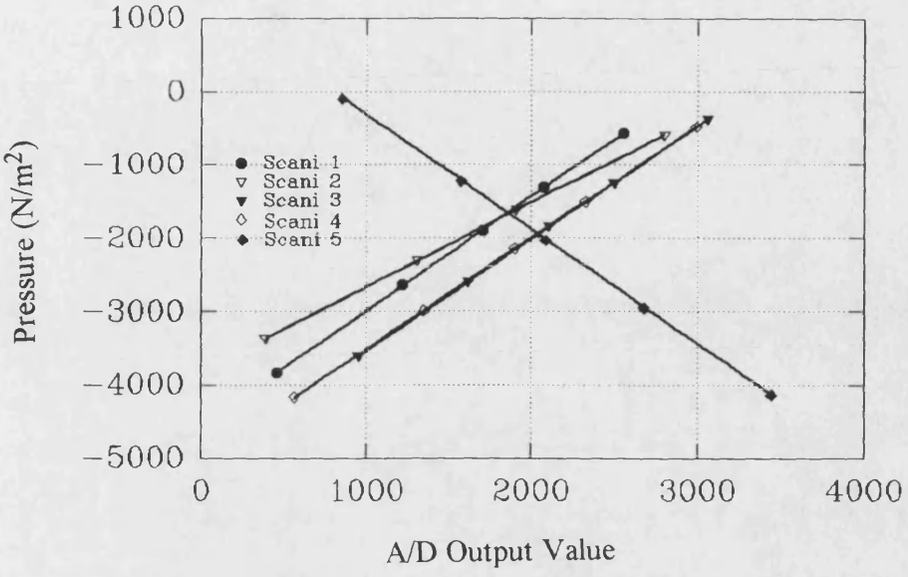

(a) Scanivalve pressure transducer calibrations

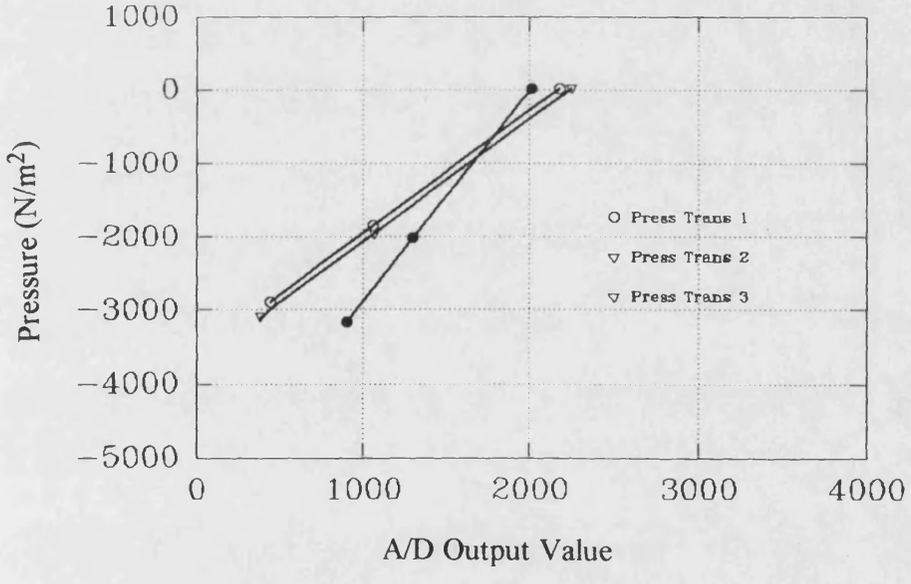

(b) Miniature pressure transducer calibrations

Fig. 4.4 - Pressure transducer calibrations

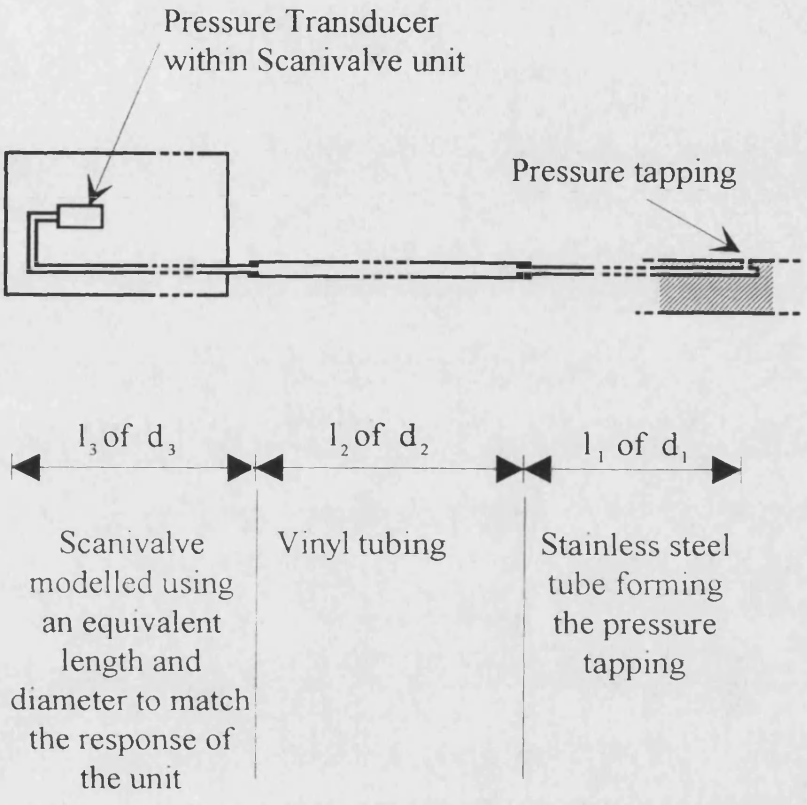

Fig. 4.5 - Typical pressure measurement, tubing system.

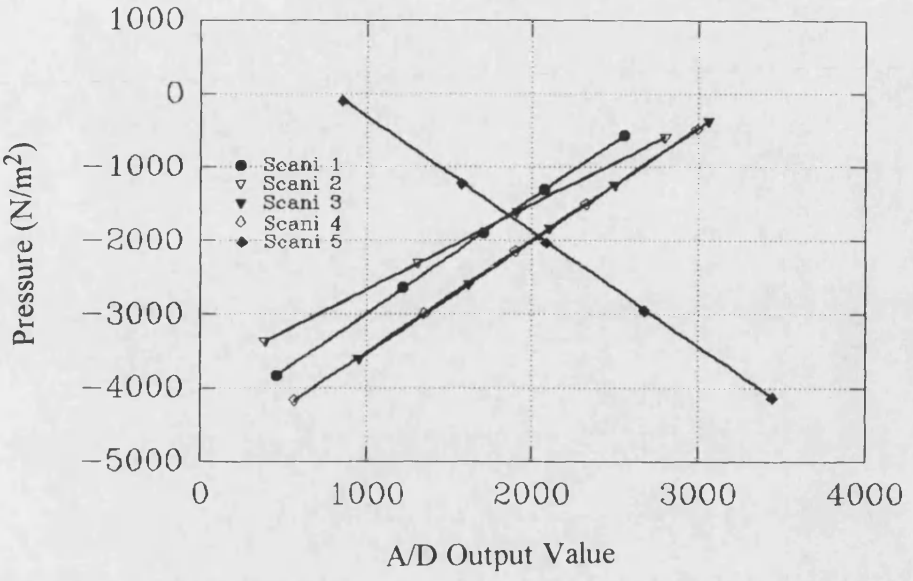

(a) Scanivalve pressure transducer calibrations

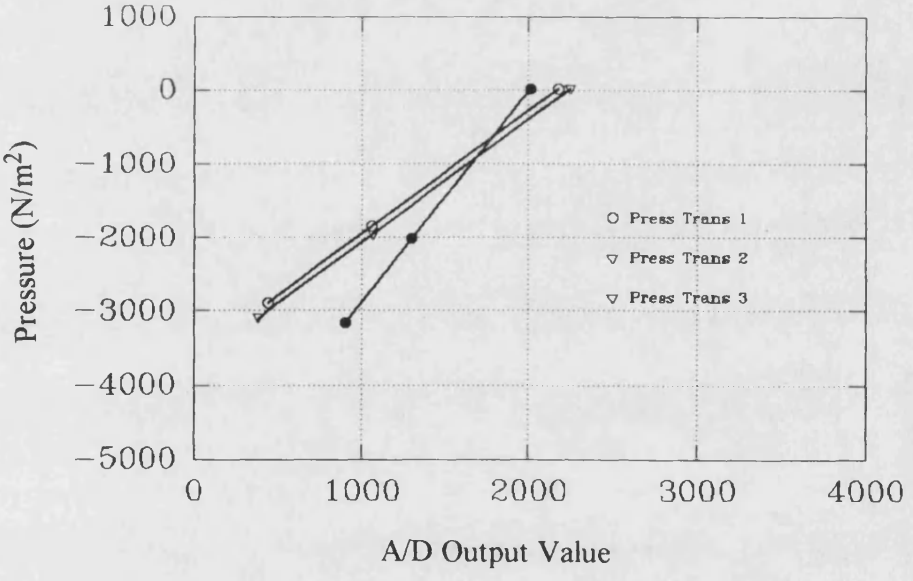

(b) Miniature pressure transducer calibrations

Fig. 4.4 - Pressure transducer calibrations

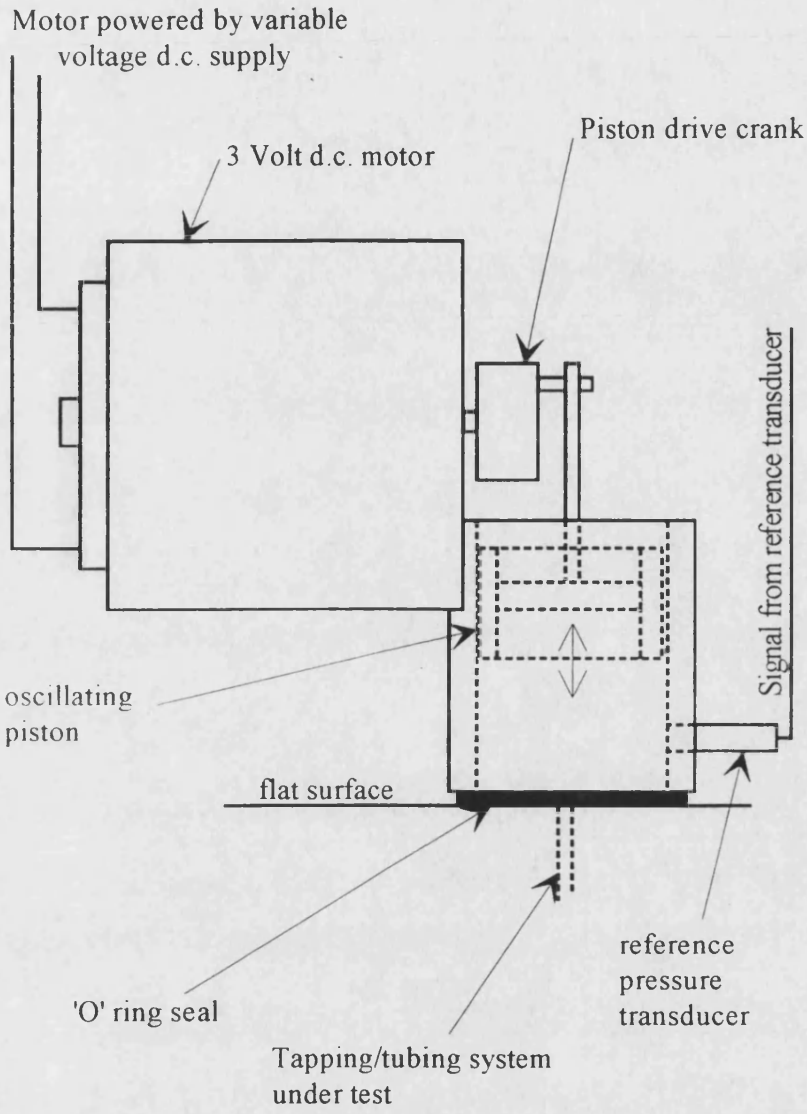

NOTE : Drawn twice actual size

Fig. 4.6 - Oscillator pressure generator for calibrating tubing systems.

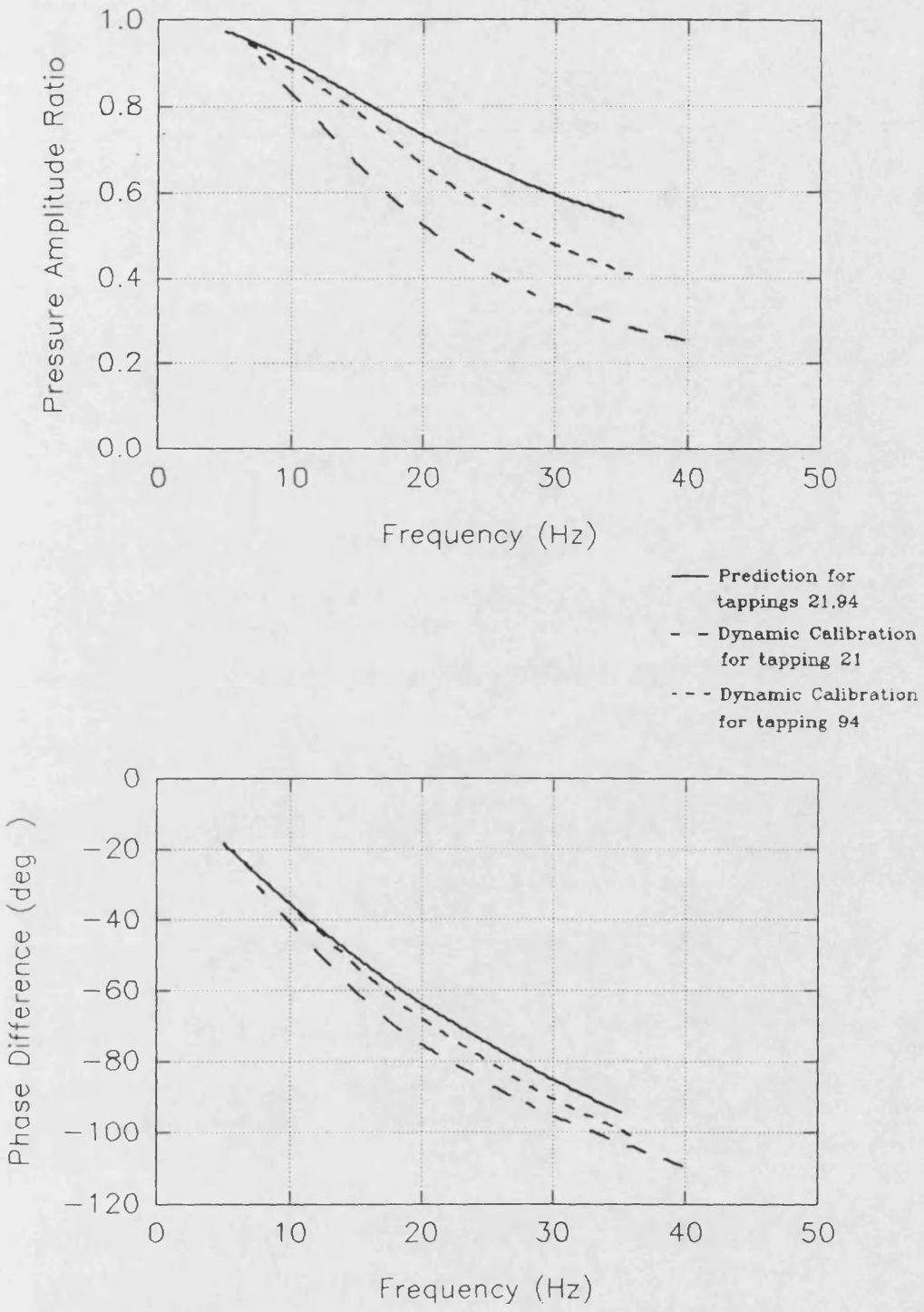

Fig. 4.7 - Comparison of dynamic calibrations for tappings 21 and 94

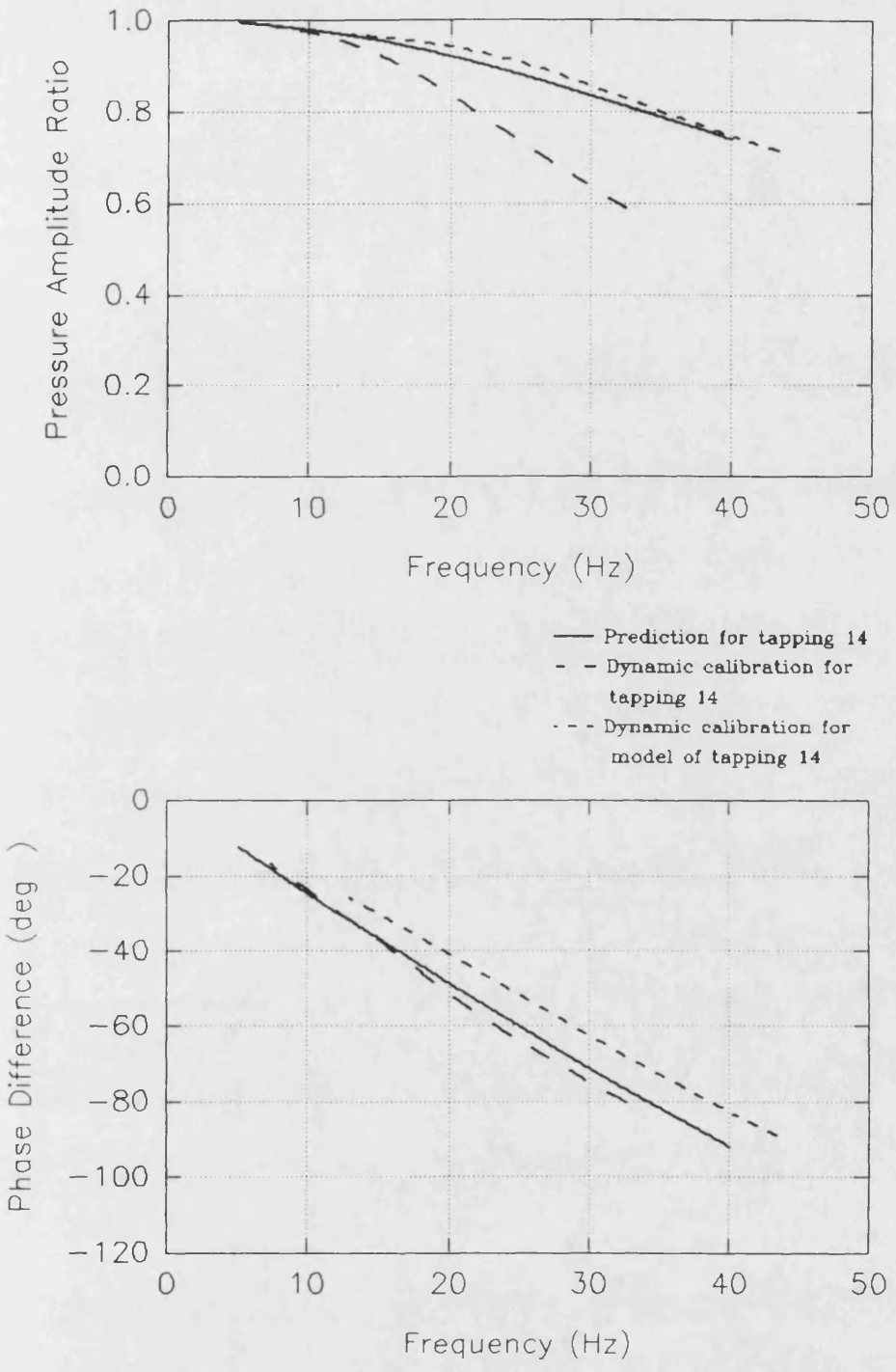

Fig. 4.8 - Dynamic calibration for tapping 14

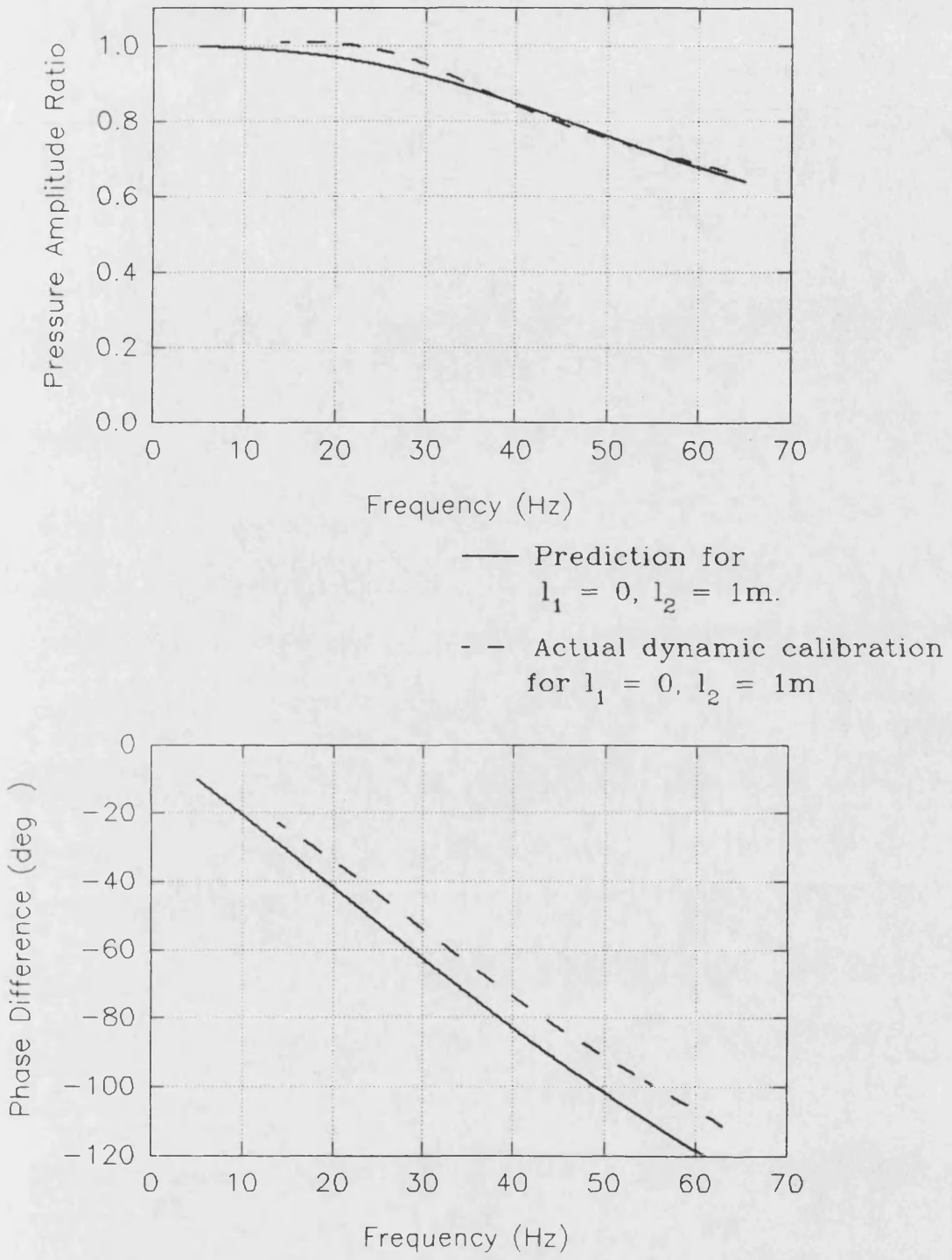

Fig. 4.9 - Dynamic calibration for a 1m length of vinyl tubing connected to a Scanivalve unit

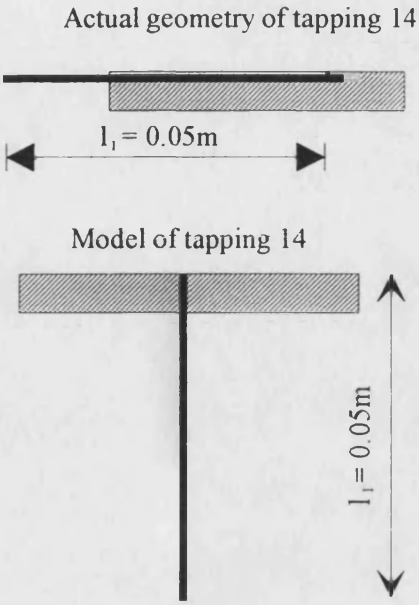

(a) comparison of tapping 14 and simplified model.

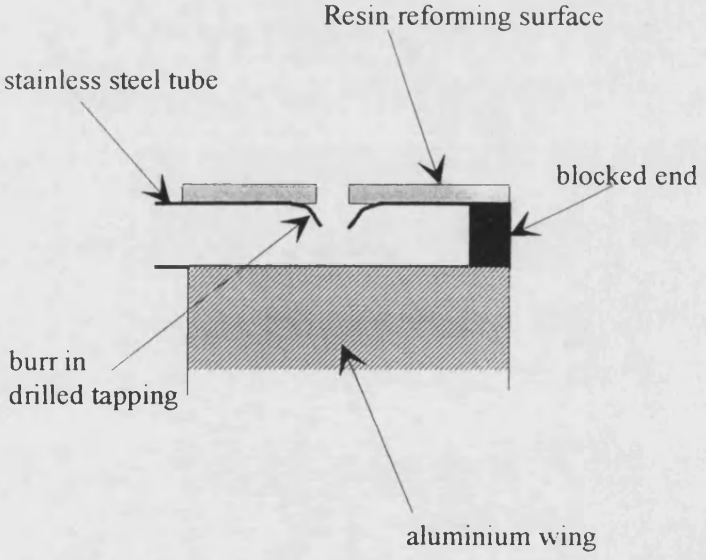

(b) enlarged view of burr on inside of tube

Fig. 4.10 - Investigation into effect of tapping geometry on dynamic calibration.

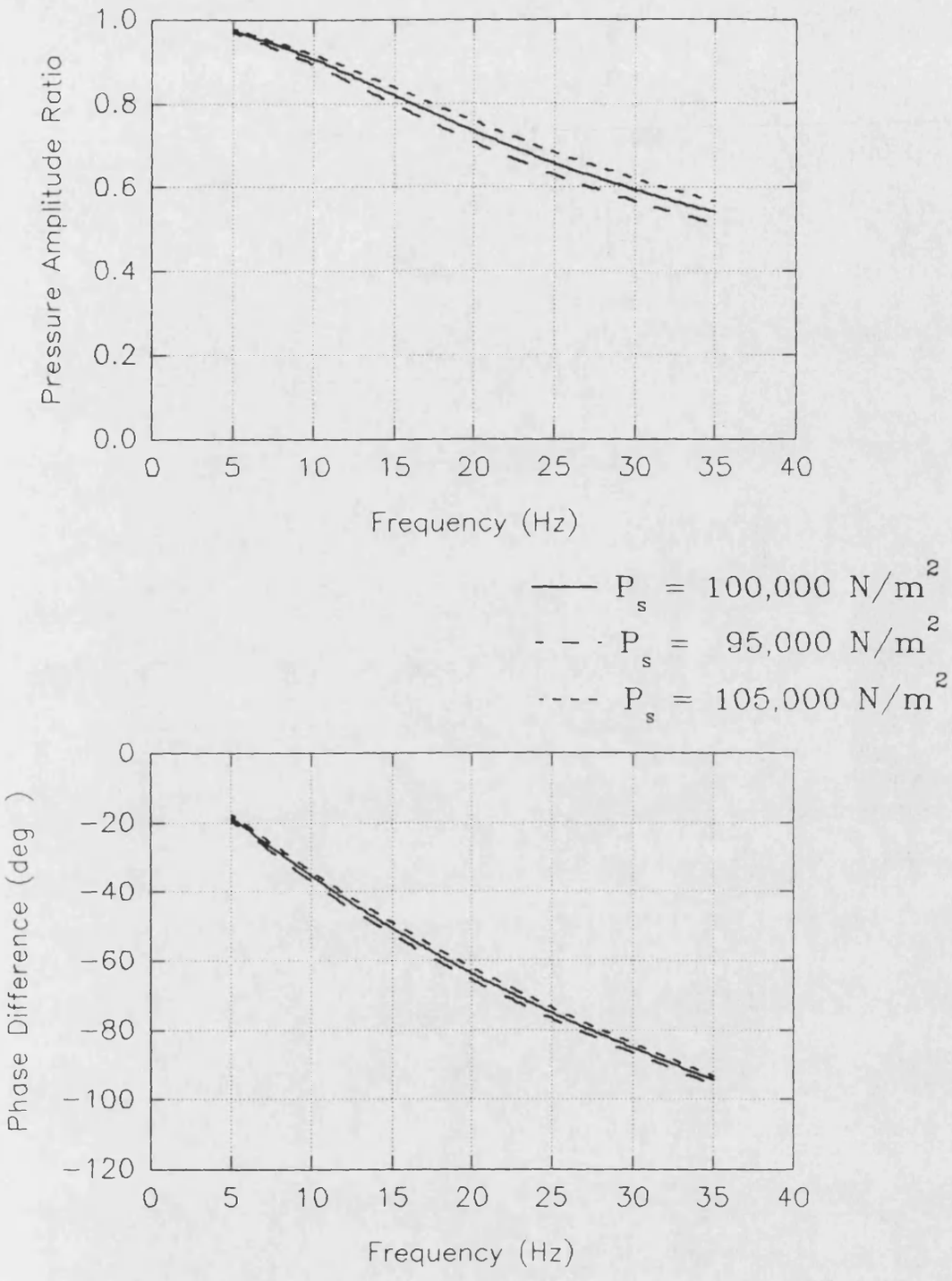

Fig. 4.11 - Predicted dynamic calibrations for various mean static pressures

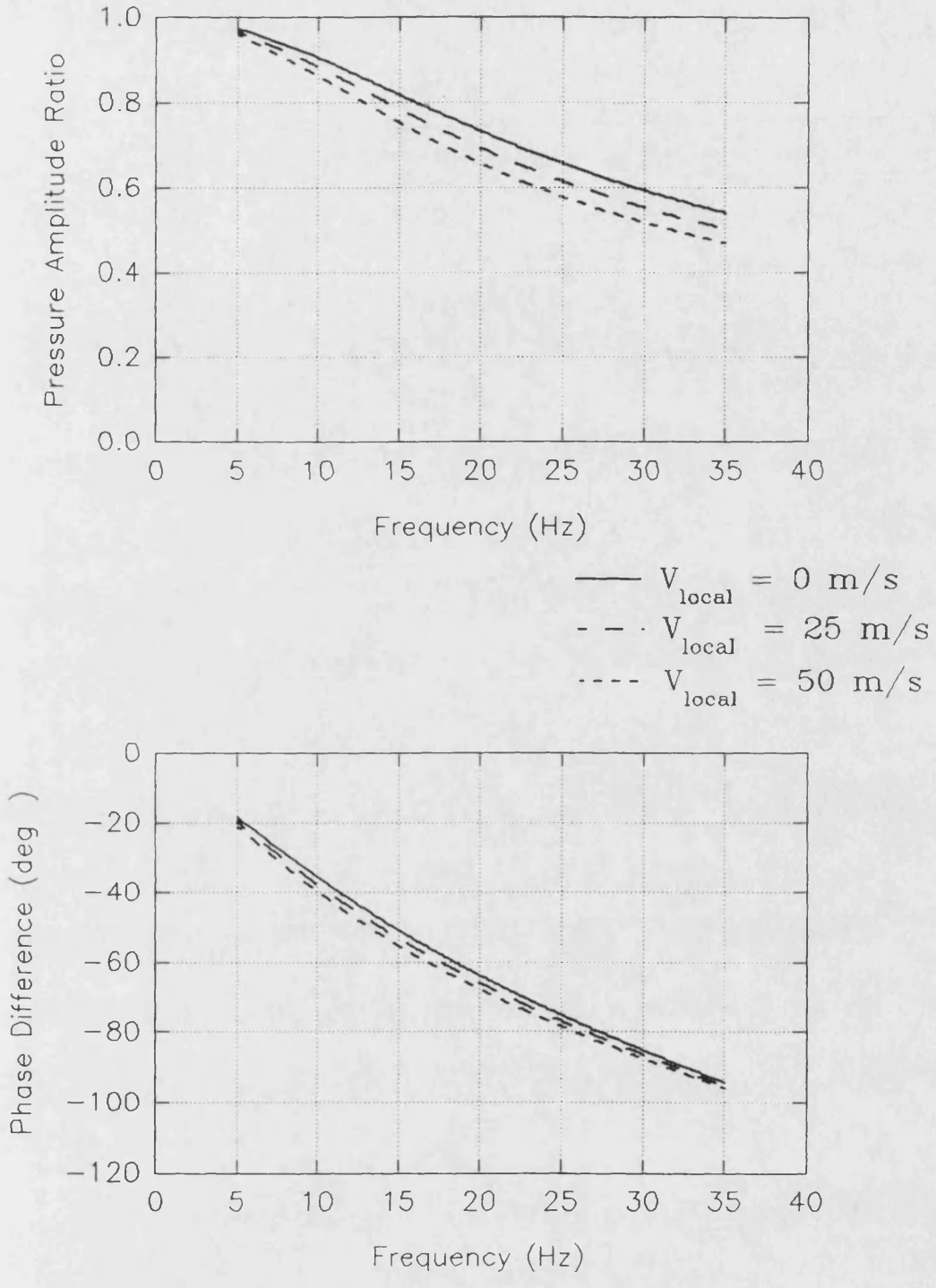

Fig. 4.12 - Predicted dynamic calibrations for various local velocities

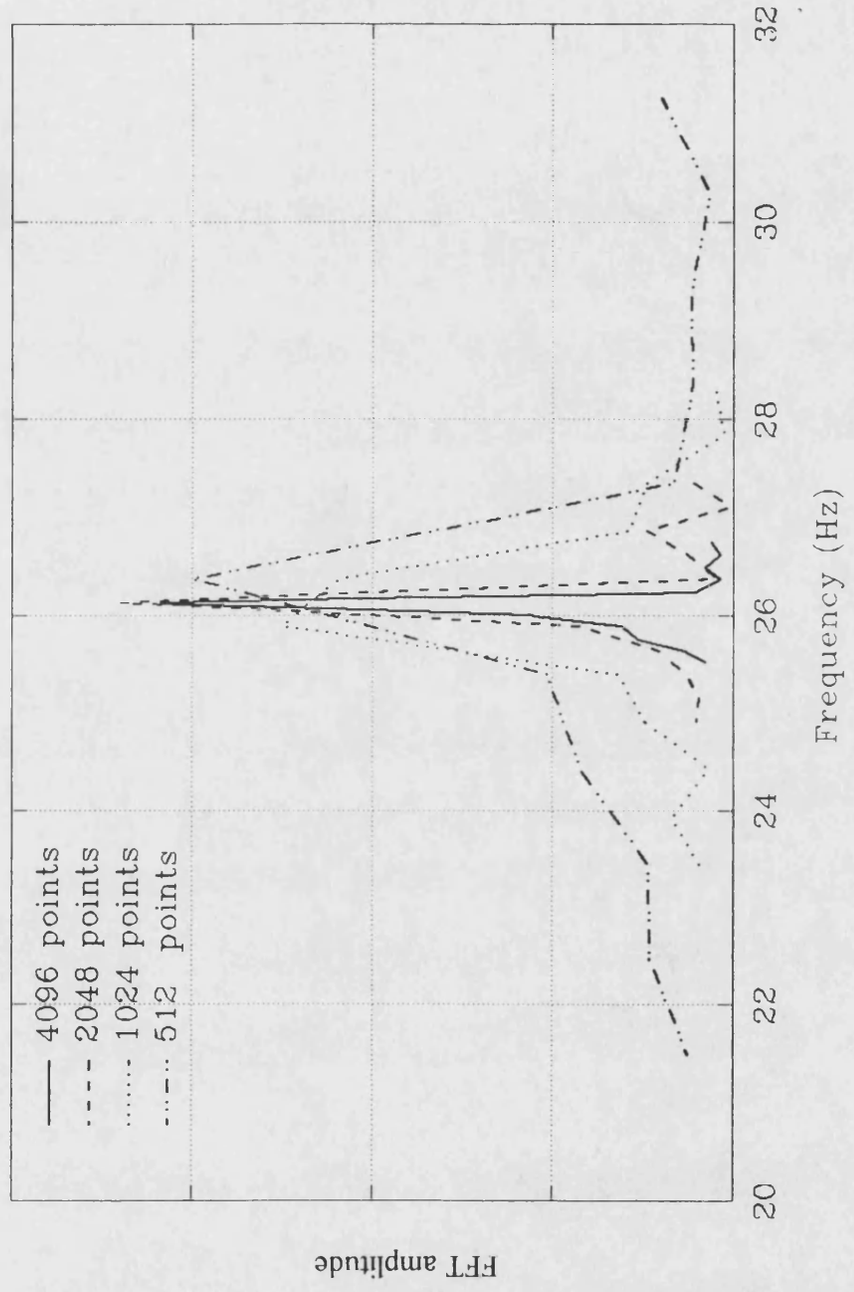

Fig. 4.13 - Fourier Transform amplitudes for various sample lengths

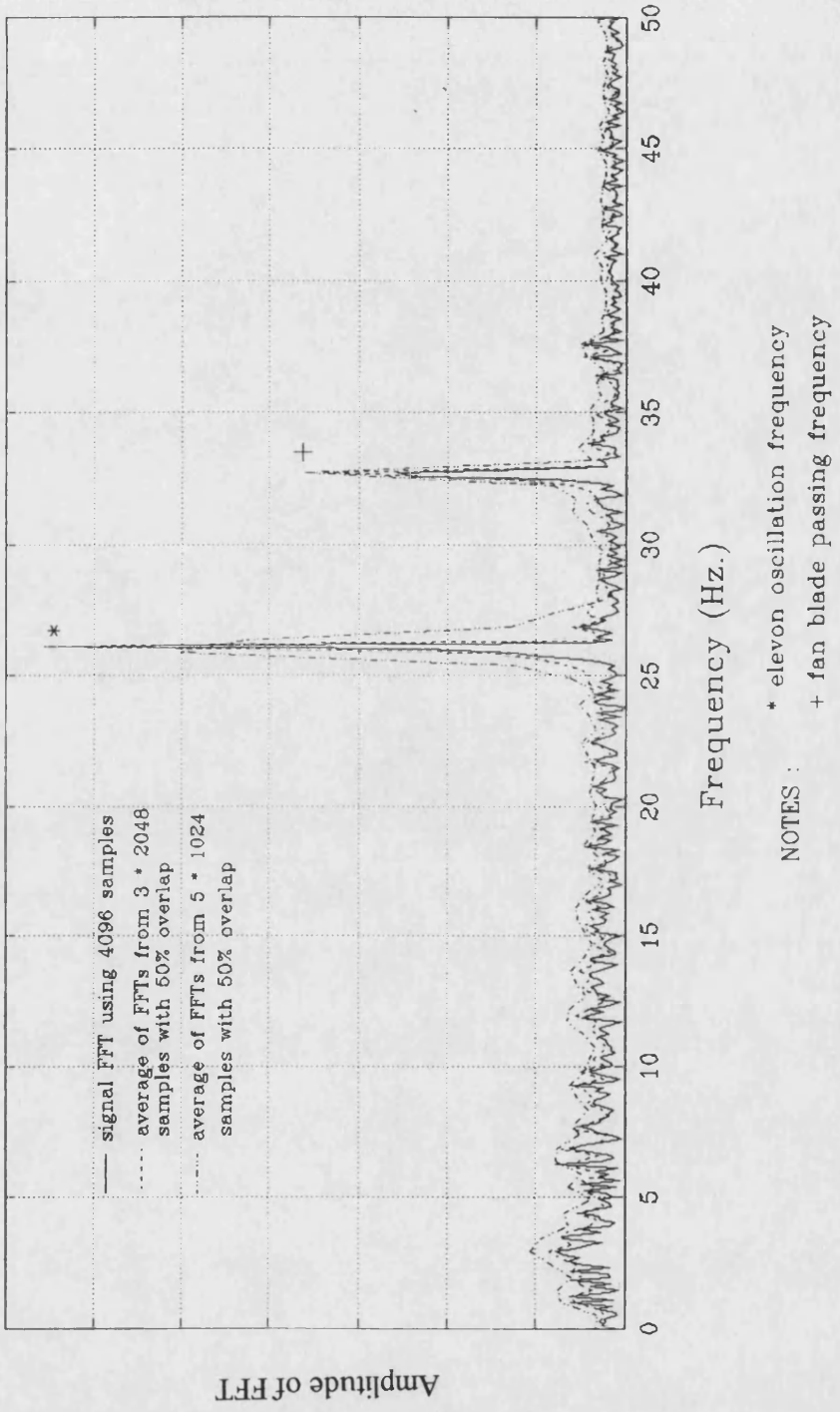

Fig. 4.14 - Fourier Transform results for various sample overlapping techniques

5. DATA ANALYSIS TECHNIQUES.

5.1 Steady Pressure Results.

The pressure coefficient is defined as follows :

$$C_p = \frac{P_s - P_\infty}{\frac{1}{2}\rho V_\infty^2} \quad .$$

The integration of the pressures was carried out by integrating in y followed by x to produce the overall force and moment results as follows :

$$C_n = \frac{1}{A}\int_0^{c_r}\int_0^{s_{local}} C_p \, dy \, dx$$

where, for the half wing model:

$$A = \frac{s}{\frac{1}{2}(c_{tip} + c_r)} \quad .$$

Similarly, the pitching moment coefficient about the aerodynamic centre is calculated as follows :

$$C_{m_{a.c.}} = \frac{1}{A\bar{c}}\int_0^{c_r}\left[\int_0^{s_{local}} C_p \, dy\right](x - x_{a.c.}) \, dx \quad .$$

The steady hinge moment coefficient is defined as :

$$C_h = \frac{1}{A_\eta c_\eta}\int_{c_{\eta le}}^{c_r}\left[\int_{s_{\eta root}}^{s} C_p \, dy\right](x - x_{h.l.}) \, dx \quad .$$

Finally, the bending moment coefficient about the root (x axis), for later analysis of the flexible root mounting arrangement is calculated as follows :

$$C_r = \frac{1}{A\bar{c}} \int_0^{c_r} \left[\int_0^{s_{local}} C_p.y \; dy \right] dx \quad .$$

5.2 Unsteady Pressure Results.

If a sinusoidal elevon motion is assumed, then an elevon angle can be defined as

$$\eta(t) = \eta_0 \sin(\omega t) \quad .$$

Assuming a sinusoidal pressure response at this frequency gives

$$C_p(t) = C_{p_0} \sin(\omega t + \phi) + C_{p_m} \quad .$$

A complex Fast Fourier Analysis of both the elevon angle and unsteady pressure produces results of the form

$$C_p(\nu) = C_p'(\nu) + i C_p''(\nu)$$

$$\eta(\nu) = \eta'(\nu) + i \eta''(\nu)$$

where $\nu = \omega s/V$.

A transfer function between the unsteady pressure component and the elevon at frequency parameter, ν, can be formed, i.e.

$$\frac{C_p}{\eta}(\nu) = C_{p_\eta}(\nu) + i C_{p_{\dot{\eta}}}(\nu) \quad ,$$

or in polar form

$$\frac{C_p}{\eta}(\nu) = \frac{C_{p_o}}{\eta_o} \sin(\phi)$$

$$\text{where} \quad \frac{C_{p_o}}{\eta_o} = \sqrt{C_{p_\eta}{}^2 + C_{p_{\dot\eta}}{}^2}$$

$$\phi = \tan^{-1} \frac{C_{p_{\dot\eta}}}{C_{P_\eta}} \; .$$

By integrating these in-phase (real C_{p_η}) and out-of-phase (imaginary $C_{p_{\dot\eta}}$), unsteady pressure components over the surface of the model, it is possible to obtain the unsteady normal force, n(ν), and pitching moment, m(ν), coefficients, where,

$$n(\nu) = n_\eta + i n_{\dot\eta}$$

and (representing the double integral as a single integral with respect to area)

$$n_\eta = \frac{1}{A} \int_0^A C_{p_\eta}(\nu)\, dA \qquad \text{and} \qquad n_{\dot\eta} = \frac{1}{A} \int_0^A C_{p_{\dot\eta}}(\nu)\, dA$$

or in polar form,

$$\frac{n}{\eta}(\nu) = n_o \sin(\phi_n)$$

$$\text{where} \quad n_o = \sqrt{n_\eta{}^2 + n_{\dot\eta}{}^2}$$

$$\phi = \tan^{-1} \frac{n_{\dot\eta}}{n_\eta} \; .$$

Similarly for m(ν),

$$m(\nu) = m_\eta + i m_{\dot\eta}$$

where

$$m_\eta = \frac{1}{A\bar{c}} \int_0^A C_{p_\eta}(\nu) x\, dA \qquad \text{and} \qquad m_{\dot\eta} = \frac{1}{A\bar{c}} \int_0^A C_{p_{\dot\eta}}(\nu) x\, dA$$

or in polar format,

$$\frac{m}{\eta}(\nu) = m_0 \sin(\phi_m)$$

$$\text{where} \quad m_0 = \sqrt{m_\eta^2 + m_{\dot{\eta}}^2}$$

$$\phi = \tan^{-1} \frac{m_{\dot{\eta}}}{m_\eta} \quad .$$

The unsteady root bending moment is similarly defined,

$$r(\nu) = r_\eta + i r_{\dot{\eta}}$$

where

$$r_\eta = \frac{1}{A\bar{c}} \int_0^A C_{p_\eta}(\nu) y \, dA \qquad \text{and} \qquad r_{\dot{\eta}} = \frac{1}{A\bar{c}} \int_0^A C_{p_{\dot{\eta}}}(\nu) y \, dA$$

or again in polar form,

$$\frac{r}{\eta}(\nu) = r_0 \sin(\phi_r)$$

in the same manner as above.

Integrating over the control surface alone allows the unsteady hinge moments, h(ν) to be calculated, where,

$$h(\nu) = h_\eta + i h_{\dot{\eta}}$$

and

$$h_\eta = \frac{1}{A_\eta c_\eta} \int_0^{A_\eta} C_{p_\eta}(\nu)(x - x_h) \, dA_\eta \qquad \text{and} \qquad h_{\dot{\eta}} = \frac{1}{A_\eta c_\eta} \int_0^{A_\eta} C_{p_{\dot{\eta}}}(\nu)(x - x_h) \, dA_\eta$$

or in polar form, using the same form as above,

$$\frac{h}{\eta}(\nu) = h_0 \sin(\phi_h)$$

A library of 'C' programs was developed to deal with this analysis. Each section is

described below.

5.3 General Analysis Program - ANAL_STY.

The code listing for this program is given in Appendix 1. Fig. 5.1 shows a flowchart for the program. Each block of data for the 5 pressures are loaded from the raw data file and analysed in turn. Having applied the static calibrations, corrected for the tunnel calibrations and non-dimensionalised with q_{cl}†, the mean pressures are calculated and written in binary form to a file. The mean elevon angle is also recorded. The use of binary files allows random access of the analysed data by other parts of the analysis system. A complex Fast Fourier Transform is then applied to the elevon angle and pressure signals.

5.3.1 Fast Fourier Transform (FFT) Algorithm - FFT_BIN (Appendix 2).

A Danielson-Lanczos algorithm for an FFT was used (Press et al [1986]). This allows two real data signals to be analysed at one time. Cosine windowing (Bendat and Piersol [1971]) was applied to the data, before analysis, and was corrected for, once the FFT had been found. This analysis results in a complex Fourier spectrum.

5.3.2 Effect of Acquisition Board.

Because the acquisition board only read and converted one channel at a time, there was a time lag between the sampling of sequential signals. (Note : this would not have been the case if a Simultaneous Sample and Hold board had been used). Although this time lag was constant, the effect on the phase angle of the FFT depended on the frequency, i.e. the higher the frequency, the greater the phase lead of each successive channel. To correct for this effect, the following equation was used,

$$\Delta\phi = 2\pi \times \frac{\text{(elevon frequency)} \times \text{(number of channel rel. to elevon)}}{\text{(total acquisition frequency)}}$$

† centreline dynamic pressure, $q_{cl} = 0.5*\rho V^2_{\text{tunnel CL}}$

Since the elevon angle was the first signal read, the acquisition board, in effect, produced a false lead in the pressure signals. The FFTs were corrected by subtracting $\Delta\phi$ from the phase angle of the FFT.

5.3.3 Tube Dynamic Calibration Correction.

At each frequency in the FFT spectrum, the phase lag and amplitude effect due to the tube system of the relevant tapping are calculated using the regression coefficients obtained, section 4.3.1. By dividing by the complex tube effect, the amplitude reduction and phase lag corrections can be applied to the FFT.

5.3.4 Calculation of Transfer Function (TF).

Each pressure signal is related to the elevon motion by calculating the transfer function between them. The transfer function gives the C_p variation per radian of elevon rotation and the phase angle between the unsteady pressure and the elevon angle. The TF was actually calculated by dividing the cross-spectrum by the amplitude of the elevon motion (Bendat and Piersol [1971]). This in effect is the same as dividing, in complex form, the FFT results for the pressure by the FFT results for the elevon angle.

The five peak values from each pressure FFT and the results from the TFs were recorded in a separate file from the steady results.

This analysis program was checked by processing numerically created data. Various phase angles, means, frequencies and amplitudes were tested and checked against the known exact results. The accuracy was very high, with only small errors due to the numerical conversions and manipulations within the computer processor. Hence, the numerical errors were considered to be insignificant within the context of the wind tunnel tests.

5.4 Further Post-Processing techniques.

Various programmes were used to integrate the mean pressures and unsteady transfer function components to calculate the various normal force, pitching moment and hinge moment coefficients. This was done by applying the cubic spline curve fit of Chapra and Canale [1987] to the analysed data. This also allowed the peak $-C_p$ values to be found.

Since only the upper surface of the wing was covered with pressure tappings, the lower surface pressure distributions were found by testing at negative angles-of-attack. It must be remembered that the wing section was not symmetrical and hence the integrated overall normal force etc. are not directly comparable with the steady force measurements made with the 6-component mechanical balance.

5.5 Analysis of Flexible Wing Tests.

The data from the flexible wing tests were analysed using the STATPACK® module of the Data Translation GLOBALAB® package. This allowed the Fourier Transform of each signal to be calculated. The transfer function at the frequency of the test, between the tip accelerometer and elevon angle was also obtained as defined below :

The elevon oscillation is again assumed sinusoidal

$$\eta(t) = \eta_0 \sin(\omega t)$$

and the accelerometer response is likewise sinusoidal,

$$k(t) = k_0 \sin(\omega t + \phi) \ .$$

Since the sensor used is an accelerometer, the displacement of the wing at the sensor location, g(t), is

$$z(t) = -\frac{k_0}{\omega^2} \sin(\omega t + \phi) \ .$$

$$z(t) = \frac{k_0}{\omega^2} \sin(\omega t + (\phi - \pi)) \ .$$

Hence, using the same analysis as in section 5.1, the transfer function between g(t) and $\eta(t)$ can be written as (in polar form) :

$$\frac{z}{\eta}(\nu) = \frac{(k_0/\omega^2)}{\eta_0}\sin(\phi-\pi) = z_0\sin(\phi-\pi) \ .$$

As for the unsteady pressures, there is an error associated with the acquisition board only sampling one channel at a time. The equation of section 5.1.2 was used to correct for this effect.

The three accelerometer responses were compared using the ratio of their amplitudes, i.e. using A and B to denote two accelerometers, the ratio of amplitudes can be expressed simply as k_{0_A}/k_{0_B}

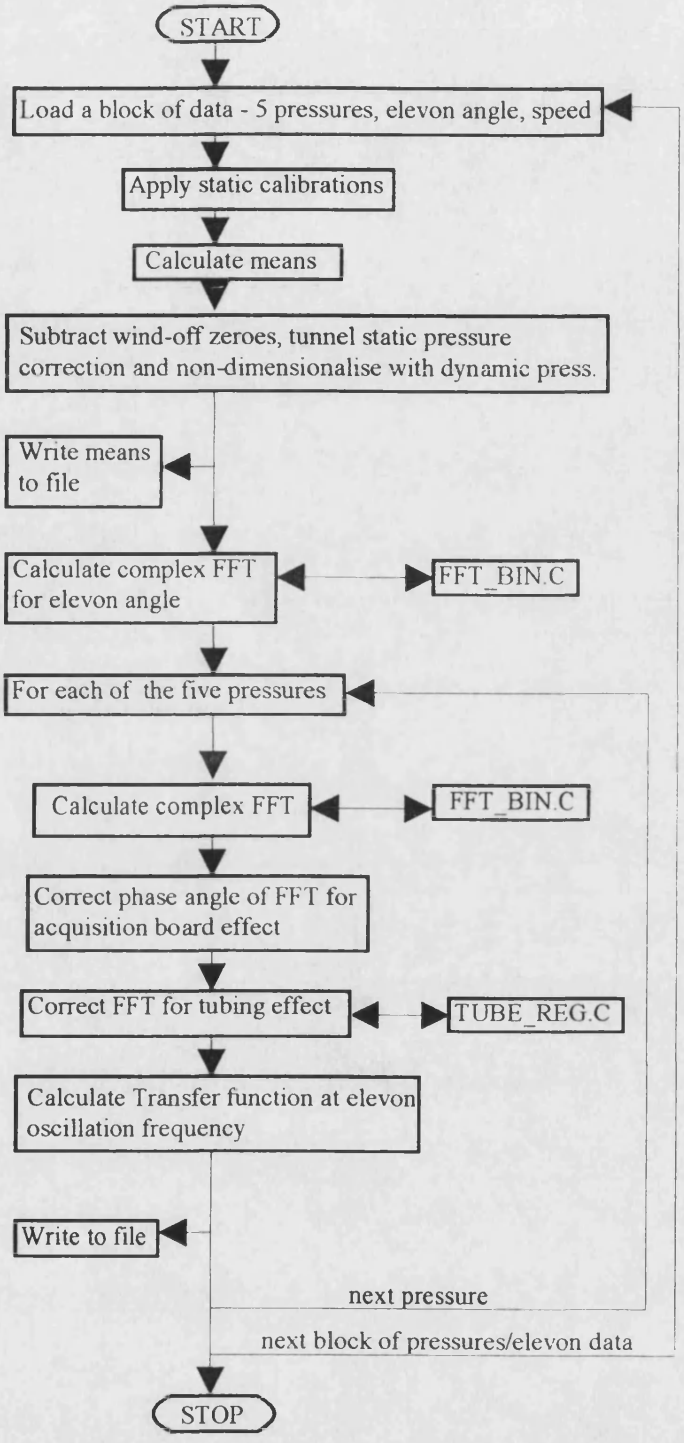

Fig. 5.1 - Flowchart for ANAL_STY.C - general analysis.

6. RESULTS FROM STEADY TESTS.

This chapter presents results for steady tests at α=0° to 35°, upper and lower surface, for various steady elevon angles. The first section deals with the effects of α on the overall flow characteristics for η=0°.

The second section presents and discusses the results for steady elevon deflections. These can then be used to as a reference for the unsteady results, especially in terms of the amplitude of the responses, and hence give an insight into the characteristic response of the vortex and attached flow to this form of forcing.

6.1 Steady Results, η=0° - effect of α.

Within this section, the upper and lower surface pressure distributions are described, before considering how these contribute to the overall normal force and pitching moments.

6.1.1 Upper surface pressures.

The pressure distributions at constant x values (spanwise sections) are typical of those found under a vortex system (fig. 6.1). Consider α=10° at x=375.5mm, the peak in $-C_p$ marks the lateral position of the core (as demonstrated by Greenwell and Wood [1992,B]) and the Cp level and peak half width are functions of the vortex strength. The primary attachment point is shown by the location of maximum Cp (e.g. at y/s_{local}=0.55 for this case). There is a weak secondary vortex present outboard of the primary core.

At α=12.5°, the primary core has moved inboard slightly and increased in strength. However, at α=15°, the peak $-C_p$ level has reduced and the vortex 'footprint' has increased (primary attachment has moved inboard) suggesting the vortex has burst upstream of this location at this angle-of-attack. It is worth noting that the lift produced (area under these curves) at this station, at α=15° is still greater than at α=12.5° even though the vortex is burst. At x=451mm, the vortex is burst for both α=12.5° and 15° - the peak C_p is lower than for α=10°, though again, the normal force contribution still increases with α.

Greenwell and Wood [1992] produced a technique (described on the following page) to determine the location of the vortex burst by comparing the 'half-width' (a measure of the width of the suction peak) as α increases. The relatively weak vortex present above this 55° leading edge sweep wing results in a relatively large attached flow contribution to the pressure distribution (not allowed for in the Greenwell and Wood technique) which prevented the half-width and its variation with α from being measured accurately and thus prevented this technique from being used here.

By plotting the minimum C_p level (C_{pmin}) at each constant x (spanwise row), it is possible to estimate the location of the breakdown point at each α (fig. 6.2). As discussed above, and as predicted by slender body theory, the peak suction at each x station should increase with α. When the vortex bursts, the C_{pmin} downstream of the breakdown point increases compared to that for lower α. This can be seen in fig. 6.2 where at the same x value, C_{pmin} is greater than at a lower angle-of-attack, e.g. comparing α=12.5° and 15°, this occurs at x≈280mm. Downstream of the burst, the C_{pmin} values are similar for all α, except at α=10°, suggesting that the burst is beyond the trailing edge at this incidence. [Note : the small number of tappings on the outboard elevon prevents the accurate determination of the core pressure peak over the control].

Using data taken every 2.5°, the breakdown locations in fig. 6.3 were estimated using the above principle. Allowing for the accuracy of the technique used, the breakdown location appears to be less sensitive to changes in α as the burst approaches the apex.

There is a discontinuity in the C_{pmin} curves of fig. 6.2 at x=180mm. This results from the lack of tappings towards the apex, in particular the absence of one near the peak suction. Fig. 6.4 demonstrates this problem by showing the cubic spline fit from which the C_{pmin} level is determined, for α=12.5° at x=173mm and 203mm, i.e. either side of the change in the curves of fig. 6.2. The suction peak at x=173mm should be greater than at x=203mm. The lack of a tapping close to the peak C_p for x=173mm has prevented an accurate interpolation of the C_{pmin} value at this location.

Oil surface flow visualisation shows the track of the vortex over the surface of the wing. Fig. 6.5 gives two examples, for α=10° and 17.5°. At α=10°, there is no evidence of the vortex bursting over the wing. The rotation within the off-surface

Description of the Greenwell and Wood Half-Width Method

The method involves measuring the spanwise distance between the points either side of the peak vortex suction, where the Cp level is half that of the peak suction value. When the vortex burst crosses a spanwise location, there is a sudden change in the half-width measurement at that point, and hence the position of the burst point can be estimated. The technique requires that there is a strong vortex present so that the change in half-width is well defined and so that any effects of the attached flow on the pressure field are small compared to those of the vortex system.

primary vortex is clearly shown by the pattern of flow between the primary attachment line (which is not very distinct) and the secondary separation (appears as the region towards the leading edge where there is an absence of dye). Outboard of the secondary separation, there is a faint line indicating the presence of a weak secondary vortex, as was shown by the pressure distributions of fig. 6.1. [Note : these surface flow visualisation tests were conducted at the same Reynolds number as the pressure measurement tests]. The flow inboard of the vortex has a considerable spanwise component. This is a consequence of suspending the model vertically in the tunnel, thus allowing the oil to flow under gravity in this area of low surface velocity. In fact the flow in this region is aligned more with the root chord than it appears from the picture.

At α=17.5°, the vortex burst is seen as an increase in the width of the vortex footprint/width at the point marked on the figure. The rotation of the burst portion also appears to be less than for the unburst section - the surface flow lines are orientated more streamwise.

The surface oil flow visualisation in fig. 6.6 (α=30°) shows the fully burst vortex/bluff body flow covering the whole upper surface. There is still significant circulation within the flow.

Colour contour plots of surface pressure for various incidences are presented in fig. 6.7(a) and (b) to extend the above discussions to the whole surface. Selected contour lines are included for reference to emphasise key features. As α increases, so the vortex strength increases - both the peak width and maximum suction level increase under the vortex. C_{pmin} also increases towards the apex. The breakdown location can be seen as a widening of the suction peak (emphasised by the contour lines), e.g. at x=280mm for α= 15°. As determined previously (fig. 6.3), the relatively weak vortex bursts over the wing for α>10°. As incidence is increased, the breakdown location moves towards the apex. Ahead of the burst, the suction level continues to increase (increasing vortex strength), whilst downstream of the burst, the suction level is similar for all α, independent of the length of the burst section. The width of the peak also increases with α, thus, the normal force contribution from both the burst and unburst portions increases. Above α=27.5°, the burst point reaches the apex of the wing, resulting in a fully burst vortex. The suction level is still relatively high due to the circulation present within the burst vortex. Beyond this incidence, the leading edge

separated flow begins to change into bluff-body flow (as shown by α=32.5°).

The primary attachment line appears as a 'trough' (dark blue) in the contours, inboard of the suction peak. The weak secondary vortex is most clearly seen by the shape of the contour lines outboard of the primary. Inboard of the primary vortex, there is little change in the attached flow $C_{p\ level}$ with α.

6.1.2 Lower surface pressures.

Fig. 6.1 includes spanwise lower surface pressure levels. Looking at x=375.5mm, the C_p level increases towards the leading edge. At x=451mm (on the crop of the wing), C_p tends to reduce under the influence of the tip vortex. The full surface contours of fig. 6.8 exhibit a reduction in pressure level towards the trailing edge, with an increased C_p towards the leading edge. As α increases, the leading edge pressure increases. The sweep effect also reduces and the contours become aligned more perpendicular to the freestream. At the trailing edge, a region of lower C_p develops on the outboard elevon at the location where the vortex is present on the upper surface. As α increases, this region becomes greater following the trend of increasing vortex width. At α=30° (fully burst vortex), this area covers the trailing edge of both the outboard and inboard elevons.

6.1.3 Overall steady normal force and pitching moments for η=0°.

The normal force and pitching moment coefficients measured from the 6 component balance are given in fig. 6.9, as well as the coefficients obtained by integrating the surface pressure results. The integrated pressures predict a greater C_n value with a 12% difference in peak C_n value. Because only the upper surface had pressure tappings, the lower surface pressures were obtained by testing at negative incidence. The section is not symmetrical, thus these are not the true lower surface pressures and this will affect the comparison with the balance results. The contribution of the mounting arrangement also had to be removed from the balance results. It was not possible to measure the unsteady forces and moments using the 6 component balance due to the low natural frequency of the system. [Note : the balance was locked

during the oscillatory tests to maintain a high natural frequency for the complete mounting arrangement]. Hence, the following discussion refers to the integrated pressures as these will be compared with the unsteady results.

The aerodynamic centre was calculated to be at $0.51 \times c_r$ from the apex, at $\alpha=0°$. C_n increases almost linearly with α up to $\alpha=22.5°$ and is maximum at $\alpha \approx 27.5°$. Despite the presence of the burst above the wing, the circulation from the leading edge shear layer increases with α, forming a stronger vortex, whilst the width of the burst portion also increases, with little change in peak suction once burst (fig. 6.1). The change in upper surface contribution with α is shown in fig. 6.9(b). The stall point is associated with vortex breakdown reaching the apex at $\alpha \approx 27.5°$. The upper surface contribution reduces rapidly as bluff-body flow develops. The lower surface contribution is seen to vary almost linearly with α to beyond the stall point for the wing.

At the stall point, there is a reduction in the pitching moment about the aerodynamic centre. This is again associated with the complete vortex breakdown over the upper surface which results in a large reduction in peak C_p at the apex and hence in pitching moment (fig. 6.7(b), $\alpha=32.5°$).

The upper surface contribution to C_n consists of both attached flow and vortex effects. By assuming the effects of thickness and camber are small, it is possible to use superposition to remove the potential flow component from the upper surface results, as described by Er-El and Yitzhak [1988]. Performing this analysis, the curves of fig. 6.10 are produced, where C_{np} is the combined potential contribution from both surfaces, and C_{nv} the vortex effect. The vortex contribution to C_n is very similar to that of the potential flow, suggesting the unsteady response of the attached flow is likely to be at least as important as the characteristic response of the vortex to control oscillations. Thus, in determining the overall unsteady elevon effects on aircraft manoeuvring and structural coupling, the response of both the attached flow and of the vortex must be considered.

6.2 Steady Elevon Displacement Results.

It is necessary to consider the steady elevon deflection effects in some detail to form the basis for later analysis and comparison with the unsteady results. To that end, the pressure results for various η are presented and discussed before giving the change in overall normal force and pitching moment coefficient with η, to produce the elevon effectiveness at various α and mean η ($\bar{\eta}$). By considering the change in C_p for a change in η, $\Delta C_p/\Delta\eta$, it will be possible to compare the amplitude of the unsteady response to elevon oscillations, C_{p_o}, with the steady results.

The spanwise pressure distributions of fig. 6.11, for α=10°, show the change in peak suction on the upper surface to be reasonably linear with elevon angle for η=20° to -20°, at both x=375.5mm and x=504mm. There is a large change in the peak suction at x=375.5mm but the width of the peak is unchanged. The peak, associated with the vortex core location, moves outboard very slightly as η increases. At x=504mm, the change in C_p level at the attachment point is as large as the suction peak change, suggesting a change in the attached flow condition. This is not the case at the more forward station, suggesting a change in the elevon effect on the flow with distance from the apex. Off-surface, smoke visualisation, using a laser light sheet orientated to produce a cut across the core of the vortex, indicated a change with η of the height of the vortex above the wing surface, with an associated change in the strength of the vortex. A negative change in η moved the vortex away from the surface and weakened it. Further smoke visualisation at the tip of the wing showed the strength and orientation of the shear layer from the crop of the wing to alter significantly with η. The changes in the flow are further clarified in the surface flow visualisation in fig. 6.12. The width of the vortex in each case is similar towards the apex. Thus, the vortex strength must increase with η to produce the pressure variations of fig. 6.11, at x=375.5mm. Near the elevon, the vortex width appears to reduce with η. The attached flow is accelerated by positive elevon, causing the primary attachment to appear to move outboard and the secondary separation to move inboard with η, reducing the vortex footprint. This was not obvious from fig. 6.11. The vortex strength is still increased (as it is further forward) and the core moves slightly closer to the surface. All these interactions combine to produce a greater peak suction and $-C_p$ values across the whole vortex, especially over the elevon (fig. 6.11, x=504mm) where the change in attached flow appears to be large. The sketches in fig. 6.13 attempt to further clarify these arguments by comparing the vortex and pressure levels at two elevon

angles. These complex interactions make it impossible to determine the actual change in the vortex from the measured surface pressures.

In fig. 6.12, at η=18.4°, there is a vortex structure on the upper surface at the inboard tip of the outboard elevon, resulting from the vertical gap between the ends of the inboard and outboard elevons (fig. 6.14). At η=-18.4°, this vortex forms on the lower surface of the outboard elevon. Its effect is seen on the upper surface tip of the inboard elevon as a region of accelerated flow with a significant spanwise flow component.

The lower surface pressure variations at x=375.5mm again appear linear with η, but are smaller than for the upper surface, except inboard of the attachment point where the effect on the attached flow is similar for both surfaces. On the elevon, at x=504mm, the lower surface effect is greater than the change of the vortex pressures.

The complete upper surface pressure contours for α=10° are presented in fig. 6.16, for η=20°, 0° and -20°. The characteristic changes described above are seen to be consistent over the whole surface. To emphasise the changes in C_p, fig. 6.17 gives the $\Delta C_p/\Delta\eta$ (ΔC_{p_η}) contours for mean elevon angles of $\bar{\eta}$= 15°, 0°, -15° (e.g. $\bar{\eta}$=15° calculated by subtracting η=10° from η=20° results. The largest $-\Delta C_p/\Delta\eta$ appear along the length of the peak suction as already mentioned. It is apparent that the response is, in fact, not linear. Near the hinge line, the elevon is less effective as $\bar{\eta}$ decreases. This is further emphasised in fig. 6.18(a) where the ΔC_{p_η} results have been integrated with respect to y to give longitudinal loadings. For the upper surface, the effect of $\bar{\eta}$ is immediately obvious. By moving the core away from the surface and reducing its strength, the elevon effectiveness on the upper surface is greatly reduced at $\bar{\eta}$=-15°. This reduction is significant right to the apex of the wing. Returning to fig. 6.17, the effect of the vortex emanating from the gap between the inboard and outboard elevons (as sketched in fig. 6.14) can be seen as a region of dark blue at the tip of the inboard elevon at $\bar{\eta}$=-15°, and as a region of yellow/green at the root of the outboard elevon at $\bar{\eta}$=15°.

The lower surface contours of fig. 6.19 again show that the effects described from fig. 6.11 are repeated over the complete surface. The change due to elevon deflection, $\Delta C_p/\Delta\eta$

(ΔC_{p_η}) is again emphasised in fig. 6.20. The C_p change is very localised to the outboard elevon and to near the hinge line on the main surface. The elevon is most effective at negative mean deflections where the flow is accelerated near the hinge line due to the curvature in the geometry. For positive deflections, the flow is decelerated towards stagnation and the elevon is less effective. Again, the tip vortex from the inboard end of the elevon is seen at $\overline{\eta}$=15°. The longitudinal loadings of fig. 6.18(a) demonstrate the rapid reduction in elevon effectiveness with increasing mean angle. The localisation around the hinge line is also evident. The change in loading with elevon deflection reduces greatly towards the apex of the wing.

At α=12.5°, x=375.5mm, a negative elevon deflection is seen to cause the vortex burst to cross this station (fig. 6.21). The change in peak C_p level between η=0° and -10° is much greater than between η=0° and 10°. The width of the peak also increases at η=-10°. A negative change in η increases the adverse pressure gradient towards the trailing edge. It is also likely to alter the formation of the shear layer from the leading edge, as seen at α=10°, where the vortex strength was changed. The overall effect is to move the burst point forward. The sensitivity of the vortex to the external pressure gradient was discussed in Section 2. The $\Delta C_p/\Delta\eta$ contours in fig. 6.22 show the burst motion as a region of highly negative values at x=340mm under the suction peak, caused by the sudden change in C_p through a burst. The widening of the vortex footprint is implied by the region of positive ΔC_p along the reattachment line, downstream of the burst. There is still a change to the suction peak level of the unburst portion of the vortex, despite the presence of the burst.

The lower surface change at x=504mm (fig. 6.21) is similar to that at α=10°, and is greater than the change in the vortex C_p's suggesting the elevon is affecting the potential flow contribution on the upper surface of the elevon, as well as the vortex itself. At this x location, the vortex is burst for all η shown.

Increasing the angle-of-attack further to α=15° produces a burst vortex at x=375.5mm for all η shown in fig. 6.23. The elevon effect on the burst vortex is still significant. At x=504mm, the effect on the burst vortex is lower than for lower α, whilst the lower surface ΔC_p's are as large. This demonstrates the importance of the attached flow to the effectiveness of the elevon at higher α's. The $\Delta C_p/\Delta\eta$ contours of fig. 6.24 (upper surface) again show the

main upper surface change to be to the vortex suction level, though at much lower levels than those of fig. 6.20 (α=10°). The lower surface $\Delta C_p/\Delta\eta$ contours in fig. 6.25 again show the effect to be localised around the hinge line and outboard elevon. The longitudinal loadings of fig. 6.18(b) emphasise that the elevon effectiveness at α=15° reduces as $\overline{\eta}$ reduces, for the same reasons as at α=10°, described earlier. The apparently large increase in loading at x=488mm between $\overline{\eta}$=-15° and 0° is partly the result of the steepness of the peak. Small changes in the response to elevon deflections are emphasised in this region.

The spanwise pressure contours in fig. 6.26, for α=20°, show a reduction in the level of response of the burst vortex to that at α=15°. The longitudinal loadings show little difference between the 3 mean elevon angles in terms of upper surface effectiveness (fig. 6.18(c)). The changes in lower surface distribution are, however, similar to those at lower α. The upper surface flow visualisation results of fig. 6.27 do not show as clearly the change in the burst vortex observed at α=10° for an unburst vortex (fig. 6.12), except on the elevon itself. Here, the changes in flow pattern are similar. The lower surface flow visualisations of fig. 6.28 (α=20°) are very similar to those at α=10°, suggesting the lower surface effectiveness does not change greatly with α. These trends are repeated at α=27.5° (fig. 6.29) where the burst point has reached the apex.

The change in elevon effectiveness with α is summarised (for $\overline{\eta}$=0°) by the longitudinal loadings of fig. 6.30. The lower surface effect is constant for α=10° to 35°, suggesting it is relatively independent of both the actual C_p level, which varies significantly in this range (fig. 6.8), and of the changing flow characteristics present on the upper surface, or that these changes cancel each other.

The effectiveness of the elevon on the upper surface reduces greatly when the burst appears on the wing. The movement of the burst for α=12.5° and 15° is shown by points 1 and 2 respectively. Here the loading characteristic has changed compared to α=10°. In front of the burst, however, the loading is independent of α, i.e. of vortex strength and of burst location. Once the burst reaches the apex at $\alpha\approx$27.5°, the loading reduces rapidly.

6.2.1 Overall normal force and pitching moment coefficient variations.

By integrating the surface contour C_p's (equations given in Section 5.1), the C_n and $C_{m_{a.c.}}$ values for the upper and lower surfaces are obtained (fig. 6.31). The overall force and moment changes with η, C_{n_η} and $C_{m\ a.c._\eta}$ are shown in fig. 6.32 for $\bar{\eta}$=15°, 0° and -15°. These values are the same as the gradients of the curves in fig. 6.31 at each $\bar{\eta}$. The upper and lower surface effects are plotted separately. The upper surface C_{n_η} reduces with α. A positive $\bar{\eta}$ results in a greater value than for a negative one. On the lower surface, however, this trend is reversed. Unlike the upper surface, the lower surface C_{n_η} is reasonably constant with α, for all mean elevon angles, except at low α for $\bar{\eta}$=-15°. This can be explained by returning to the longitudinal loadings of fig. 6.18. At α=10°, the change in loading in front of the hinge is greater for $\bar{\eta}$=0° than for $\bar{\eta}$=-15°. This counteracts the greater effectiveness on the elevon for $\bar{\eta}$=-15°, giving similar C_{n_η} in fig. 6.32. As α increases, the loadings in front of the hinge line become very similar. Thus, the C_{n_η} value for $\bar{\eta}$ = -15° is greater than for 0°. By α=20°, the C_p levels towards the trailing edge are low (as discussed in section 6.1.2) and thus the difference in elevon effectiveness between $\bar{\eta}$=0° and $\bar{\eta}$=-15° reduces as both are accelerating the flow on the elevon and near the hinge line from a mean pressure level that is more similar than at lower incidences. Hence, C_{n_η} values for these two mean angles are similar in fig. 6.32 for $\alpha \geq 20°$. It is worth emphasising that the lower surface contribution remains to high α, whilst the upper surface reduces rapidly.

The above trends are mirrored in the $C_{m\ a.c._\eta}$ results for both upper and lower surfaces. This mirroring effect is simply because a positive $\Delta\eta$ produces a positive ΔC_n but a negative ΔC_m. When this is taken into account (i.e. the pitching moment derivatives are multiplied by -1) then it can be seen that the results do indeed follow the same trends. Combining the surface contributions produces the overall elevon effectiveness results of

fig. 6.33. The diagram also gives the results obtained using the 6-component balance, about $\bar{\eta}$ =0°. Again, there are large differences between the balance results and the integrated pressures (as discussed in Section 6.1.3). The overall control effectiveness for each of the mean angles shown is similar at each α, except at the extremes of α=10° and 35°, for $\bar{\eta}$ =-15°. The explanation for these results is a combination of the factors already discussed.

6.2.2 Hinge moment variations with η.

Integrating the pressures over the elevon to produce the hinge moment coefficients produces the results of fig. 6.34. The non-linearity of the upper surface response with η is emphasised by the change in gradient along the curves, the gradient being more negative as η increases. Despite the presence of regions of stagnated flow on the elevon at higher η, the lower surface hinge moment results are linear with η, though the gradient becomes more negative as α increases.

The change in hinge moment with η (gradients of previous curves) are given in fig. 6.35, again for $\bar{\eta}$=15°, 0°, -15°. These results confirm the above remarks concerning changes with $\bar{\eta}$ and α. The upper surface effects becomes less negative with increasing incidence and decreasing mean incidence. The lower surface change in hinge moments becomes more negative with α and are similar for all $\bar{\eta}$. Combining the surfaces gives total hinge moment changes similar for all α and $\bar{\eta}$. At α=35°, where bluff body flow exists above the upper surface, the values for the three mean elevon angles are virtually the same. All this is despite the gross changes in flow characteristics with α, and the separated flow regions on and near the elevon at large negative η. If the amplitude of response of the aerodynamics to elevon motion are found to have similar trends to the results of fig. 6.35, then the hinge moment term within the FCS would be practically constant with little or no scheduling required with α or η.

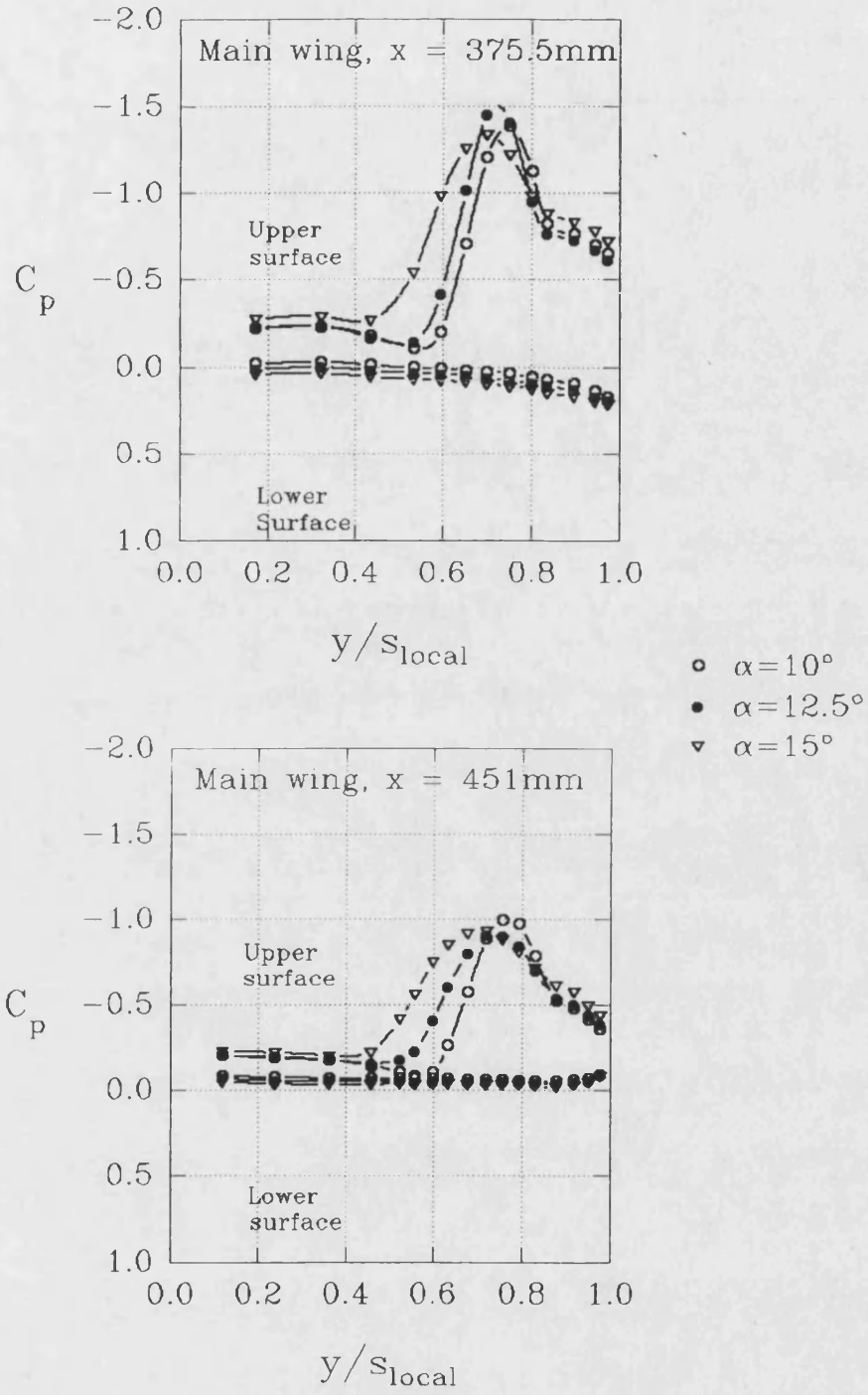

Fig. 6.1 - Spanwise pressure distributions

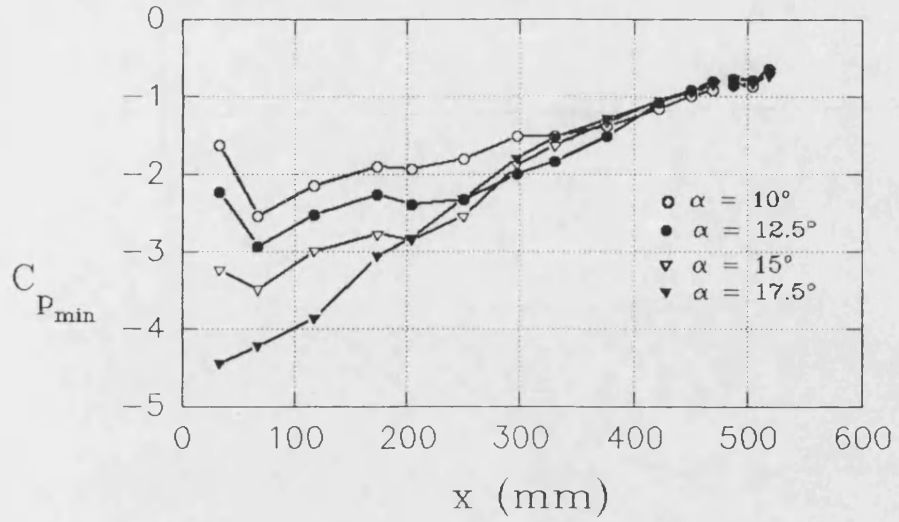

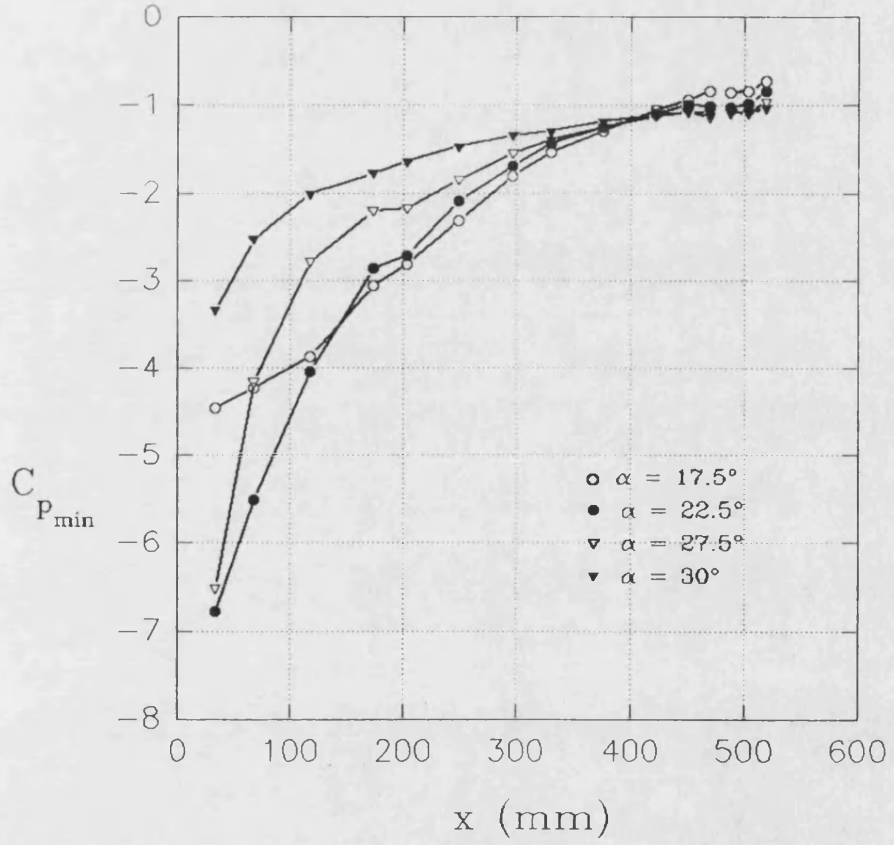

Fig. 6.2 - Peak suction under the primary vortex

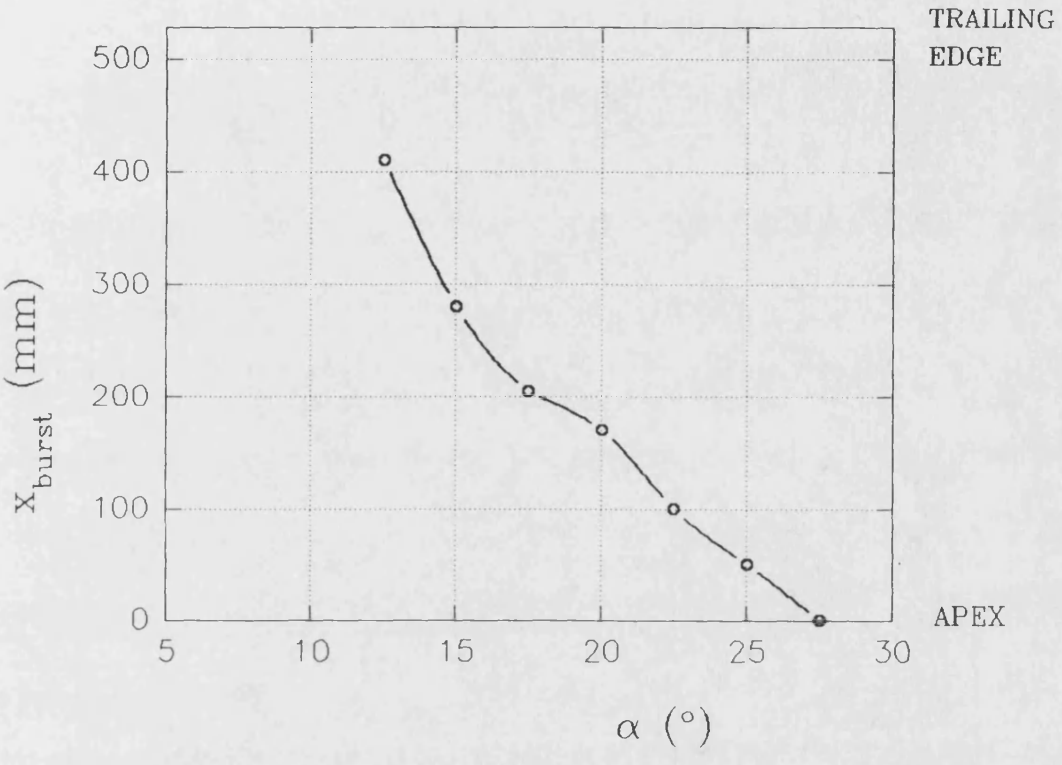

Fig. 6.3 - Estimated vortex breakdown locations

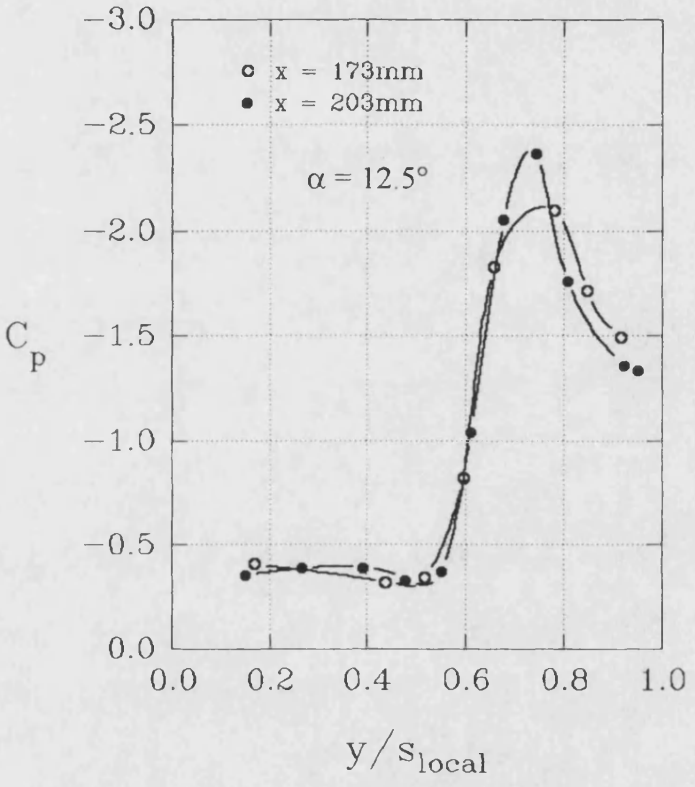

Fig. 6.4 - Source of error in calculating the peak suction under the primary vortex

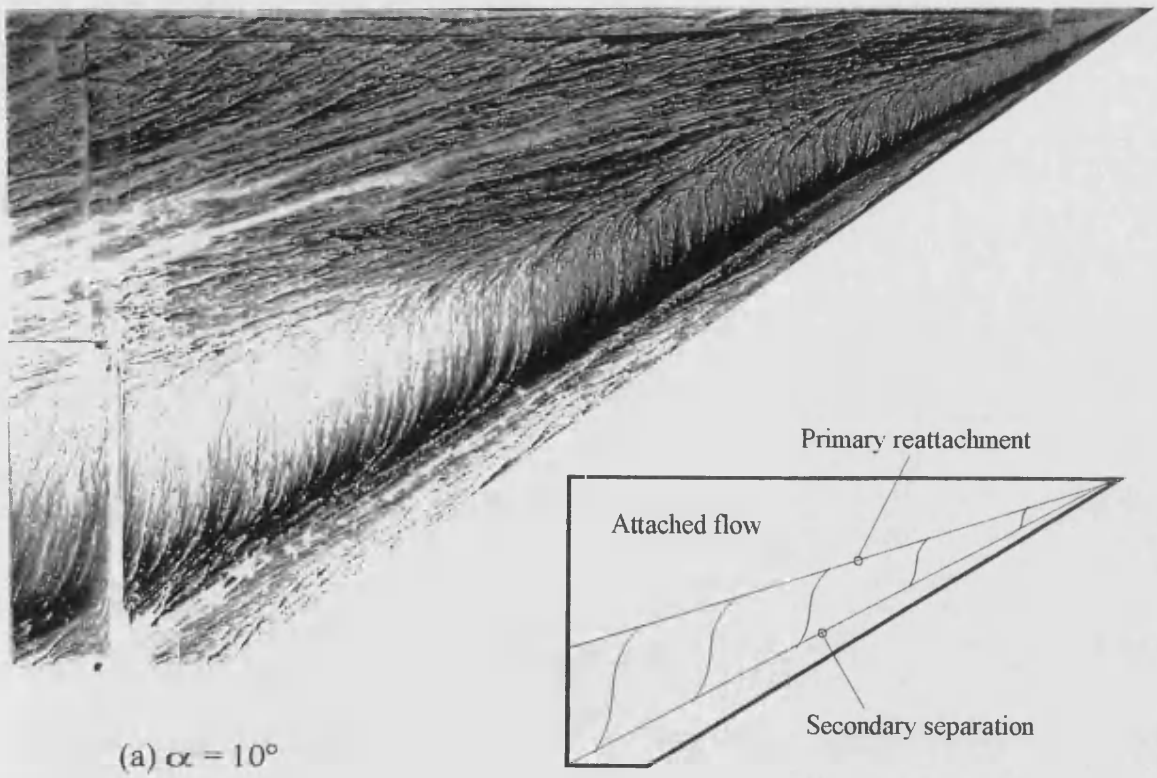

(a) $\alpha = 10°$

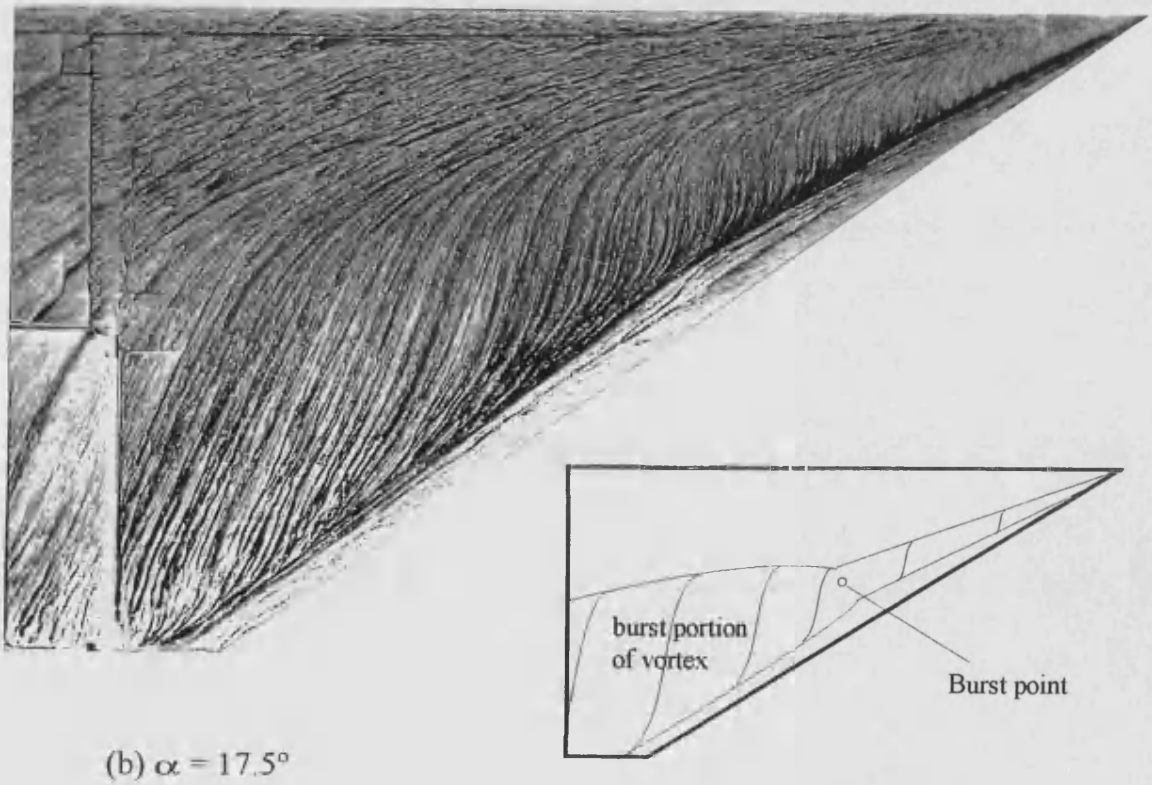

(b) $\alpha = 17.5°$

Fig. 6.5 - Upper surface flow visualisation

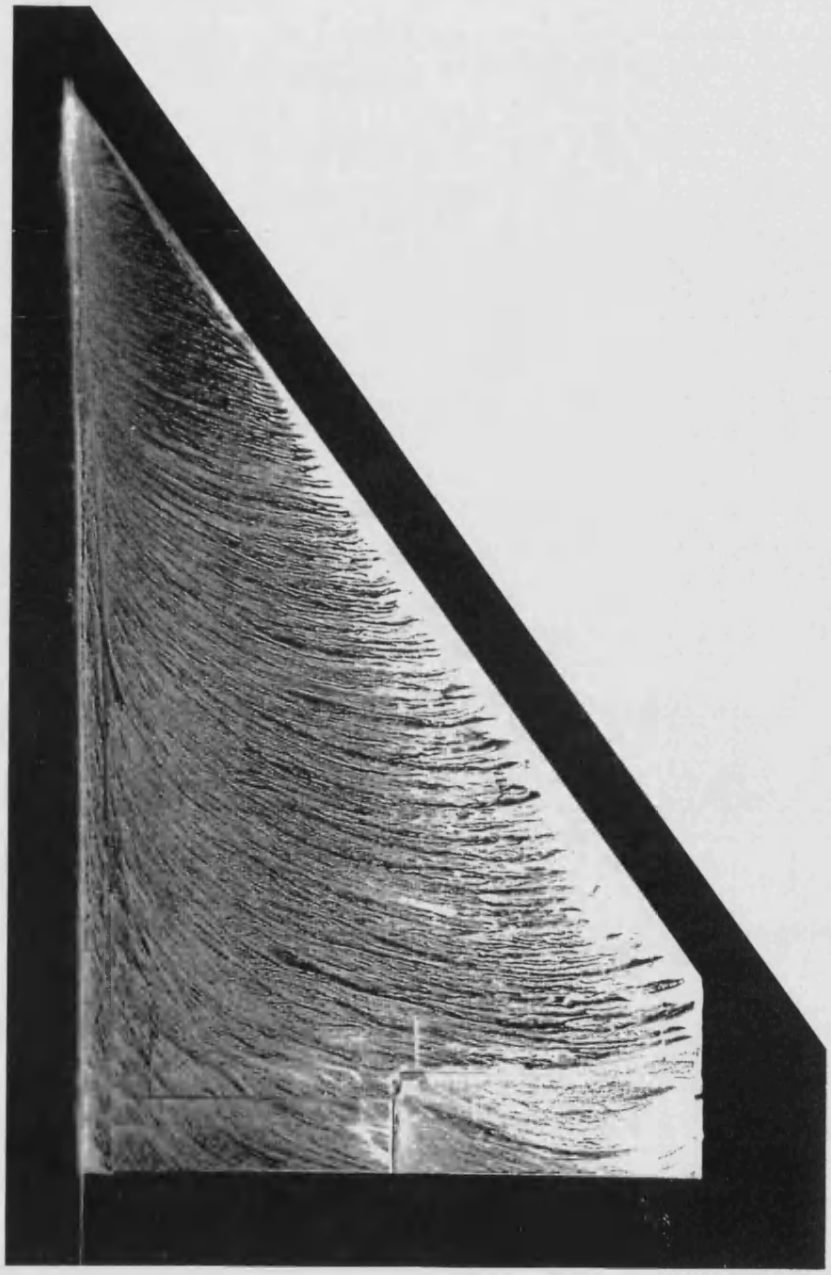

Fig. 6.6 - Bluff-body type flow over upper surface at $\alpha = 30°$

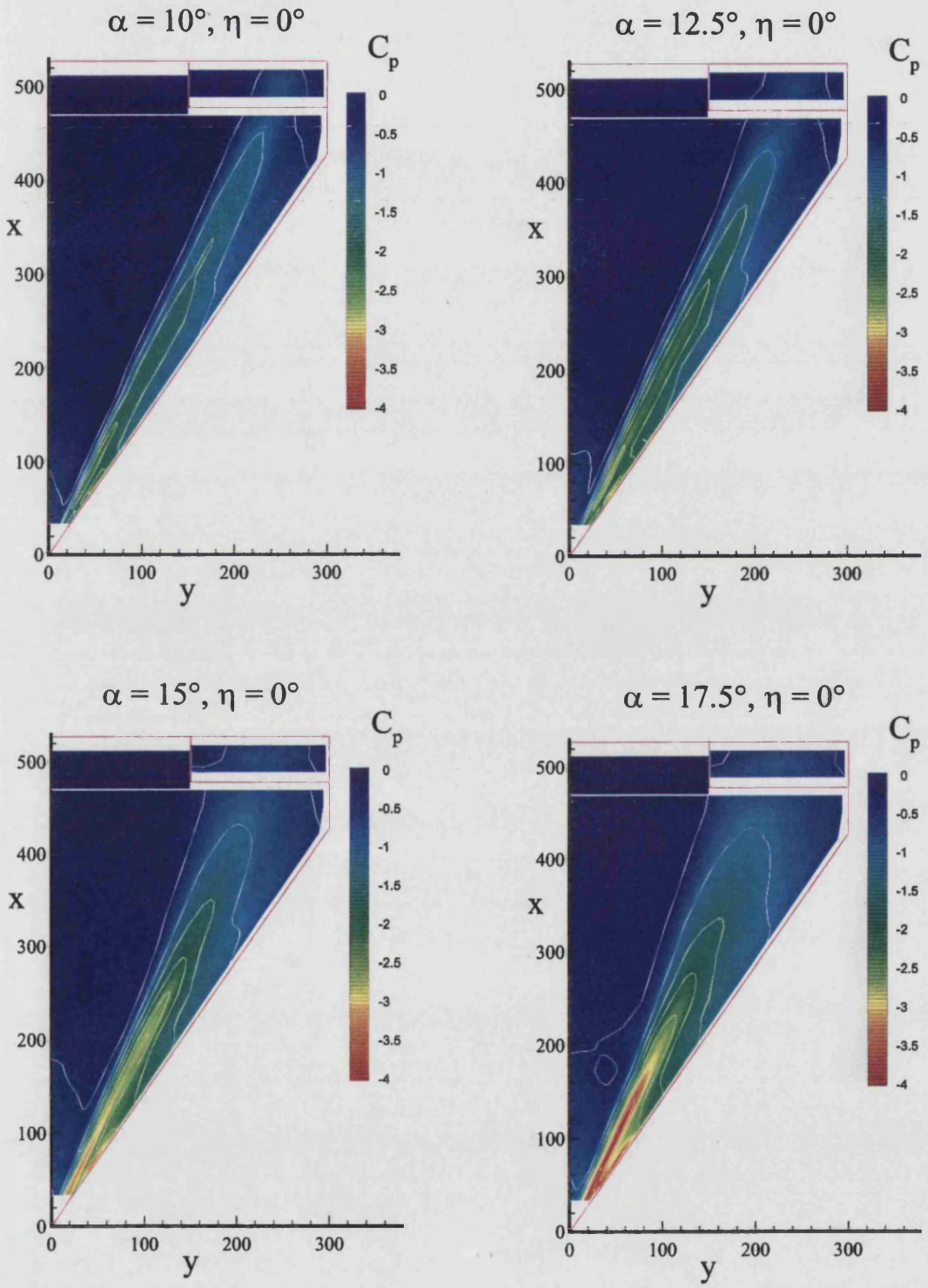

Fig. 6.7(a) - Upper surface pressure contours for various α

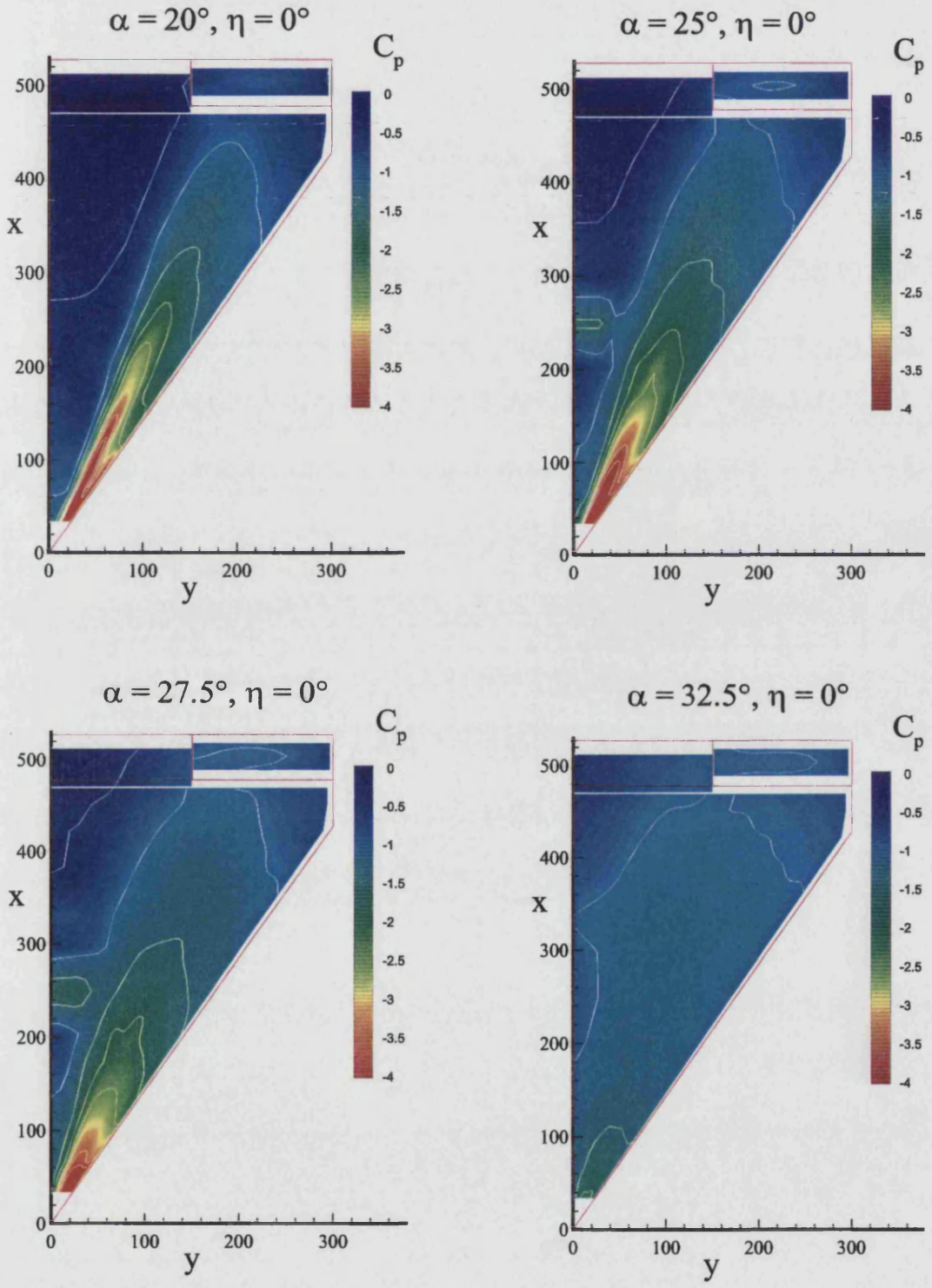

Fig. 6.7(b) - Upper surface pressure contours for various α

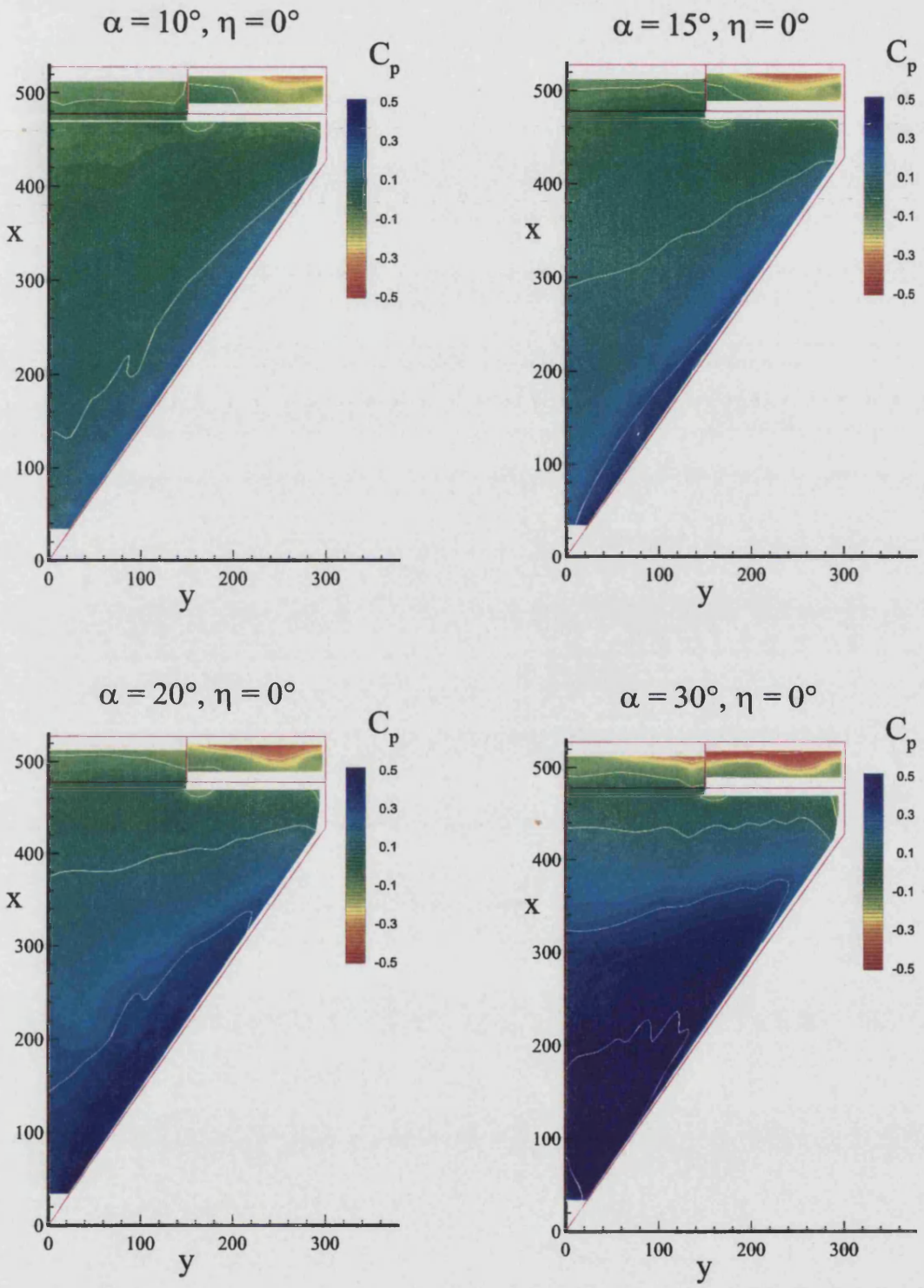

Fig. 6.8 - Lower surface pressure contours for various α

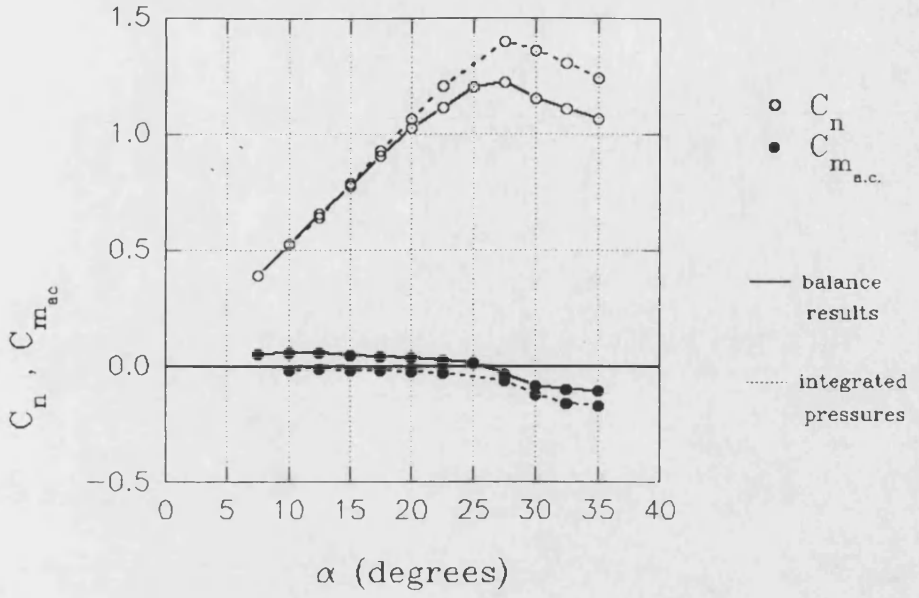

(a) total overall coefficients.

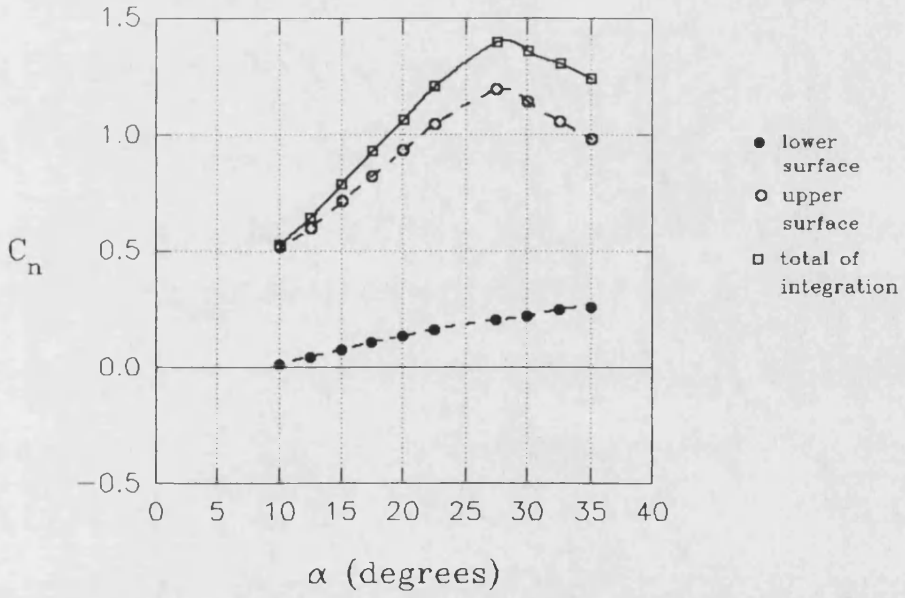

(b) components of normal force coefficient

Fig. 6.9 - Normal force and pitching moment curves

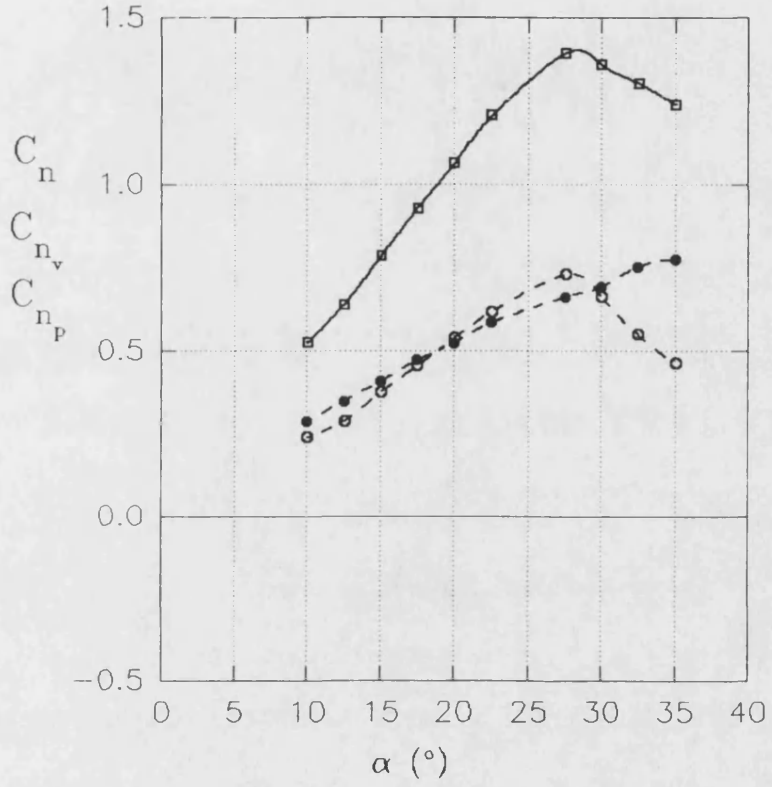

Fig 6.10 - Potential flow and vortex contributions to normal force

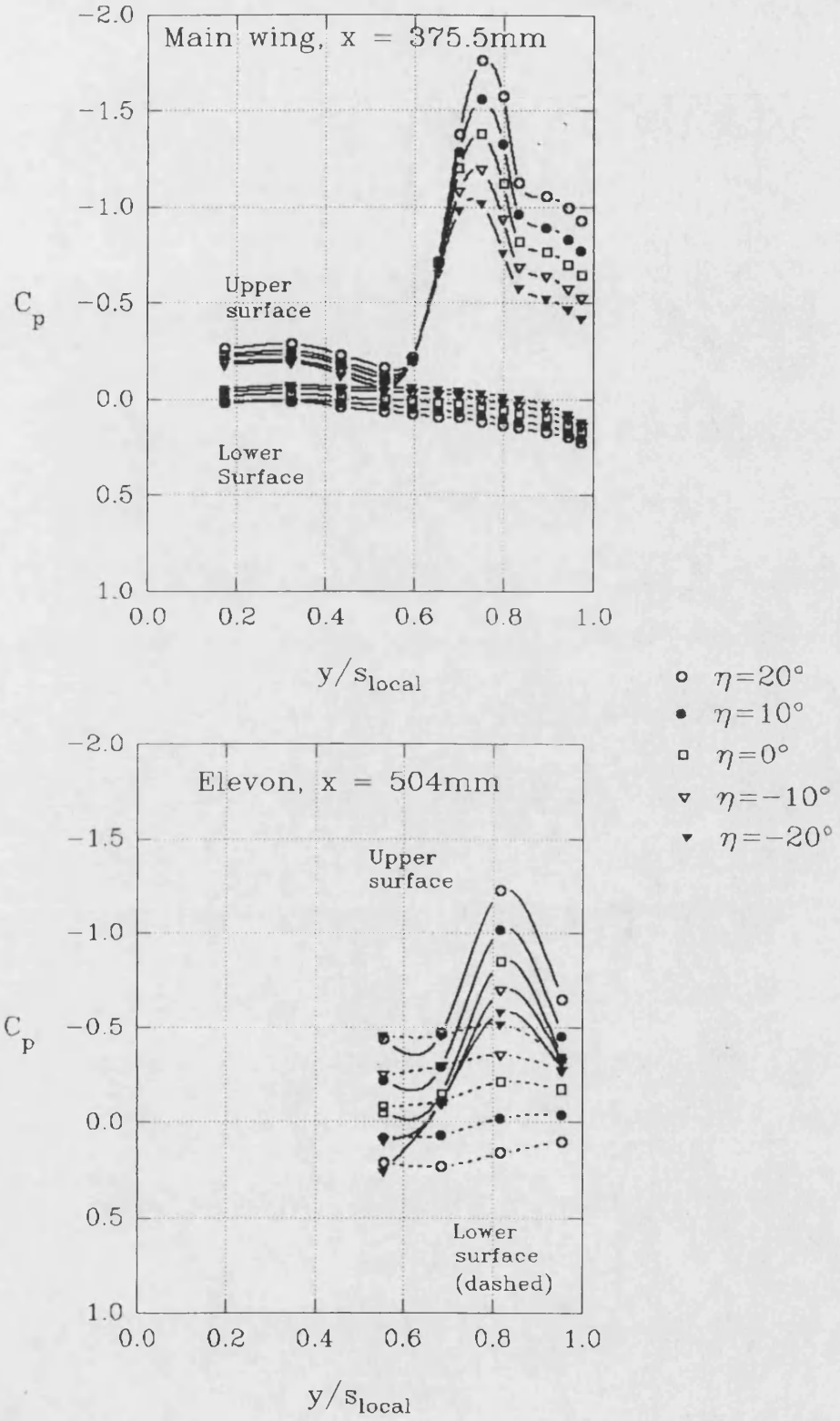

Fig. 6.11 - Spanwise pressure distributions for α= 10°

(a) $\eta = 0°$

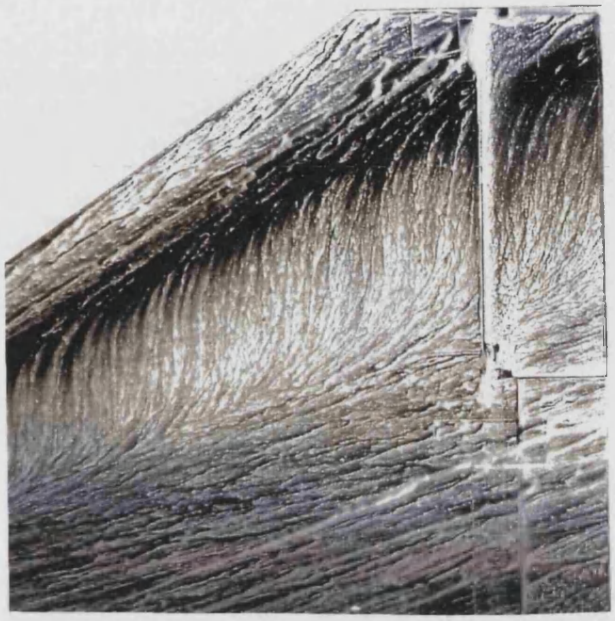

(b) $\eta = -18.4°$

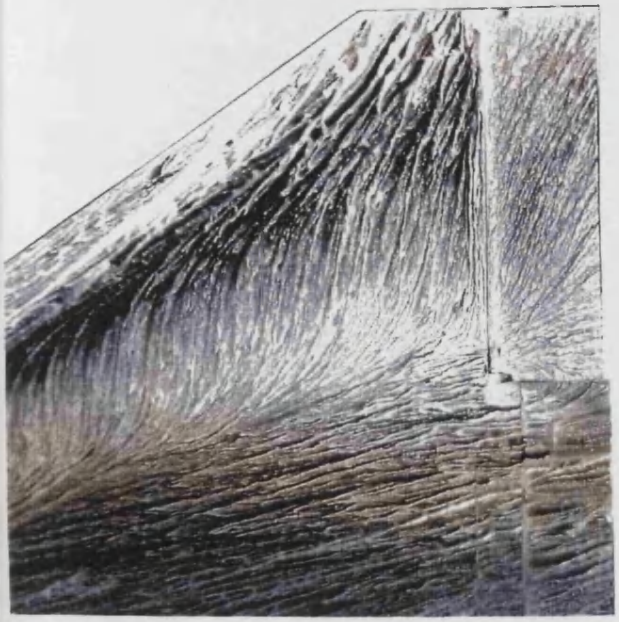

(c) $\eta = 18.4°$

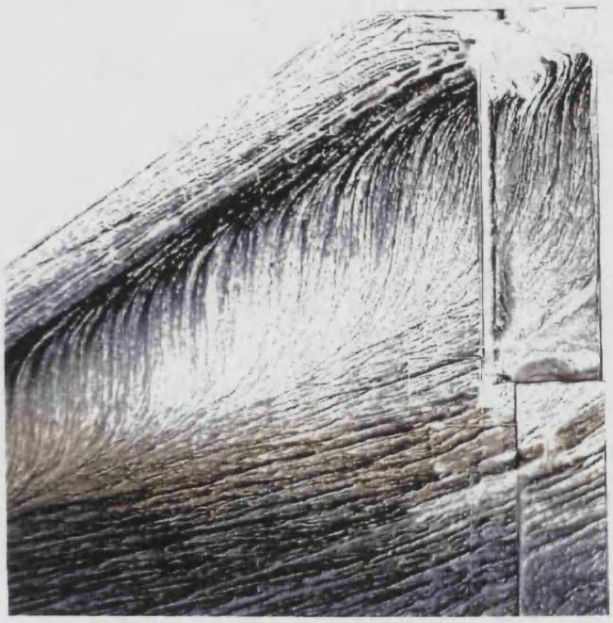

Fig. 6.12 - Upper surface flow around the elevon at $\alpha = 10°$

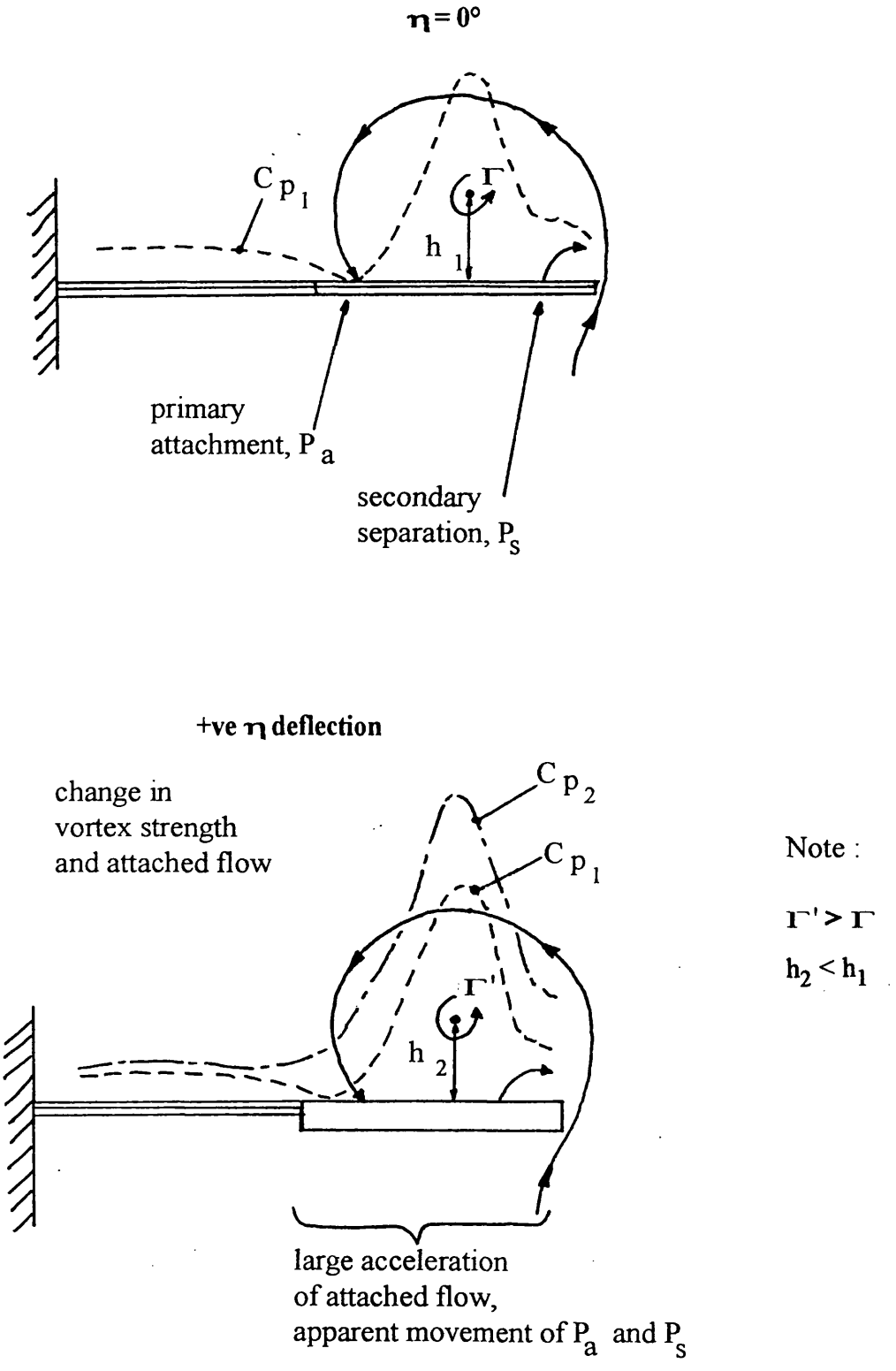

Fig. 6.13 - Change of vortex structure with elevon angle

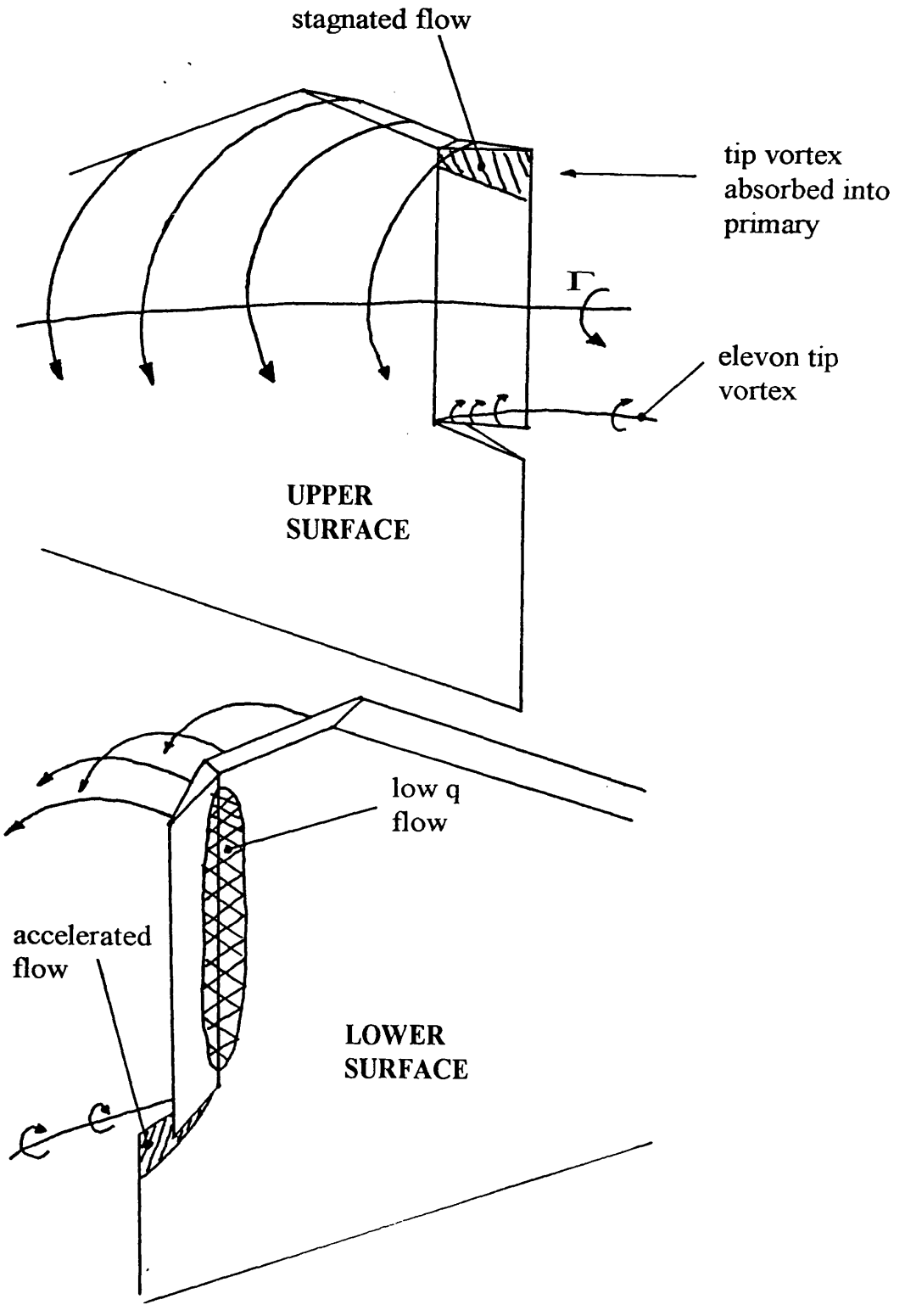

Fig. 6.14 - Details of flow around hinge line and elevon

(a) $\eta = 0°$

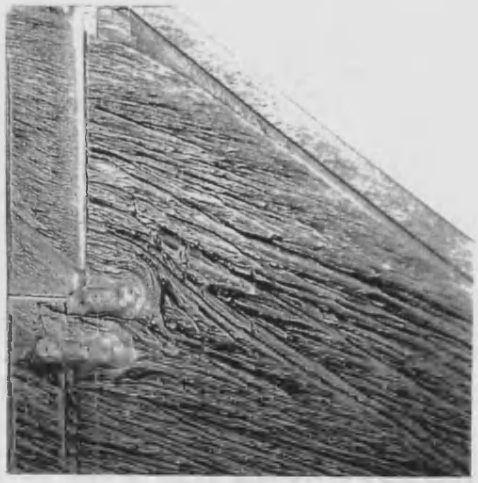

(b) $\eta = -18.4°$

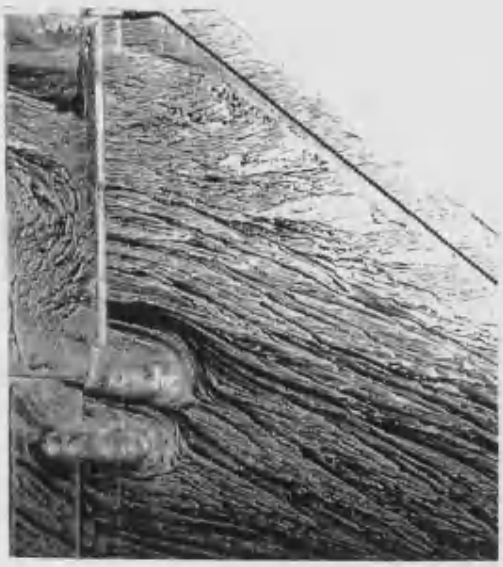

(c) $\eta = 18.4°$

Fig. 6.15 - Lower surface flow around the elevon at $\alpha = 10°$

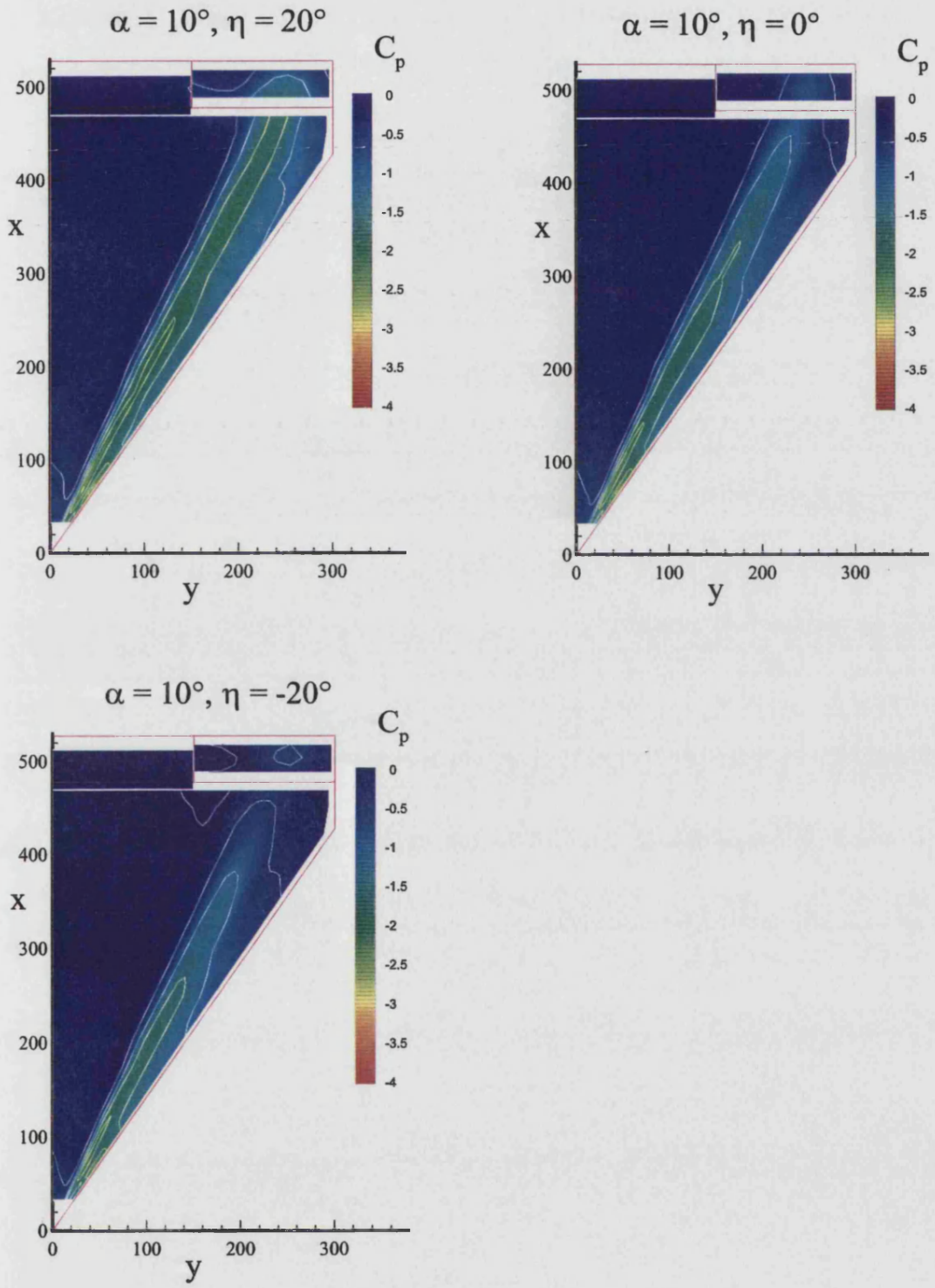

Fig. 6.16 - Upper surface pressure contours at α= 10°

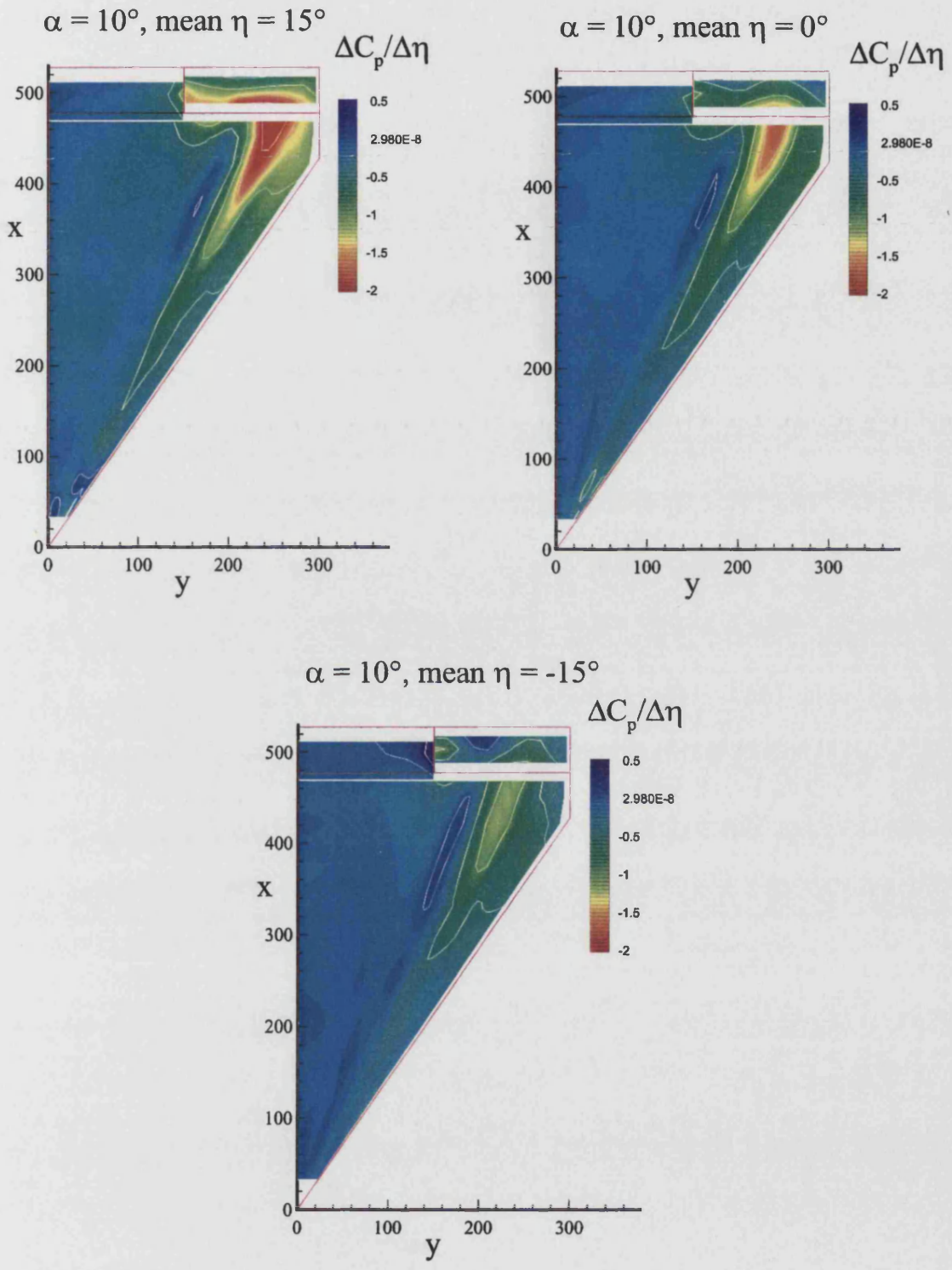

Fig. 6.17 - Incremental upper surface pressures due to elevon deflections, at α= 10°

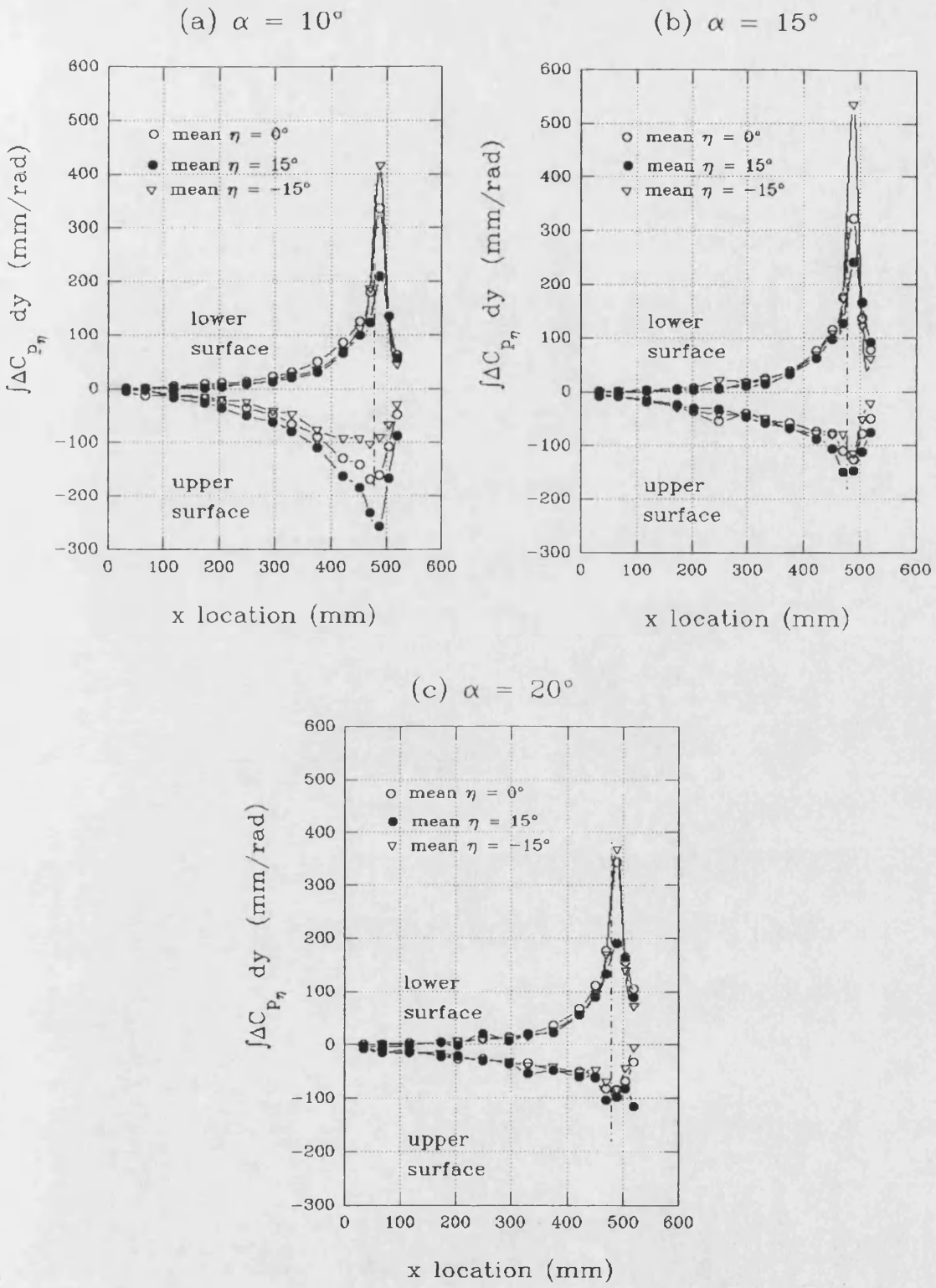

Fig. 6.18 - Incremental longitudinal loadings due to elevon deflection, for various α

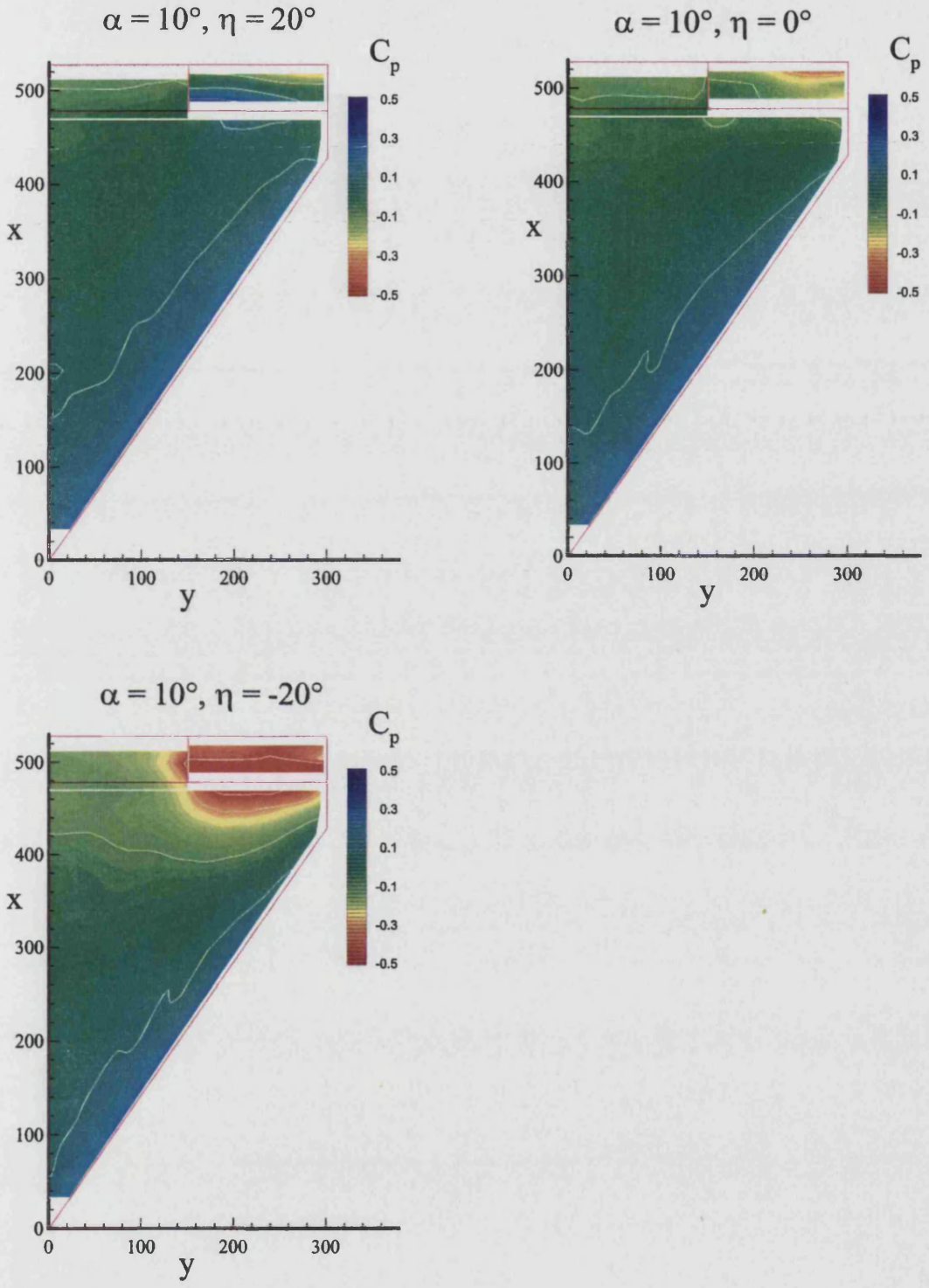

Fig. 6.19 - Lower surface pressure contours at α= 10°

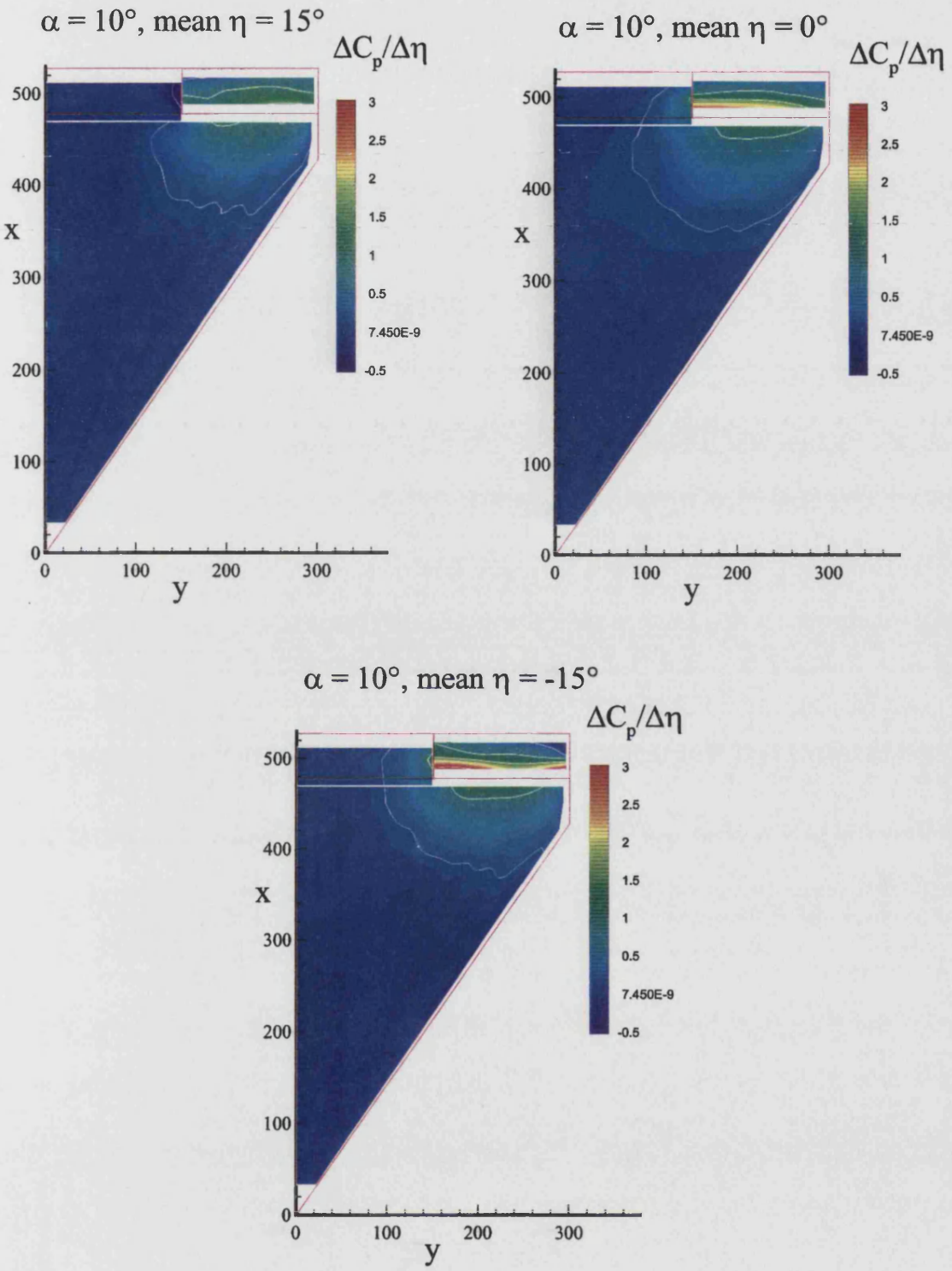

Fig. 6.20 - Incremental lower surface pressures due to elevon deflection at $\alpha = 10°$

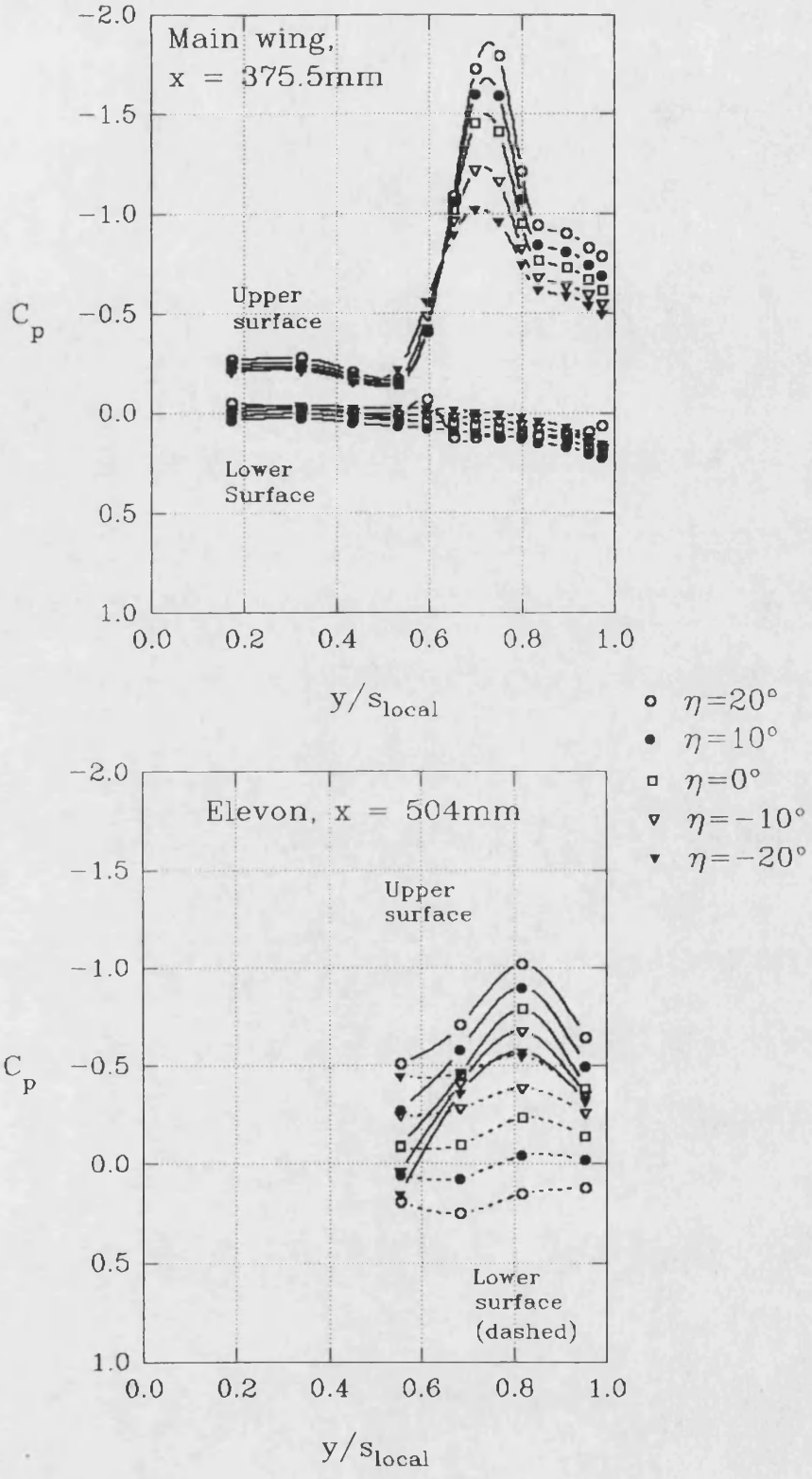

Fig. 6.21 - Spanwise pressure distributions at α= 12.5°

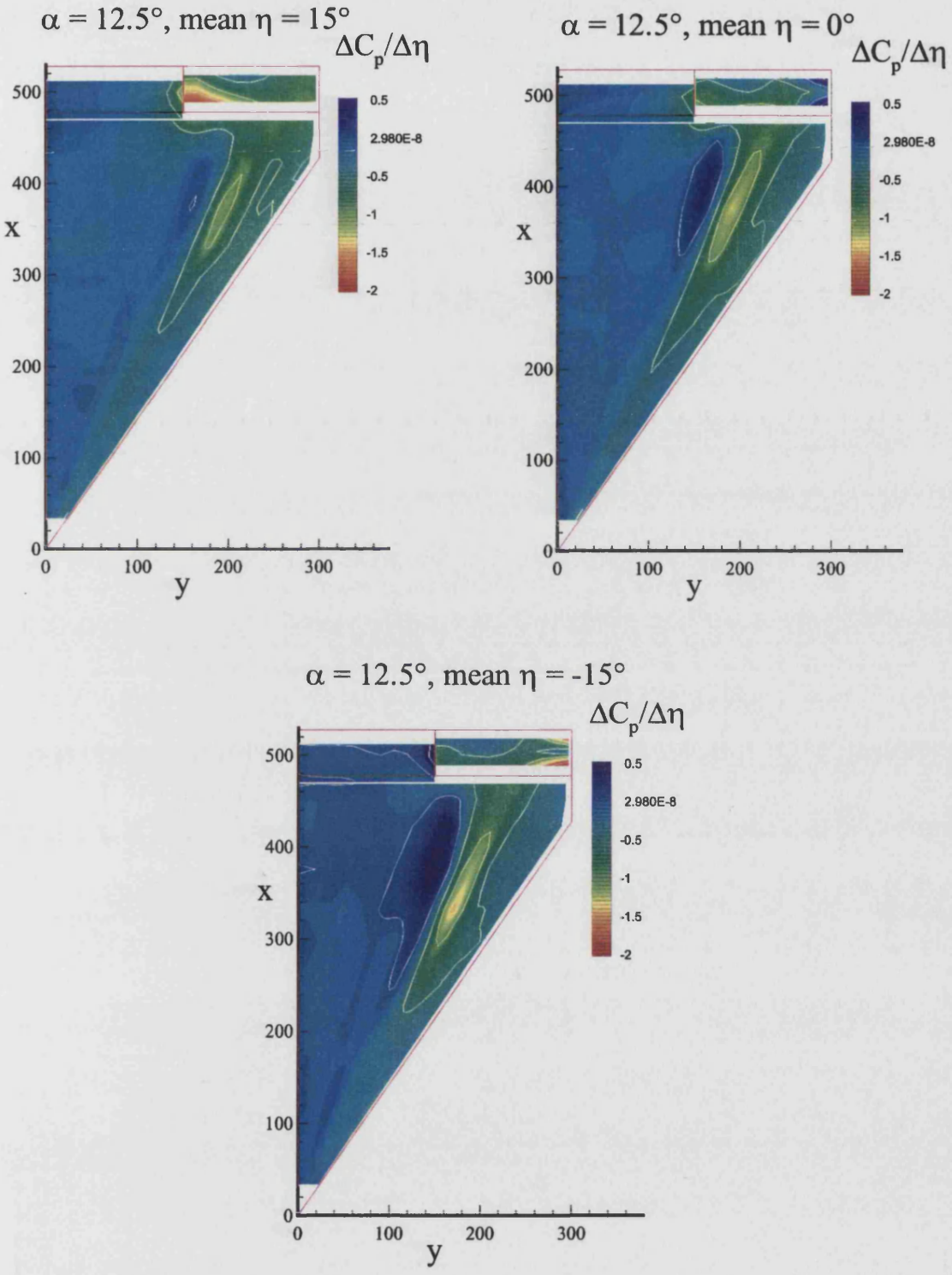

Fig. 6.22 - Incremental upper surface pressure contours due to elevon deflections at α= 12.5°

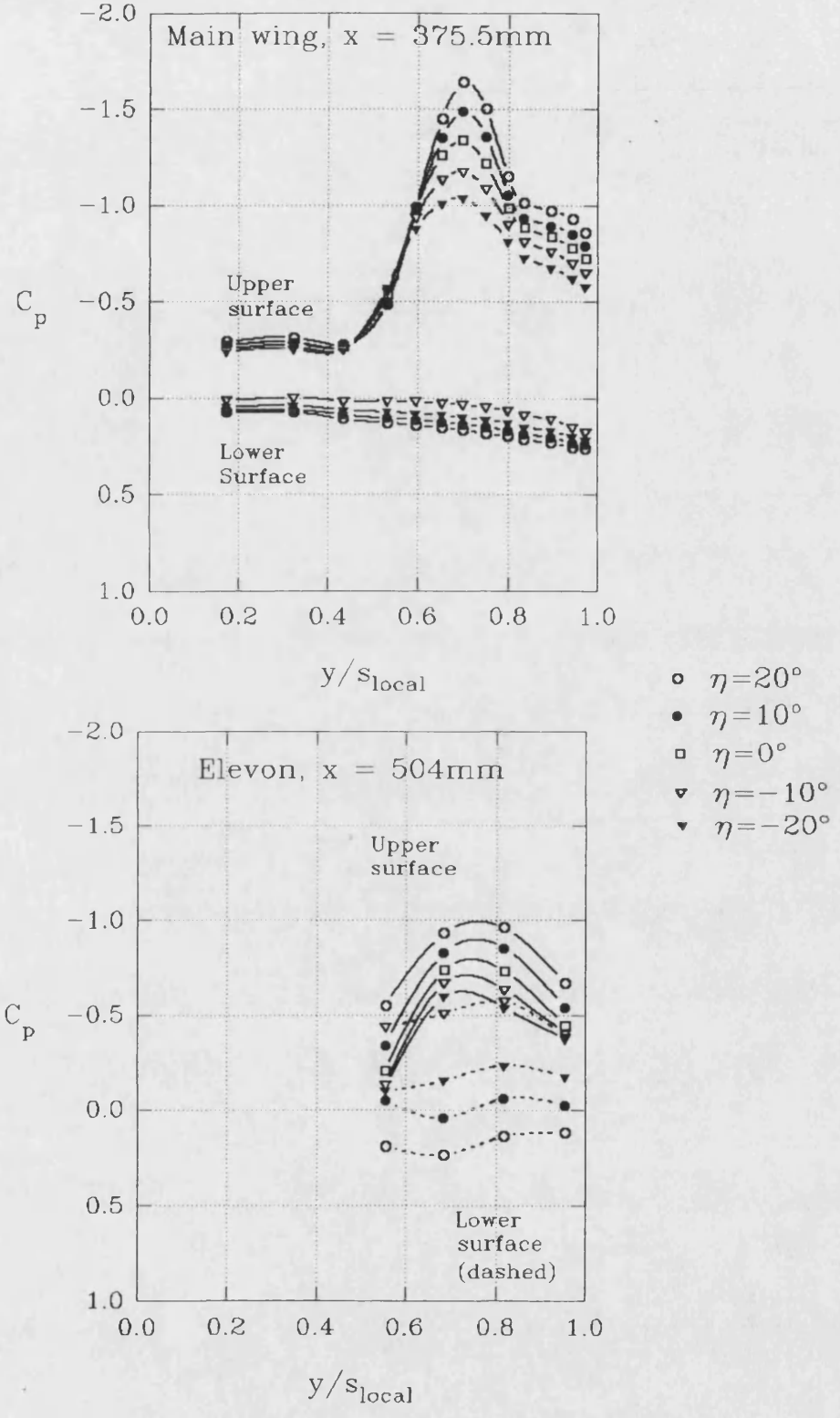

Fig. 6.23 - Spanwise pressure distributions for α= 15°

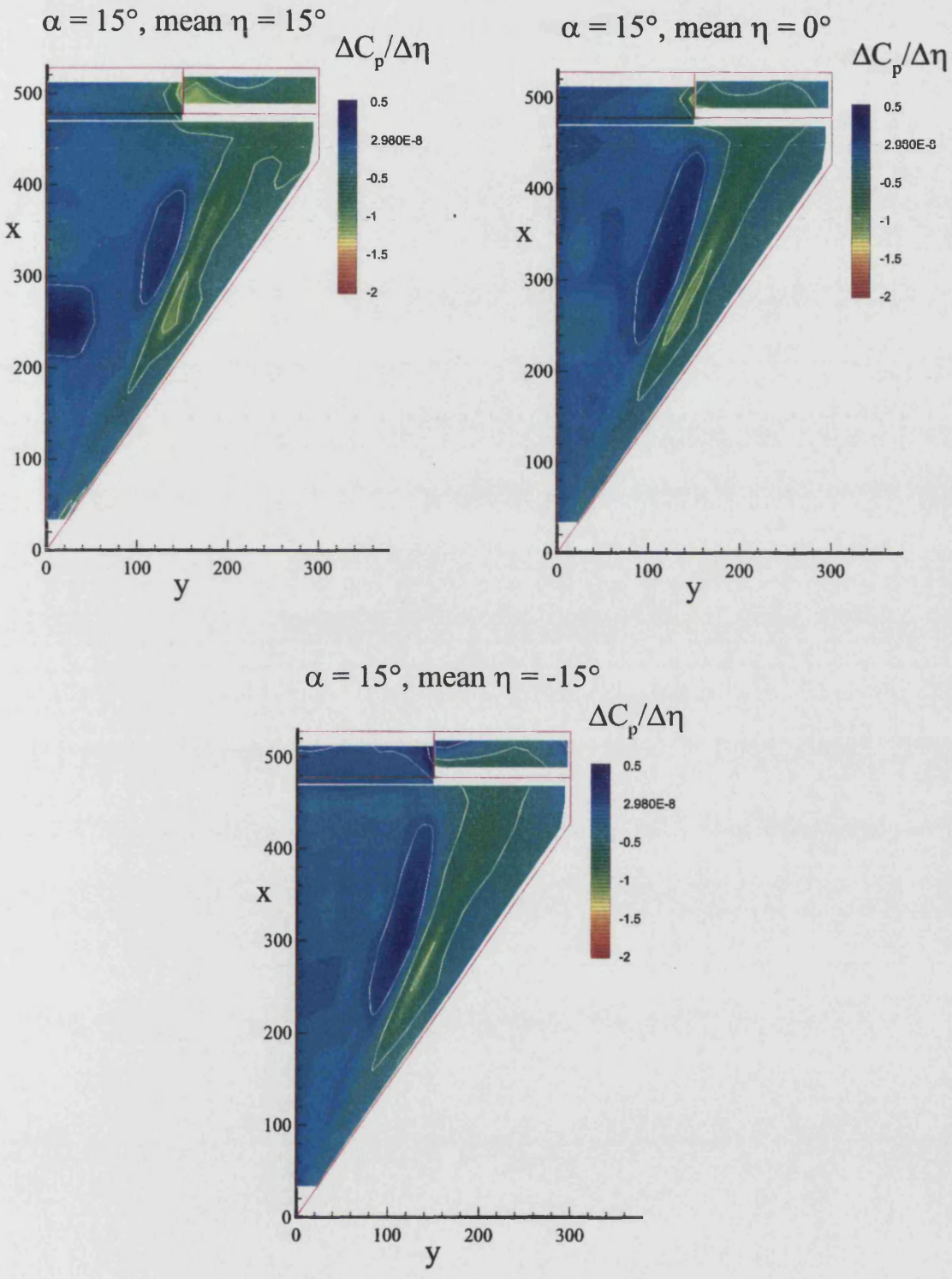

Fig. 6.24 - Incremental upper surface pressure contours due to elevon deflections at α= 15°

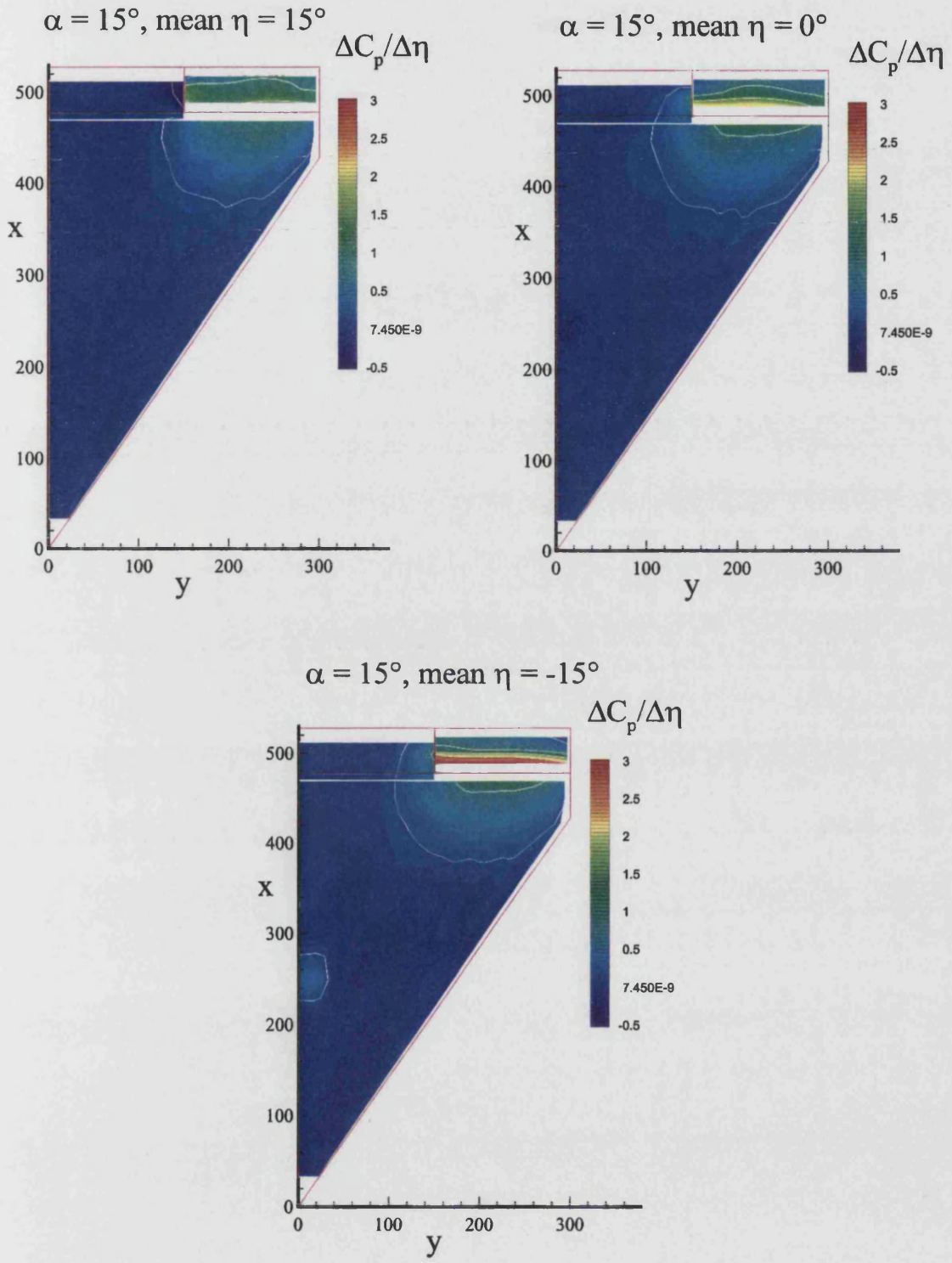

Fig. 6.25 - Incremental lower surface pressure contours due to elevon deflections at α= 15°

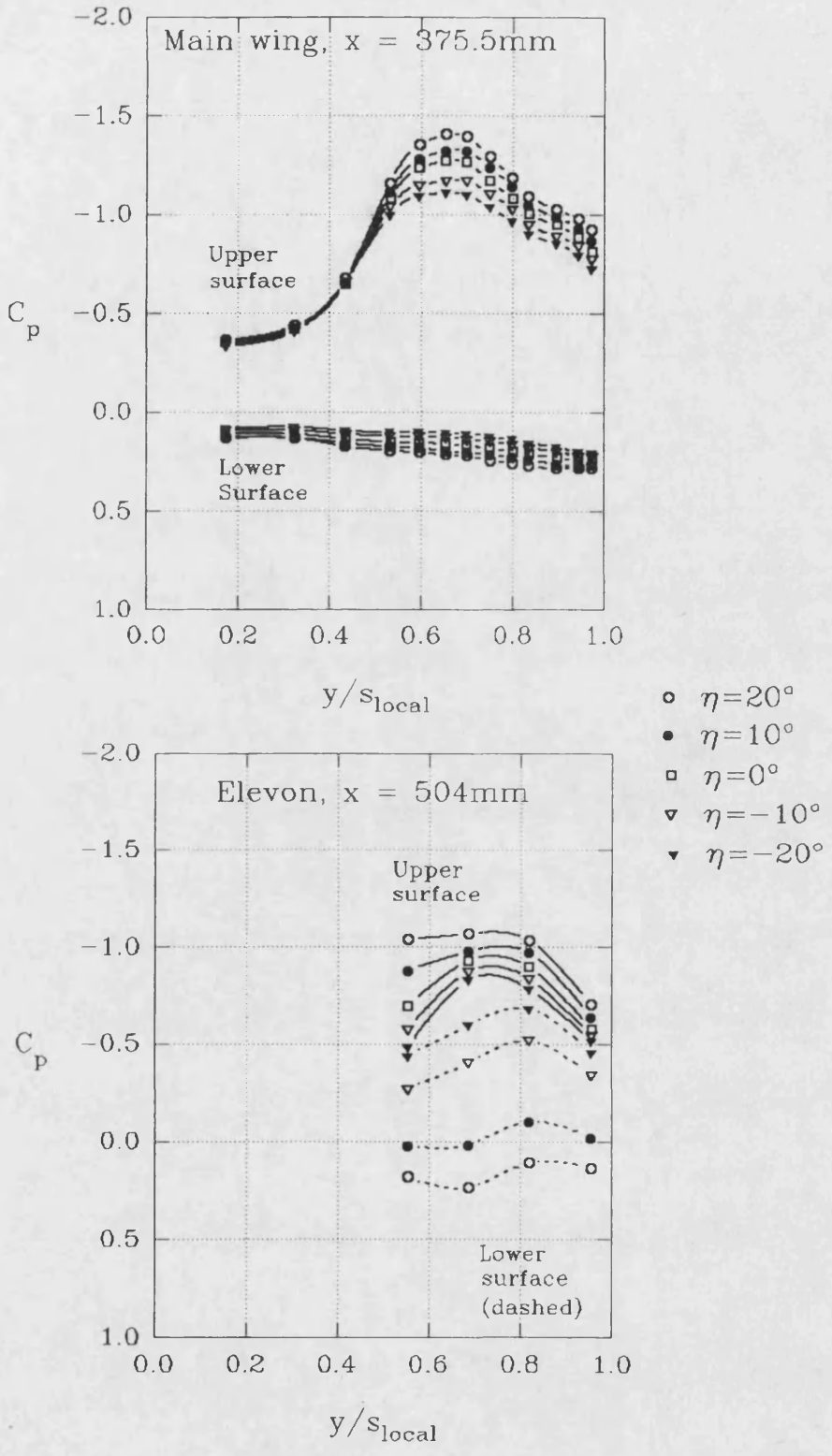

Fig. 6.26 - Spanwise pressure distributions for α= 20°

(a) $\eta = 0°$

(b) $\eta = -18.4°$

(c) $\eta = 18.4°$

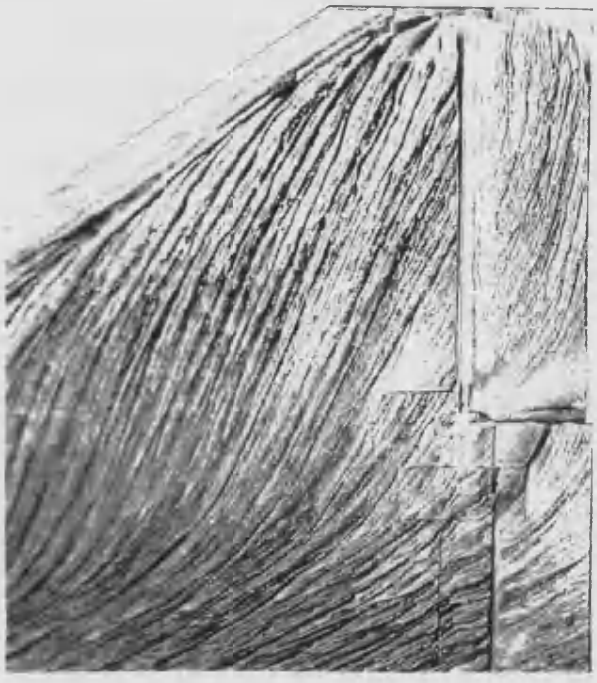

Fig. 6.27 - Upper surface flow around the elevon at $\alpha = 20°$

(a) $\eta = 0°$

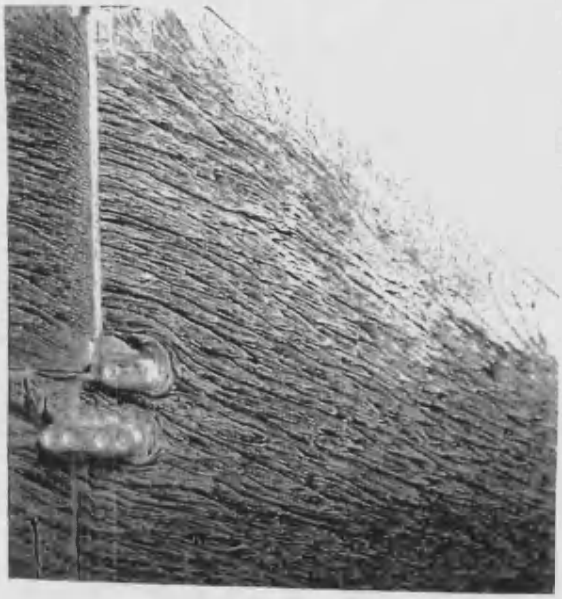

(b) $\eta = -18.4°$

(c) $\eta = 18.4°$

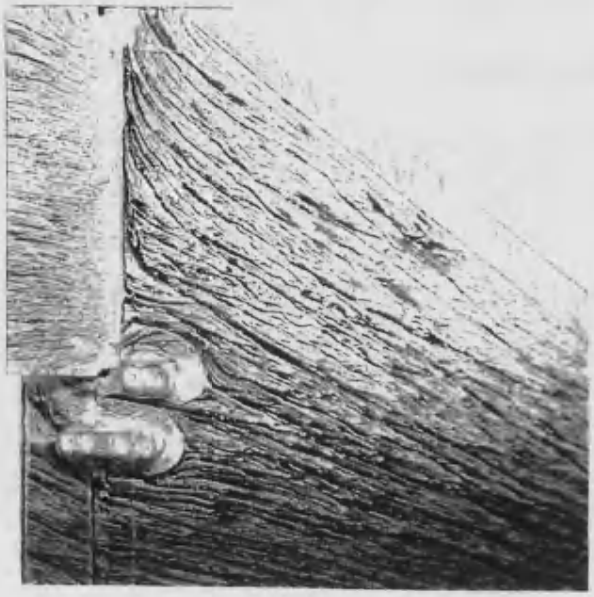

Fig. 6.28 - Lower surface flow around the elevon at $\alpha = 20°$

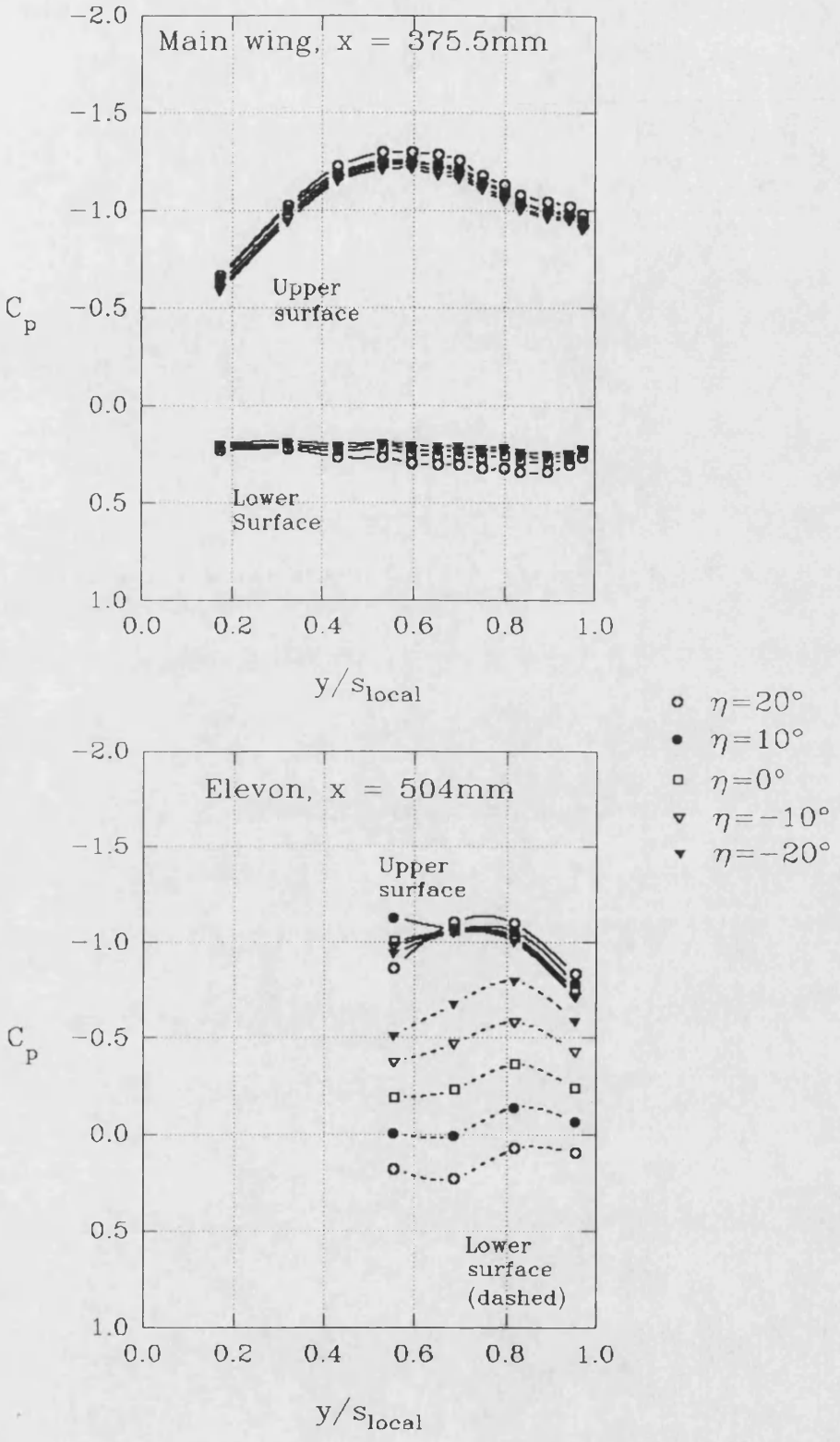

Fig. 6.29 - Spanwise pressure distributions for α= 27.5°

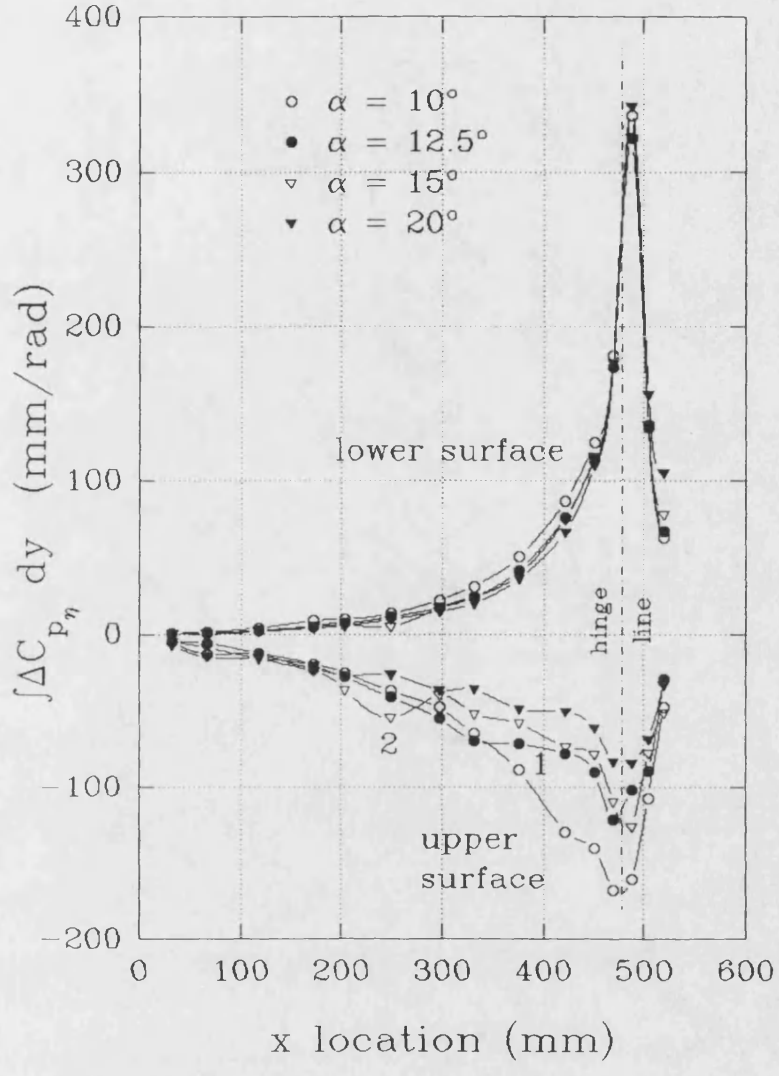

Notes : 1,2 result of movement of vortex burst location with elevon deflection

$$\Delta C_{p_\eta} = \frac{C_p(\eta=10°) - C_p(\eta=-10°)}{\Delta\eta}$$

Fig. 6.30(a) - Incremental longitudinal loadings for various α at zero mean elevon angle

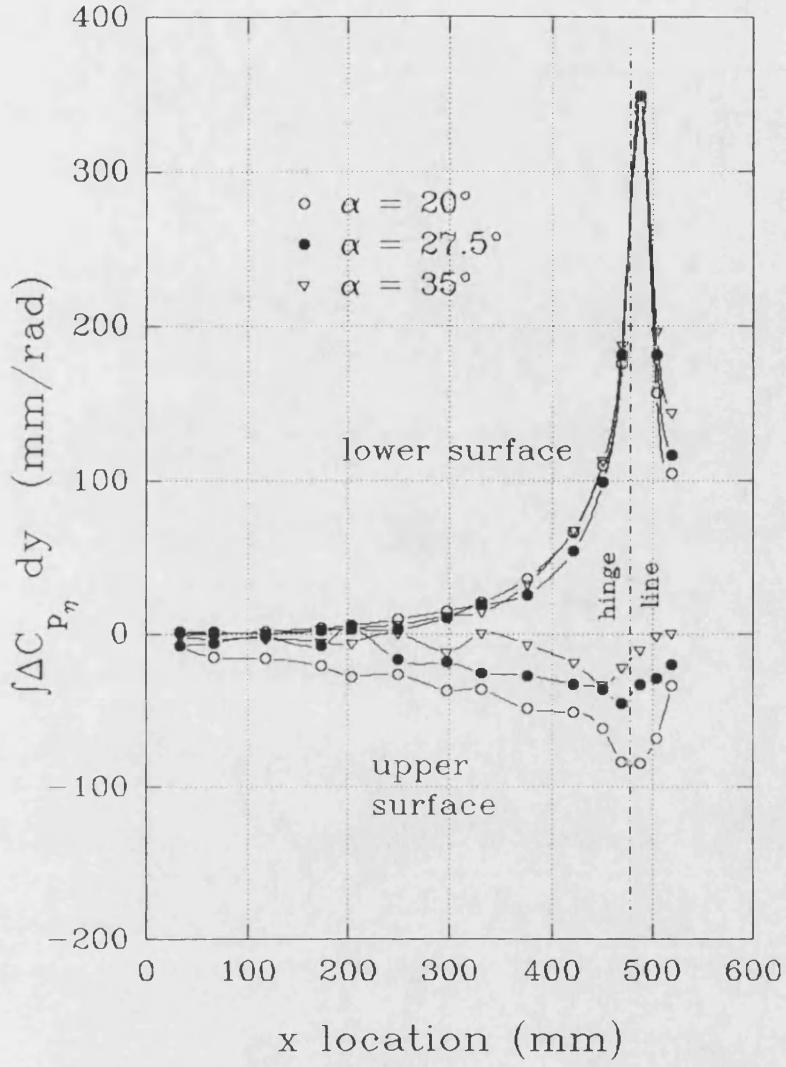

$$\Delta C_{p_\eta} = \frac{C_p(\eta=10°) - C_p(\eta=-10°)}{\Delta\eta}$$

Fig. 6.30(b) - Incremental longitudinal loadings for various α at zero mean elevon angle

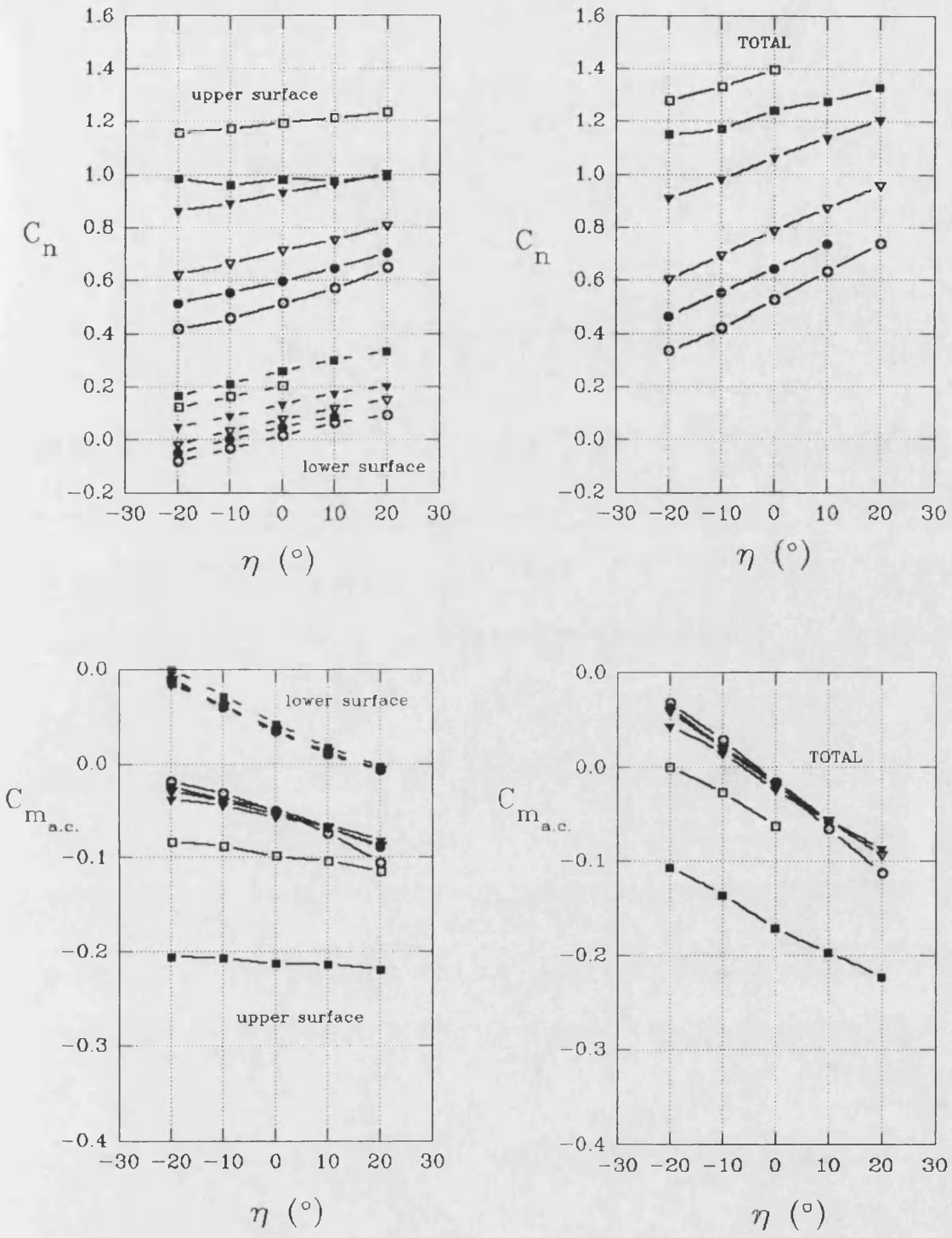

Fig. 6.31 - Normal force and pitching moment variations with elevon angle and incidence

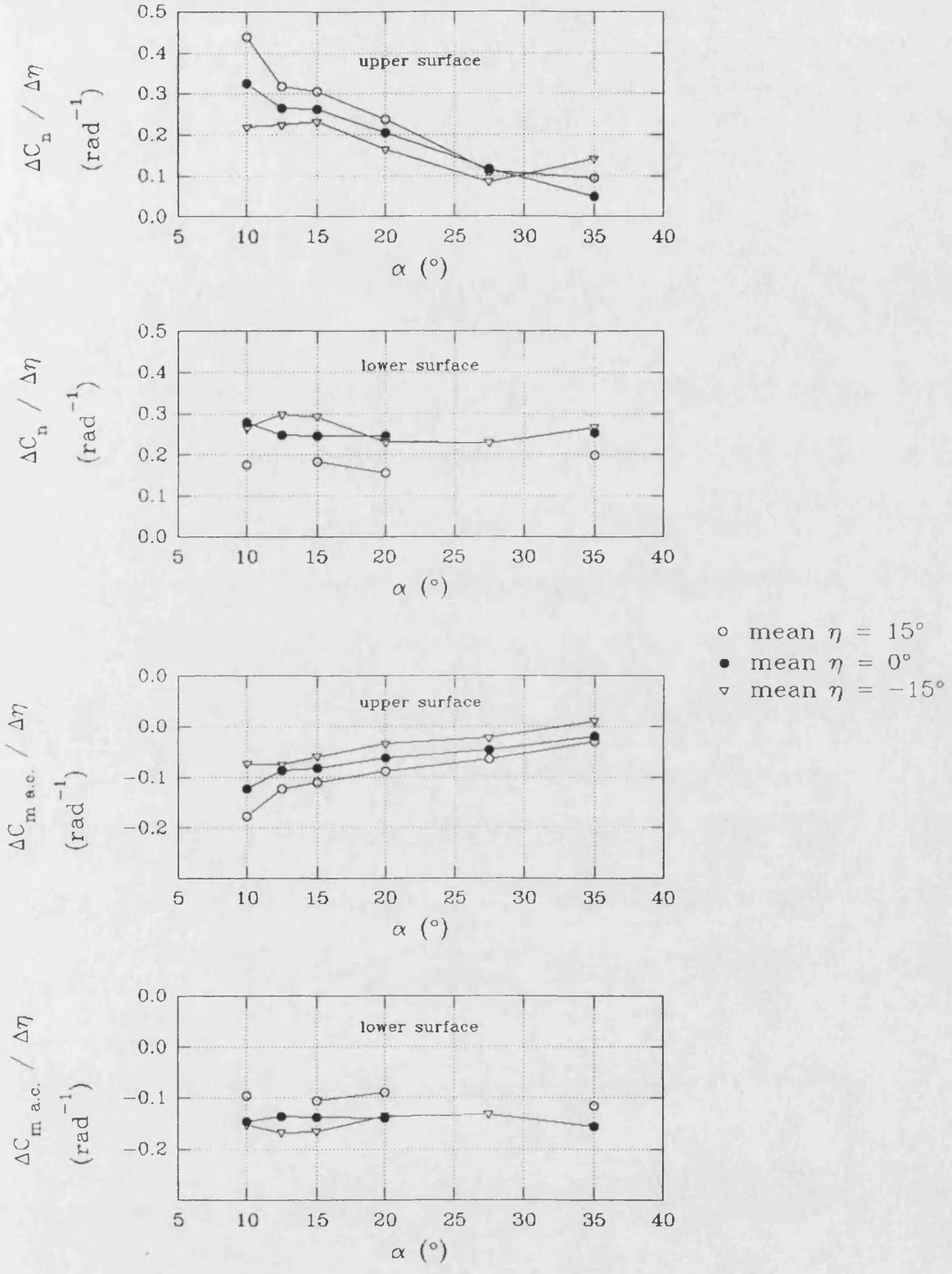

Fig. 6.32 - Upper and lower surface increments in C_n and $C_{m_{a.c.}}$ for various mean η

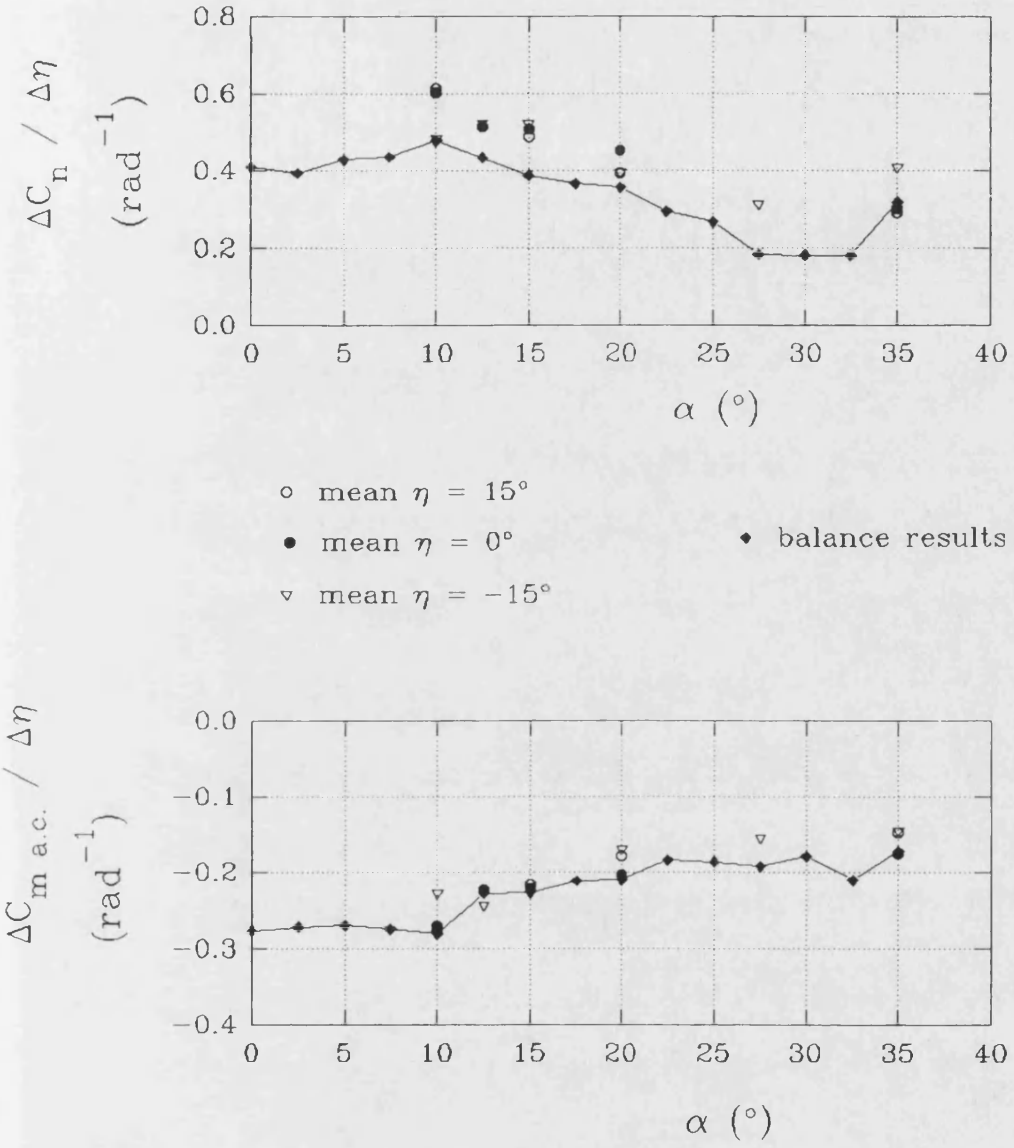

Fig. 6.33 - Steady control effectiveness - normal force and pitching moments

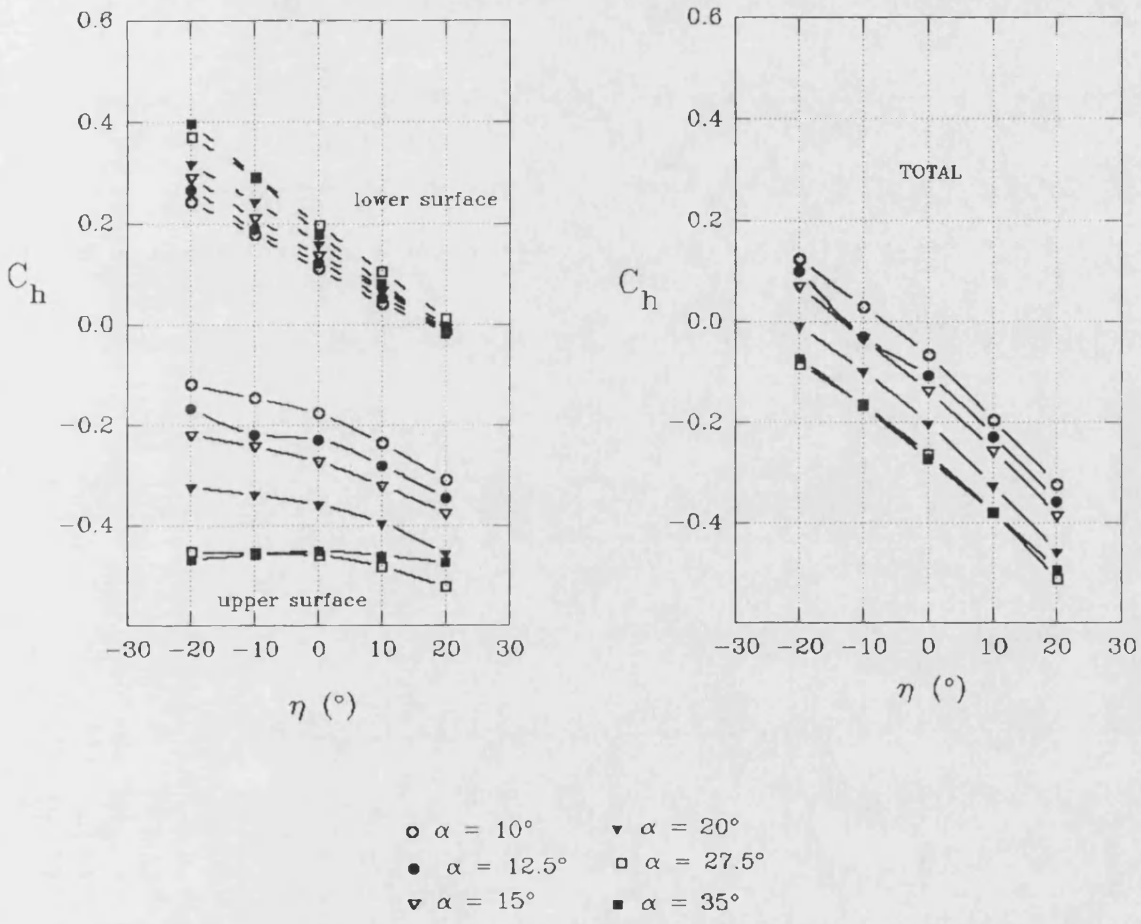

Fig. 6.34 - Hinge moment variations with elevon angle and incidence

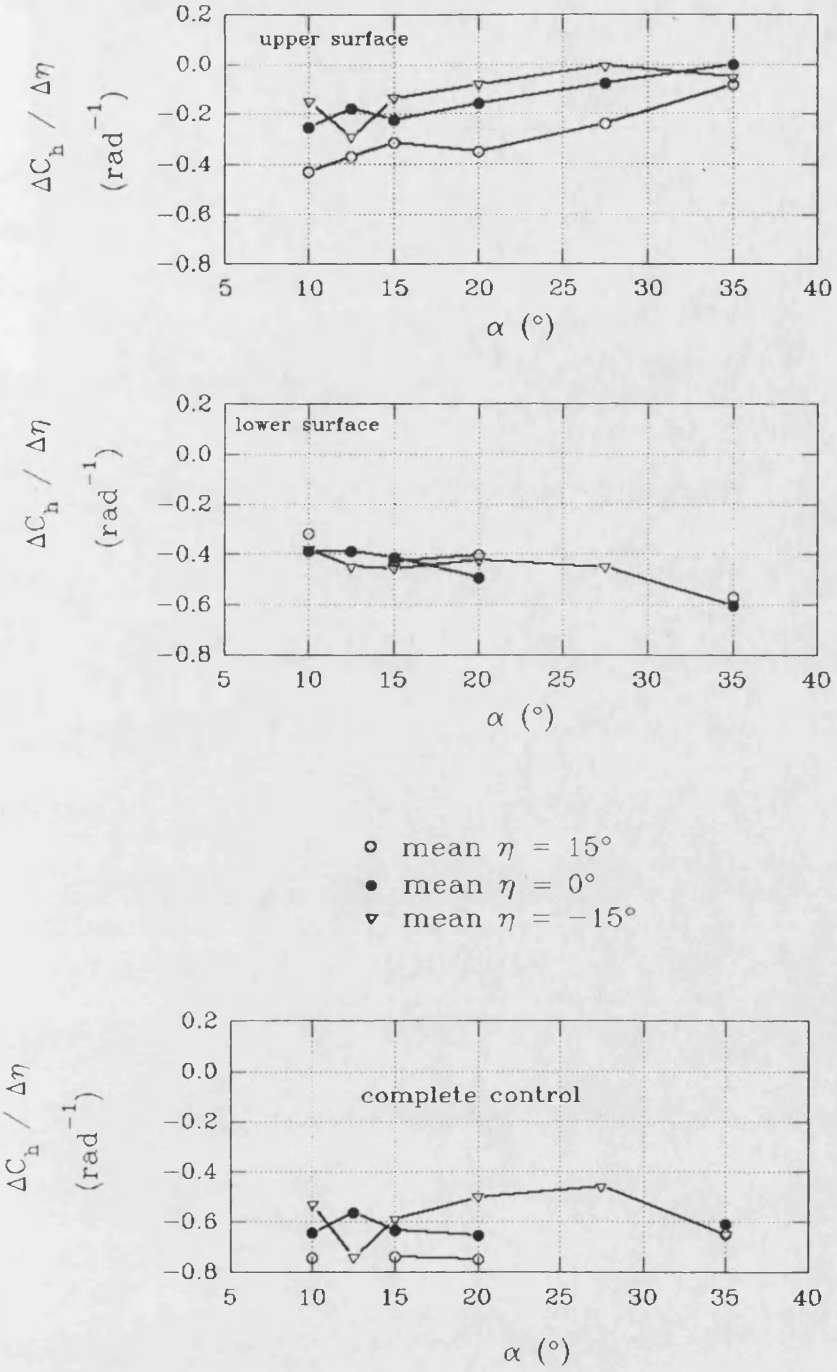

Fig. 6.35 - Steady control effectiveness - hinge moments

7. RESULTS FOR ELEVON OSCILLATION TESTS.

Elevon oscillation tests with an amplitude of oscillation, η_0=5°, were conducted at mean elevon angles of $\bar{\eta}$=0°, 15°, -15°. Since combat aircraft of the type considered here are often longitudinally statically unstable, large elevon deflections are often required as α increases. An aircraft of this type may typically require a 1° increase in elevon angle for every 1° increase in α to balance the destabilizing pitching moment (Kelly [1994]). Also, as discussed in Chapter 6, the response of the upper and lower surface pressures to steady elevon deflections varied with the mean angle, hence the need to consider various $\bar{\eta}$. Any oscillatory tests must determine whether the steady trends are repeated in the unsteady responses to forcing. Particular angles-of-attack were tested, relating to the different upper surface flow characteristics: α=10° - no burst; α=12.5°, 15°, 20° - burst point moving towards the apex; α=27.5°, 35° - fully burst vortex, post-stall. For mean elevon angles of $\bar{\eta}$=±15°, only α=10°, 15° and 20° were used to determine whether the change in mean elevon angle produced different responses of the vortex and burst point.

7.1 Mean elevon angle, $\bar{\eta}$=0°.

7.1.1 Unsteady pressures at α=10°, upper and lower surfaces.

Considering first the upper surface, unsteady pressure contours at α=10°, ν=0.32, fig. 7.1 gives the transfer function, amplitude C_{p_0}/η_0, and phase angle, ϕ between C_p and η (as defined in section 5.2), as well as the incremental pressure coefficients, $\Delta C_p/\Delta\eta$, due to steady elevon deflection previously given in Section 6 (fig. 6.17). By comparing the unsteady amplitude with the steady increment, the response of the primary vortex suction level is seen to be less than in the steady deflection case. On the elevon, the unsteady amplitude is greater towards the root of the control than in the steady case. In contrast, the response under the vortex on the elevon is reduced, though it extends over a slightly larger area of the control.

The phase angle contours show a lag in the response of the vortex peak suction which

increases towards the apex. There is a region of significant phase lead near the attachment line (y/s_{local}=0.55), though the amplitude in this region is low. By reconstructing the pressure time history (by adding the amplitude/phase values at this frequency to the mean pressure levels) it was found that there is a slight lateral motion of the suction peak during the cycle of oscillation. This causes a sign change in Cp level in the area between the attachment line and the peak suction which is opposite to that under the core itself. This induces a 180° difference in phase across the vortex in this region. Fig. 7.2 further clarifies this point by schematically showing the spanwise pressure distributions for 2 different times during an oscillation cycle. This lateral motion was not as large in the steady tests (fig. 6.11). Taking the above into account, for each spanwise row of tappings, the phase angle across the vortex reduces from near 0° at the leading edge to a slight lag under the core. The phase is then constant inboard of the peak suction. Hence, in the lateral direction, there is no lag in the primary vortex response at each spanwise station. As already discussed, however, there is an increasing phase lag towards the apex. Hence, in the longitudinal direction, there is a time lag associated with the vortex response to elevon motion.

These points become even clearer at higher frequency parameters. Fig. 7.3 shows the unsteady responses for ν=0.64, 0.98 and fig. 7.4 for ν=1.31, 1.65. As ν increases, the phase angle under the vortex continues to decrease (increasing lag) and the phase difference between the apex and the hinge line under the vortex increases further. The amplitude of the vortex response also decreases as ν increases, particularly towards the apex. Both these facts demonstrate the presence of a significant damping associated with the vortex response and that there is a delay in the longitudinal response.

On the elevon, the unsteady response under the vortex suction peak reduces greatly over the frequency parameter range tested. Inboard of the suction peak, however, the amplitude increases between ν=0.32 and 0.65 before reaching a constant level at ν=0.98. The area covered by this region on the elevon also increases though it does not extend to outboard of the peak suction location. This region has an increasing lead with ν. The suggestion is that this region is the response of the attached flow on the elevon. The surface flow visualisation of fig. 6.5 showed attached flow in this area, inboard of the reattachment line. As the vortex response reduces, so the attached flow responds more as though the vortex was not present. Although less obvious from the figures, the amplitude of response of the region inboard of the primary reattachment line tends to increase with ν as the vortex response reduces.

Although the amplitude is small, the large area it covers makes this effect important.

The mean pressure levels for oscillatory tests at ν=0.32, 0.98, 1.65 (fig. 7.5) do not show any change in the form of the flow with frequency parameter, although there is a significant reduction in the peak suction on the elevon compared with the steady pressure results. This suggests that either the mean strength or the vertical location of the core (or both) over the control surface changes when the elevon is oscillated. On the main wing (e.g. at x=451mm) this effect is much lower but is still present. The oscillation does not, however, appear to induce a premature breakdown of the vortex.

The unsteady longitudinal loadings on fig. 7.6 help to summarise the response of the upper surface flow at this angle-of-attack. The results from the steady tests are also presented to allow comparison with the unsteady amplitudes. The reduction in the amplitude of vortex excitation only causes a small reduction in loading on the main wing. As ν increases and the response of the attached flow inboard of the vortex increases, so the amplitude of loading in this region becomes greater than at lower ν. Similarly on the elevon, the amplitude at ν=0.32 is lower than in the steady case, but as the vortex response reduces and the region near the root (where the attached flow begins to respond) increases, so the net elevon loading increases. The phase results show a continual increase in phase from apex to hinge line. The phase difference between these two points increases between ν=0.32 and 0.98 before reducing again as ν increases further. The ϕ values at the hinge line have an increasing lead with ν. The increasing lead on the elevon is also very evident (as explained in Section 7.5)

The lower surface results for α=10°, ν=0.32 are compared against the steady incremental results on fig. 7.7. The unsteady amplitudes are very similar to the steady results. The unsteady response is limited to the region near the hinge line and on the elevon. There is only a small phase difference between the main wing and the elevon angle, and ϕ is nearly constant across the whole surface. As ν increases (fig. 7.8 ν=0.64 and 0.98, fig. 7.9 ν=1.31 and 1.65) the amplitude of response remains similar whilst the phase angles show an increasing lead with ν.

The integrated, unsteady, longitudinal loadings (integrated spanwise rows) further emphasise the almost constant amplitude of response with ν of the lower surface pressures (fig. 7.10). These loadings are also very similar to the steady incremental values shown. The loadings indicate a reduction in response at the apex and an increase near the hinge line as

ν increases. A slight increase in phase angle from the apex to hinge line is also evident. The phase difference between apex and hinge line reduces as ν increases. There is a rapid increase in phase over the elevon.

Returning to the upper surface, there appears to be a similarity between the response of the region on the elevon inboard of the suction peak in both phase and amplitude to that of the lower surface, suggesting the elevon may be exciting the attached flow inboard of the peak suction on the upper surface.

7.1.2 Change in upper surface unsteady pressures with α and ν.

Increasing the incidence to α=12.5°, the unsteady (and steady increments) on the upper surface at ν=0.32 are shown in fig. 7.11. At this α, the burst point is at x=410mm (from the steady results). As discussed in Section 6.2, the change in burst position with steady elevon deflection is shown by the large negative value contours under the peak of the vortex. Similarly, the region of large amplitude unsteady response centred at this location is associated with the dynamic motion of the burst. At ν=0.32, the amplitudes in this area are similar to the steady results, suggesting the burst point motion is similar to the steady case. The vortex lags the elevon motion and the lateral motion of the suction peak is evident from the region of large phase lead. The red area on the phase plot is where the arctangent has produced a sudden change in phase (180°).

On the elevon, inboard of the suction peak, the unsteady response is already greater than in the steady case. As the frequency parameter increases (fig. 7.12 and 7.13), the vortex response reduces. The region associated with the burst motion reduces in size in the x-direction, suggesting a reduction in burst motion. The phase angle along the vortex, towards the apex, reduces (increasing lag). On the elevon, the region inboard of the burst vortex suction peak again increases in amplitude and area between ν=0.32 and 0.98 as the vortex change reduces, though not to the same extent as at α=10°. The area of attached flow inboard of the vortex, on the elevon, is smaller than at α=10°. The phase in this region increases with ν.

Increasing the angle-of-attack further to α=15° produces the results of fig. 7.14 (ν=0.32 and ν=0), fig. 7.15 (ν=0.64, 0.98) and fig. 7.16 (ν=1.31, 1.65). Though similar to the results

at α=12.5°, the increase in the proportion of burst to unburst vortex has produced certain important differences. The vortex suction amplitude reduces more rapidly with ν, particularly under the burst portion of the vortex. At ν=0.64, the burst vortex is hardly responding to the oscillation whilst there is still evidence of burst point motion and change in the peak suction of the unburst section towards the apex. The phase lag associated with the breakdown location and unburst vortex decreases more rapidly with ν (larger lag) than at lower α.

By ν=1.65, the phase in front of the hinge line (under the burst vortex) has become almost constant with y. Thus, although the amplitude in this region is small, this constant phase produces a larger integrated effect than at lower ν. This is demonstrated by the longitudinal loadings of fig. 7.17 (for α=12.5° and 15°). At both angles-of-attack, there is a significant increase in loading under the burst portion of the vortex (towards the hinge line) with ν, whilst the loading 'peak' at the burst point (marked as A and B) and under the unburst portion continues to decrease. The larger phase difference between apex and hinge line at α=15° is also shown by the increased gradient of the phase curves compared with α=12.5° and 10° (fig. 7.6 and fig. 7.17).

The region at the elevon inboard end of increased amplitude response is now larger than at lower α (though the amplitude is reduced) and covers the whole hinge line area.

The upper surface results for α=20° (fig. 7.18 and 7.19) are an extension of α=15°. At α=20°, the burst point is approximately at x=170mm (fig. 6.3). The amplitude of response of the vortex reduces with ν even more rapidly than at lower α.

Once the vortex is fully burst (α>27.5°), the form of the unsteady pressures changes completely with no evidence of a change associated with the vortex. Instead, there is a small amplitude response over the whole surface. Hence, the best indication of the trends with ν are obtained by considering the longitudinal loadings, as given on fig. 7.20. At α=27.5° and 35°, the upper surface amplitude of response is greater than the steady increments suggesting the elevon oscillation is producing some form of excitation of the flow. At α=35°, there is a peak in this excitation at ν=0.98. Up to this frequency parameter, the phase is reasonably constant with x, though it reduces with ν. By ν=1.65, there is a significant phase difference between the apex and hinge line and the elevon loadings have a significant lead associated with them. This unsteady response of the bluff-body flow at this incidence is not understood.

Integrating up the unsteady loadings produces the unsteady normal force, pitching moment (about the aerodynamic centre) and hinge moment results for the upper surface of fig.

7.21. The steady force and moment derivatives with η are included at ν=0. Consider first the normal force derivatives. Below the stall angle-of-attack, the amplitude is reasonably constant with ν and reduces with α. The values tend to the steady results at low ν. The phase angles are also similar with ϕ_n increasing with ν. At α=35°, where bluff-body type flow is present above the wing, n_0 is much greater than the steady value up to ν=0.98, before dropping suddenly. The surface pressure contours suggest a low amplitude response over the complete surface producing the longitudinal loadings of fig. 7.20. The amplitudes on this figure show a peak in level at ν=0.98 with almost constant phase along the wing. This lack of phase difference means the low amplitude response must sum to the given value, with no cancellation of different areas due to phase differences. The unsteady longitudinal loadings are also much greater than the steady increments, hence the disparity at low ν between the results. Beyond ν=0.98, there is a large phase difference between apex and trailing edge, producing a cancelling effect in terms of normal force and a low no value. The ϕ_n at α=35° are also a consequence of this balance between amplitude and phase changes with x and ν.

The above ϕ_n characteristics also explain the change in m_0 with ν at α=35°.The lack of phase difference with x at ν=0.98 produces a low pitching moment about the aerodynamic centre which increases as the phase difference increases suddenly with ν to very large values. At α below the stall point, m_0 is nearly constant with ν (a slight increase being evident). However, the phase change over the surface from apex to trailing edge results in m_0 values lower than in the steady case. The phase, ϕ_m, increases with ν and slightly with α, especially as the burst point moves towards the apex at higher α, producing a larger burst vortex portion. In fig. 7.18 and fig. 7.19, this was seen, at α=20°, to induce a large phase lag in the burst point motion, and hence a larger ϕ_m value.

The unsteady aerodynamic pitching terms within an FCS are important to the response of the aircraft and in determining the necessary gains/control motion required to execute a manoeuvre. Hence, the characteristics of m_0 and ϕ_m in fig. 7.21 are important in determining the gains required within the FCS. This point is discussed again later when the total m_0 and ϕ_m values are presented.

The hinge moment, $-h_0$, reduces with α but is reasonably constant with ν. ϕ_h shows similar trends, except above α=15° where the phase suddenly increases, and at α=35° where bluff-body flow exists over the elevon. Also, at low ν, α=10°, $-h_0$ is lower than at higher ν, the reverse being true at higher α. The unsteady pressure amplitude contours of figs. 7.1, 7.3

and 7.4 showed that the unburst vortex to suppress the response of the region of attached flow at the inboard end of the elevon at low α, thus producing lower $-h_0$ at ν=0.32 than at 0.64. Above α=10°, the slight reduction in $-h_0$ from ν=0.32 to 0.64 results from the phase characteristics of $C_p(\nu)$ over the elevon.

At α=35°, $-h_0$ increases rapidly with ν as the amplitude of the response on the elevon also increases (fig. 7.20). The h_0 values tend towards the steady derivative values at low ν for all α shown.

7.1.3 Change in lower surface unsteady pressures with α and ν.

Returning to the lower surface, the trends described at α=10° (Section 7.1.1) are repeated for all other α up to α=35°. This is illustrated in fig. 7.22 where results for α=15° and 35°, at ν=1.65, are presented. The only difference is in the phase lead at the trailing edge of the elevon which is greater at α=15°. The nearly constant response of the lower surface with α is further demonstrated by the longitudinal loadings in fig. 7.23 (α=15° and 20°) and fig. 7.24 (α=35°). The near constant steady increments in loading with α, for a mean elevon angle of 0°, was discussed in Section 6.2 and on fig. 6.18. This characteristic is repeated for the unsteady amplitudes. All the loadings are similar to the steady increments with a slight increase with ν, especially above ν=0.98. The phase angles show a linear trend with ν and are very similar for each α, except at α=35°. Due to the small amplitudes of the responses towards the apex, the phase angles calculated in this region show large variations. However, in general, there is a slight increase in phase angle with distance from the apex. All the curves show a reduction in ϕ near the hinge line. As ν increases, the phase angle at each x location increases. This change appears linear with ν. Because the lower surface loadings are so similar for all α shown, it is suggested that the lower surface unsteady response is independent of the upper surface characteristics until bluff-body type flow exists.

As discussed in Section 2.4, Kienappel and Round [1980] carried out low speed wind tunnel tests on a 2-d section with an oscillating flap. Their results can now be used for comparison with the lower surface results presented in this section. Fig. 7.25 shows Kienappel and Round's unsteady pressure results for α=0° with η_0=2°. The amplitude and phase are for the difference in $C_p(t)$ between upper and lower surfaces. Results for four different

frequencies are shown. The equivalent frequency parameter values are also given. The unsteady amplitudes are similar for all ν shown. The phase angle increases with x and increases linearly with ν at each x location. These trends are consistent with those described for the lower surface of the delta wing model. A more direct comparison is given in fig. 7.26. Here, the results from the present tests (at α=10°) and those of Kienappel and Round, at ν=1.65, are shown together. No scale is given for the amplitudes as the differences in wing and control geometry make the scale meaningless. The delta wing longitudinal amplitudes have, however, been non-dimensionalised by the local semi-span at each x location to produce a form more comparable to the 2-d section results. The amplitude trends with x are very similar, despite the difference in relative control chord dimension. The peak in the 2-d tests, in front of the hinge line, is associated with the gap geometry of the section, this particular tapping being in the gap between main surface and control. The increase in amplitude towards the leading edge evident on the 2-d results is not present for the delta wing. The phase angles over the the control show a remarkably similar trend and the phase angle in front of the hinge line tends to 20° in both cases. On the delta wing, however, ϕ does not reduce as sharply towards the leading edge/apex. This comparison of results is very encouraging, suggesting it may be possible to determine the likely lower surface results on a delta wing using a much simpler geometry and possibly even from existing results. Also, if the unsteady characteristics are known at low α, it appears they are also known with reasonable accuracy for all α as there is little change with incidence. Since the lower surface response does not appear to be dependent on the highly separated, upper surface flow, it may also be possible to predict the attached flow, unsteady pressures using a simple unsteady computational/numerical approach, such as those described in Section 2.7.2.

The unsteady normal force, pitching moment (about the aerodynamic centre) and hinge moment contributions from the lower surface are given in fig. 7.27. As would be expected from the consistency of the longitudinal loadings with α and ν, n_0 and m_0, and ϕ_n and ϕ_m change little with α, though all increase with ν. The only exception is at α=35° where n_0 and $-m_0$ are larger than at lower α. The n_0 values tend towards the steady results (ν=0) whilst the change in phase with x of the longitudinal loadings (fig. 7.23 and 7.24) produce $-m_0$ values lower than in the steady case.

The $-h_0$ values, though constant with ν, increase with α, especially between α=27.5° and 35°, though they again tend towards the steady derivatives at low ν. The increase in

amplitude is a result of the slight reduction in phase difference with x across the elevon at higher incidences.

These lower surface coefficient derivatives appear very predictable and have simple, consistent changes with ν and α.

7.1.4 Unsteady normal force, pitching moment and hinge moment derivatives for complete model.

Combining the upper and lower surface results gives the total unsteady normal force, pitching moment and hinge moment values of fig. 7.28. The near constant values of the lower surface contributions act to suppress the changes with α and ν of the upper surface. For example, the n_0 values reduce only slightly with α and tend towards the steady values at low ν. The phase variations with ν are the same at all α. The $-m_0$ values also reduce with α and increase slightly with ν. The low ν values, however, do not tend towards the steady values. Hence, to produce the same pitching moment contribution at higher frequencies, the gain in the FCS for pitching moment would have to be greater than would be predicted assuming the steady derivative results applied. This larger gain may increase the potential for structural excitations. Conversely, using the gains predicted from the steady results for all frequencies would produce a degraded aircraft response or prevent full stabilisation of the unsteady motion effects at high-α.

The $-h_0$ values are constant with α and reasonably constant with ν, and again tend towards the steady values. Thus, the unsteady aerodynamic loads on the control actuators could be modelled by a constant gain at all α and ν for $\bar{\eta}=0°$. Hence, no scheduling would be required for this aerodynamic term about this zero mean angle.

There is no evidence of significant flow excitation due to control oscillations in the range of ν tested, except at $\alpha=35°$. Such excitation would show up as a large increase in the aerodynamic derivative terms and change in phase angle.

7.2 Upper surface results for $\bar{\eta}$=15° and $\bar{\eta}$=-15°.

Both non-zero $\bar{\eta}$'s are discussed together, each having similar trends and comparisons with the steady results. Fig. 7.29 shows the unsteady upper surface pressures for ν=0.32 and the steady results, both for $\bar{\eta}$=15°. The steady and unsteady vortex response levels on the main wing are similar, with a small phase lag, and again a lead near the primary attachment line associated with a slight lateral movement in the suction peak. On the elevon, however, the amplitudes inboard of the suction peak are already greater than in the steady case and the vortex response is reduced. As ν increases (fig. 7.30 ν=0.98 and 1.65) the change in peak suction reduces rapidly and has an increasing lag associated with it. On the elevon, the region of attached flow type response increases with ν and has an increasing ϕ with increasing ν. The unsteady pressure results for $\bar{\eta}$=-15° are given in fig. 7.31 and 7.32. Again, the vortex response, which is already lower than for $\bar{\eta}$=15°, reduces rapidly with ν and has a lag associated with it. The region at the inboard end of the elevon has an increasing amplitude, phase and area of coverage with ν.

The longitudinal unsteady (and steady) loadings for α=10°, 15° and 20°, $\bar{\eta}$=15° are presented in fig. 7.33. The amplitude reduces towards the apex and increases at the hinge line with ν. The values again agree with steady incremental results. The phase over the rear portion of the wing (and elevon) increases with ν, whilst the phase difference between apex and hinge line also increases. These characteristics are repeated in fig. 7.34 for $\bar{\eta}$=-15°, though the amplitude at the hinge line increases more rapidly with ν than for the other mean elevon angles. A more direct comparison of the longitudinal loadings at α=10° is given on fig. 7.35 where the results for $\bar{\eta}$=0°, 15° and -15°, ν=0.98 are plotted together. As $\bar{\eta}$ increases, so the unsteady amplitude increases, (though each is similar to the steady increments for that $\bar{\eta}$) whilst the phase angle at each x location reduces with increasing $\bar{\eta}$. This increase in ϕ coincides with a reduction in vortex response with decreasing $\bar{\eta}$, and vice versa. Since the unsteady amplitude is the combination of both the response of the vortex and attached flow, this phase characteristic again suggests a significant lag associated with the vortex response, whilst the attached flow has a phase lead under these conditions (as already determined from the lower surface responses). Hence, as the vortex response reduces, so the phase angle of the

loading increases. This is most evident on the elevon where the vortex response reduces rapidly whilst that of the attached flow increases, thus inducing a lead on the control.

The change in vortex amplitude with $\bar{\eta}$ is for the same reasons as for the steady results discussed in Section 6.2. A positive elevon angle appears to increase the strength of the vortex and reduce its height from the surface, thus producing a higher suction level. Oscillation of the vortex in this condition causes a greater amplitude of response than say for a negative mean elevon angle where the strength of vortex suction is reduced due to increased height and reduced strength with a negative mean angle.

Increasing the angle of attack to α=15°, where the burst is above the wing, produces the same trends of reducing response and increasing ϕ associated with the vortex as ν increases (fig. 7.36 to 7.39) at both $\bar{\eta}$ values. In both cases, the burst point motion reduces rapidly and ϕ at this location reduces. Also, as the vortex response on the elevon decreases, the region of attached flow excitation on the elevon and near the hinge line increases greatly, particularly in area of coverage. The longitudinal unsteady loadings of fig. 7.33 and 7.34 (showing results at various α for two mean elevon angles), show the similarity between steady and unsteady amplitudes at α=15°, though for $\bar{\eta}$=-15°, the loadings are less negative than in the steady case on the main wing. For both mean angles, however, the trends in amplitude and phase with ν are the same at lower α. Comparing these loadings with those for $\bar{\eta}$=0°, fig. 7.35, η=15°, shows the change in amplitude and ϕ with $\bar{\eta}$ to be less than for the completely unburst vortex at α=10°. Changes in $\bar{\eta}$ do not affect the burst vortex as greatly as for the unburst one (Section 6.2), hence the responses are similar at each $\bar{\eta}$. The only exception is over the elevon, where there is significant change in phase with $\bar{\eta}$. At $\bar{\eta}$=-15°, the elevon is immersed in the burst vortex, whilst at $\bar{\eta}$=15°, the flow over the elevon is accelerated. This difference in flow type induces a large difference in phase over the elevon with $\bar{\eta}$.

This reduction in change of response with $\bar{\eta}$ is even more evident at α=20° (fig. 7.35). However, the amplitudes, and more especially ϕ values, on the elevon , which at this angle are related more to the attached flow rather than burst vortex response, still alter significantly with $\bar{\eta}$.

As the pressure contours for α=20° are only a further extension of those at α=15° for a more forward breakdown location, the surface contours are not included. The unsteady loadings are, however, given on fig 7.33 and 7.34 for completeness.

Integrating the unsteady transfer function pressures for the upper surface produces the unsteady normal force, pitching moment about the aerodynamic centre and hinge moments given on fig. 7.40 ($\bar{\eta}$=15°) and 7.41 ($\bar{\eta}$=-15°). In both cases, n_0 tends towards the steady derivative values at low ν, but reduce with increasing ν. The n_0 values are greater for $\bar{\eta}$=15°, reflecting the larger vortex changes. There is also a greater increase in ϕ with ν for $\bar{\eta}$=-15° than $\bar{\eta}$=15°. All n_0 tend to the steady values at low ν.

The difference in phase angle of the longitudinal loadings with x, when integrated into the pitching moment about the aerodynamic centre, reduce the $-m_0$ values compared to the steady derivatives. The $-m_0$ values at $\bar{\eta}$=15° are greater than $\bar{\eta}$=-15° and in both cases, the values are reasonably constant with ν. As for ϕ_n, $\phi_{m\ a.c.}$ increases more with ν for $\bar{\eta}$=-15°.

The $-h_0$ values for $\bar{\eta}$=15° reduce with ν whilst those for $\bar{\eta}$=-15° increase slightly. The $-h_0$ derivatives for the larger mean angle are much greater. For both mean angles, ϕ_h has an increasing lead with ν but is greater for $\bar{\eta}$=-15°. For this mean angle, there is a change in ϕ_h with ν that is characteristic for angles above α=10°. Comparing the loadings over the elevon given in fig. 7.34, there is a large increase in phase at the trailing edge beyond α=10°, i.e. when the vortex over the control is burst. Again, the h_0 values tend to the steady values at low ν.

7.3 Lower surface results for $\bar{\eta}$=15° and -15°.

The lower surface results are very similar to the steady values for all α, ν and $\bar{\eta}$ tested, with very predictable phase changes with ν. The unsteady lower surface pressure results at α=10° for $\bar{\eta}$=15° are given on fig. 7.42 and fig. 7.43. As ν increases, there is an increase in excitation in front of the hinge line, whilst the level on the elevon remains constant. The phase lead on the wing and particularly on the elevon increases with ν.

The unsteady longitudinal loadings are given on fig. 7.44. The characteristics of the amplitude and phase are the same at all α shown, so are described only once. As ν increases, the amplitude over the main wing, particularly in front of the hinge line, increases. The elevon amplitudes change only slightly with ν at α=10°. The phase angle on the elevon, at each x location, increases greatly with frequency parameter, as does ϕ at the hinge line. The phase difference between apex and hinge line increases, especially between ν=0.98 and 1.65. Increasing α reduces the phase change on the elevon. Integrating up these results gives the unsteady normal force, pitching moment and hinge moments of fig. 7.45. The consistency of the changes with ν are very evident from the constant n_0 and ϕ_n values for all α. The n_0 increases slightly with ν due to the increased loading around the hinge line. The m_0 and $\phi_{ma.c.}$ values are again independent of α. The lack of phase difference between apex and hinge line means the m_0 values are closer to the steady derivatives than was the case for the upper surface.

The unsteady hinge moments show a significant change with α, $-h_0$ increasing with incidence and by a small amount with ν. The values are, however, consistent with the steady derivatives. The larger ϕ_h for α=10° are the direct consequence of the larger phase difference over the elevon as described above.

Fig. 7.46 and 7.47 present the unsteady pressure results for $\bar{\eta}$=-15°, α=10°. As for $\bar{\eta}$=15°, the results are consistent with the steady derivatives and show a slight increase in amplitude in front of the hinge line. The phase lead on the main wing and elevon increases with ν. The red region at the trailing edge, for ν=1.65 is due to the inverse tangent routine - the angle having gone beyond ϕ=90°. Also, the region near the apex has a low response and thus the phase angle can not be calculated accurately. The characteristics of the unsteady longitudinal loadings at α=10°, 15° and 20° (fig. 7.48) for $\bar{\eta}$=-15° show the same changes with ν and α, i.e. increasing amplitude and phase over the elevon and at the hinge line, and phase difference between apex and trailing edge. There is, however, a peak in the amplitude (both steady and unsteady) at α=15°, though this does not seem to affect ϕ. There is also a larger phase difference across the elevon at α=10° than at other incidences. The unsteady force and moment results for the lower surface, $\bar{\eta}$=-15° (fig. 7.49), are not as constant with α as at $\bar{\eta}$=15°, although the amplitudes are reasonably constant with ν, and tend towards the

steady derivative results at low ν. The n_0, $-m_0$ and $-h_0$ values are all greater for α=15° which coincides with the peak in longitudinal loading.

The lower surface responses for the 3 $\overline{\eta}$ are compared on fig. 7.50, for ν=0.98, and the 3 α. There is an increase in the amplitude over the elevon with decreasing $\overline{\eta}$. As $\overline{\eta}$ reduces (trailing edge up), the flow over the elevon is accelerated (Section 6.2). The elevon oscillation causes a greater excitation as this local q increases. On the main wing, however, the amplitude is larger for $\overline{\eta}$=0° than for the other two cases.

The phase angle over the elevon is nearly constant with $\overline{\eta}$, especially at higher angles-of-attack, but is slightly greater for $\overline{\eta}$=0°. On the rest of the wing, ϕ increases at each x location as $\overline{\eta}$ decreases.

Kienappel and Round [1980] also compared results for various mean elevon angles on a 2-d section. As was shown in Section 7.1.3, their results agreed with those for $\overline{\eta}$=0°, especially in terms of changes in ϕ with ν. Fig. 7.51 presents the results for three different mean control angles. These results are for the difference between the upper and lower surface unsteady pressures. The amplitude is reasonably constant with $\overline{\eta}$, except near the hinge line due to the complex slot geometry and changing gap width. The phase angles also only change slightly with $\overline{\eta}$. Being the difference between the two surfaces, the near constant amplitude and phase suggest either there is little change in the response of either surface with $\overline{\eta}$, or that the increase in amplitude of one is countered by a similar increase in the other, whilst both surfaces have the same phase characteristics for each mean elevon angle. The second explanation agrees with the results for the delta wing as implied on fig. 7.35 and 7.50. To further emphasise this point, the results for $\overline{\eta}$=15° and -15° have been added together to model a complete wing with fully attached flow. These are compared against twice the values for $\overline{\eta}$=0°, modelling a zero mean angle, on fig. 7.52. These curves are then more comparable to the Kienappel and Round plots of fig. 7.51. The phase angle for the two cases are now practically the same, as are the amplitudes, and this agrees with Kienappel and Round's results. It also implies that the delta wing, lower surface results have equal changes with $\overline{\eta}$ about $\overline{\eta}$=0°.

7.4 Total unsteady force and moment derivative values.

Combining the upper and lower surface contributions gives the complete model unsteady normal force, pitching moment (about the aerodynamic centre) and hinge moments, for $\bar{\eta}$=15° and -15° of fig. 7.53 and 7.54. As for $\bar{\eta}$=0°, the near constant contributions from the lower surface (for each $\bar{\eta}$) reduce the changes in unsteady derivatives with α and ν. Both n_0 and $-h_0$ tend towards the steady values at low ν, but showing a slight reduction with ν. The m_0 values are lower than the steady values, reflecting the difference in phase of the loadings with x, on both the upper and lower surfaces.

The effect of $\bar{\eta}$ on each derivative at α=10° (unburst vortex) is shown on fig. 7.55. The n_0 values reduce with $\bar{\eta}$, except at low ν where the values for $\bar{\eta}$=15° are slightly greater than those at $\bar{\eta}$=0°. The same is true for m_0. The $-h_0$ values increase with $\bar{\eta}$. The phase angles at each ν are independent of $\bar{\eta}$.

The results for α=15° (burst present over wing) are compared on fig. 7.56. For the burst vortex, n_0 and $-m_0$ are greater for $\bar{\eta}$=0° than for either other mean angle. The $-h_0$, however, still increase with $\bar{\eta}$. Again, the phase angles are reasonably constant with $\bar{\eta}$.

The lack of difference in these main derivative terms with either ν or $\bar{\eta}$ means little scheduling would be required within the FCS. The phase characteristics are also easily modelled, being both similar to the fully attached flow case and not altering with α. Because of these trends and the fact that the derivatives tend to the steady results, the technique often used at present, where the steady values are assumed throughout the ν range, is not unreasonable. The main, and most important exception is for m_0. Here, the longitudinal phase characteristics produce much lower $-m_0$ derivative values. This term is important for the handling of the aircraft as discussed previously. The lack of amplification of any of the derivatives or pressure results with ν means the flow is not being caused to resonate by the elevon motion at these high frequencies. Hence, the reduction of the effects of the natural flow unsteadiness on the aircraft by rapid motion of the elevons (to produce a more stable platform) would not appear to be likely to cause aerodynamic excitation of the structure

beyond the level predicted by the use of the steady values. This conclusion, however, does not account for the unsteady aerodynamic terms due to the movement/excitation of the flexible structure, the present results having been measured on a rigid model. To determine fully the aeroservoelastic stability of the system, it is necessary to determine the aerodynamic derivatives for each flexible mode of interest, or to test a model with the necessary flexibility within its structure, as described in the next chapter.

7.5 Von Kármán and Sears' airfoil theory for non-uniform motion.

It is not intuitive that there can be a phase lead between the unsteady aerodynamics and aerofoil motion. Von Kármán and Sears [1938] produced an explanation for this lead, and their analysis is summarised below. The description does not include any techniques/equations for calculating the various terms, though it is possible to do so, and for these the reader is referred to the above reference.

The aerodynamic response of attached flow to airfoil motion can be broken down into 3 components as follows :

(i) L_0 - the aerodynamic response due to the quasi-steady form of the wing. The rotation of the control forms a curved quasi-steady geometry. This induces a change in circulation on the wing. L_0 consists of 2 parts: L_{0_η} is due to, and is in phase with the elevon angle, η; $L_{0_{\dot\eta}}$ due to the induced curvature of the control resulting from the velocity of each point on the control, i.e. due to and in phase with $\dot\eta$. $L_{0_{\dot\eta}}$ is proportional to ν whilst L_{0_η} is independent of frequency.

(ii) L_1 - termed the apparent mass, this is the force required to accelerate the air volume during the control motion, and as such is in phase with $\ddot\eta$, i.e. 180° out of phase with η.

(iii) L_2 - the effect of the vorticity shed into the wake on the wing itself. The wake vortex sheet, caused by the change in circulation around the wing induces a downwash on the wing,

being of opposite rotation sense to the change on the wing, and hence L_2 lags the elevon motion, the value of this phase angle being dependent on the integration of the effect of the whole wake and hence on v and the other terms described above.

Combining these terms on a phasor diagram, as in fig. 7.57, it is seen that $L_{0_{\dot{\eta}}}$ is instrumental in producing the possibility for a phase lead in the results. The balance between $L_{0_{\dot{\eta}}}$ and the out of phase component of L_2 in this simple model determines whether the overall result has a lead or lag.

In terms of the tests reported here, the major influence on the phase over the elevon is the incidence induced by the elevon velocity (rate of rotation), which leads the elevon angle by 90°. The value of the induced velocity increases with distance from the hinge line (for a given rate of rotation) thus producing an increasing phase lead towards the trailing edge (e.g. fig. 7.6, 7.10). This effect is more evident on the lower surface, attached flow (e.g. fig. 7.9) than on the upper surface, vortex dominated flow over the upper surface of the elevon. The increased flow velocity over the elevon also affects the flow just upstream of the hinge line producing a phase lead in this region.

The term L_2, referred to above, is difficult to quantify for a vortex dominated flow due to the nature of the interactions between the attached flow, elevon induced flow, and vortex generation. For the attached flow on the lower surface, any changes to the pressures upstream of the elevon must propagate forwards from the elevon through the boundary layer and through the influence of the change in overall pressure field round the wing. This is also the case for the upper surface, but in addition, the formation of the shear layer from the leading edge, and hence the vortex, will also be affected by the changes on the lower surface. The general effect of all these interactions is to induce a phase lag on the surface pressures in front of the elevon, which increases with distance from the hinge line (see fig. 7.6, 7.10 etc.). Hence the actual phase angle of the unsteady pressures depends on the complex balance between these lead and lag effects at each point on the surface.

The pressure responses to step changes in elevon angle were measured during this investigation. They demonstrated an increasing lag in response towards the apex of the wing. Due to the small changes in pressure resulting from these step change tests, coupled with the noise in the pressure signals, it was not possible to obtain sufficient reliable data from these tests to include in this report. Further improved step change tests would, however, give valuable information about the form of the 'feed-forward' effects described above.

Notes on Interpretation of Unsteady Pressure Results.

A positive phase angle means the unsteady pressure leads the elevon angle, whilst a negative value equates to a phase lag.

As was described in Chapter 5, the phase angle of each unsteady pressure signal, relative to the elevon angle, was obtained by numerical analysis of the pressure transducer and Hall effect signals. These numerical results, plotted on the following figures can give misleading impressions of the variation of the phase angle over the surface of the model. In areas where the amplitude of the unsteady pressure is small, small errors in the measured pressures can produce large variations in the phase angle. These large changes over such a small area are thus artificial effects and can adversely effect the phase angle contour lines. This problem is most noticeable inboard of the vortex on the upper surface of the model and over large portions of the lower surface where the unsteady pressure response is very low. Hence, the phase plots must be looked at in conjunction with the amplitude results to determine the validity of the phase angles shown.

In addition, the range of phase angle given by the contours is from -90° to 90°, as given by the arctangent function. It is possible that this also leads to unrealistic changes in phase angle over certain parts of the model, though again these tend to be in areas of low amplitude response and hence do not greatly influence the integrated results of, for example, unsteady normal force.

$\alpha = 10°$, $\nu = 0.32$, mean $\eta = 0°$

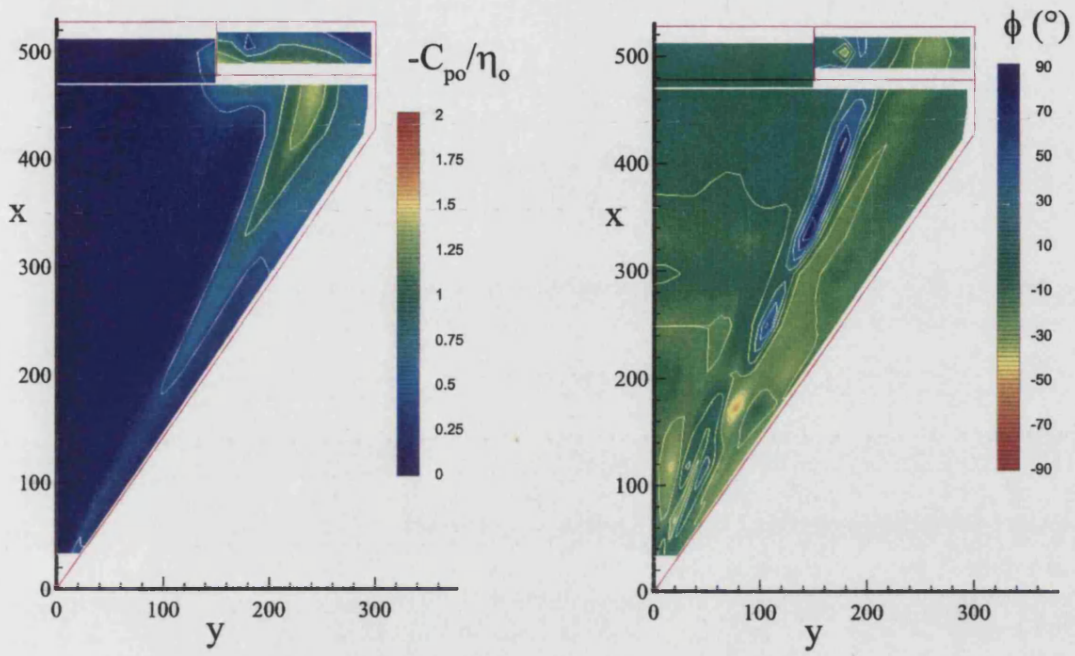

Steady Increments, mean $\eta = 0°$

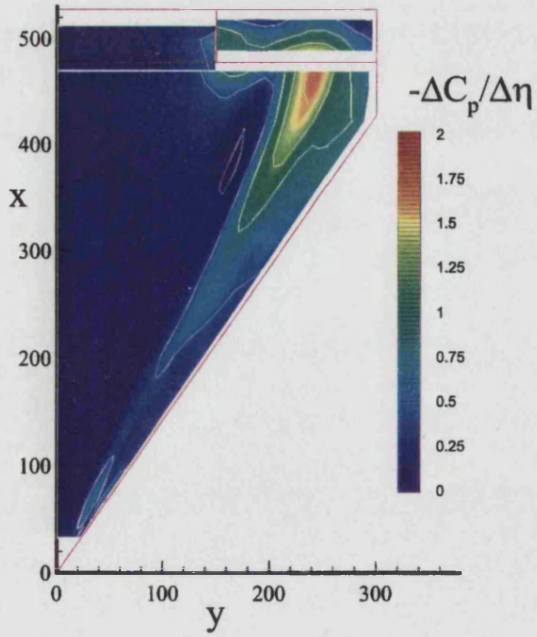

Fig. 7.1 - Upper surface unsteady pressure contours, $\nu = 0.32$, and steady incremental contours, $\alpha = 10°$

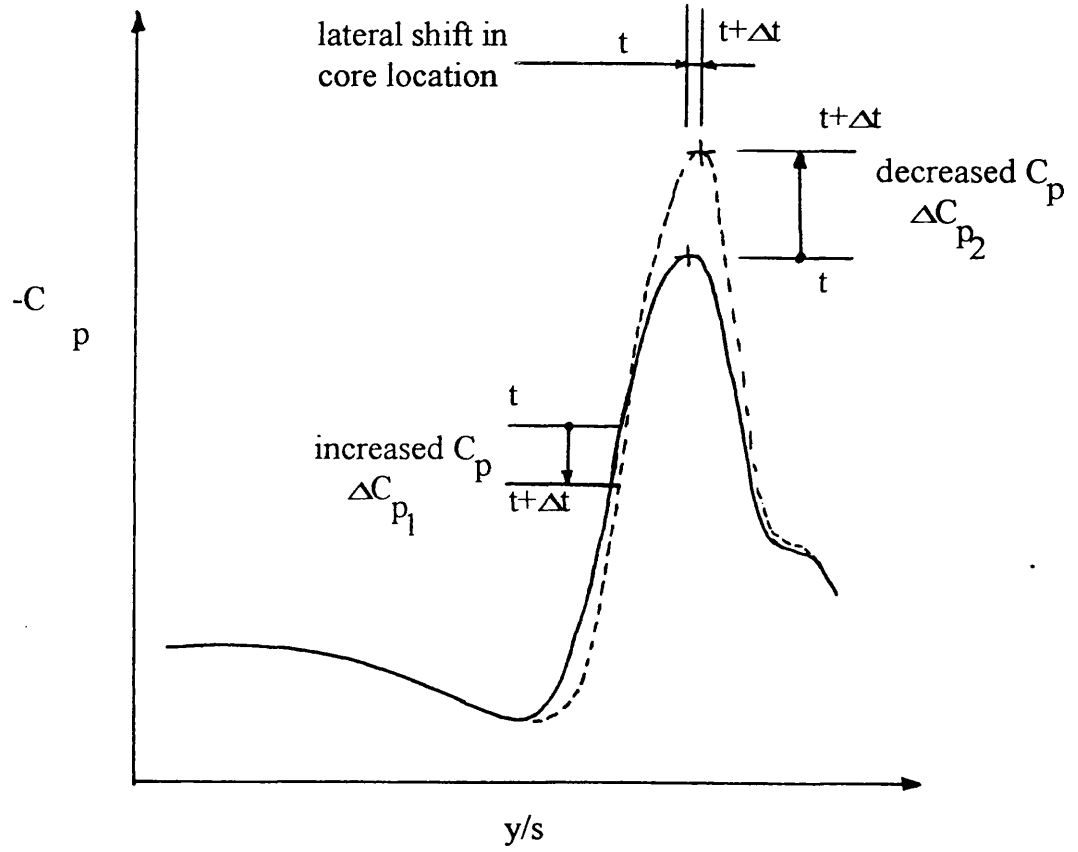

ΔC_{p_1} and ΔC_{p_2} are opposite in sign and thus are different by 180° in phase angle

——— time t

----- time t + Δt

Fig. 7.2 - Schematic representation of spanwise pressure distributions at two points during the oscillation cycle

$\alpha = 10°$, $\nu = 0.64$, mean $\eta = 0°$

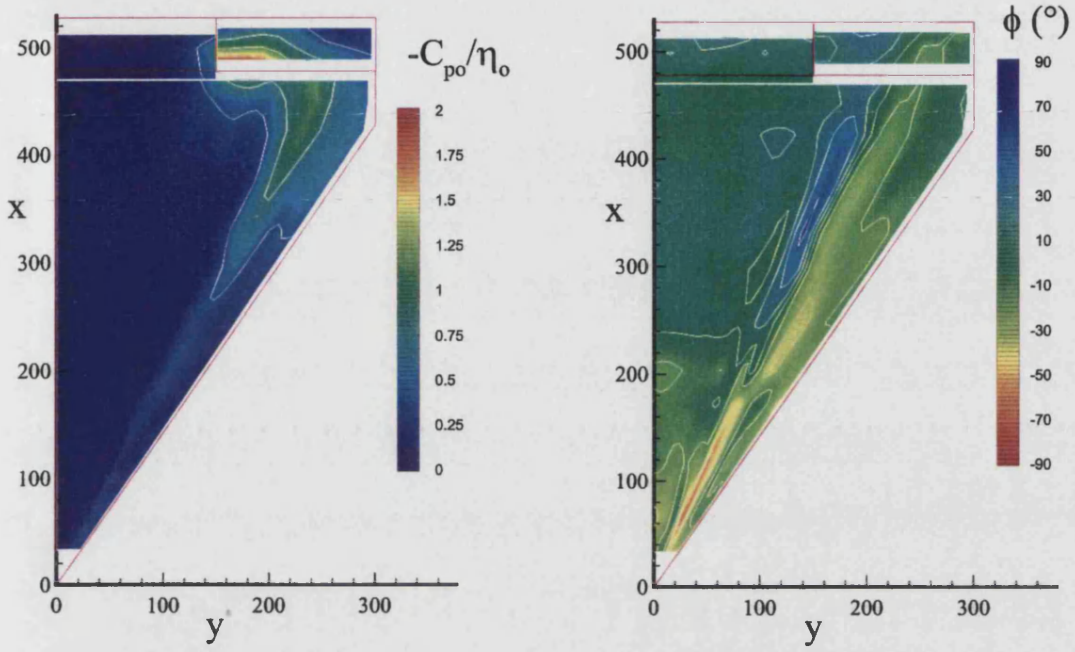

$\alpha = 10°$, $\nu = 0.98$, mean $\eta = 0°$

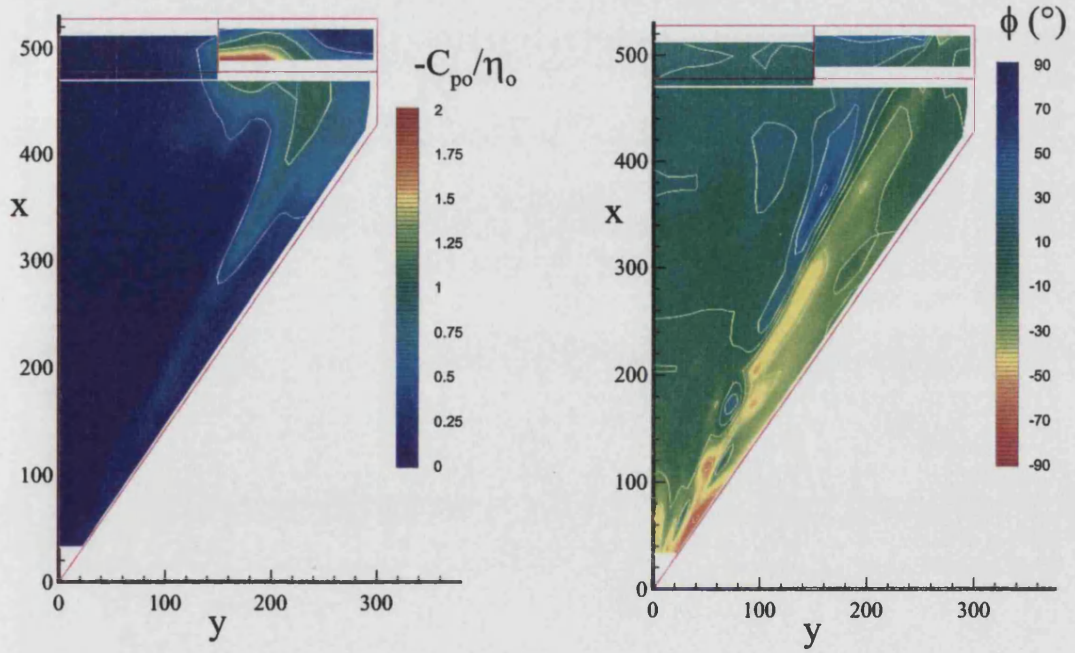

Fig. 7.3 - Upper surface unsteady pressure contours, ν= 0.64 and 0.98, α= 10°

$\alpha = 10°$, $\nu = 1.31$, mean $\eta = 0°$

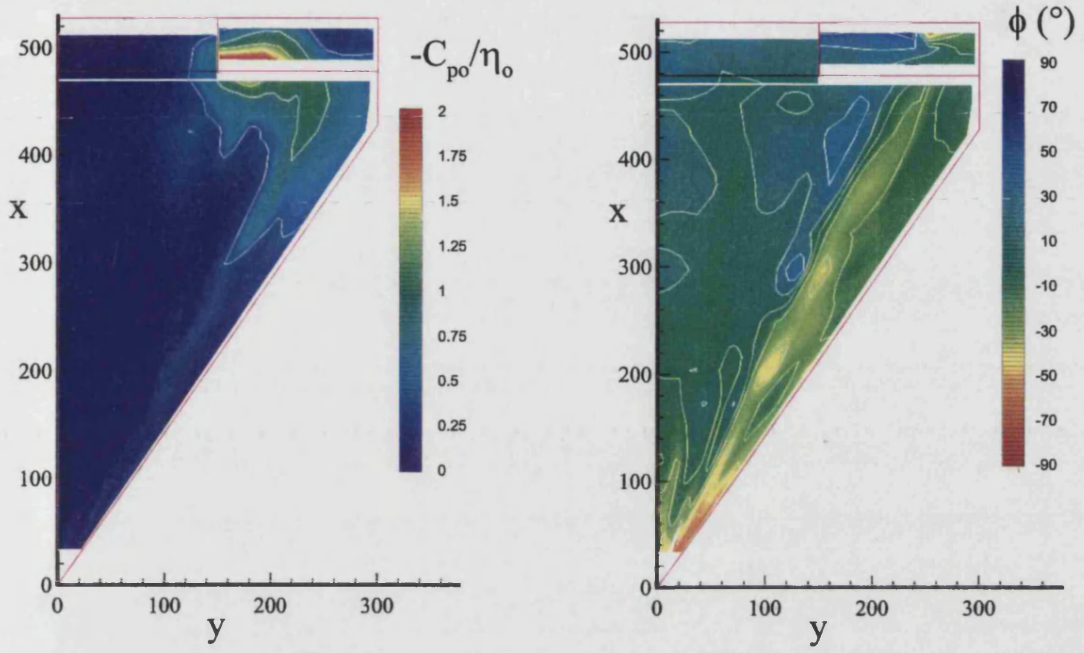

$\alpha = 10°$, $\nu = 1.65$, mean $\eta = 0°$

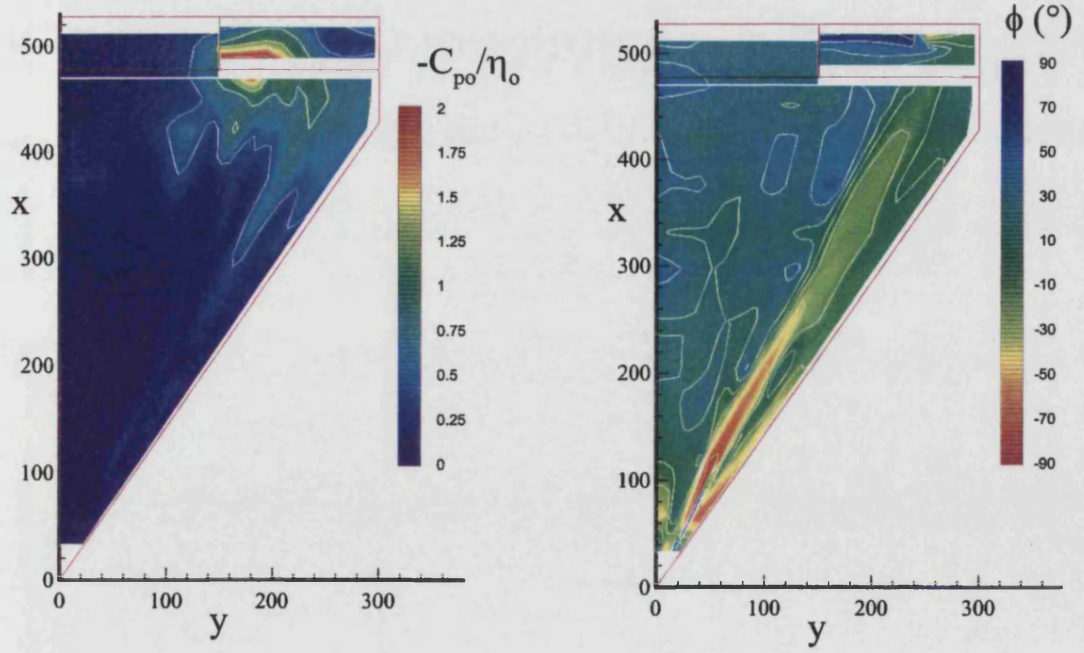

Fig. 7.4 - Upper surface unsteady pressure contours, ν= 1.31 and 1.65, α= 10°

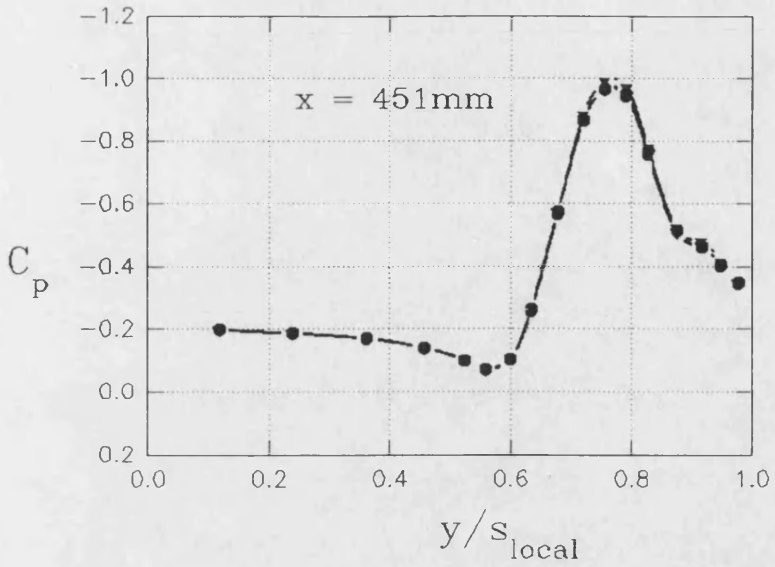

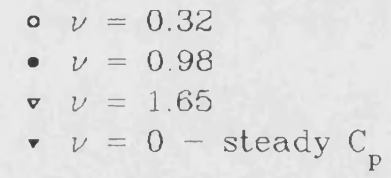

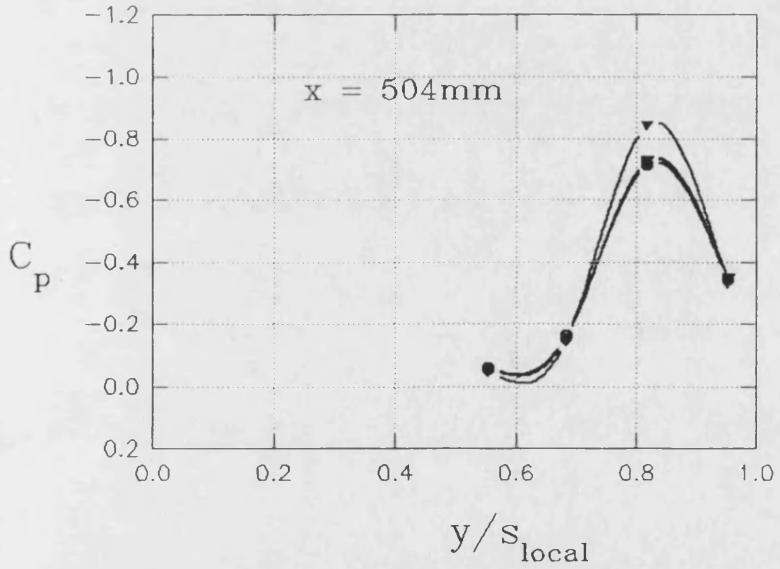

Fig. 7.5 - Comparison of mean pressures from steady and oscillatory tests at $\alpha = 10°$

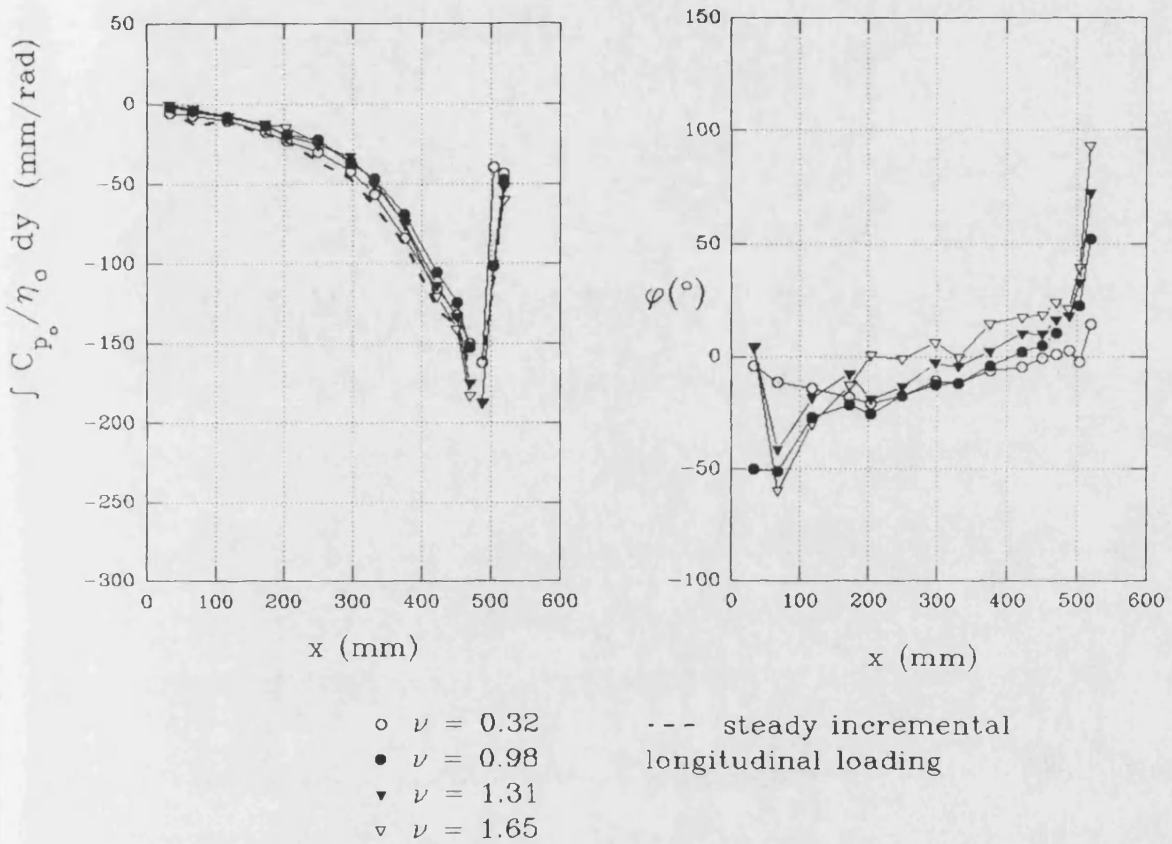

Fig. 7.6 - Unsteady, upper surface, longitudinal loadings, $\alpha = 10°$

$\alpha = 10°$, $\nu = 0.32$, mean $\eta = 0°$

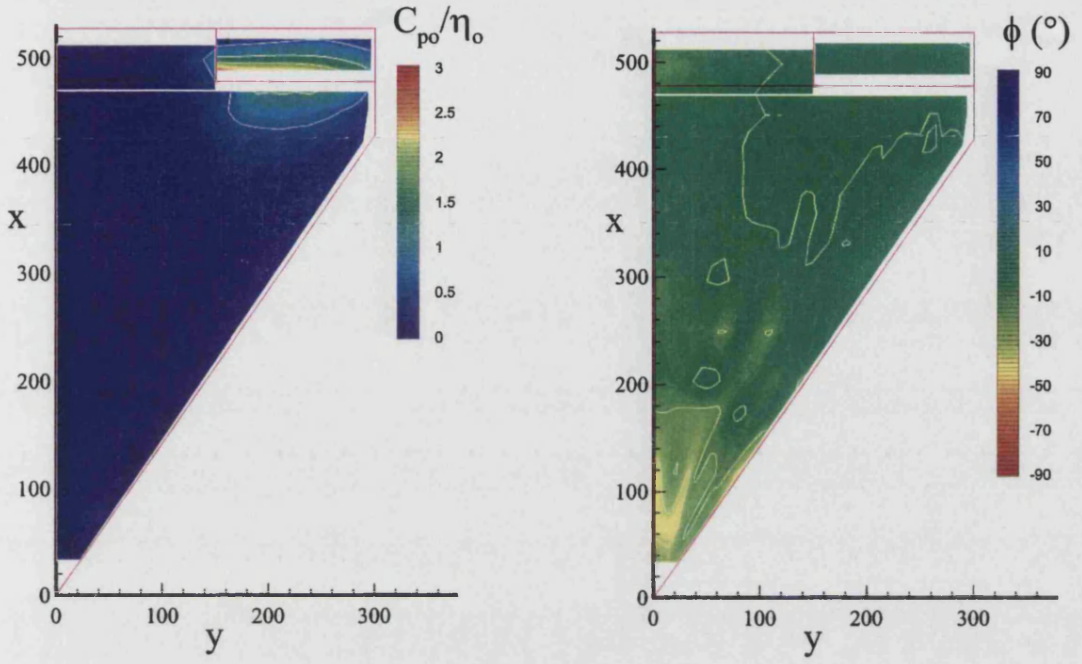

Steady increments, mean $\eta = 0°$

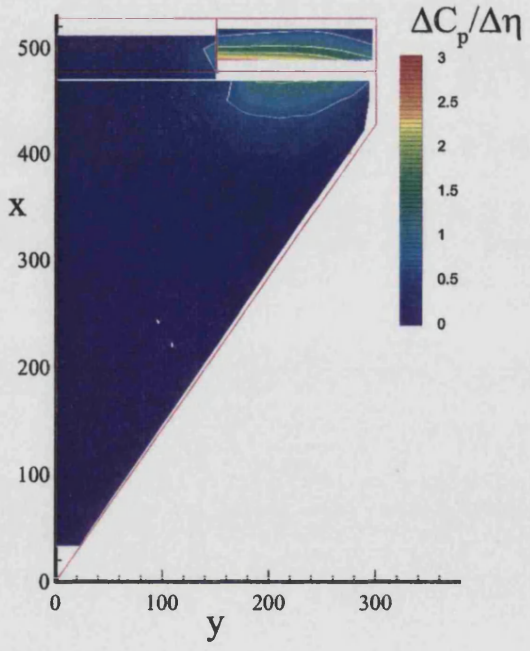

Fig. 7.7 - Lower surface unsteady pressure contours, $\nu = 0.32$, and steady incremental contours, $\alpha = 10°$

$\alpha = 10°$, $\nu = 0.64$, mean $\eta = 0°$

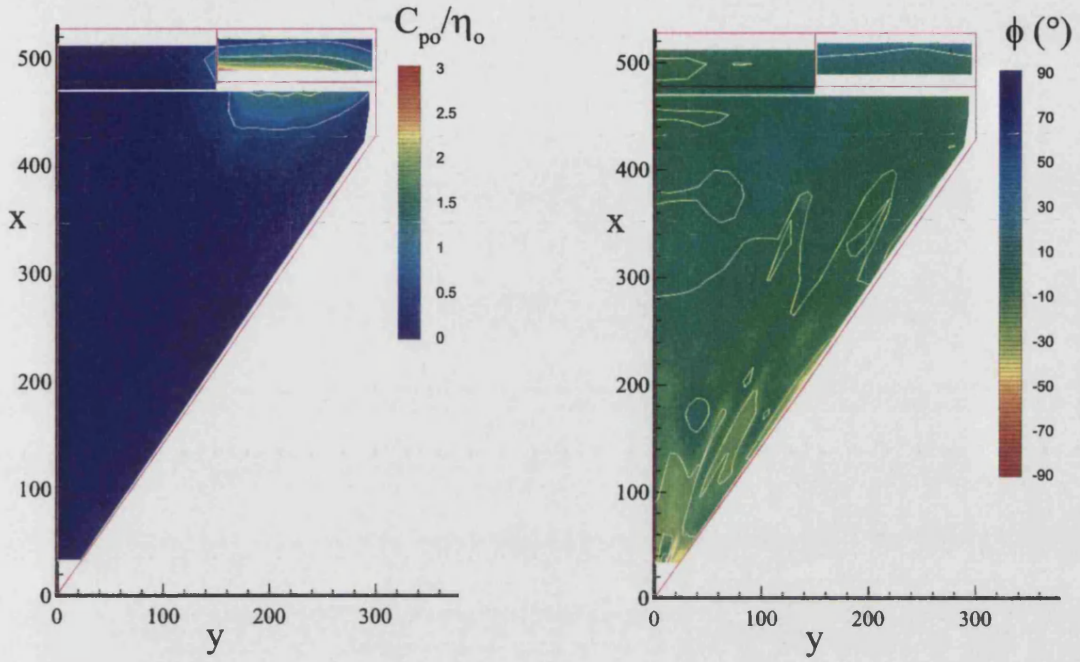

$\alpha = 10°$, $\nu = 0.98$, mean $\eta = 0°$

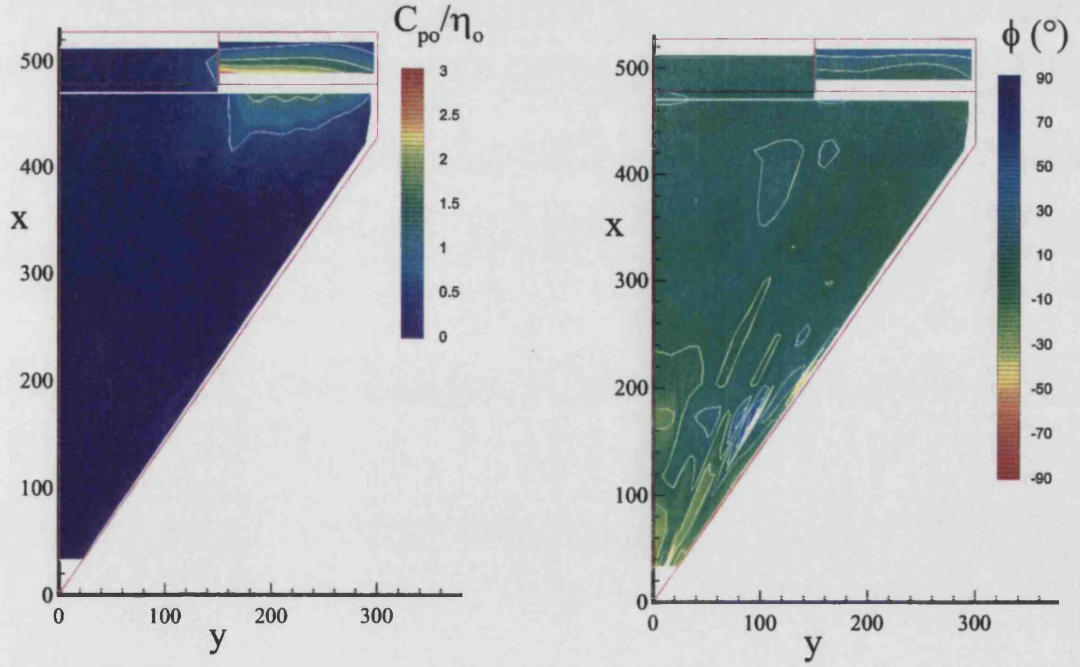

Fig. 7.8 - Lower surface unsteady pressure contours, ν= 0.64 and 0.98, α= 10°

$\alpha = 10°$, $\nu = 1.31$, mean $\eta = 0°$

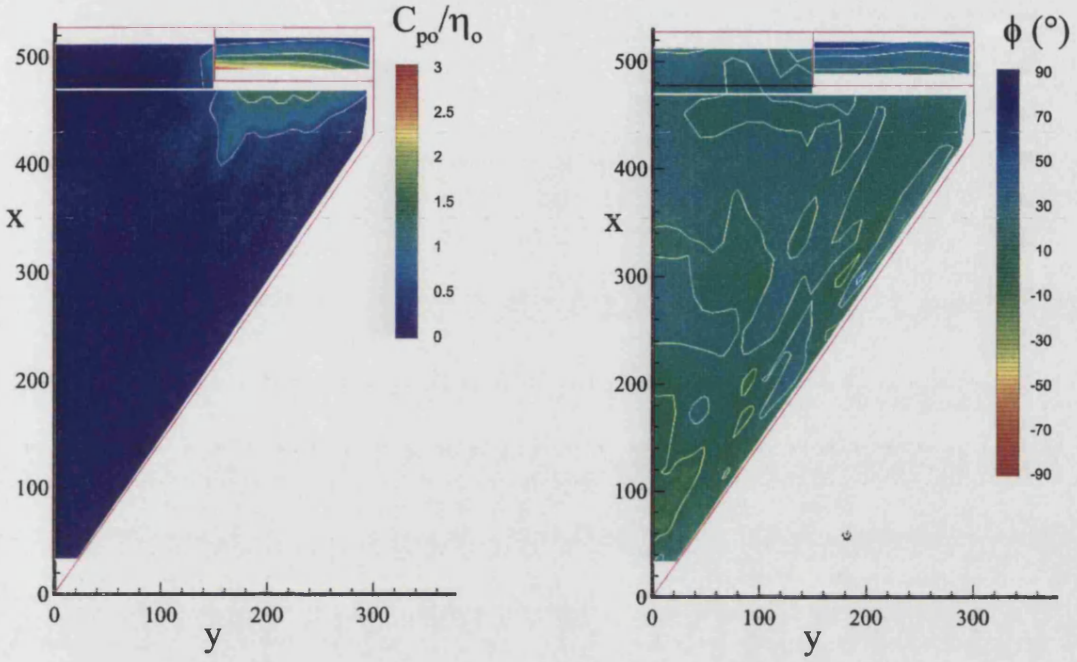

$\alpha = 10°$, $\nu = 1.65$, mean $\eta = 0°$

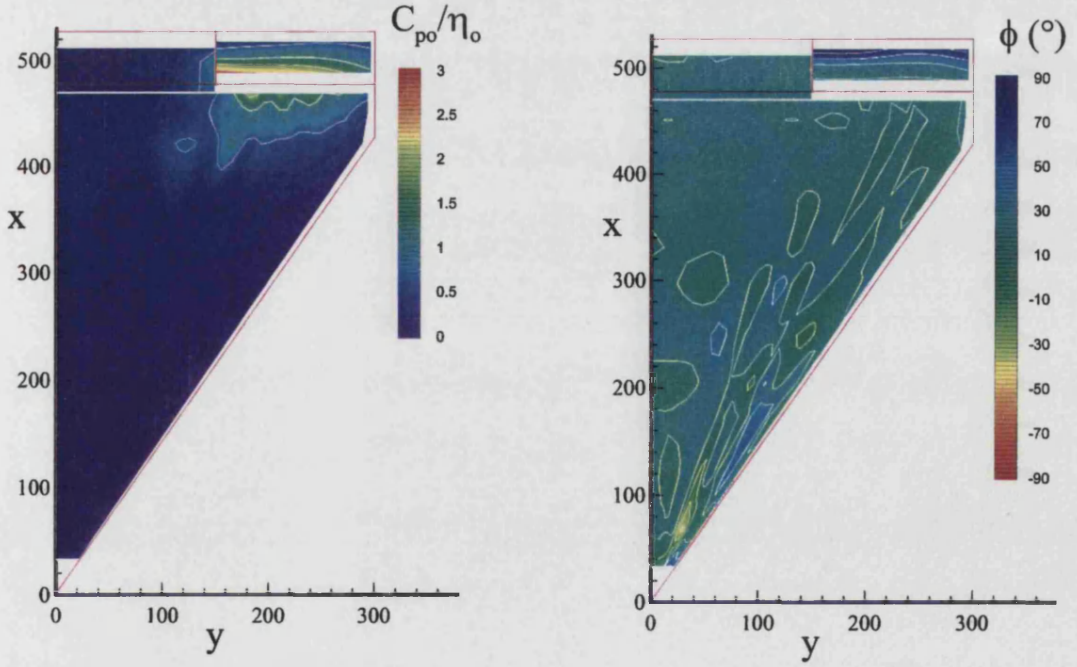

Fig. 7.9 - Lower surface unsteady pressure contours, ν= 1.31 and 1.65, α= 10°

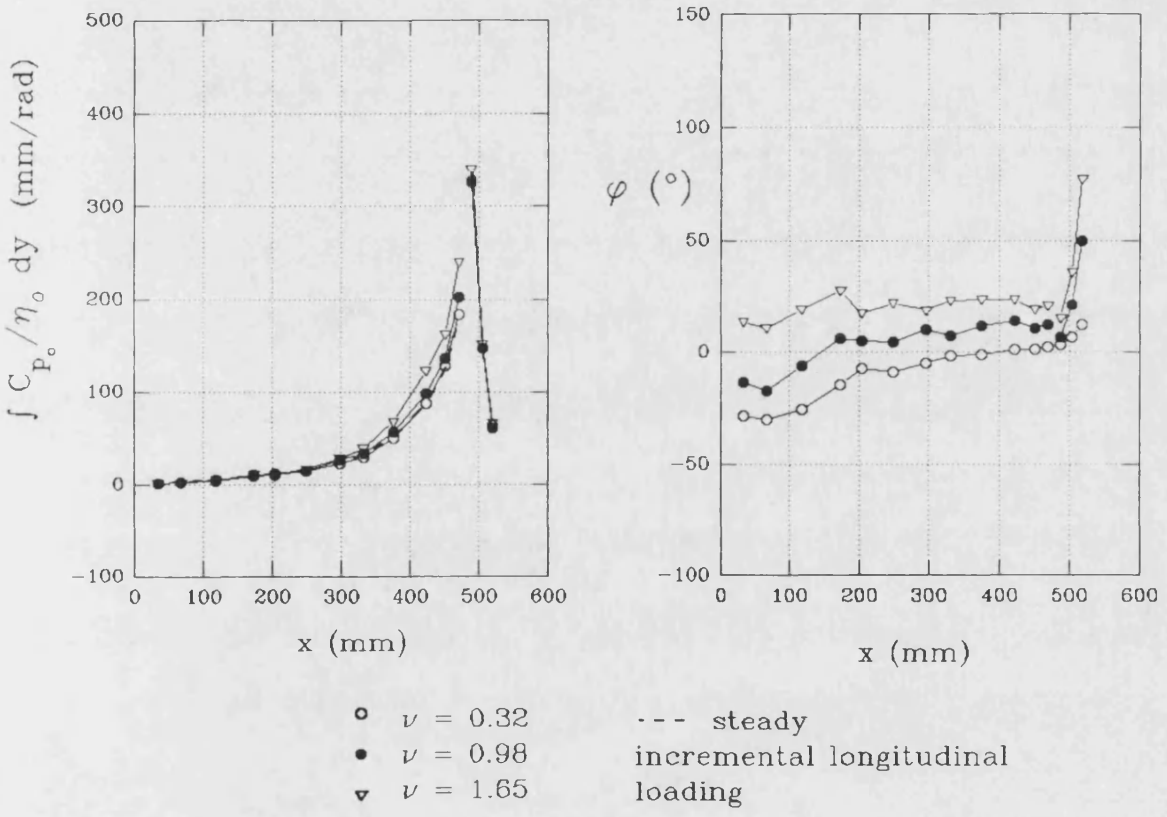

Fig. 7.10 - Unsteady, lower surface, longitudinal loadings, α= 10°

$\alpha = 12.5°$, $\nu = 0.32$, mean $\eta = 0°$

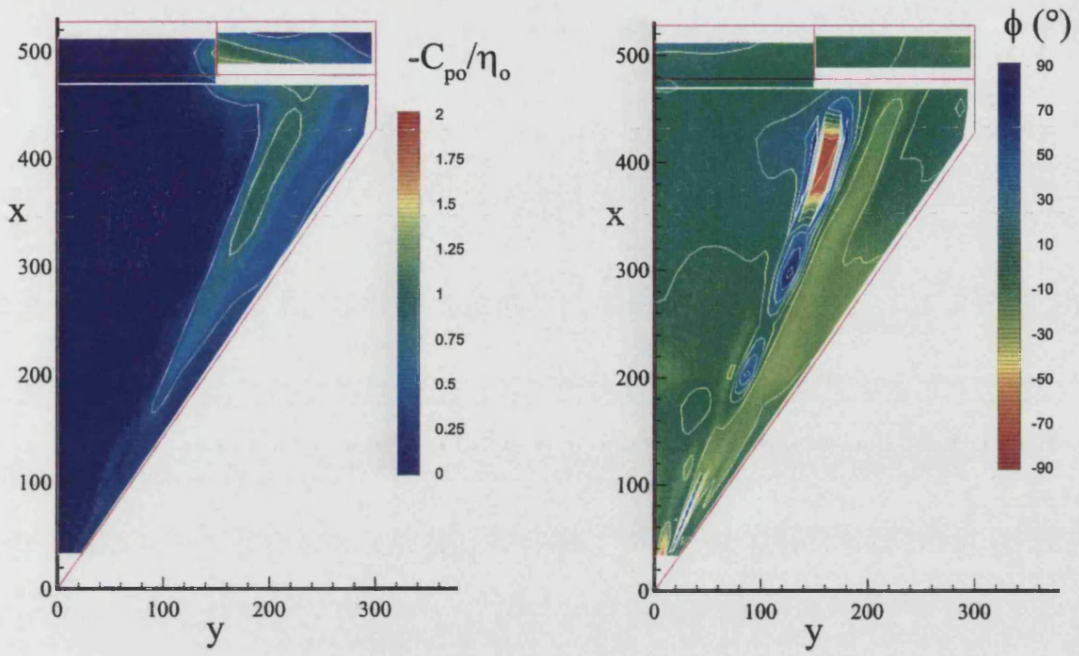

Steady Increments, mean $\eta = 0°$

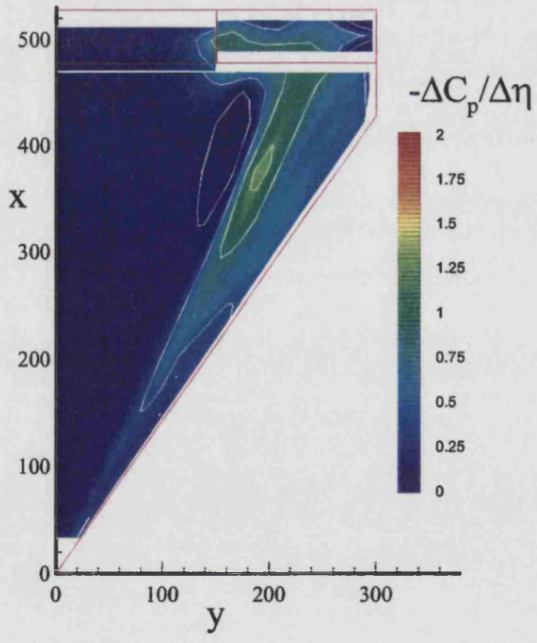

Fig. 7.11 - Upper surface unsteady pressure contours, $\nu = 0.32$, and steady incremental contours, $\alpha = 12.5°$

$\alpha = 12.5°$, $\nu = 0.64$, mean $\eta = 0°$

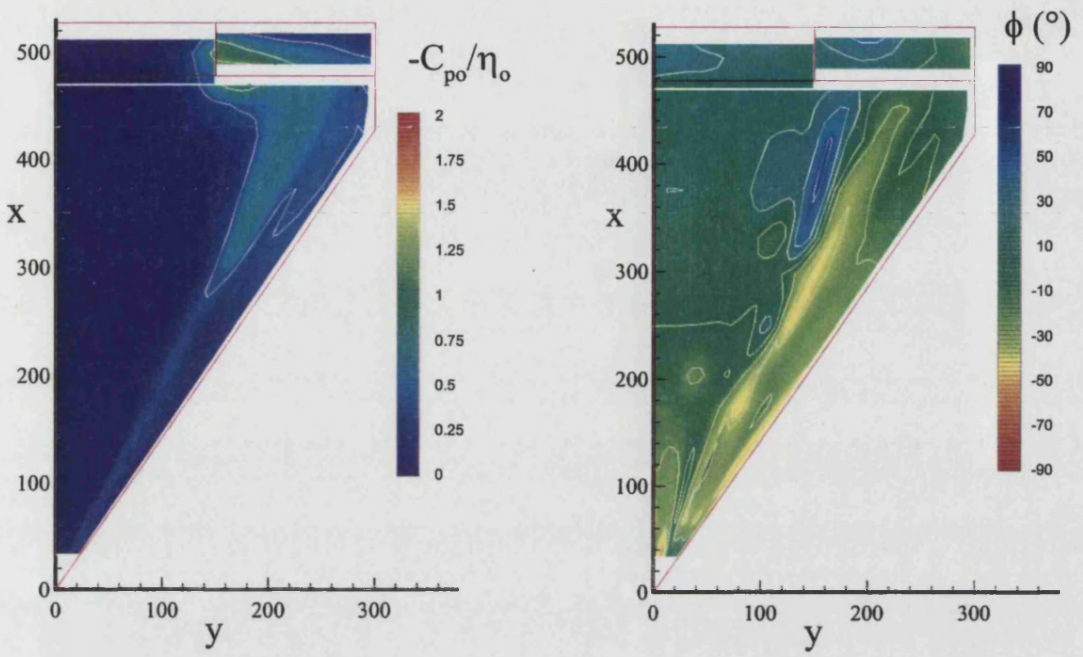

$\alpha = 12.5°$, $\nu = 0.98$, mean $\eta = 0°$

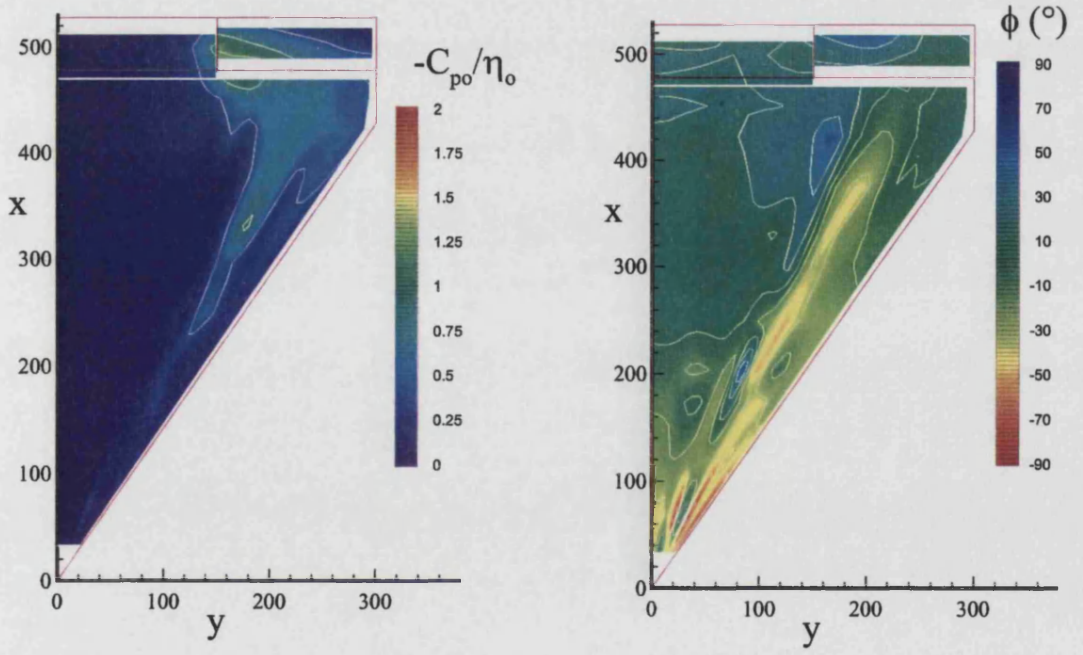

Fig. 7.12 - Upper surface unsteady pressure contours, $\nu = 0.64$ and 0.98, $\alpha = 12.5°$

$\alpha = 12.5°$, $\nu = 1.31$, mean $\eta = 0°$

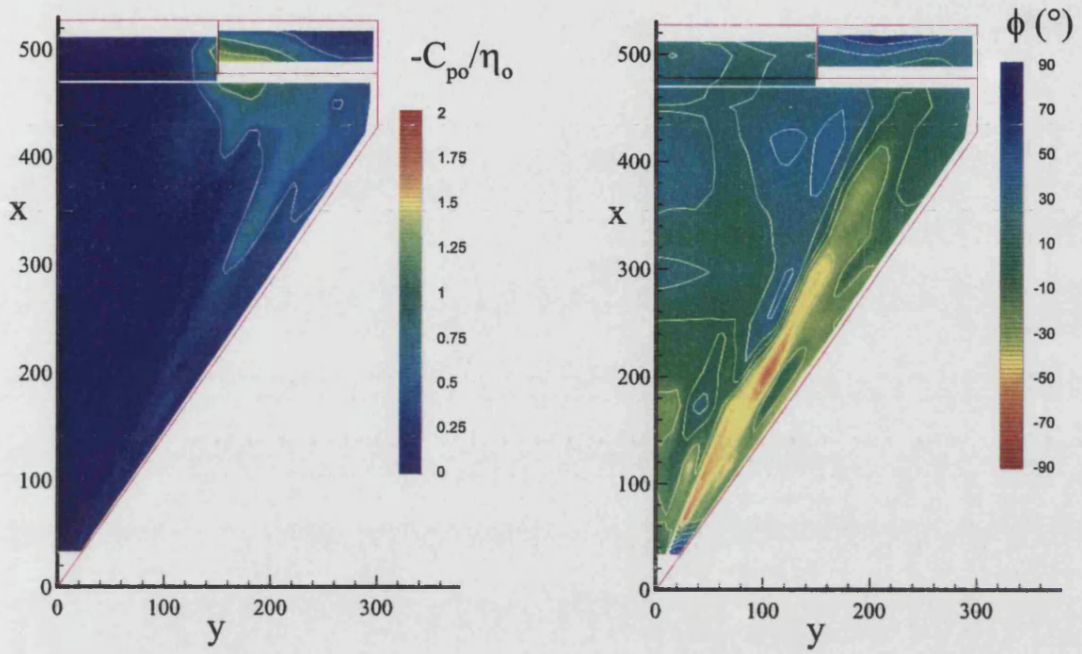

$\alpha = 12.5°$, $\nu = 1.65$, mean $\eta = 0°$

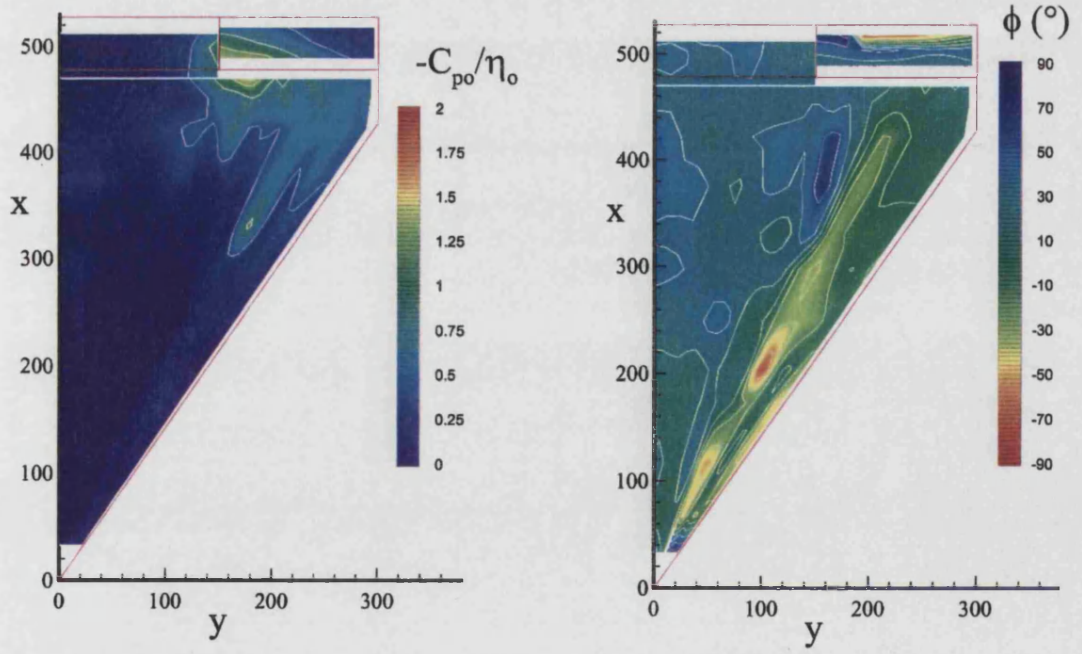

Fig. 7.13 - Upper surface unsteady pressure contours, ν= 1.31 and 1.65, α= 12.5°

$\alpha = 15°$, $\nu = 0.32$, mean $\eta = 0°$

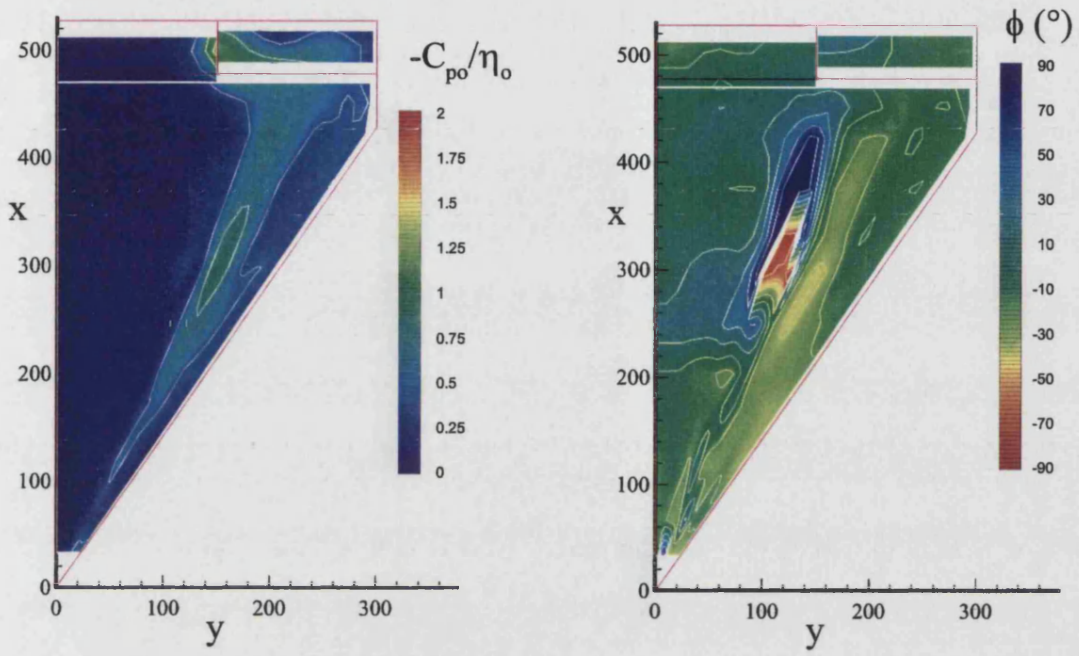

Steady Increments, mean $\eta = 0°$

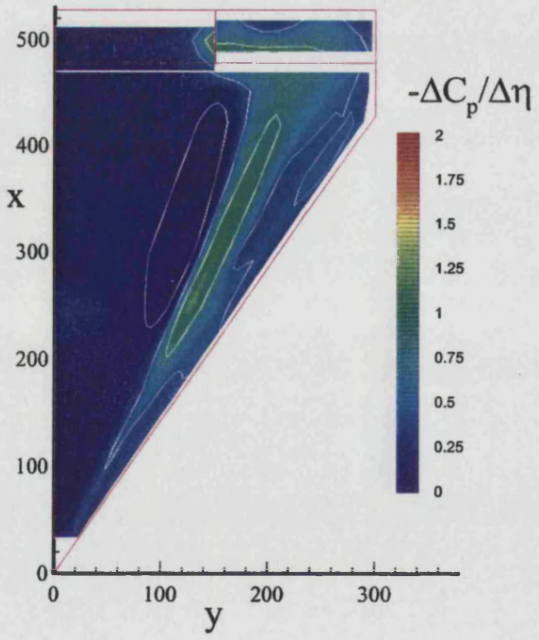

Fig. 7.14 - Upper surface unsteady pressure contours, $\nu = 0.32$, and steady incremental contours, $\alpha = 15°$

$\alpha = 15°$, $\nu = 0.64$, mean $\eta = 0°$

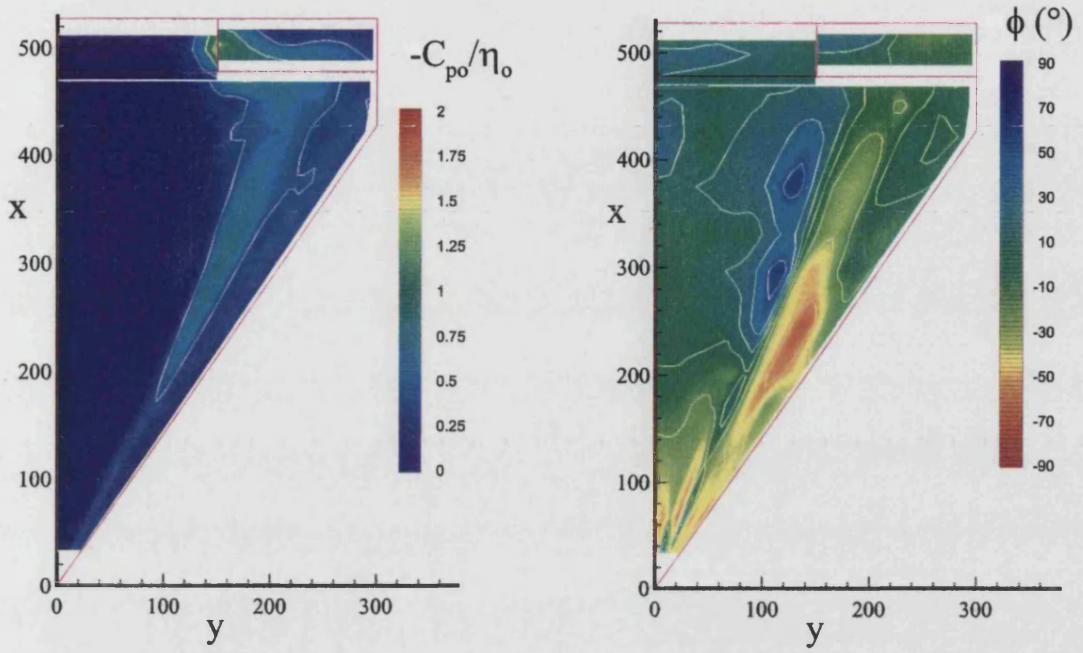

$\alpha = 15°$, $\nu = 0.98$, mean $\eta = 0°$

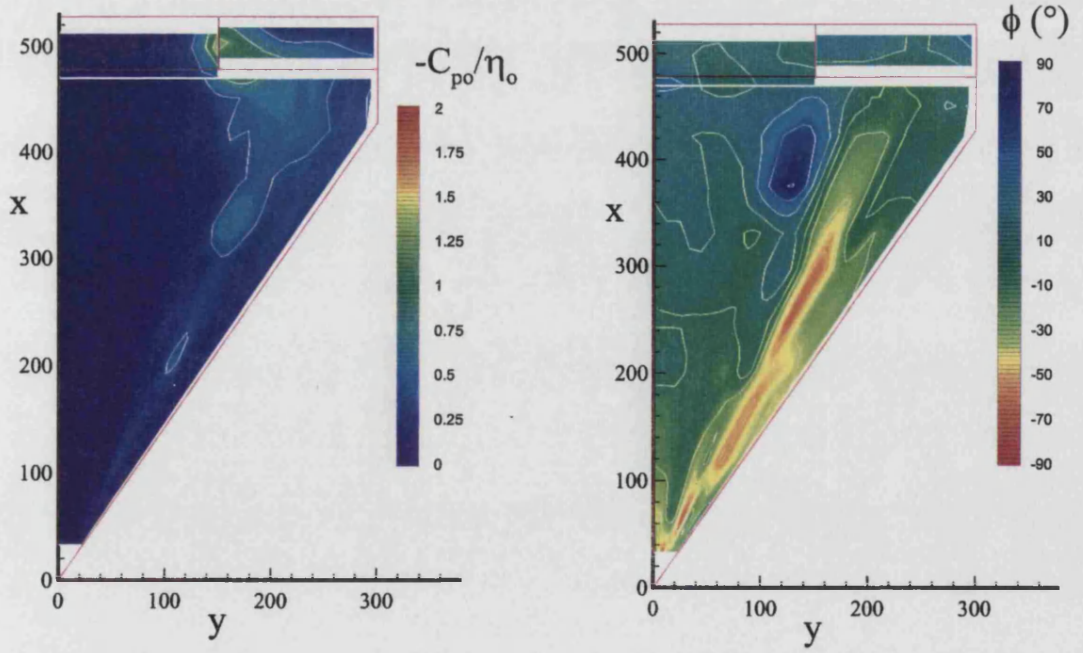

Fig. 7.15 - Upper surface unsteady pressure contours, ν= 0.64 and 0.98, α= 15°

$\alpha = 15°$, $\nu = 1.31$, mean $\eta = 0°$

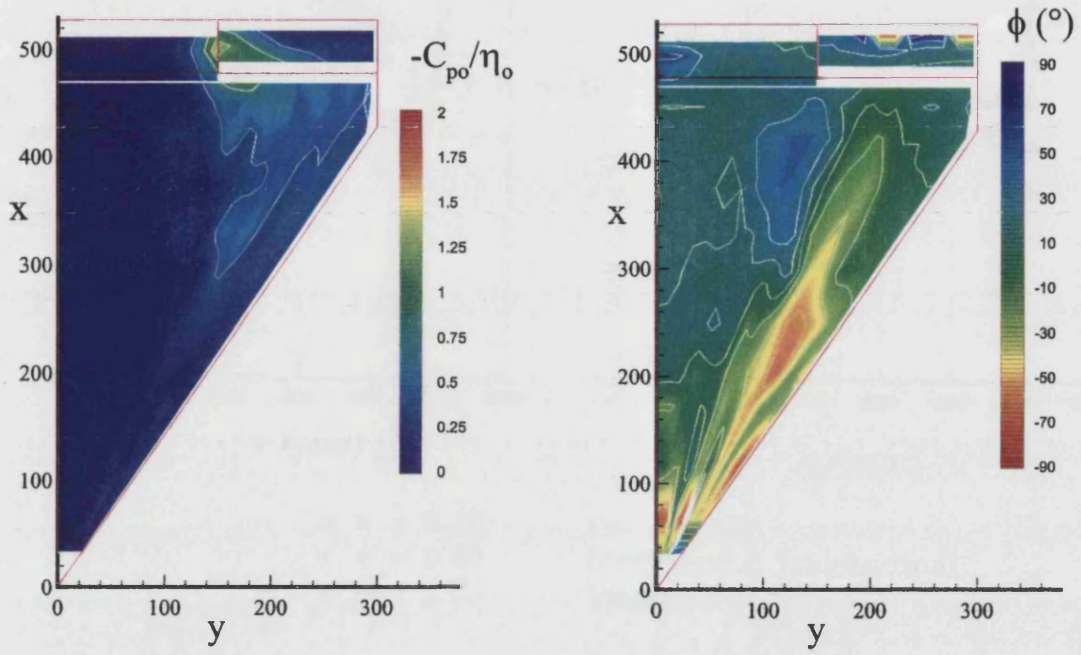

$\alpha = 15°$, $\nu = 1.65$, mean $\eta = 0°$

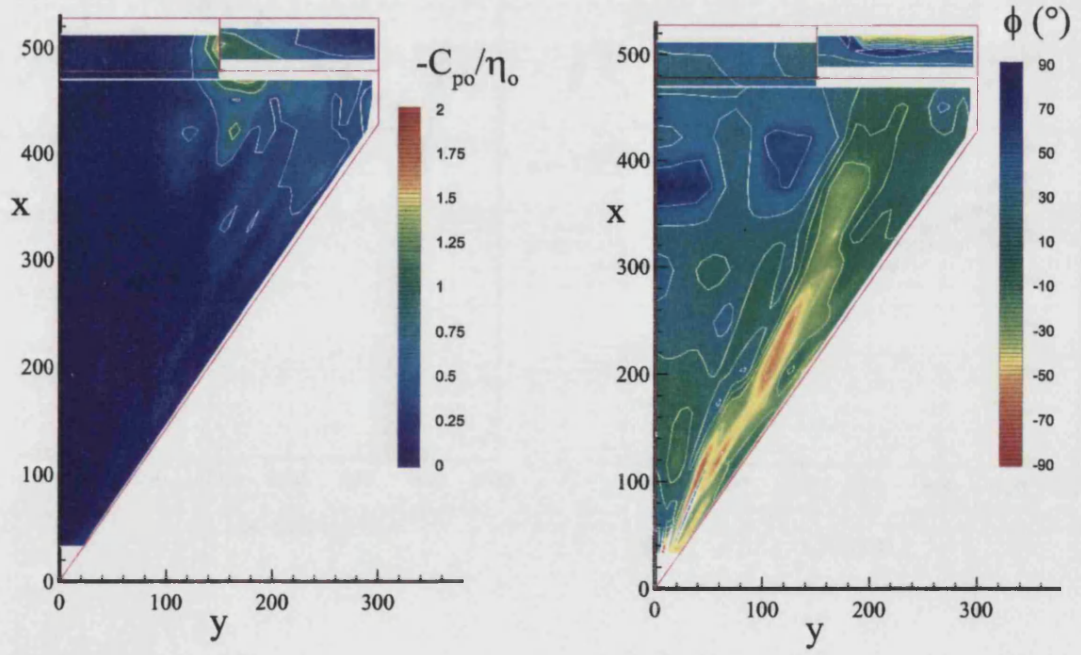

Fig. 7.16 - Upper surface unsteady pressure contours, ν= 1.31 and 1.65, α= 15°

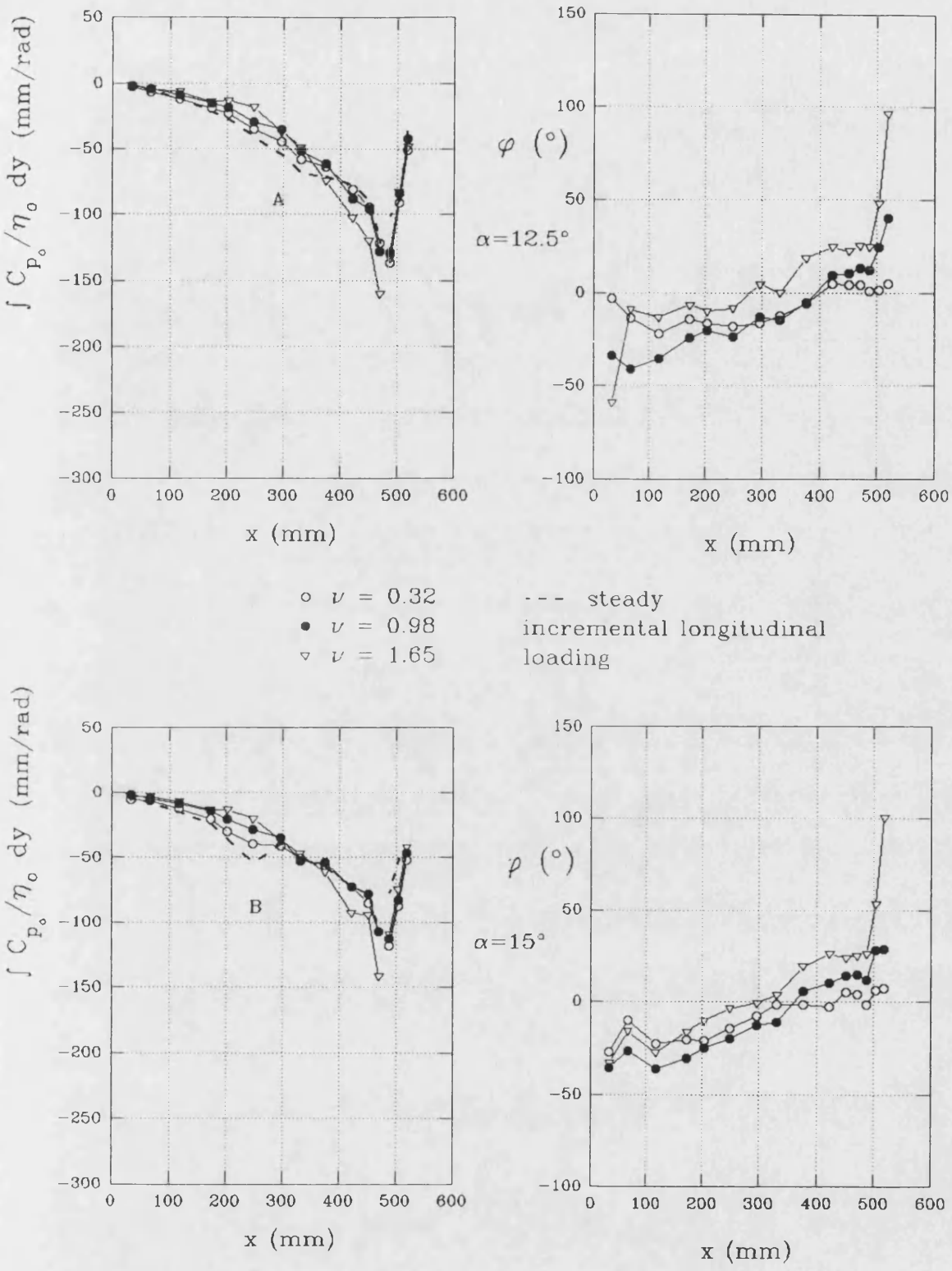

Fig. 7.17 - Unsteady, upper surface, longitudinal loadings, α= 12.5° and 15°

$\alpha = 20°$, $\nu = 0.32$, mean $\eta = 0°$

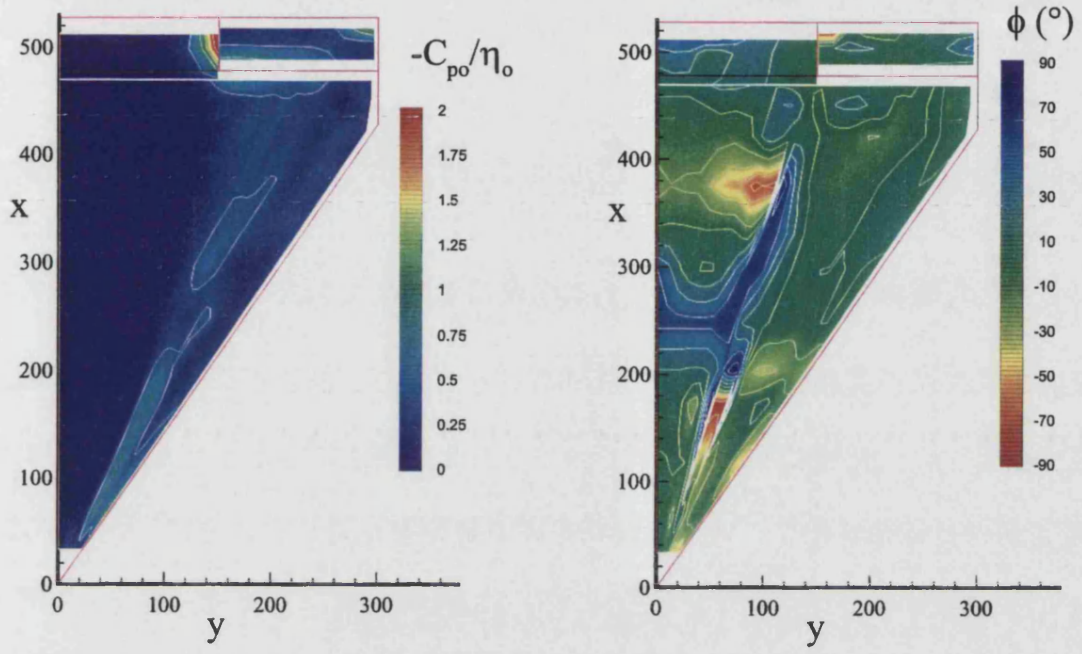

Steady Increments, mean $\eta = 0°$

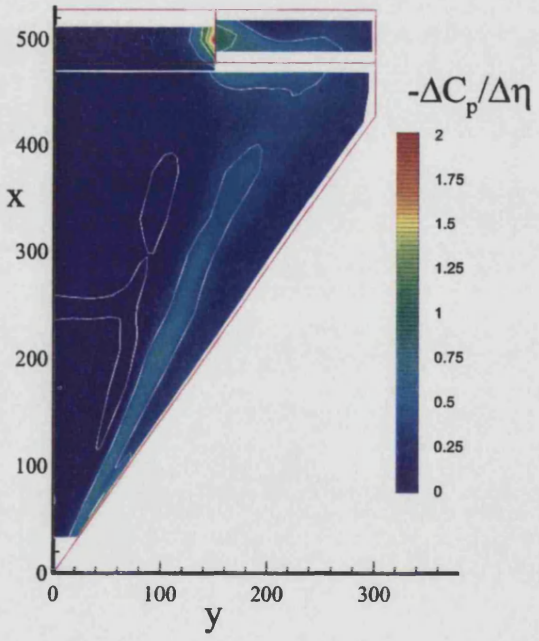

Fig. 7.18 - Upper surface unsteady pressure contours, $\nu = 0.32$, and steady incremental contours, $\alpha = 20°$

$\alpha = 20°$, $\nu = 0.98$, mean $\eta = 0°$

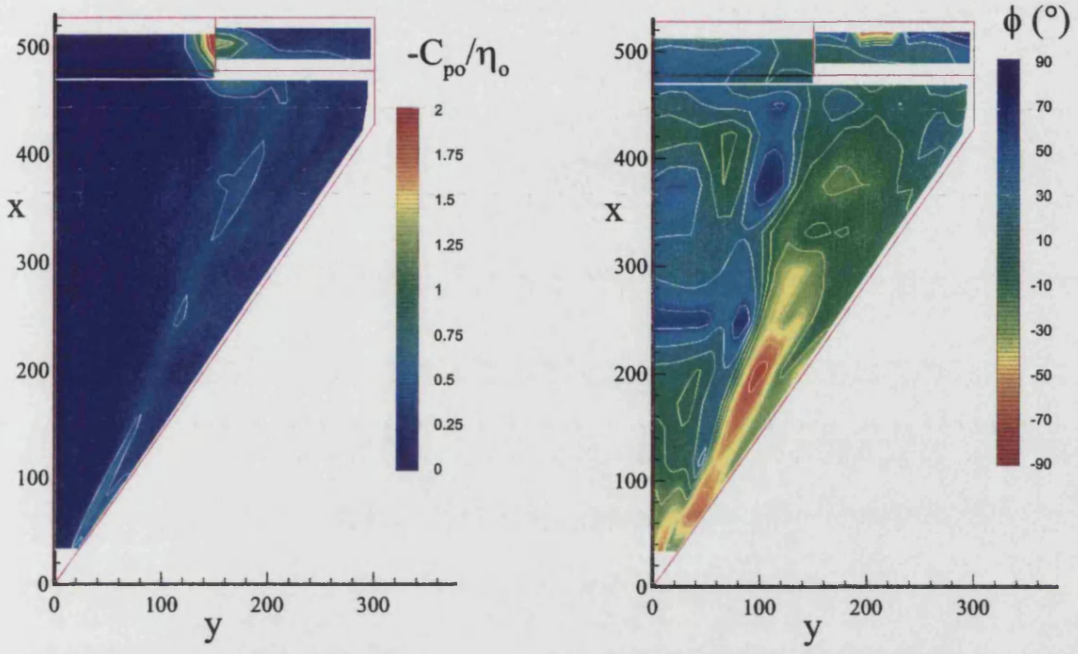

$\alpha = 20°$, $\nu = 1.65$, mean $\eta = 0°$

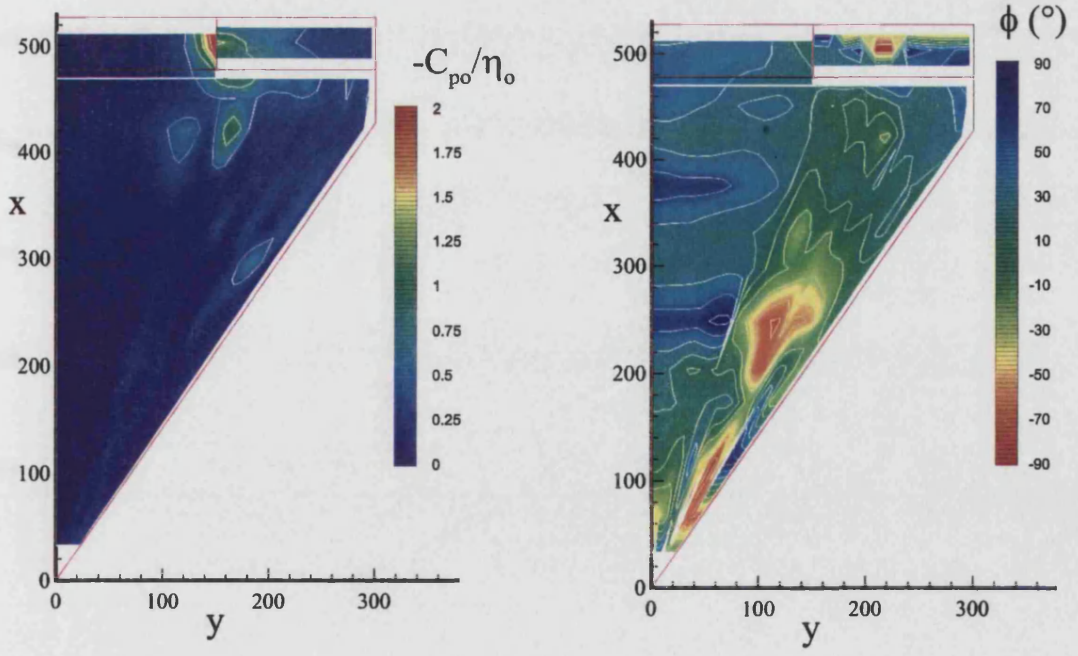

Fig. 7.19 - Upper surface unsteady pressure contours, ν= 0.98 and 1.65, α= 20°

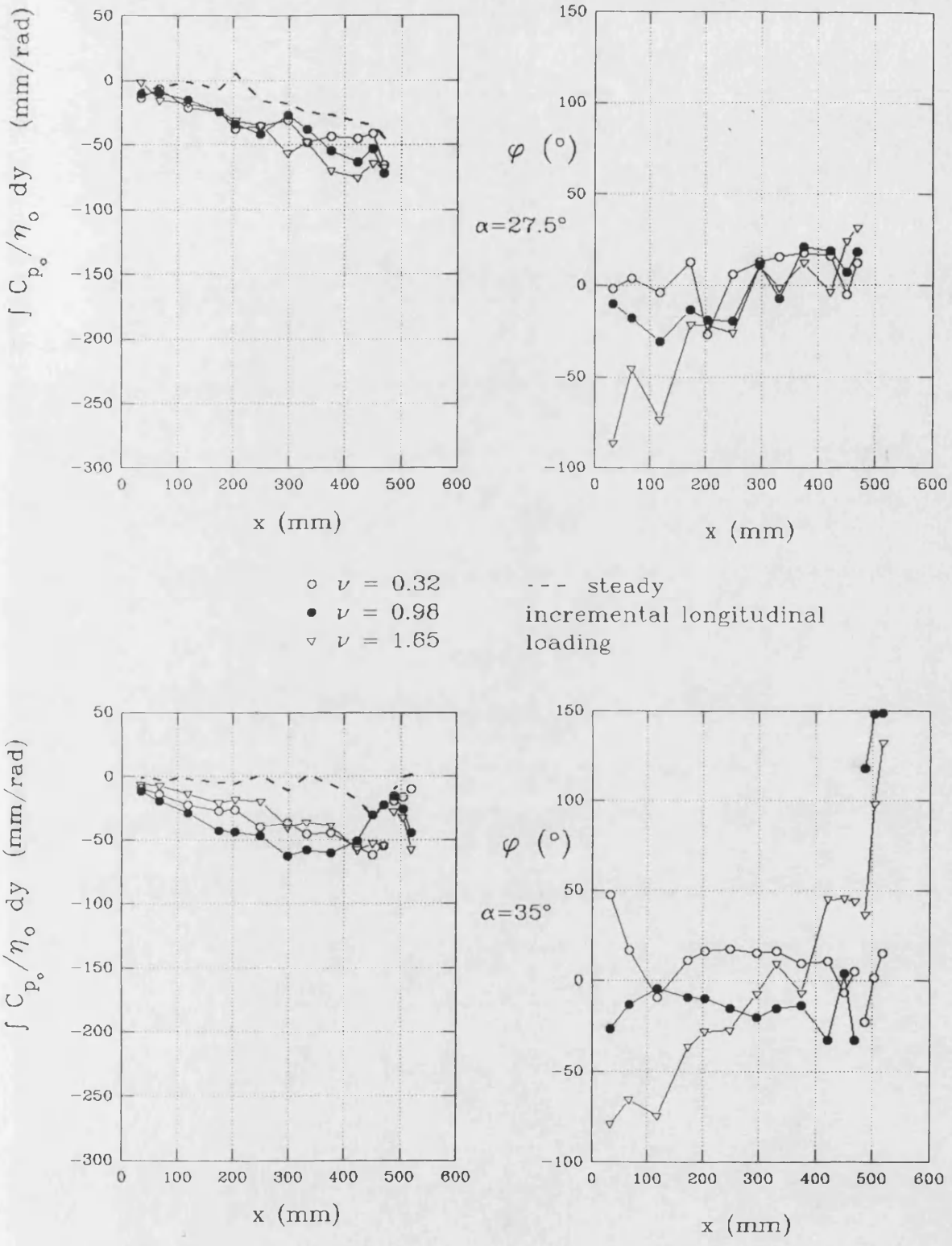

Fig. 7.20 - Unsteady, upper surface, longitudinal loadings, α= 27.5° and 35°

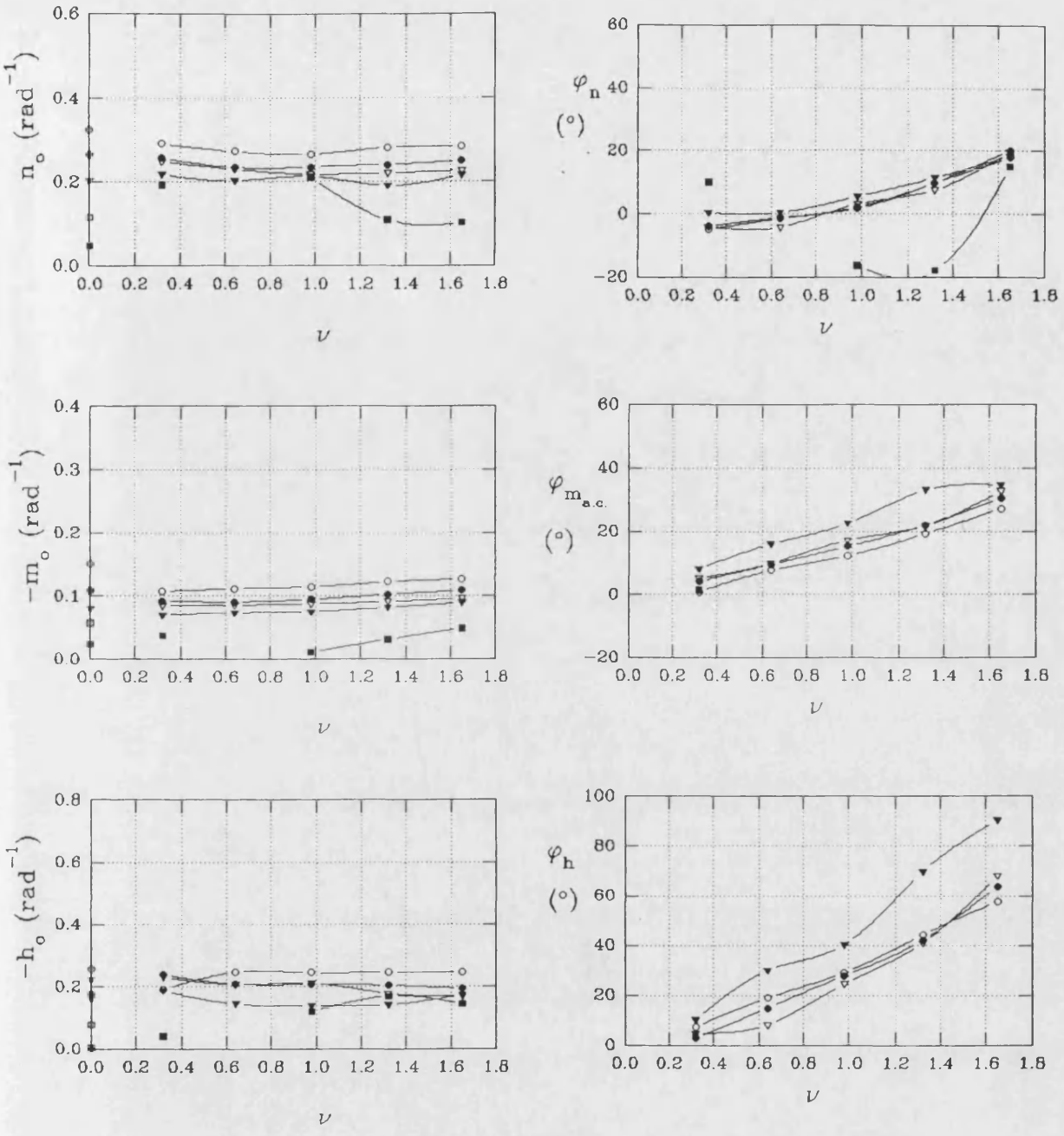

◦ $\alpha = 10°$ ▾ $\alpha = 20°$
• $\alpha = 12.5°$ ▫ $\alpha = 27.5°$
▿ $\alpha = 15°$ ▪ $\alpha = 35°$

Fig. 7.21 - Upper surface contributions to unsteady normal force, pitching moment and hinge moment, mean $\eta = 0°$

$\alpha = 15°$, $\nu = 1.65$, mean $\eta = 0°$

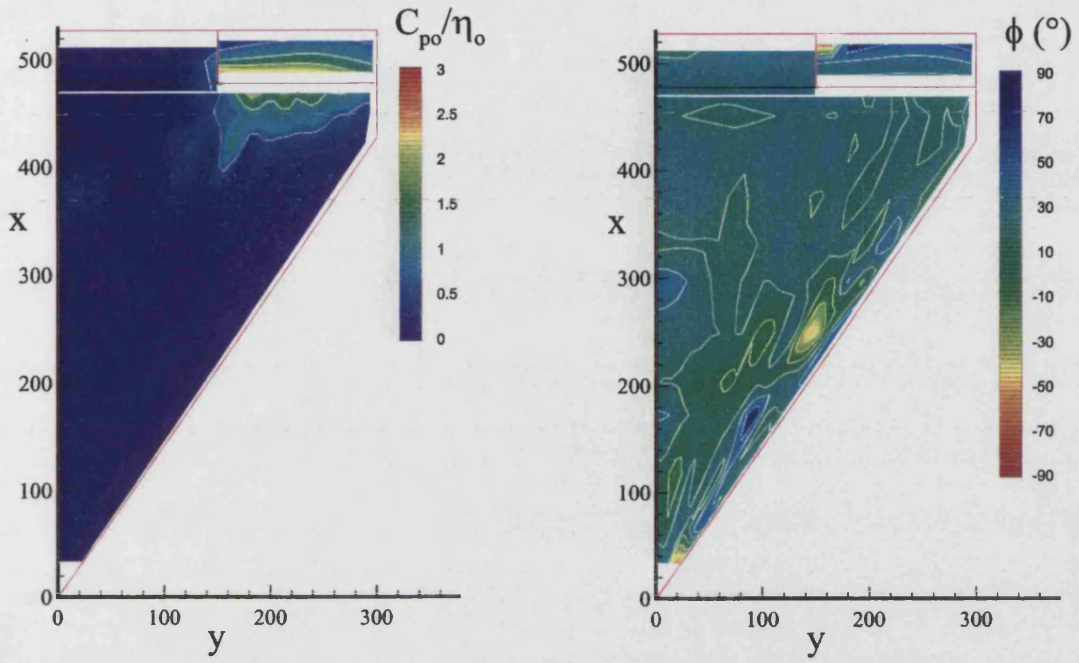

$\alpha = 35°$, $\nu = 1.65$, mean $\eta = 0°$

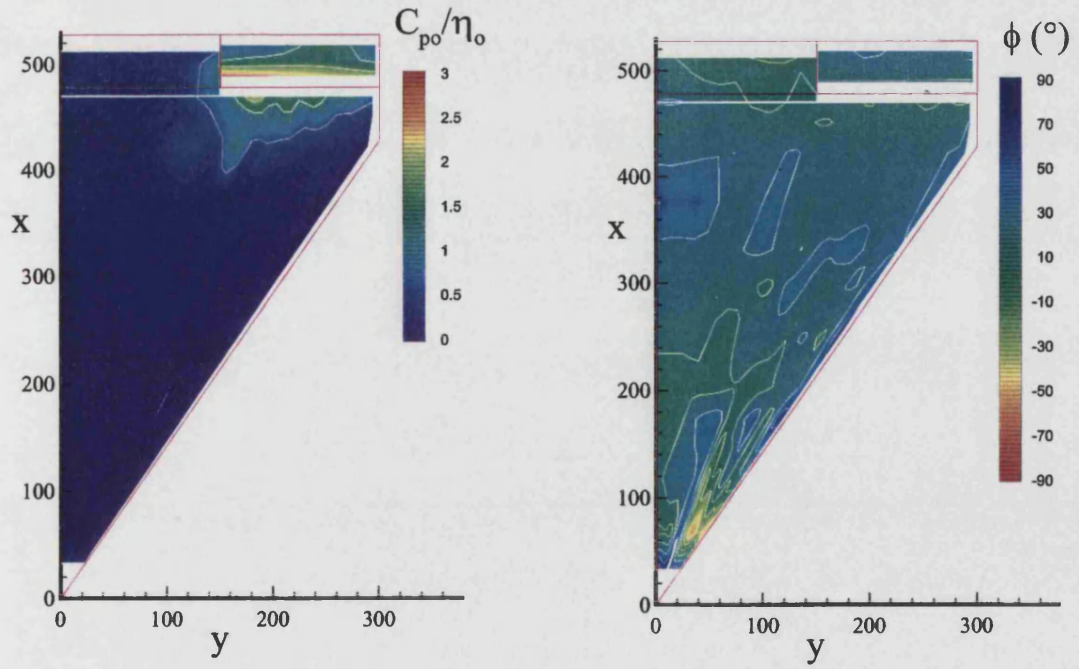

Fig. 7.22 - Comparison of lower surface, unsteady pressure contours at $\alpha = 15°$ and $35°$, for $\nu = 1.65$, mean $\eta = 0°$

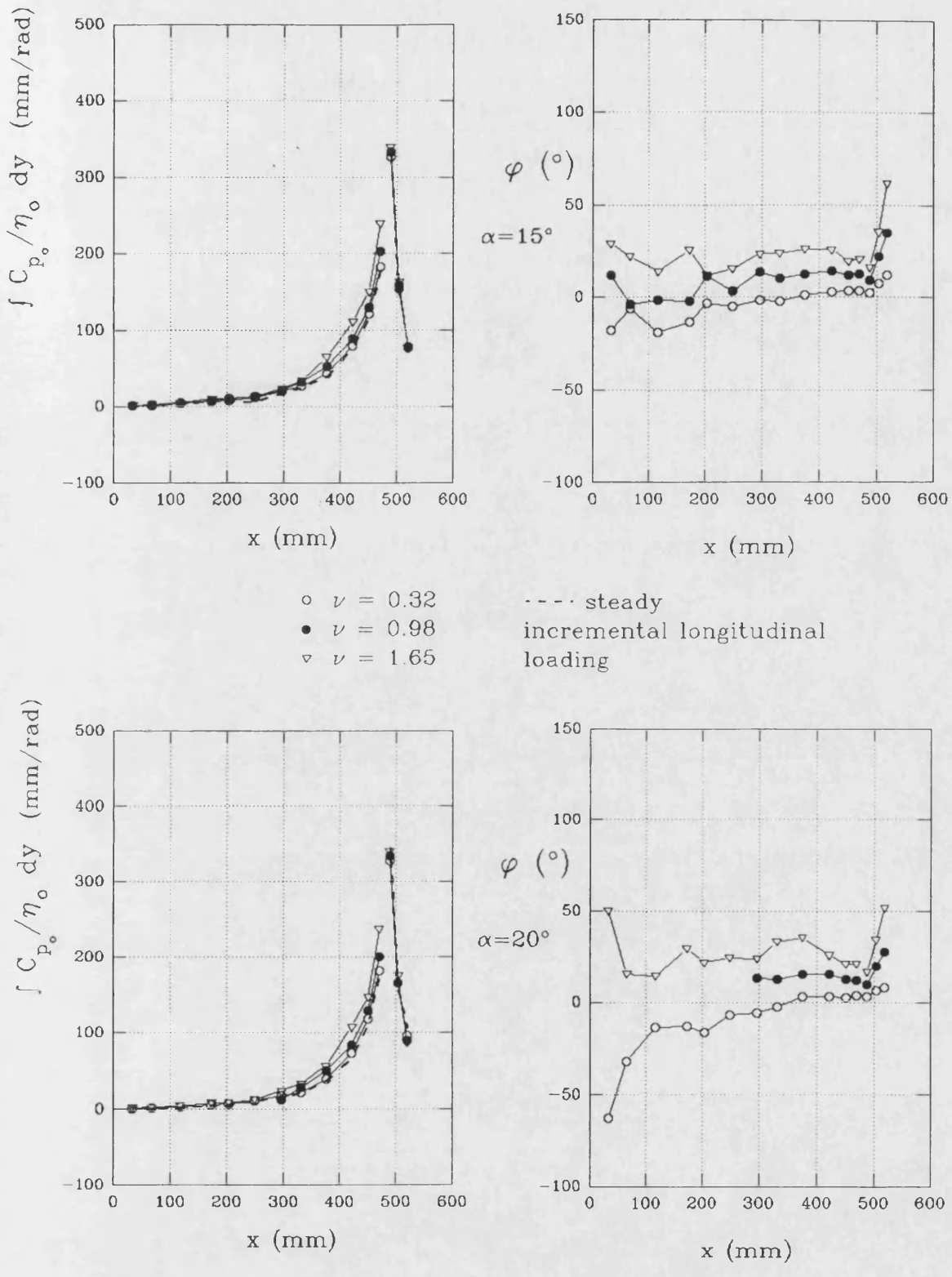

Fig. 7.23 - Unsteady, lower surface, longitudinal loadings, α= 15° and 20°, mean η= 0°

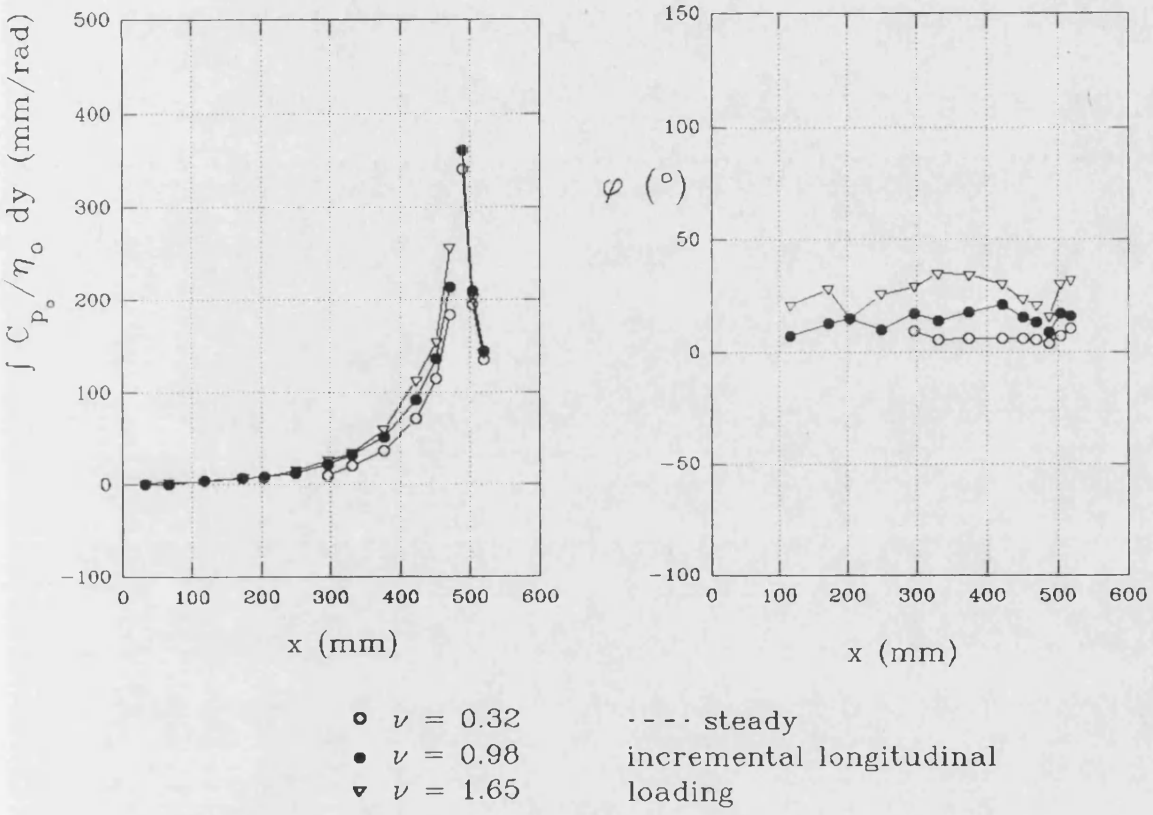

Fig. 7.24 - Unsteady, lower surface, longitudinal loadings, α= 35°, mean η= 0°

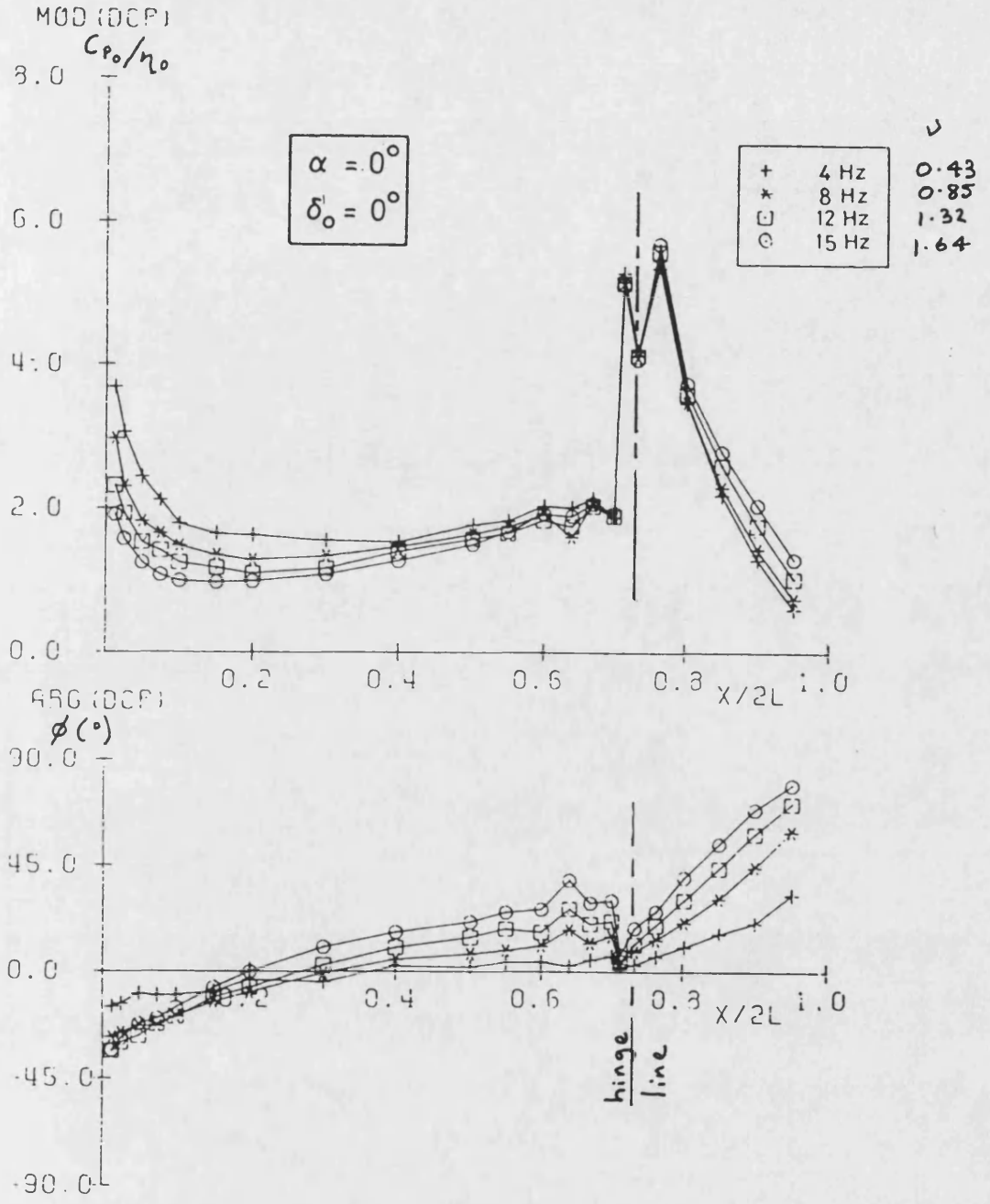

Fig. 7.25 - Unsteady pressure variations with frequency, on a 2-d section, Kienappel and Round [1980]

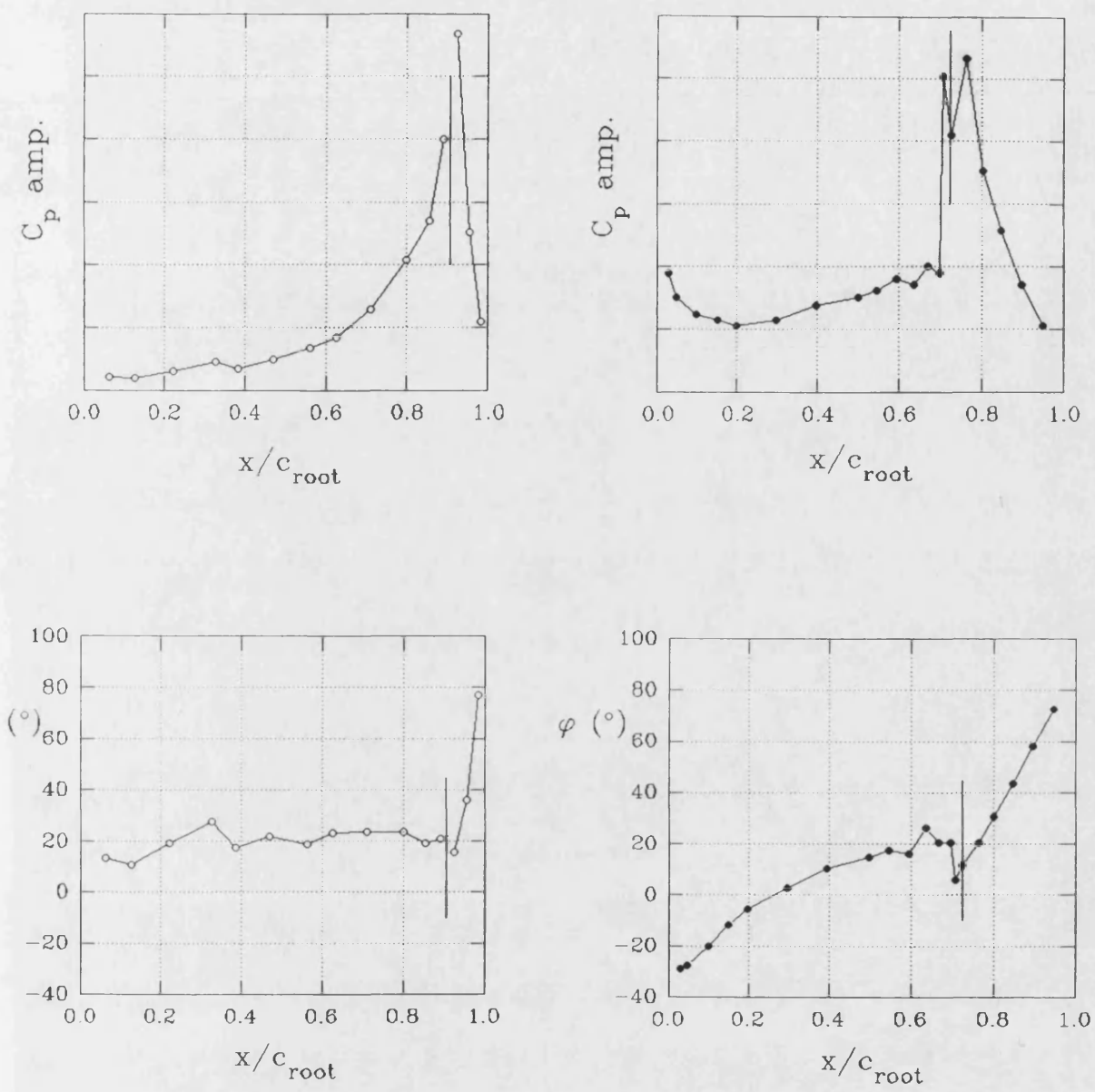

Fig. 7.26 - Comparison of lower surface delta wing unsteady pressures and results from Kienappel and Round [1980]

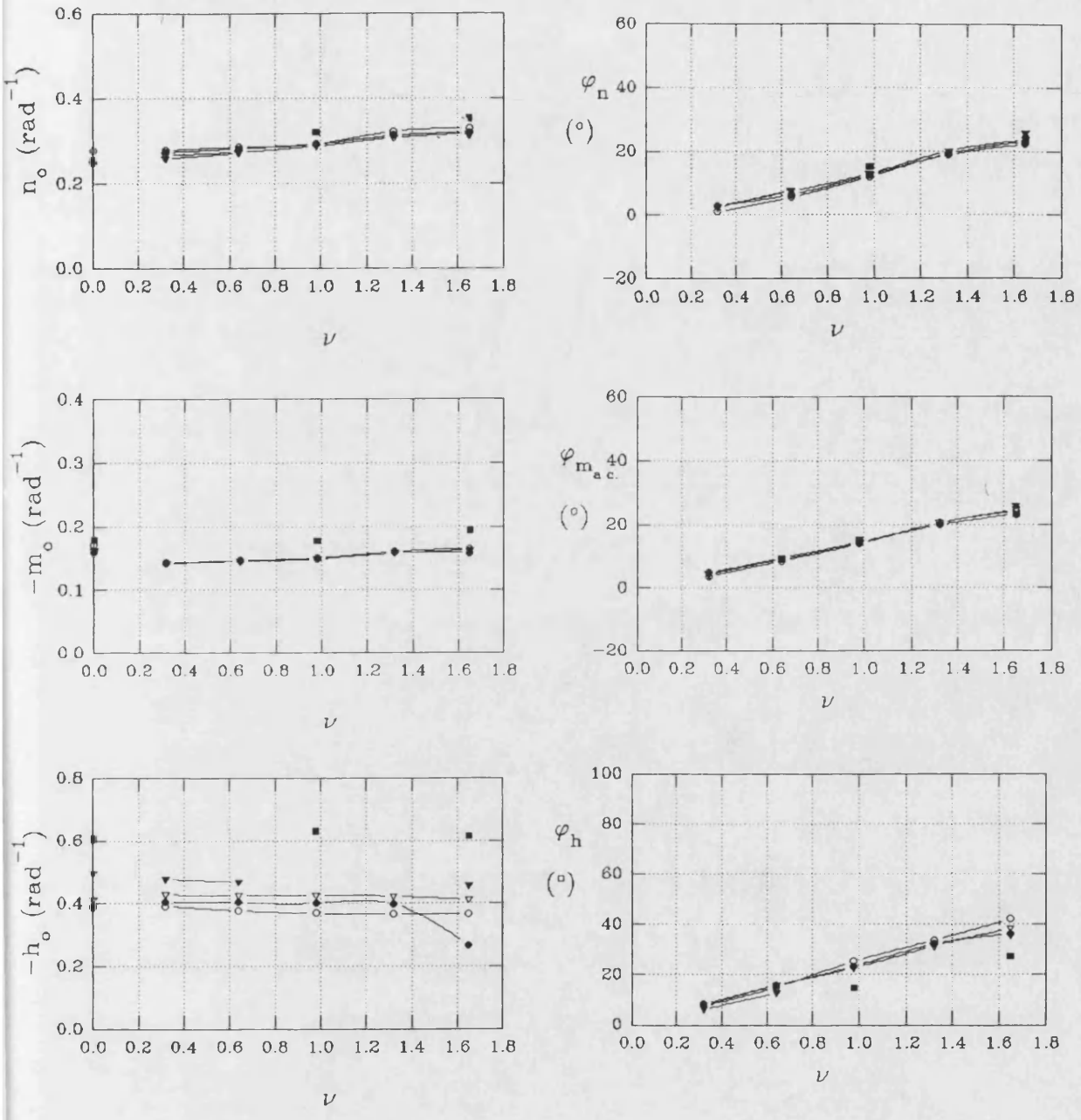

Fig. 7.27 - Lower surface contributions to unsteady normal force, pitching moment and hinge moment, mean η= 0°

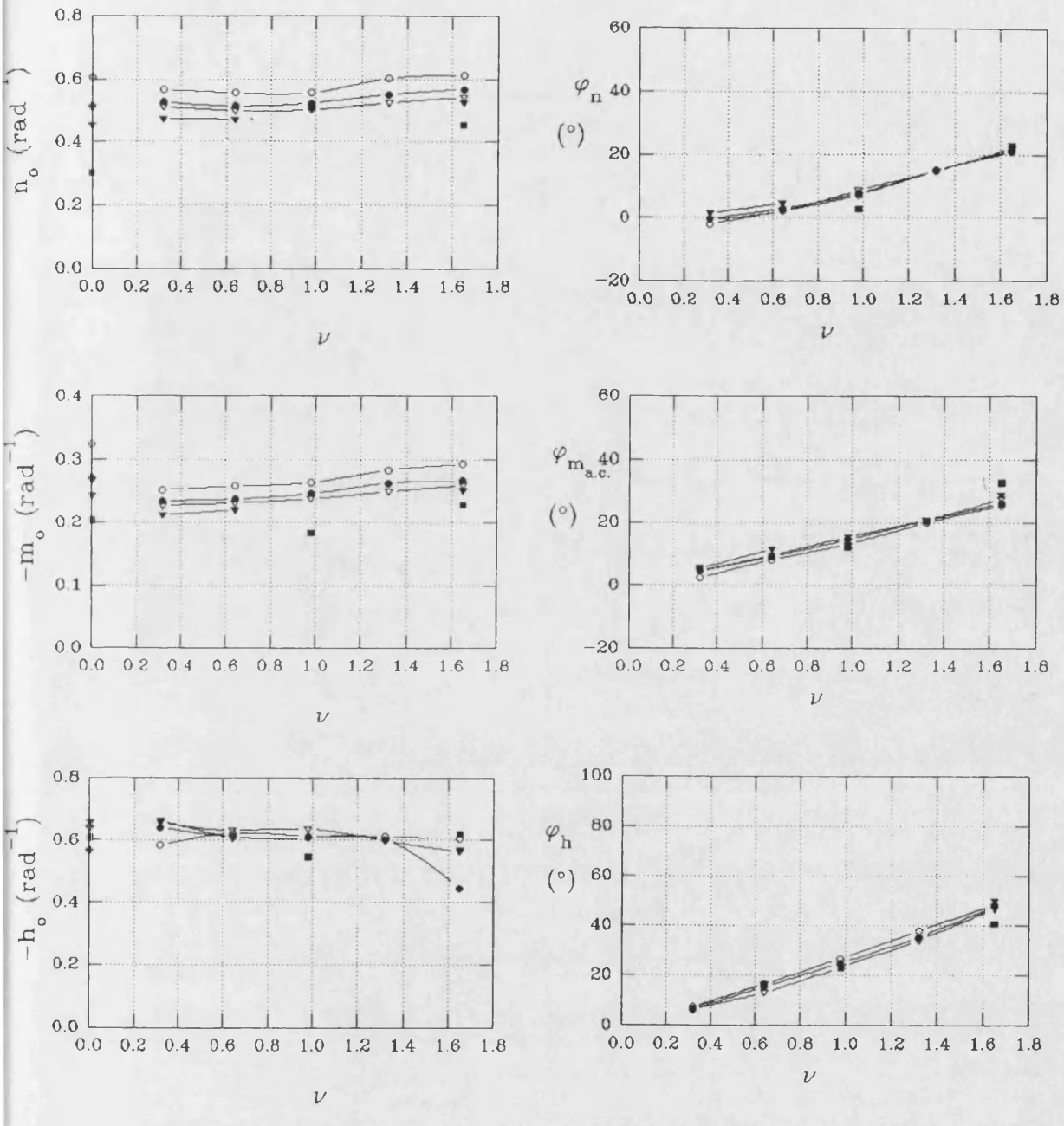

Fig. 7.28 - Total unsteady normal force, pitching moment and hinge moments, mean $\eta = 0°$

$\alpha = 10°$, $\nu = 0.32$, mean $\eta = 15°$

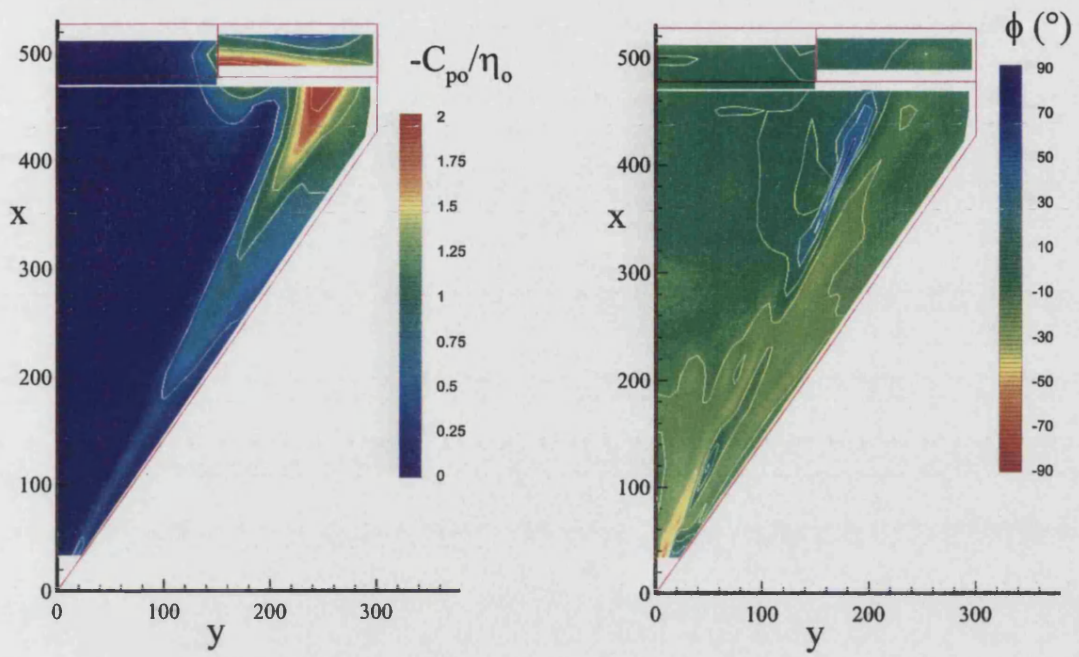

Steady Increments, mean $\eta = 15°$

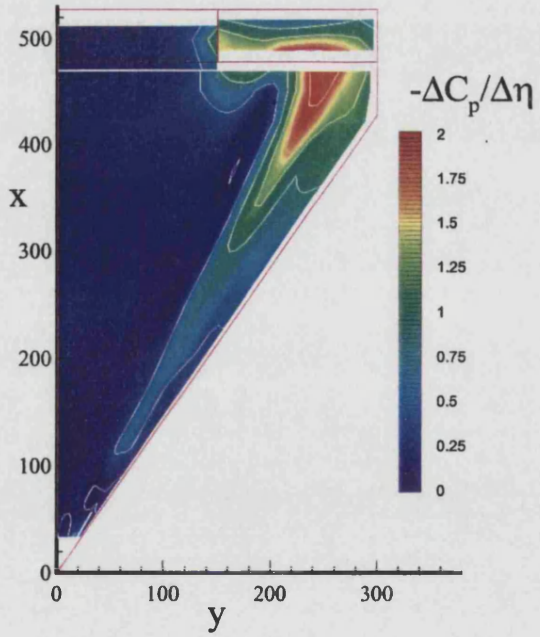

Fig. 7.29 - Upper surface unsteady pressure contours, $\nu = 0.32$, and steady incremental contours, $\alpha = 10°$, mean $\eta = 15°$

$\alpha = 10°$, $\nu = 0.98$, mean $\eta = 15°$

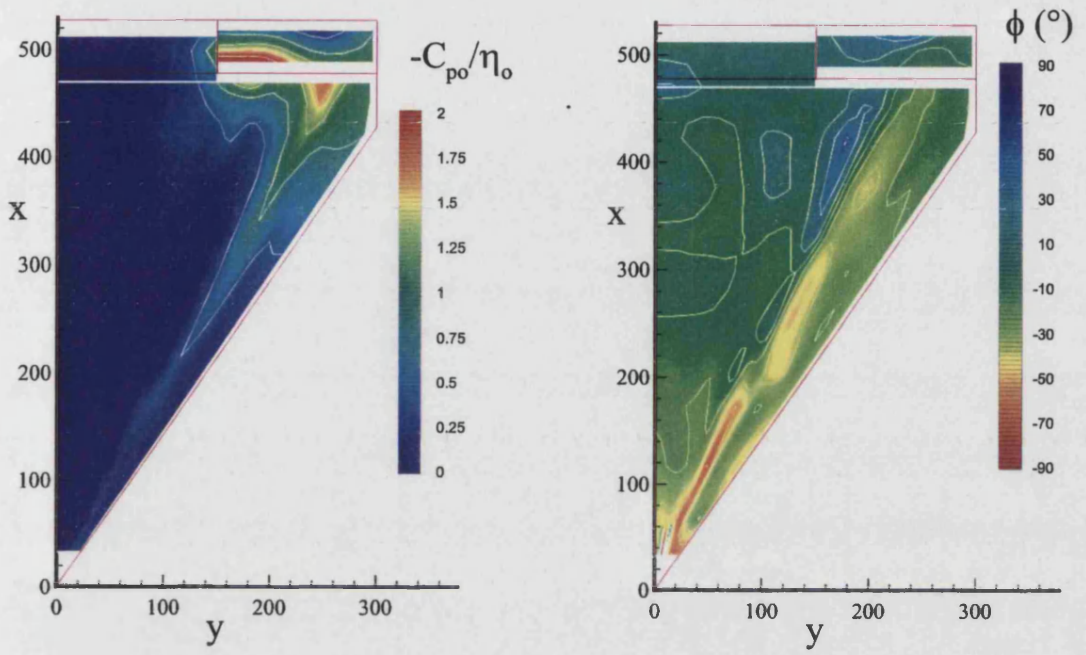

$\alpha = 10°$, $\nu = 1.65$, mean $\eta = 15°$

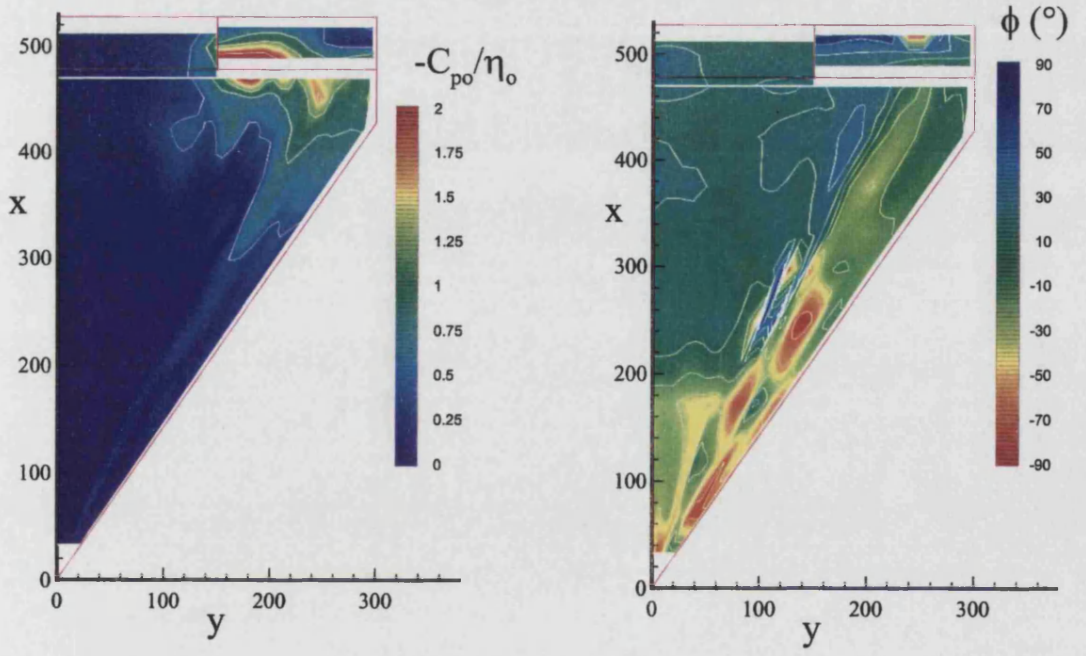

Fig. 7.30 - Upper surface unsteady pressure contours, ν= 0.98 and 1.65, at α= 10°, mean η= 15°

$\alpha = 10°$, $\nu = 0.32$, mean $\eta = -15°$

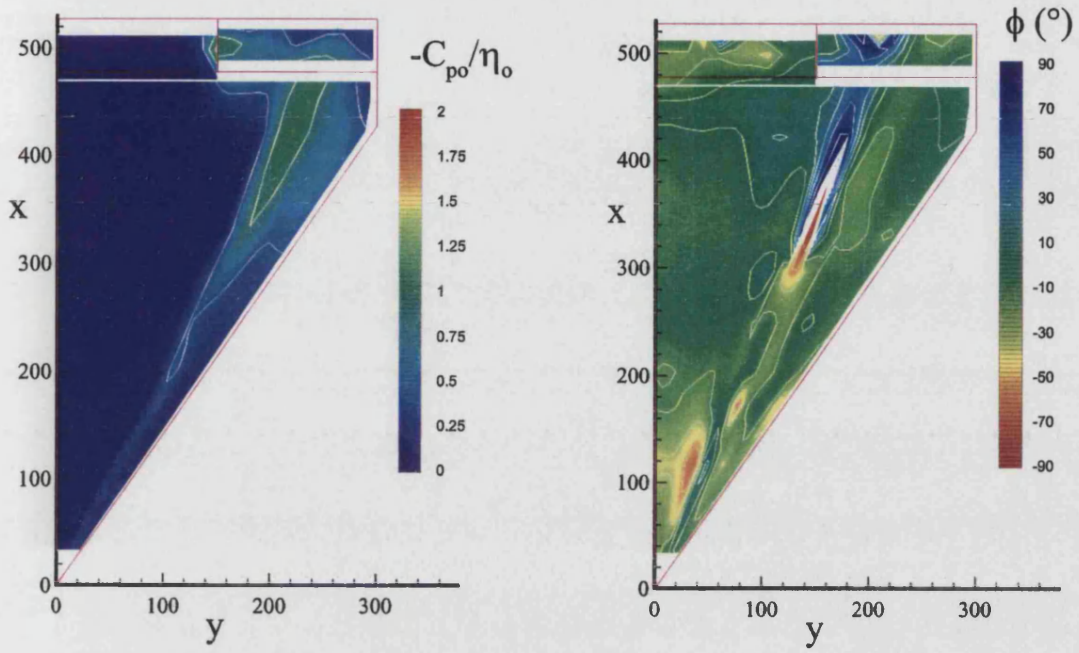

Steady Increments, mean $\eta = -15°$

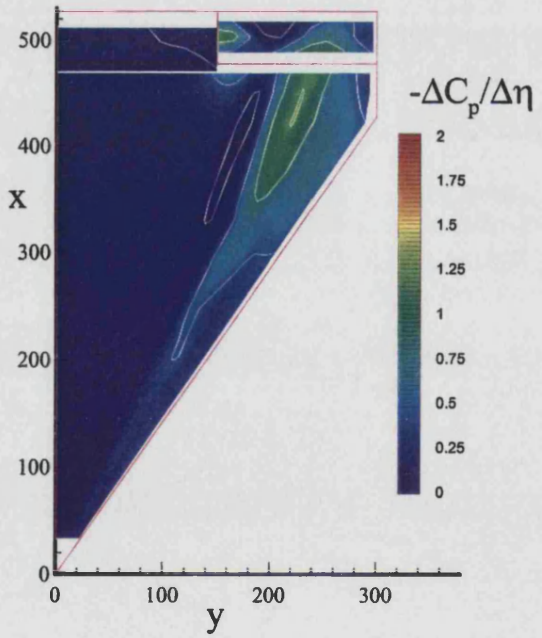

Fig. 7.31 - Upper surface unsteady pressure contours, $\nu = 0.32$, and steady incremental contours, $\alpha = 10°$, mean $\eta = -15°$

$\alpha = 10°$, $\nu = 0.98$, mean $\eta = -15°$

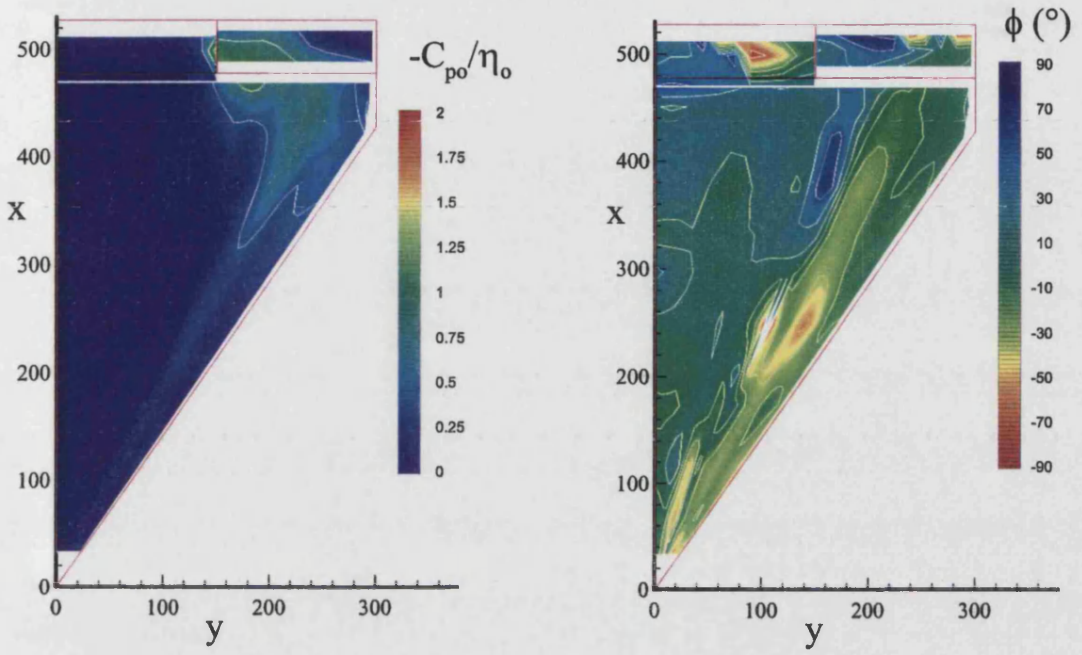

$\alpha = 10°$, $\nu = 1.65$, mean $\eta = -15°$

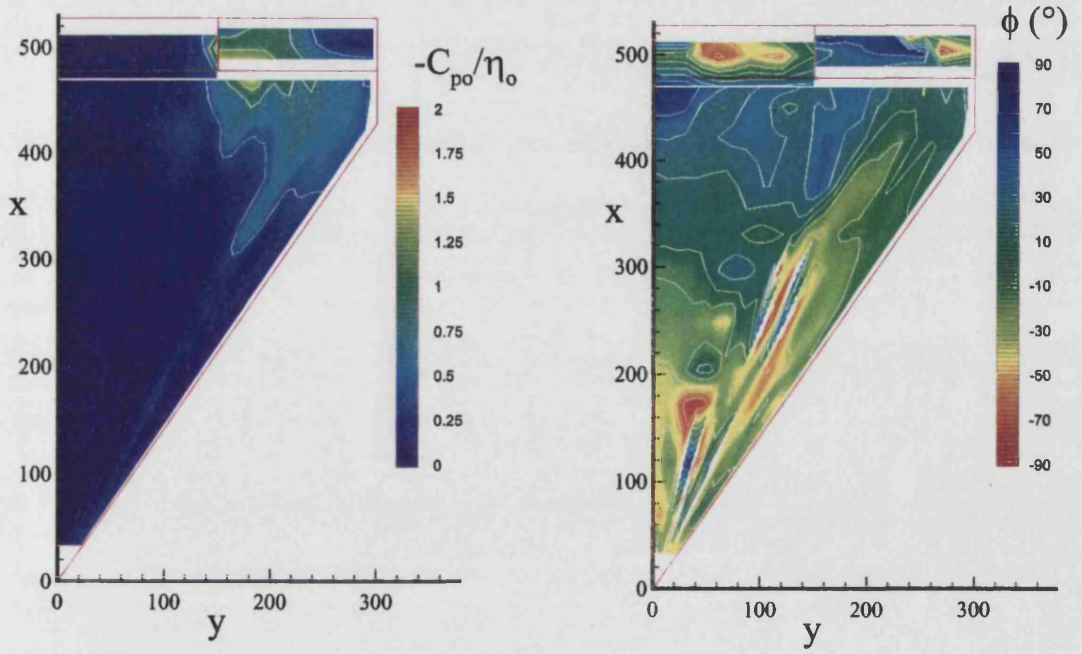

Fig. 7.32 - Upper surface unsteady pressure contours, $\nu = 0.98$ and 1.65, at $\alpha = 10°$, mean $\eta = -15°$

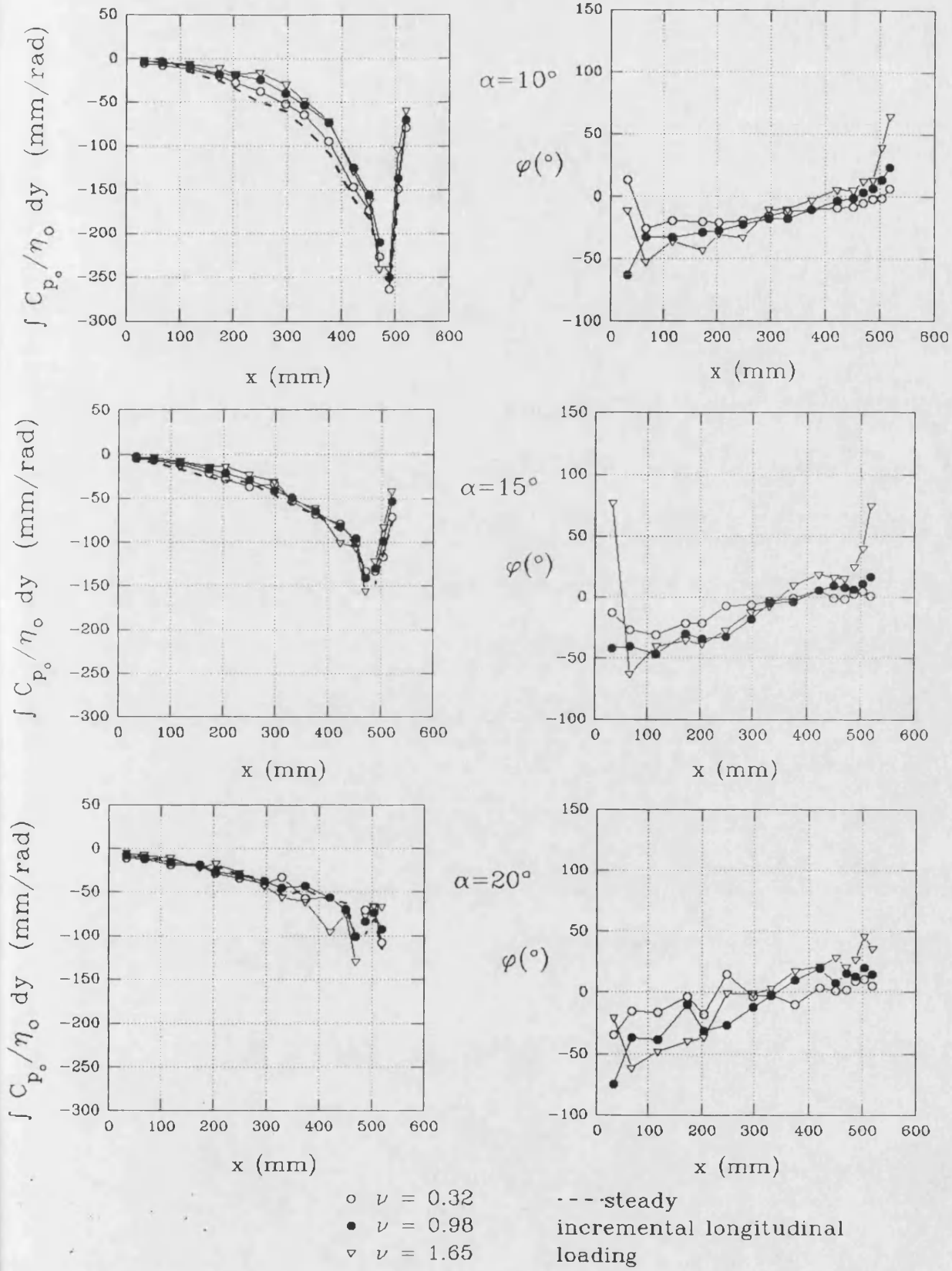

Fig. 7.33 - Unsteady, upper surface, longitudinal loadings, mean η= 15°

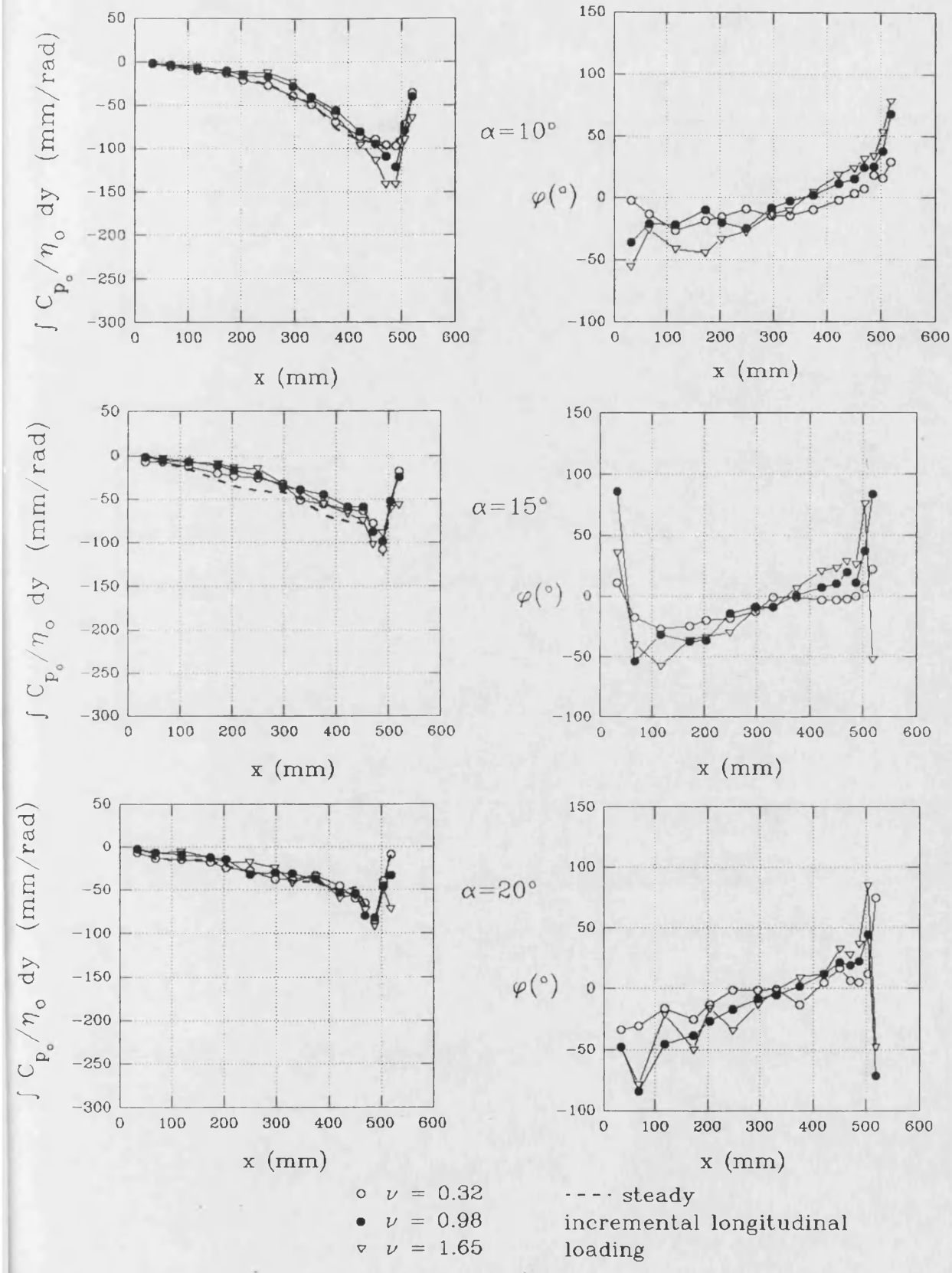

Fig. 7.34 - Unsteady, upper surface, longitudinal loadings, mean η= -15°

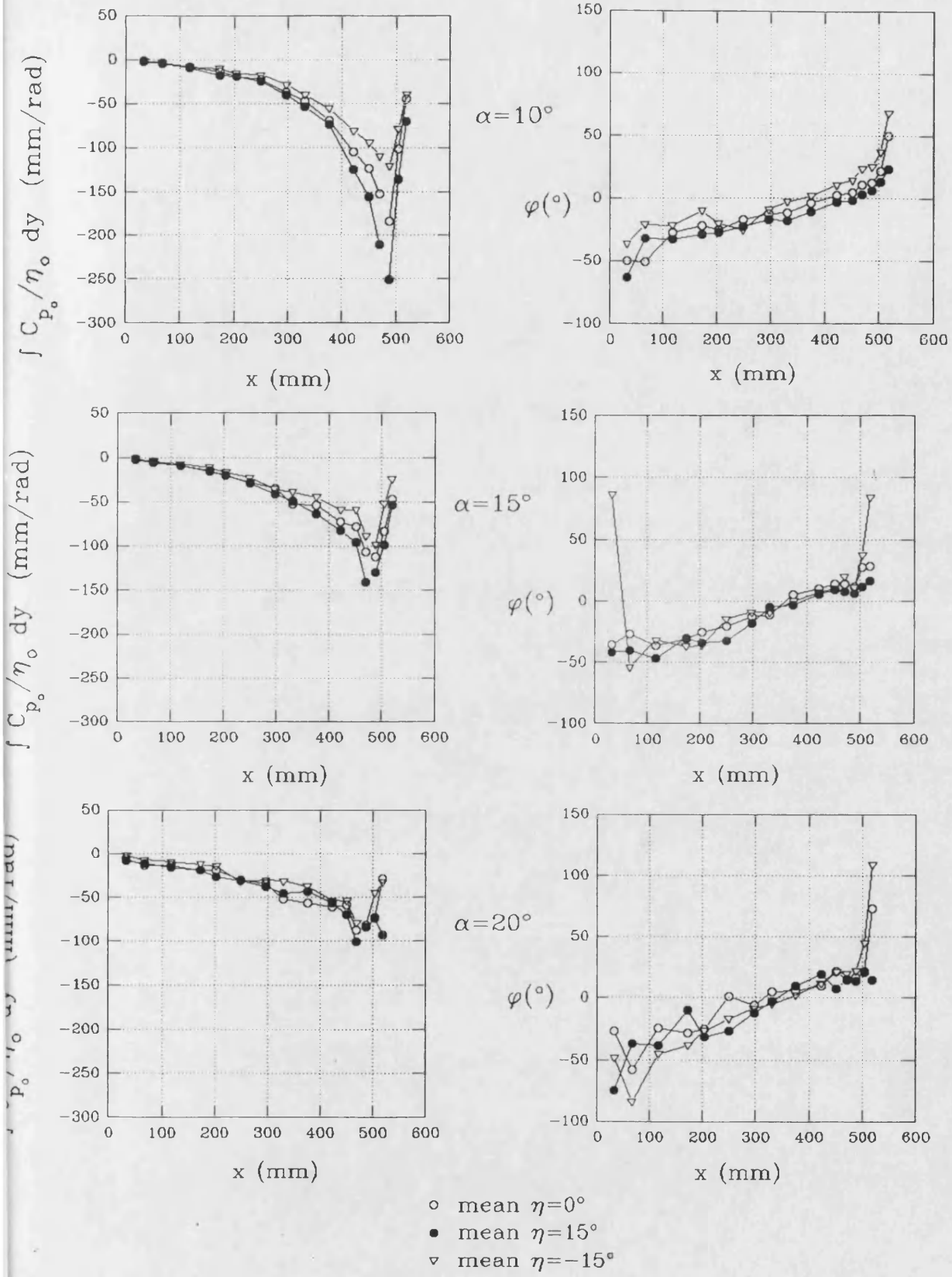

Fig. 7.35 - Comparison of upper surface, unsteady longitudinal loadings for mean η= 0°, 15° and -15°, at ν= 0.98

$\alpha = 15°$, $\nu = 0.32$, mean $\eta = 15°$

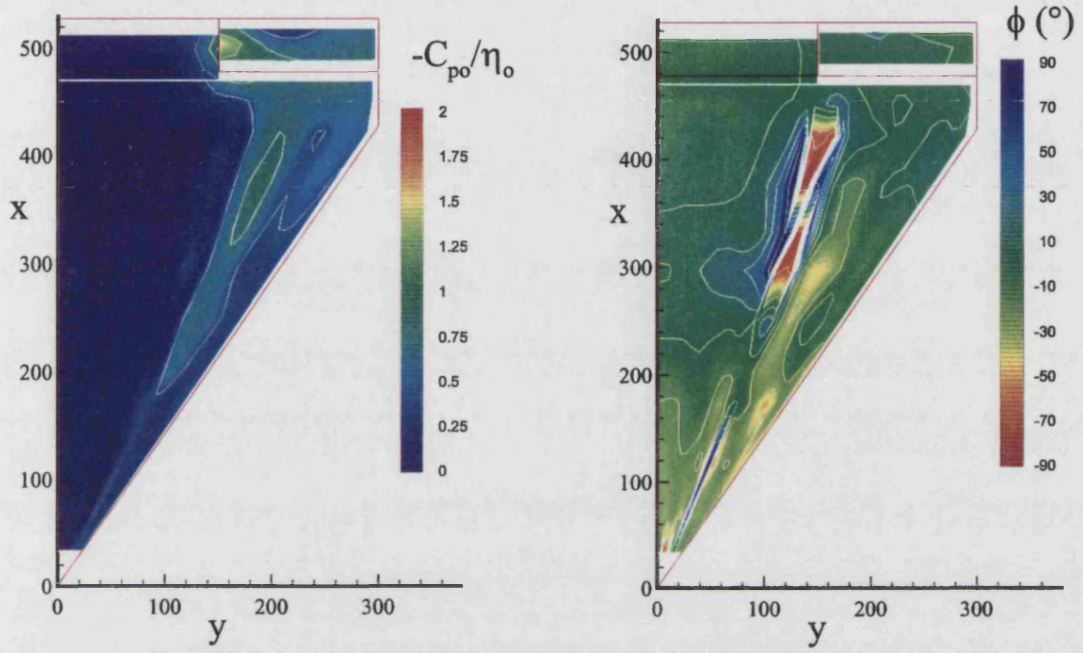

Steady Increments, mean $\eta = 15°$

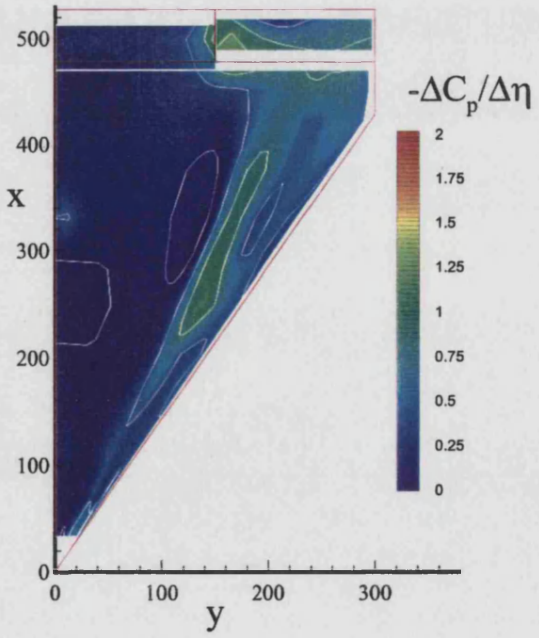

Fig. 7.36 - Upper surface unsteady pressure contours, $\nu = 0.32$, and steady incremental contours, $\alpha = 15°$, mean $\eta = 15°$

$\alpha = 15°$, $\nu = 0.98$, mean $\eta = 15°$

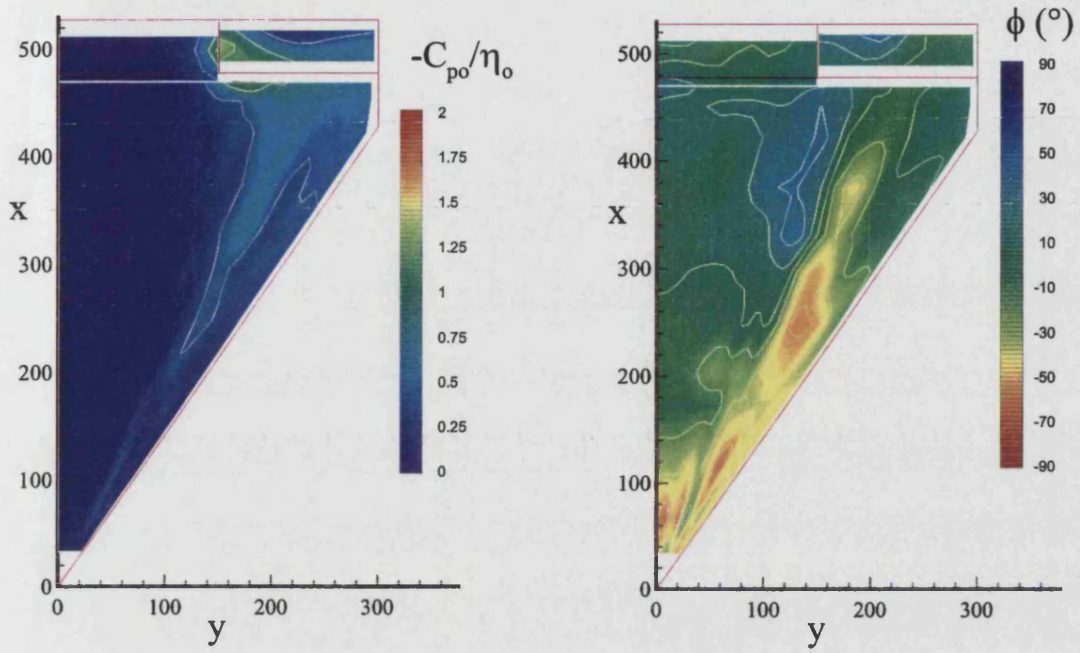

$\alpha = 15°$, $\nu = 1.65$, mean $\eta = 15°$

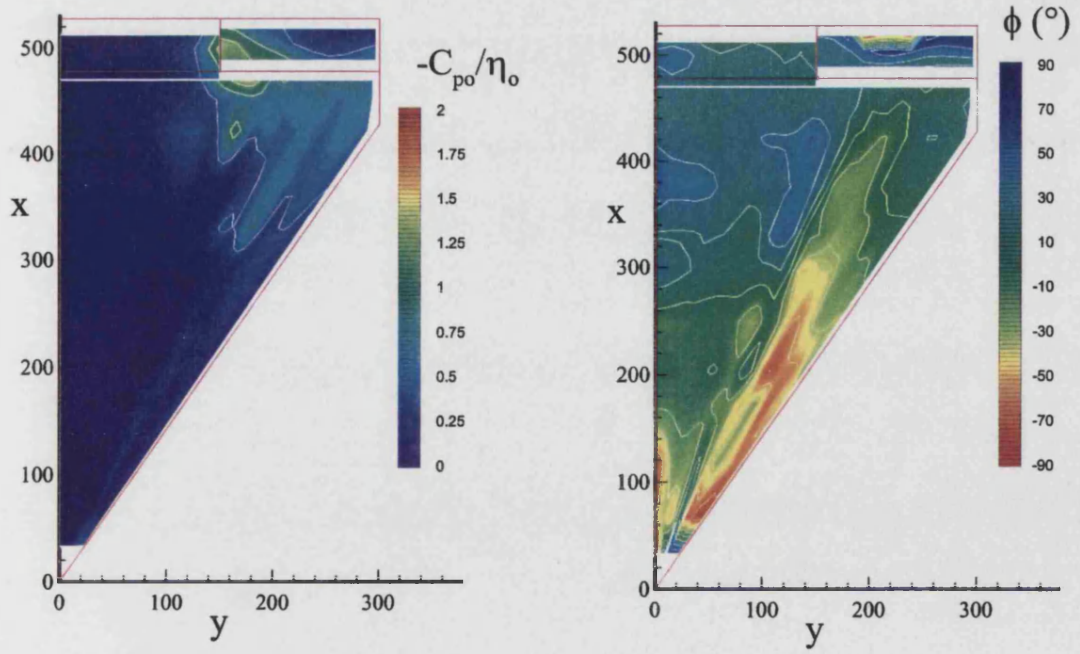

Fig. 7.37 - Upper surface unsteady pressure contours, $\nu = 0.98$ and 1.65, at $\alpha = 15°$, mean $\eta = 15°$

$\alpha = 15°$, $\nu = 0.32$, mean $\eta = -15°$

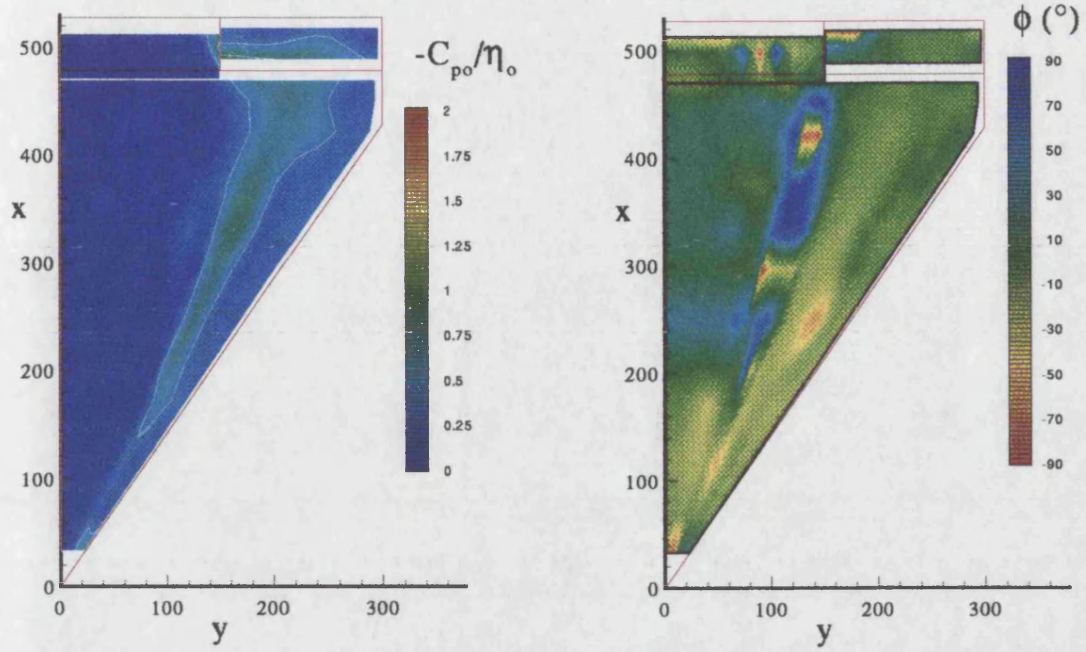

Steady Increments, mean $\eta = -15°$

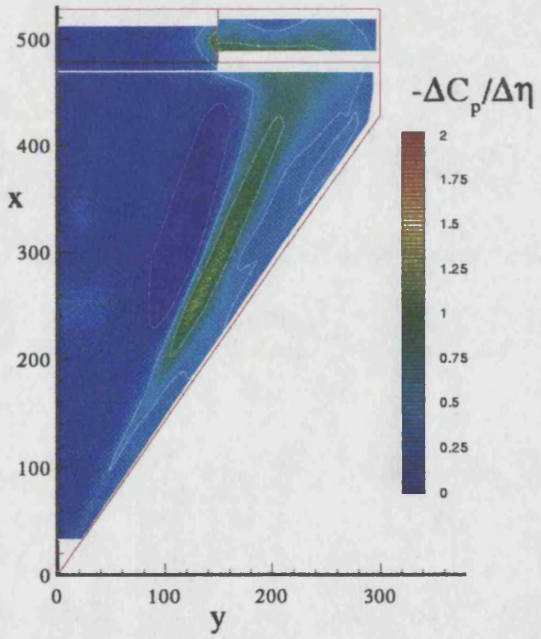

Fig. 7.38 - Upper surface unsteady pressure contours, $\nu = 0.32$, and steady incremental contours, $\alpha = 15°$, mean $\eta = -15°$

$\alpha = 15°$, $\nu = 0.98$, mean $\eta = -15°$

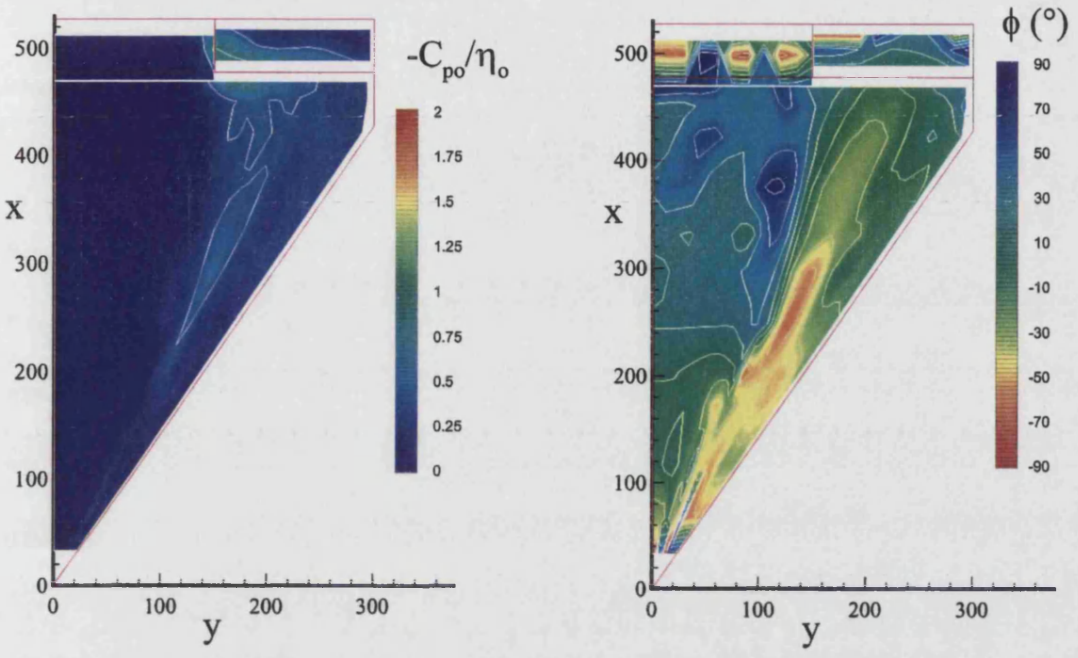

$\alpha = 15°$, $\nu = 1.65$, mean $\eta = -15°$

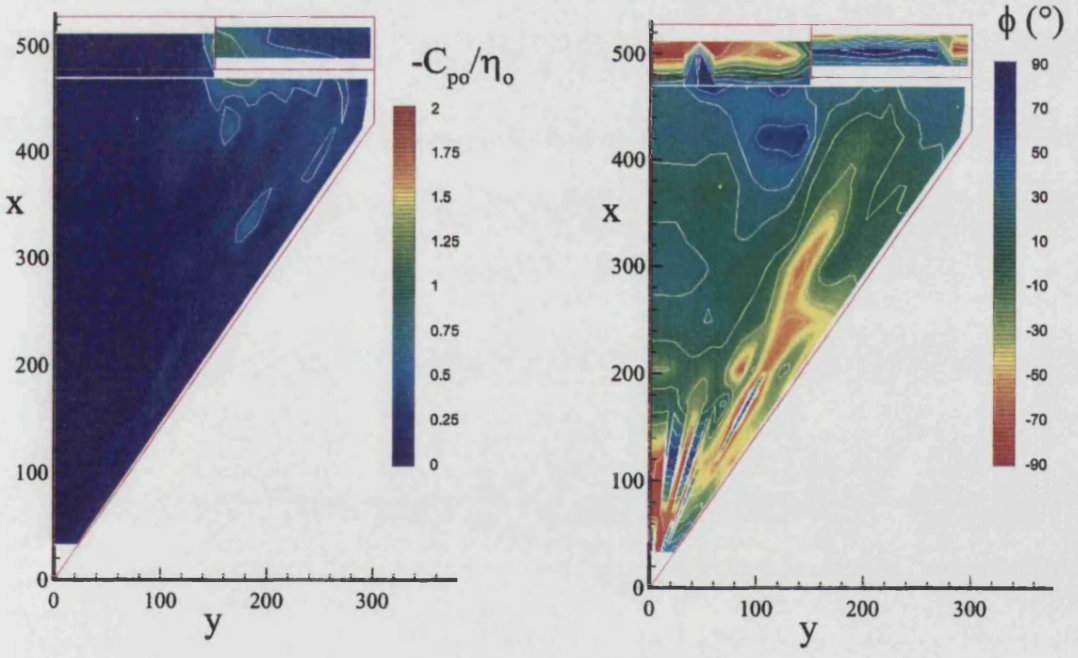

Fig. 7.39 - Upper surface unsteady pressure contours, $\nu = 0.98$ and 1.65, at $\alpha = 15°$, mean $\eta = -15°$

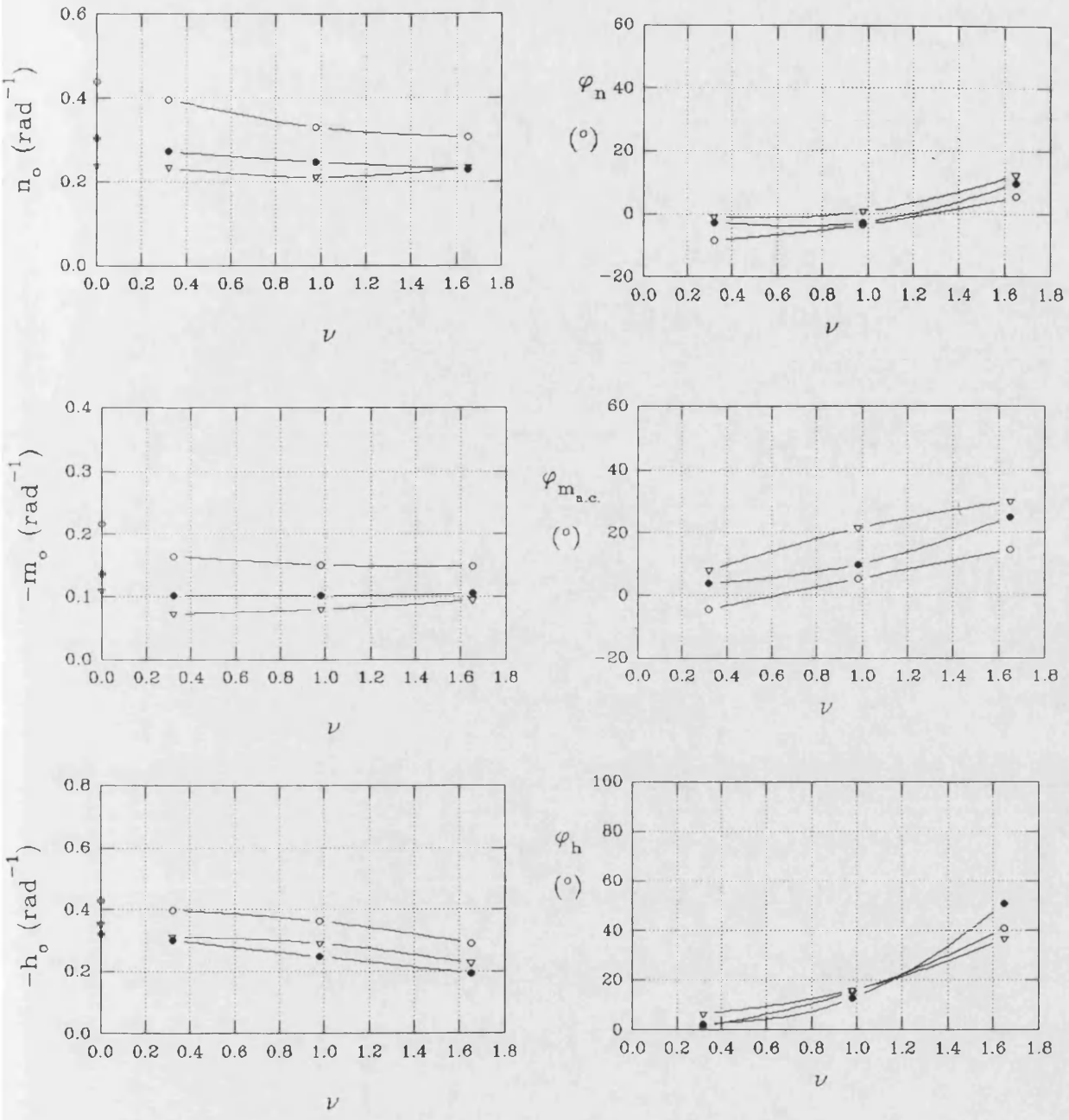

◦ $\alpha = 10°$
• $\alpha = 15°$
▿ $\alpha = 20°$

Fig. 7.40 - Upper surface, unsteady normal force, pitching moments and hinge moments for mean $\eta = 15°$

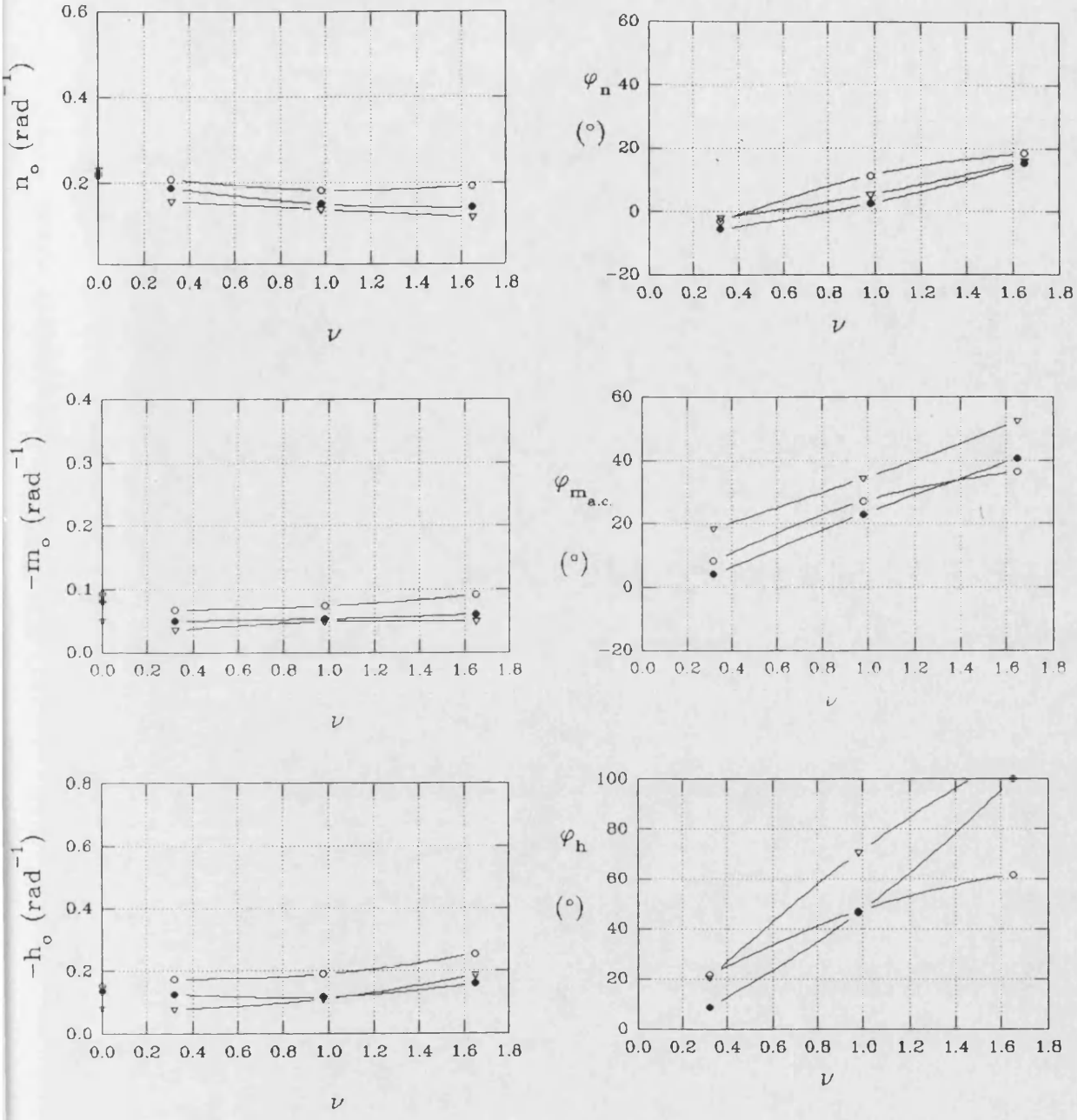

◦ $\alpha = 10°$
• $\alpha = 15°$
▿ $\alpha = 20°$

Fig. 7.41 - Upper surface, unsteady normal force, pitching moments and hinge moments for mean η= -15°

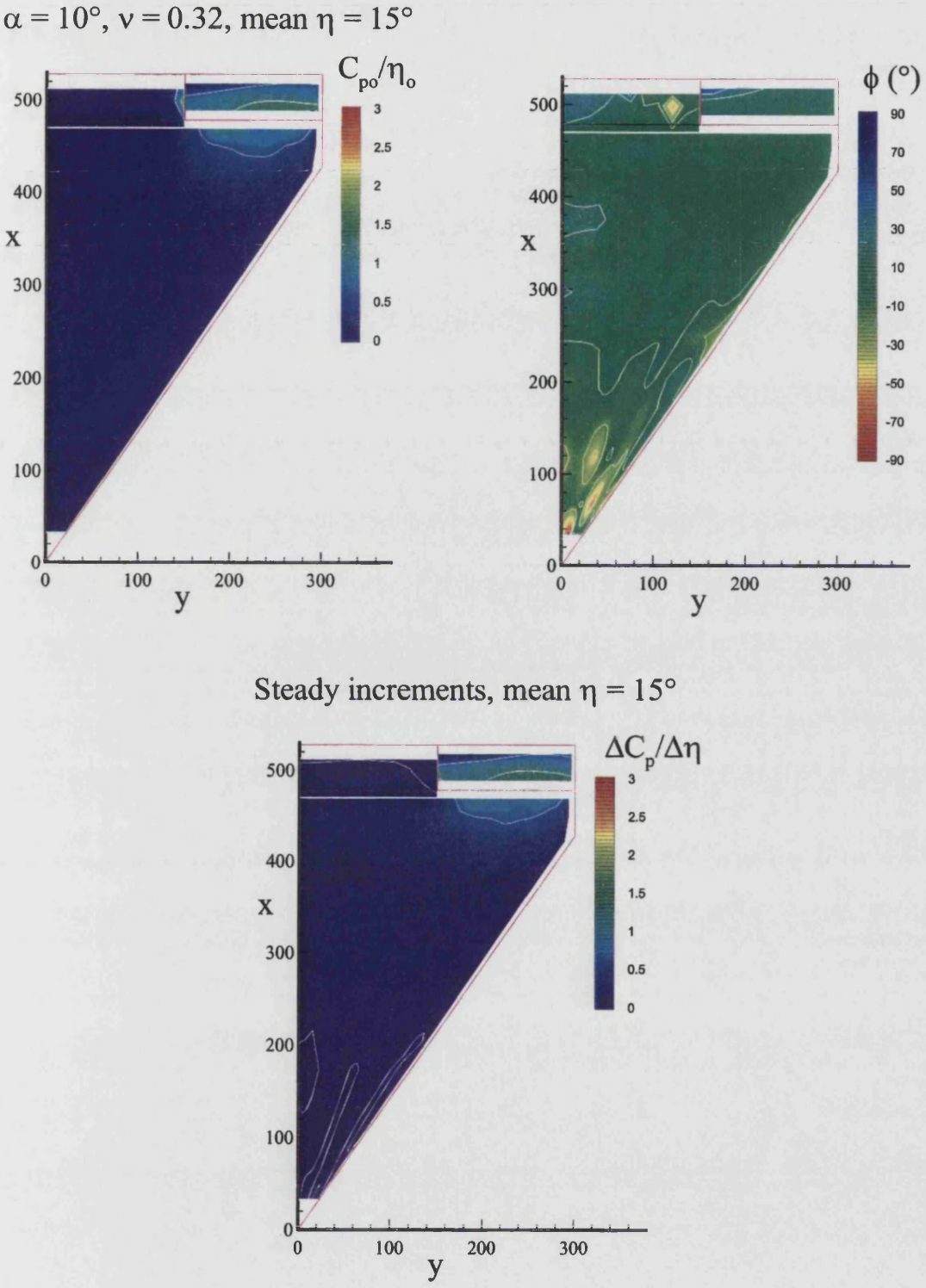

Fig. 7.42 - Lower surface unsteady pressure contours, $\nu = 0.32$, and steady incremental contours, $\alpha = 10°$, mean $\eta = 15°$

$\alpha = 10°$, $\nu = 1.65$, mean $\eta = 15°$

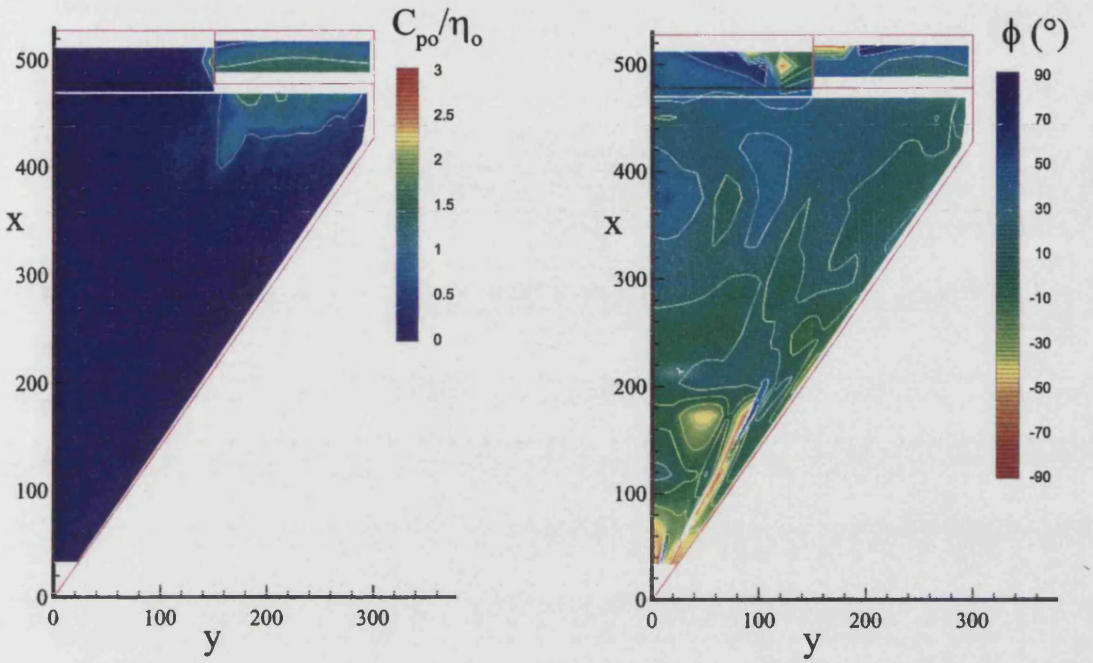

Fig. 7.43 - Lower surface unsteady pressure contours, $\nu = 1.65$,
at $\alpha = 10°$, mean $\eta = 15°$

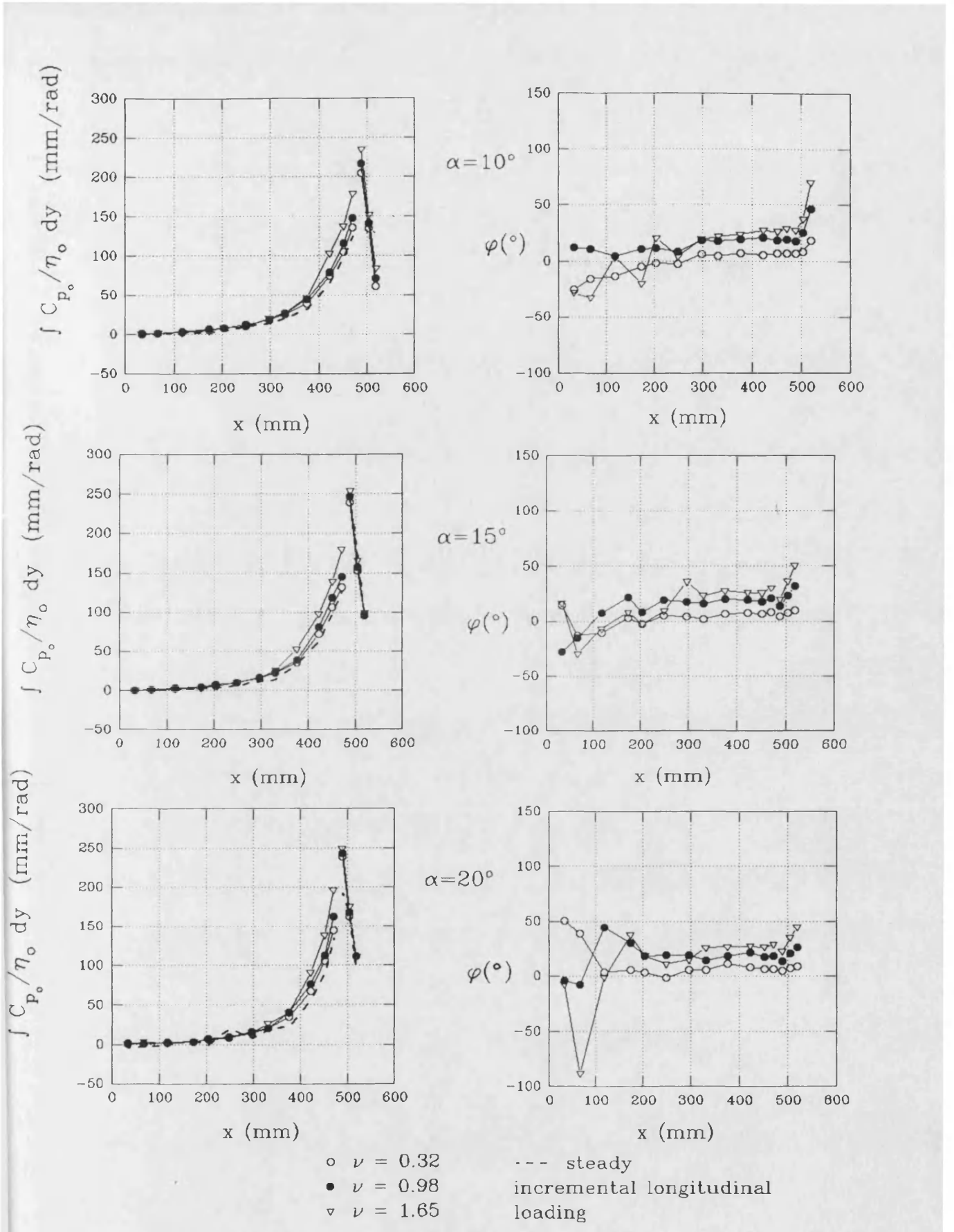

Fig. 7.44 - Unsteady, lower surface, longitudinal loadings, mean η= 15°

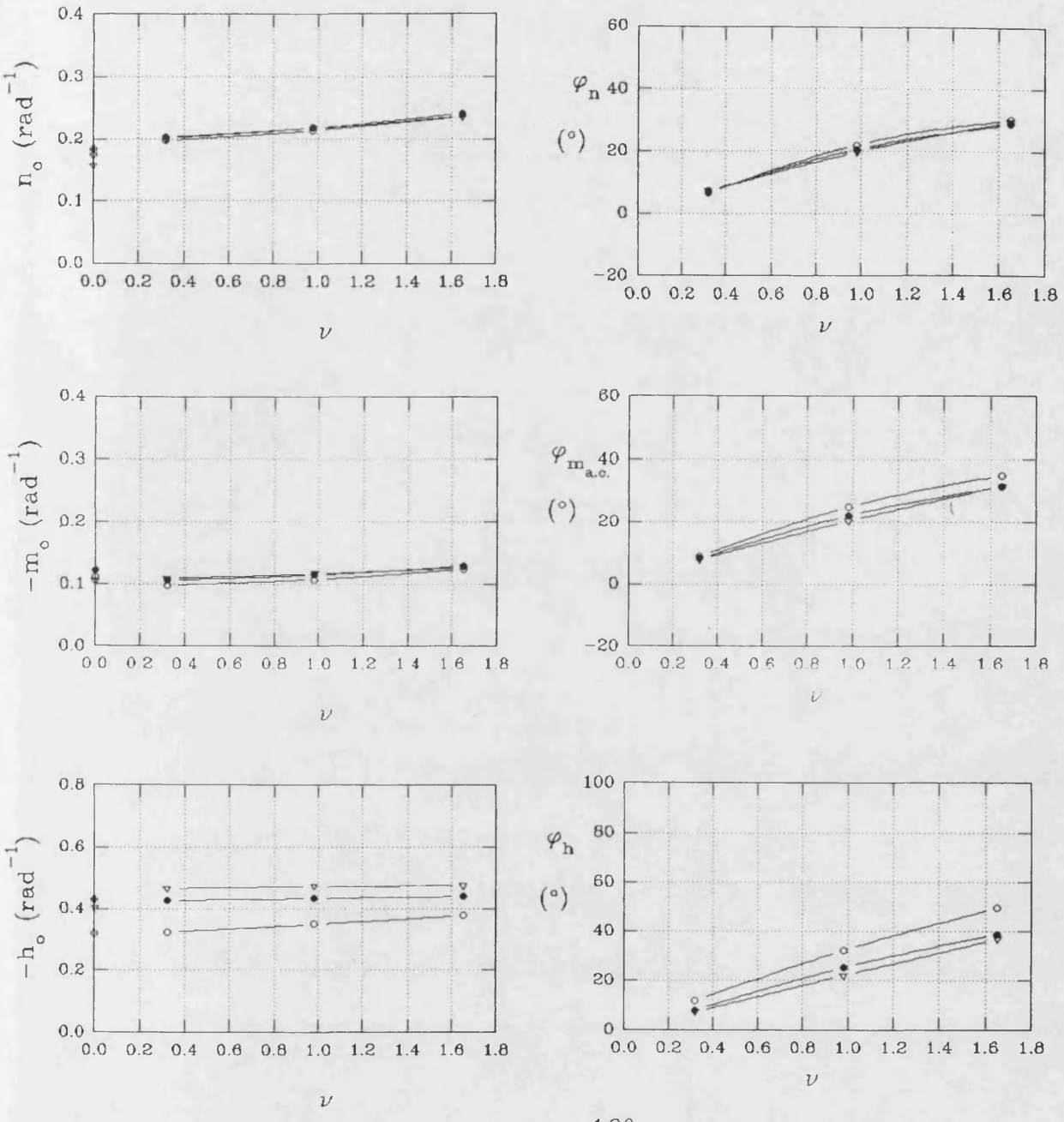

Fig. 7.45 - Lower surface, unsteady normal force, pitching moments and hinge moments for mean η= 15°

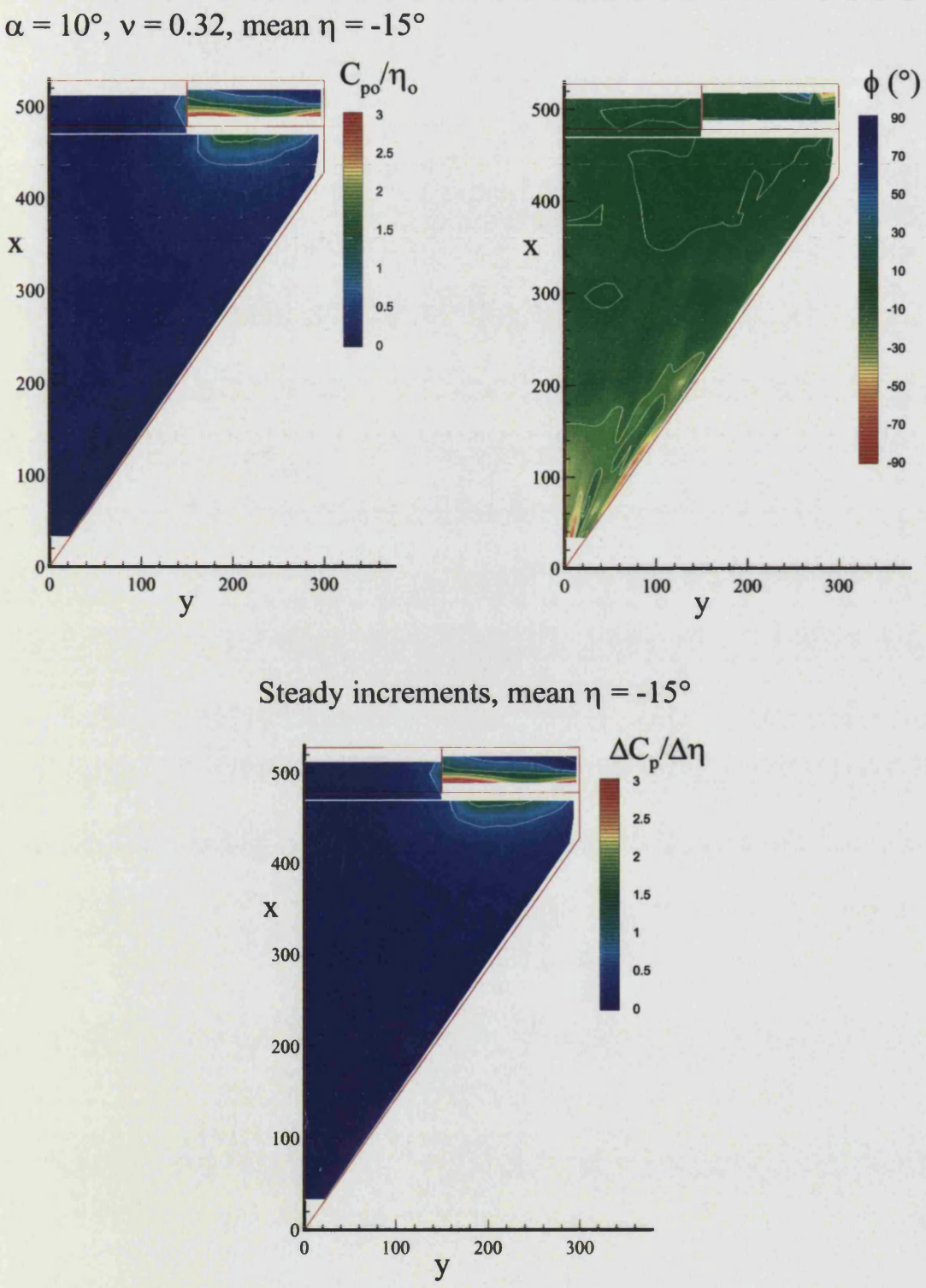

Fig. 7.46 - Lower surface unsteady pressure contours, ν= 0.32, and steady incremental contours, α= 10°, mean η= -15°

$\alpha = 10°$, $\nu = 1.65$, mean $\eta = -15°$

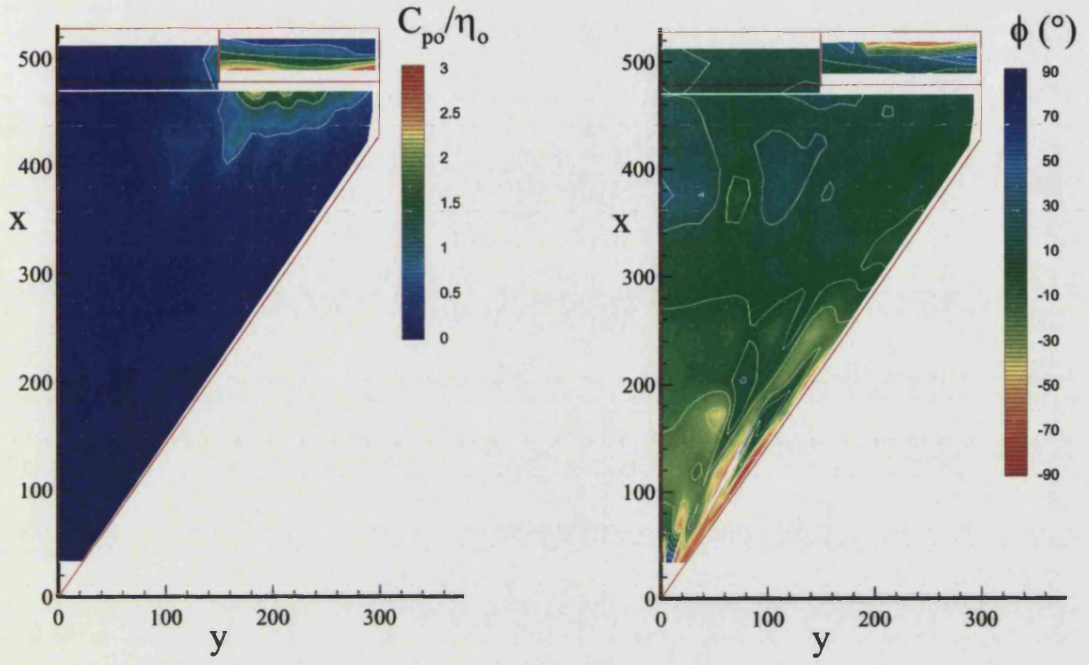

Fig. 7.47 - Lower surface unsteady pressure contours, $\nu = 1.65$,
at $\alpha = 10°$, mean $\eta = -15°$

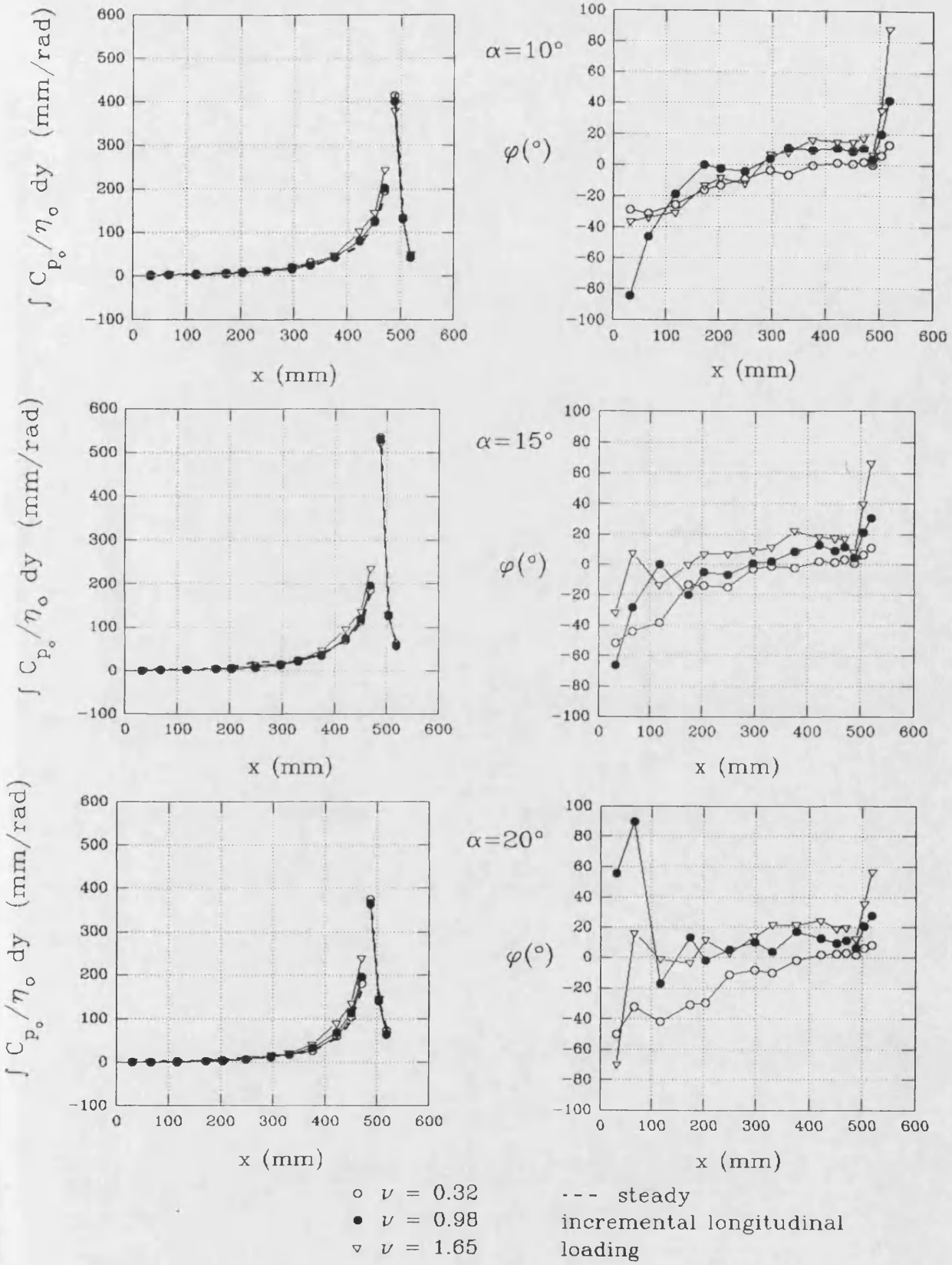

Fig. 7.48 - Unsteady, lower surface, longitudinal loadings, mean η= -15°

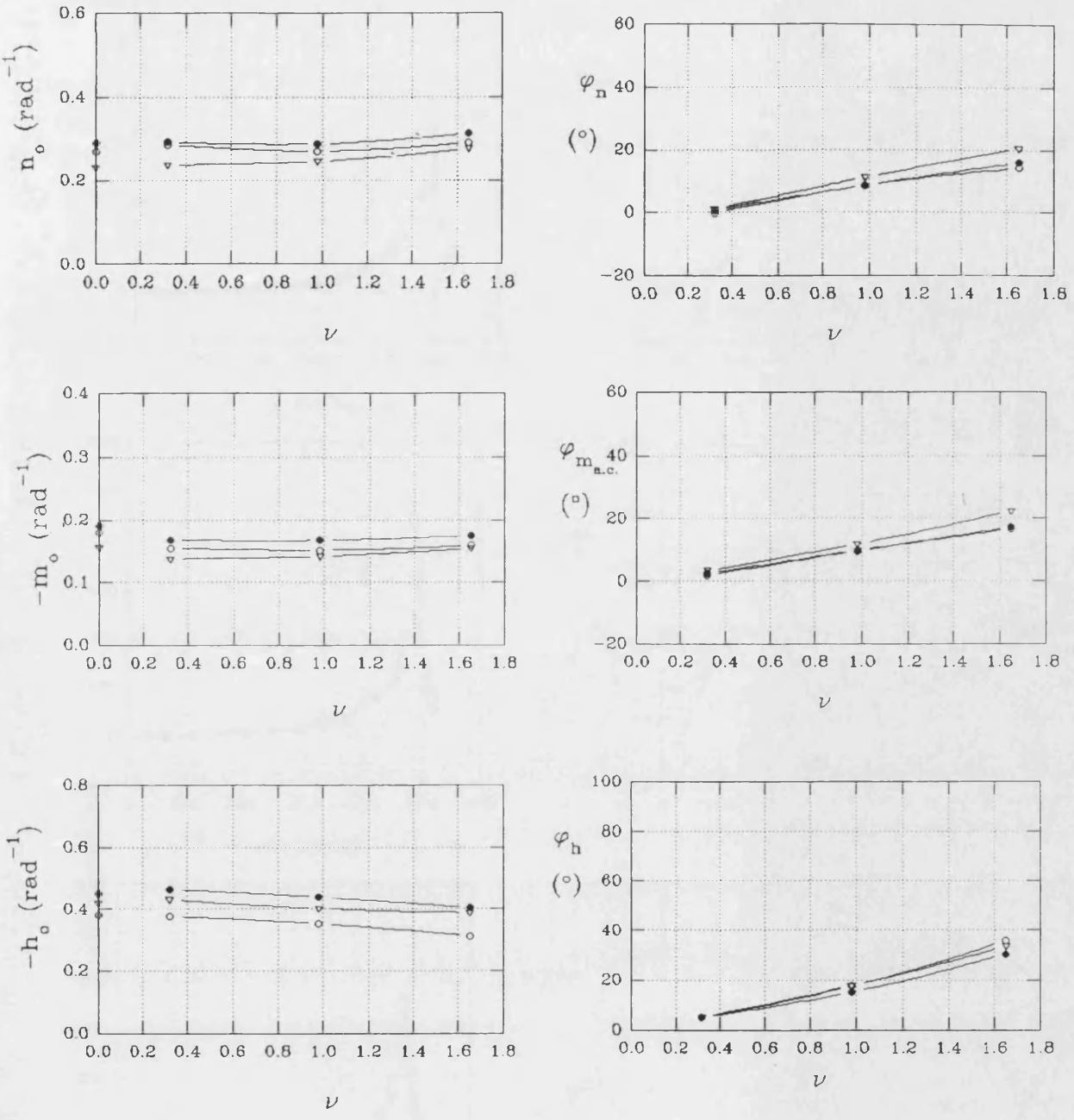

Fig. 7.49 - Lower surface, unsteady normal force, pitching moments and hinge moments for mean η= -15°

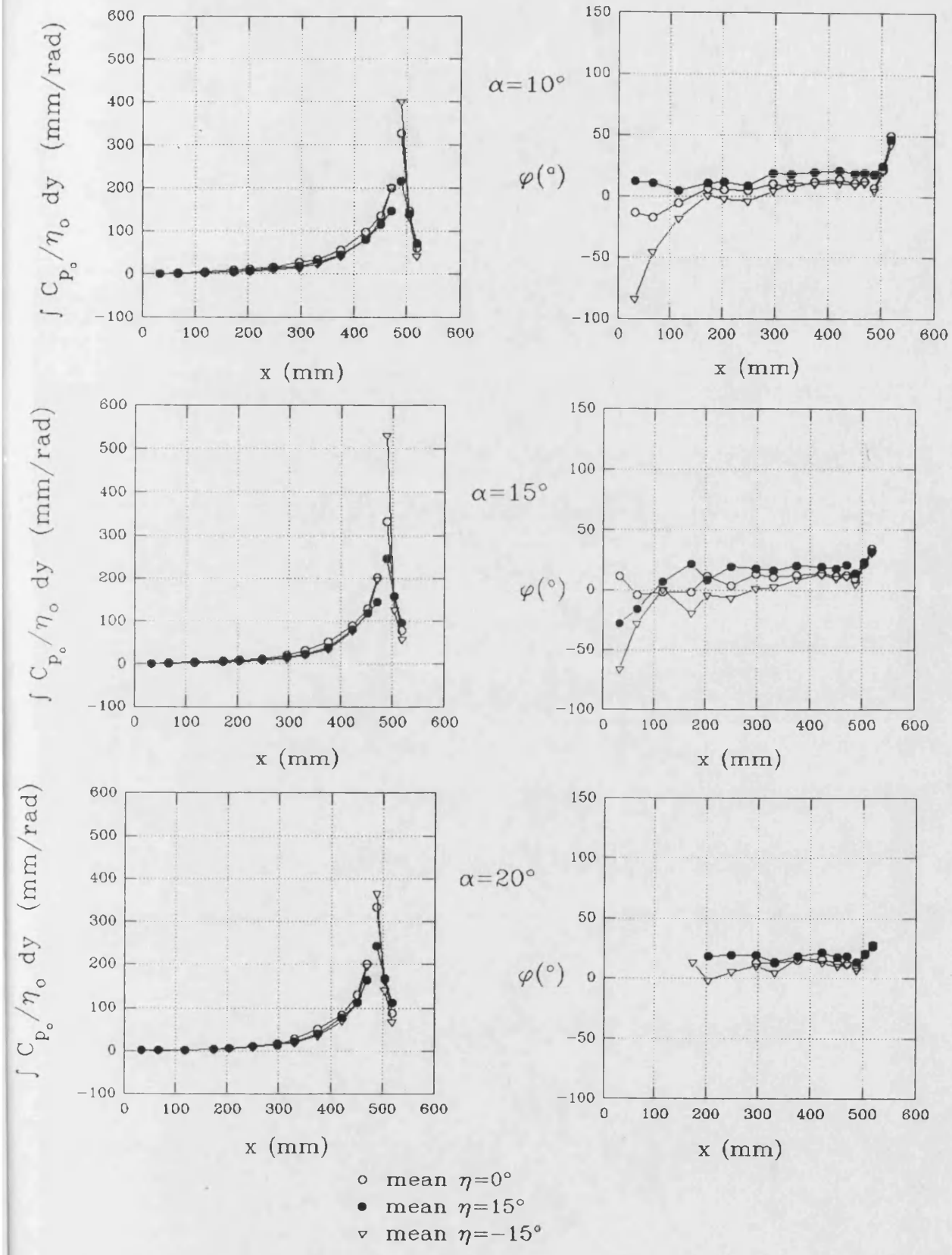

Fig. 7.50 - Comparison of lower surface, unsteady longitudinal loadings for mean η= 0°, 15° and -15°, at ν= 0.98

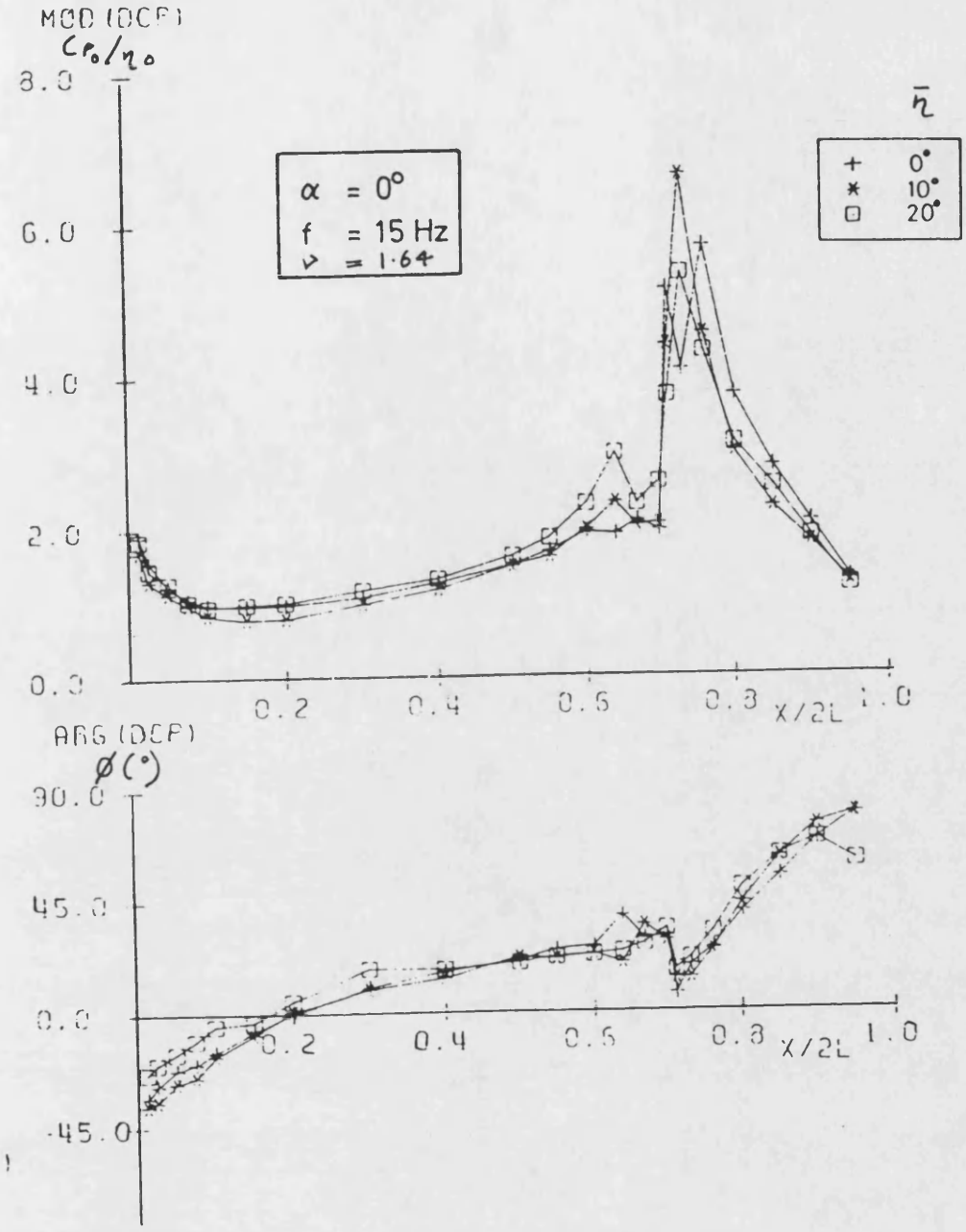

Fig. 7.51 - Unsteady pressure variations with mean flap angle on a 2-d section, Kienappel and Round [1980]

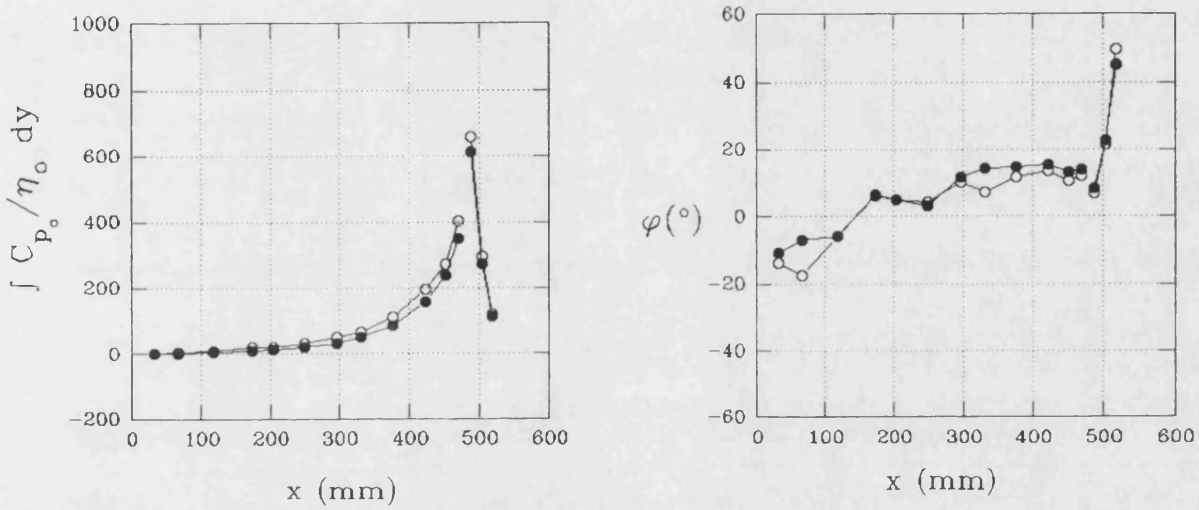

○ 2*(mean η=0°)
● (mean η=15°) + (mean η=−15°)

Fig. 7.52 - Comparison of unsteady, longitudinal loadings for assumed fully attached flow

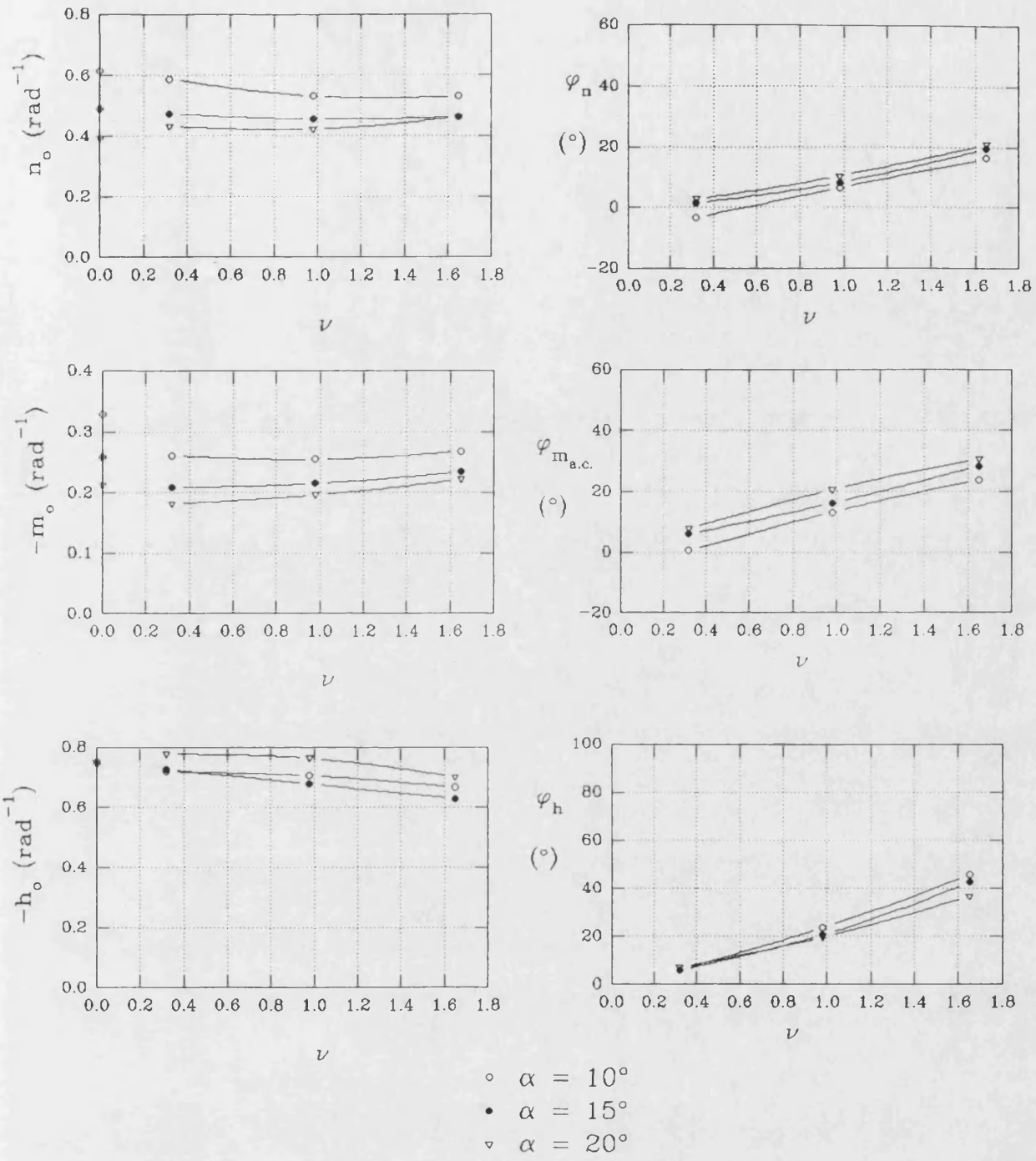

Fig. 7.53 - Total unsteady normal force, pitching moments and hinge moments for mean η= 15°

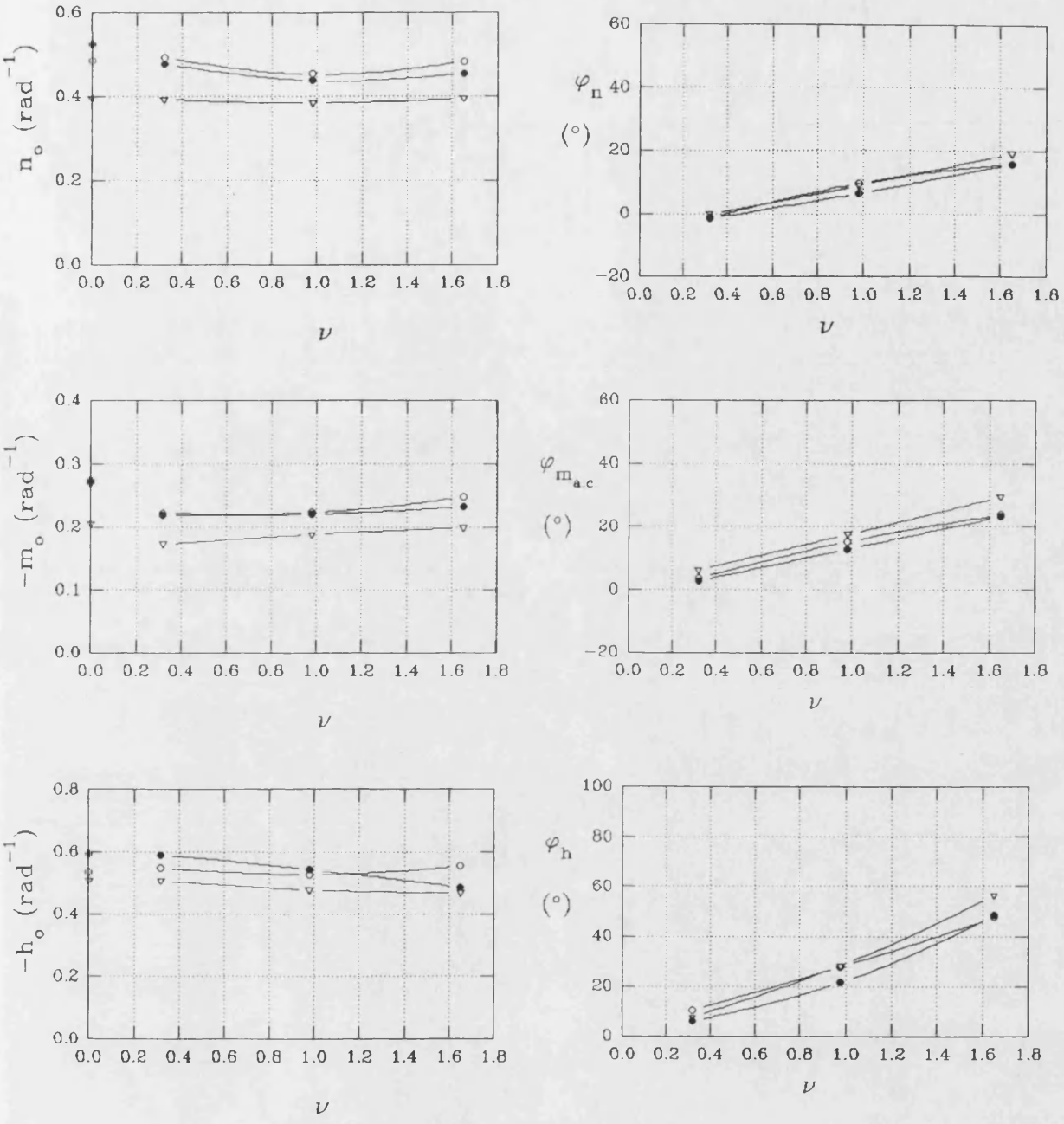

Fig. 7.54 - Total unsteady normal force, pitching moments and hinge moments for mean η= -15°

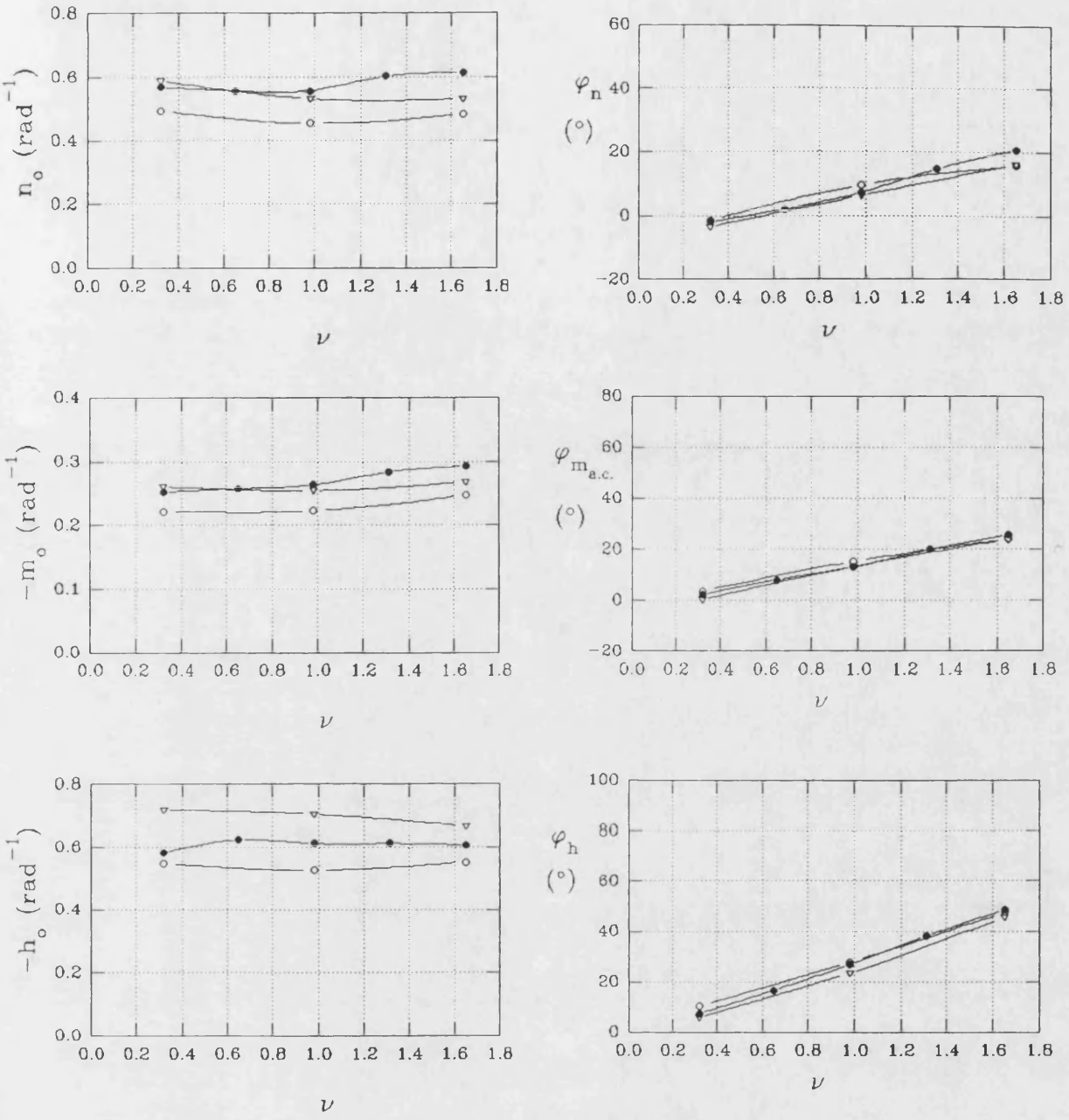

Fig. 7.55 - Comparison of unsteady derivatives for mean η= 15°, 0°, -15°, at α= 10°

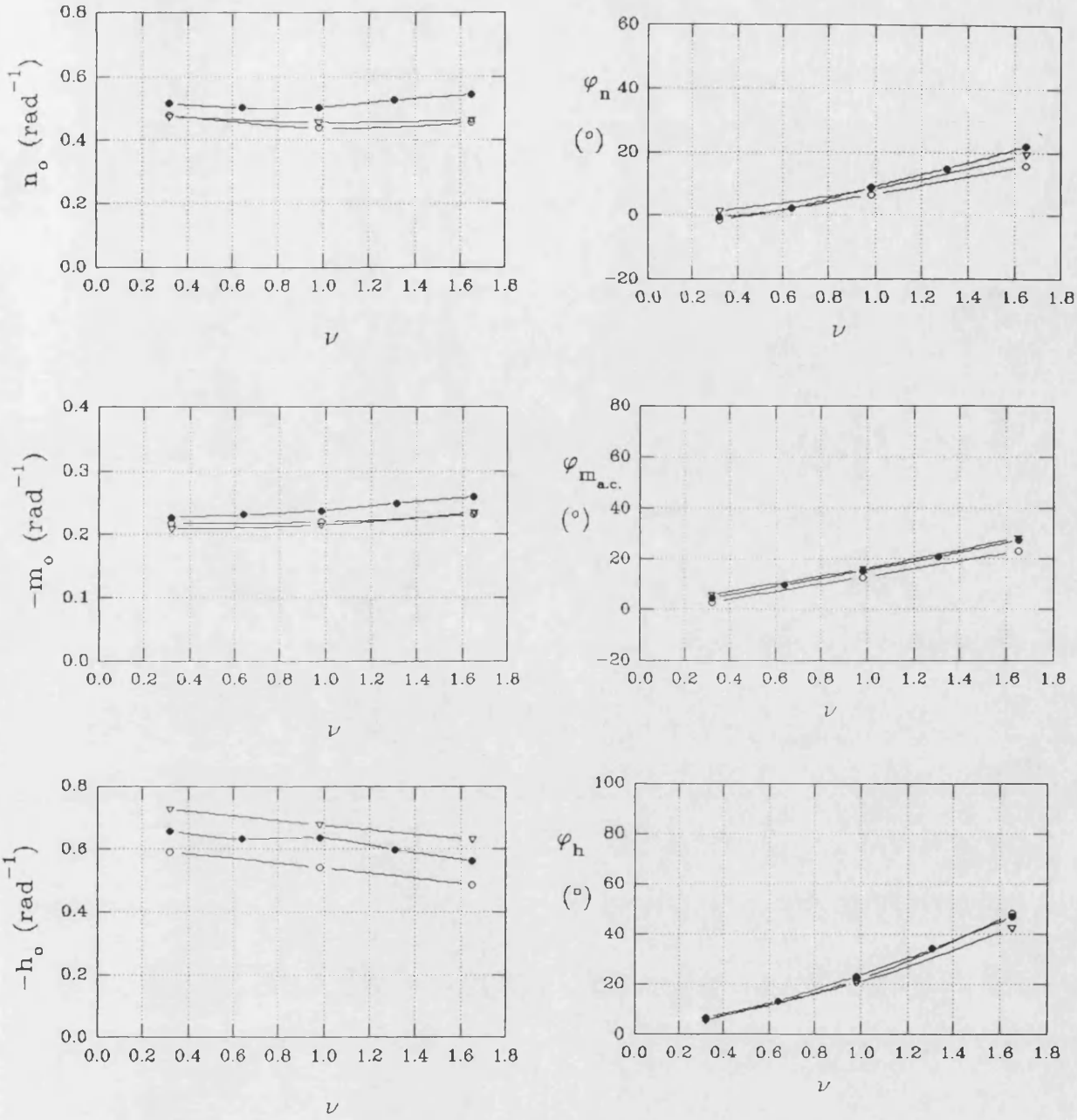

Fig. 7.56 - Comparison of unsteady derivatives for mean η= 15°, 0°, -15°, at α= 15°

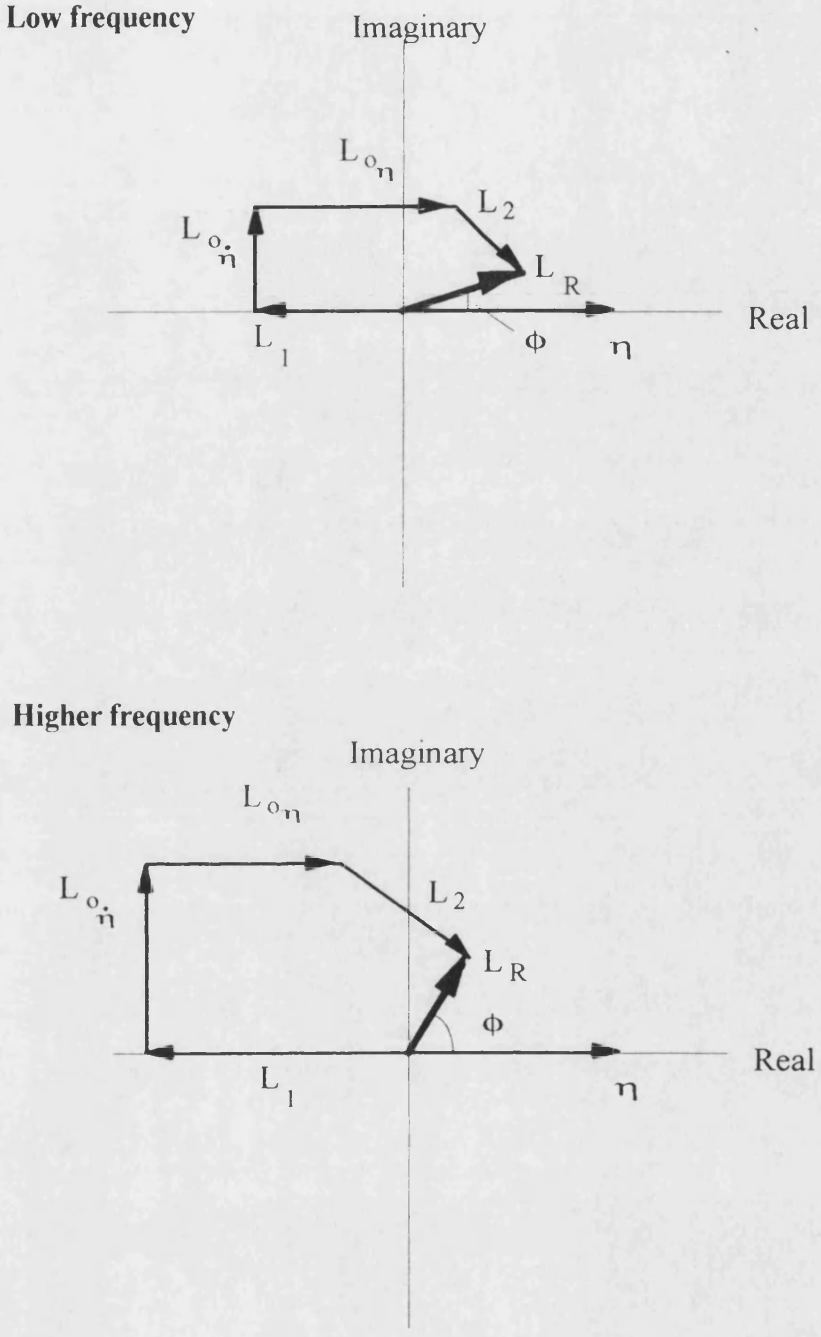

Fig. 7.57 - Vector diagram for attached flow response, Von Kàrmàn and Sears [1938]

8. FLEXIBLE ROOT MOUNTING TESTS.

It was initially planned to force the model in a root bending oscillation, and measure the resulting unsteady pressures. This would then allow the matrix solution for elevon oscillation with a flexible root to be compared to the measured response of the wing with both modes present. Unfortunately, within the period and with the apparatus available, it was not possible to produce a large enough amplitude of oscillation to be able to accurately measure the unsteady aerodynamic response to forcing in this mode. Hence, the flexible wing tests were limited to the measurement of the structural response to elevon oscillation at various frequencies of the model, with flexibility at the root (Section 3.2.3) and at various α. By altering the dimension, l, of the flexible plate, three different wing root bending natural frequencies were produced, corresponding to νn= 1.51, 1.35 and 1.07, thus covering a typical range of natural frequencies for a first wing bending mode (Section 2.5.1).

Three miniature accelerometers were mounted to the model to determine whether the wing was twisting or bending other than at the root. The model was found not to distort in this way and hence the mode was pure bending about the root. Hence, only the results for the accelerometer mounted at the tip of the wing are presented.

All tests were for η=0°, η_0=5° and at a test velocity of V_∞=30 m/s.

8.1 Root bending moments calculated from rigid model tests.

By integrating the root bending moments of the unsteady pressures, measured during the rigid wing, elevon oscillation tests, it is possible to obtain the effect of elevon oscillations on the root bending moments. This is in fact one of the aerodynamic cross terms that would be used within the matrix solution for the two-mode, flexible system. In this instance, however, it can be used as an initial indication of the effect of the control rotation mode on root bending mode.

For the rigid model, the contributions to the bending moment/control derivatives from the upper surface, lower surface and their sum are given on fig. 8.1 along with the steady moments. As would be expected following the discussions of Chapter 7, the root bending moments (as defined in 5.5) show consistent trends with α and ν. The root bending effect on the upper surface, r_0, reduces as α increases, but is constant with ν and tends to the steady values, except at α=35°

where there is a certain level of excitation of the bluff body type flow. The phase angle between r(t) and $\eta(t)$, ϕ_r increases with both ν and α. The ϕ_r values for α=35° are again the result of the phase change with distance, x, from the apex of the unsteady pressures. On the lower surface, r_0 is constant with both α and ν and are the same as steady values whilst ϕ_r increases with ν, but is the same for all α. Combining the effects from the two surfaces again reduces the changes with α due to the upper surface, r_0 now altering less with α and being constant with ν. The ϕ_r values increase only slightly with α. The root bending moment leads the elevon motion.

There is no evidence of any flow resonance due to the elevon oscillation. This is, however, for a rigid wing. With both flexible modes present (control rotation and root bending) there is the addition of the aerodynamics due to bending about the root. The following accelerometer results show how the addition of these aerodynamic terms would alter the response of the wing to elevon oscillations.

8.2 Response of flexible wing to elevon oscillations.

Due to the test apparatus and time available, only point frequency tests could be carried out, rather than a continuous frequency sweep procedure. This reduces the definition of the response curves with frequency, particularly near the resonance peak. For this reason, the results presented here can only be considered as an initial investigation into the structural response in the presence of two flexible modes. As such, however, they do give a useful indication of the level of structural excitation that can be expected at high-α.

Fig. 8.2 and 8.3 show results for a root bending, natural frequency of ν=1.51. Both wind-off and wind-on results at various α are presented. Addition of the aerodynamic terms to the wind-off response increases the peak displacement and lowers the frequency at which the peak occurs. The amplitude of displacement is greatest at α=0° and reduces as α increases, suggesting that the aerodynamic stiffness and damping terms due to the root bending mode alter significantly with α. The results presented in Section 8.1 showed that for the rigid model, the root bending moment reduced with α. The difference in frequency parameter between ϕ_z=-90° and the peak amplitude suggests the motion is quite heavily damped.

Decreasing the natural frequency to ν_n=1.35 produces the responses of fig. 8.4 and 8.5. Though similar in character, the difference between α=0° and the other incidences is less than for the higher ν_n test. Lack of definition of the peak could, however, be responsible for this. Similarly, on fig. 8.5, the responses at α=20° are greater than those at α=10° on fig. 8.4. Again, the difference in ν value at the peak amplitude and at ϕ_z=-90° suggests the motion is heavily damped. In general, the amplitude reduces with α (except at α=20°) and the ν value of the peak increases slightly suggesting the aerodynamic terms change with incidence.

Finally, fig. 8.6 and 8.7 give the results for ν_n=1.07. As for the other two natural frequencies, α=0° gives the largest amplitude of motion and z_0/η_0 reduces with increasing α. Again, there appears to be significant aerodynamic damping associated with the root bending mode.

The results presented above are only preliminary. More detailed investigations using a model specifically designed for this form of testing are needed to determine exactly the response of the wing and to allow various parameters, such as wing inertia and elevon/wing cross inertia terms, to be altered. The generation of an analytical model of this two-mode, flexible system, using the terms from the rigid wing tests, could also be useful in determining the importance of the various aerodynamic terms with regard to the level of structural response to elevon motion. Despite these reservations, it is possible to say that no divergent oscillations were encountered in the range of ν_n tested, the resonance peaks having significant damping associated with them.

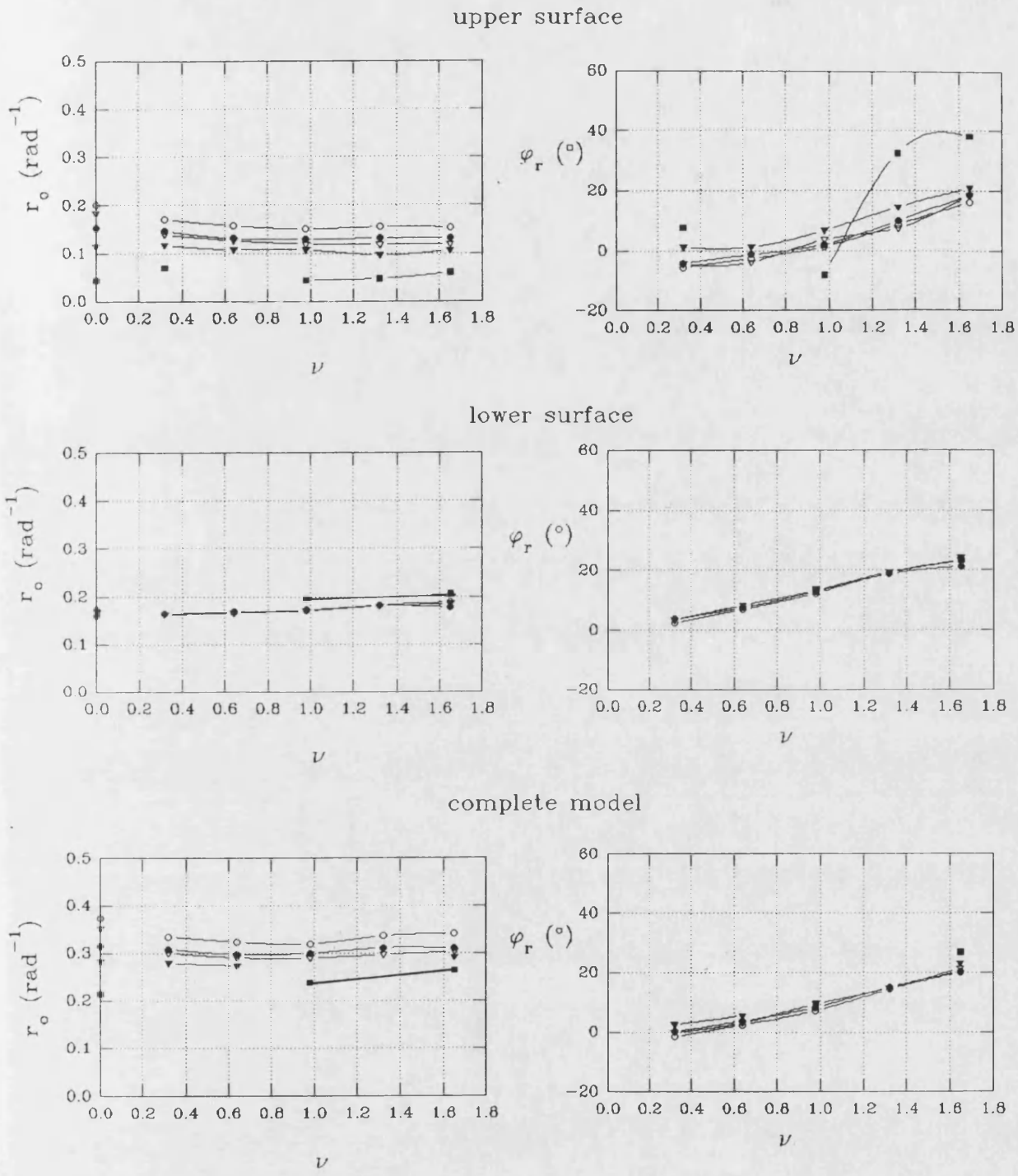

Fig. 8.1 - Root bending moments calculated from the control oscillation tests on the rigidly mounted wing

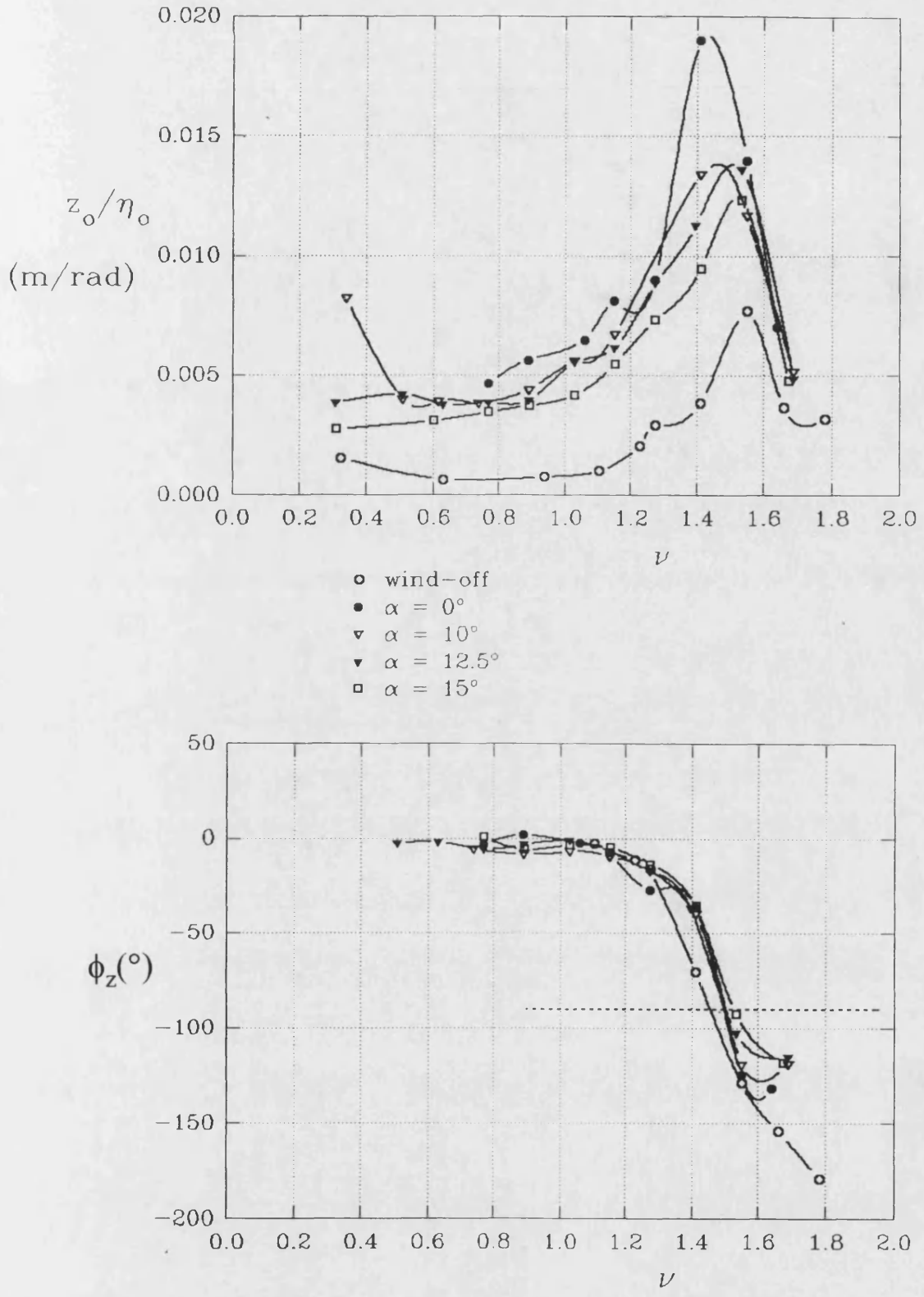

Fig. 8.2 - Wingtip response to elevon oscillations, wing natural frequency at ν=1.51

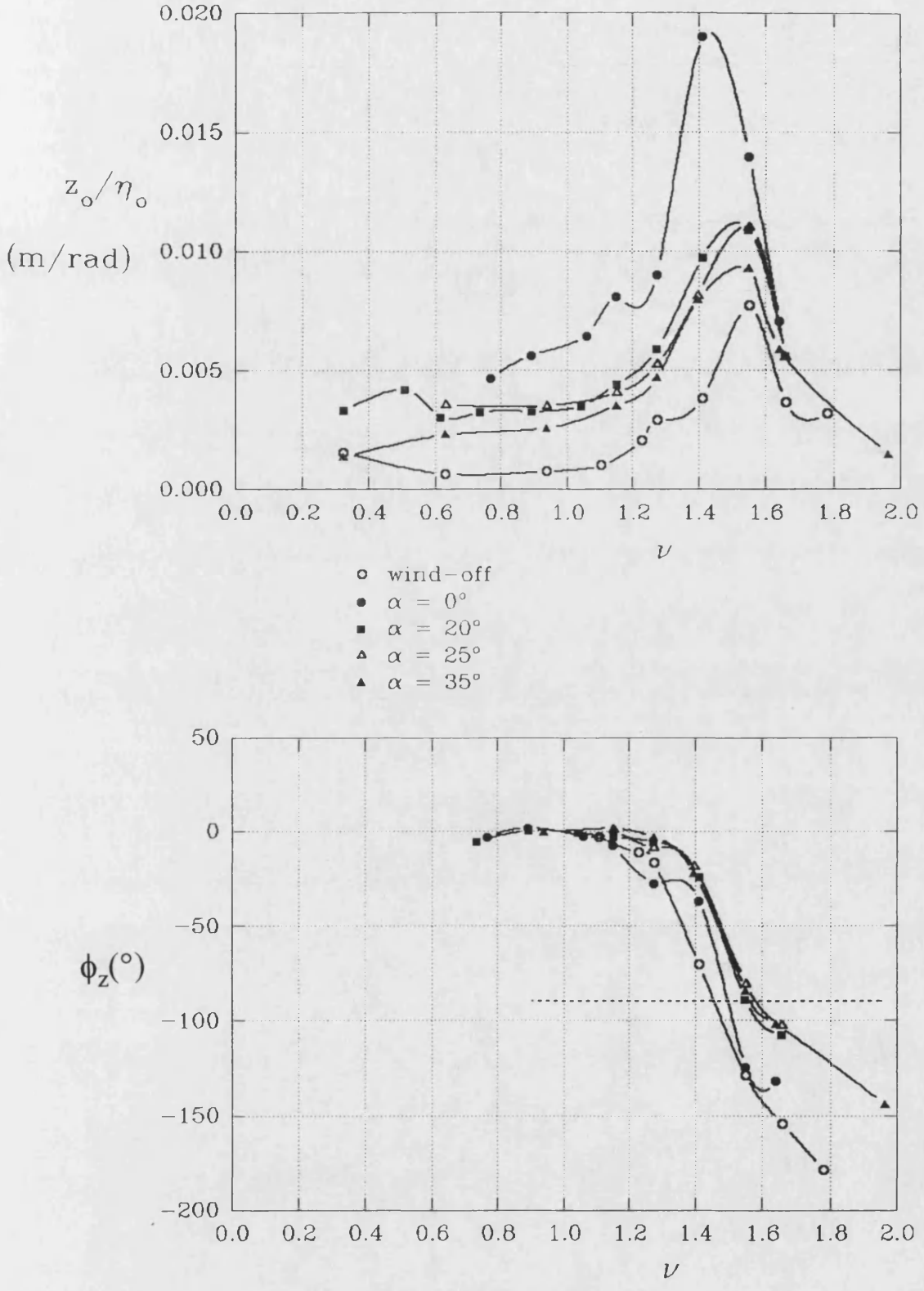

Fig. 8.3 - Wingtip response to elevon oscillations, wing natural frequency at ν=1.51

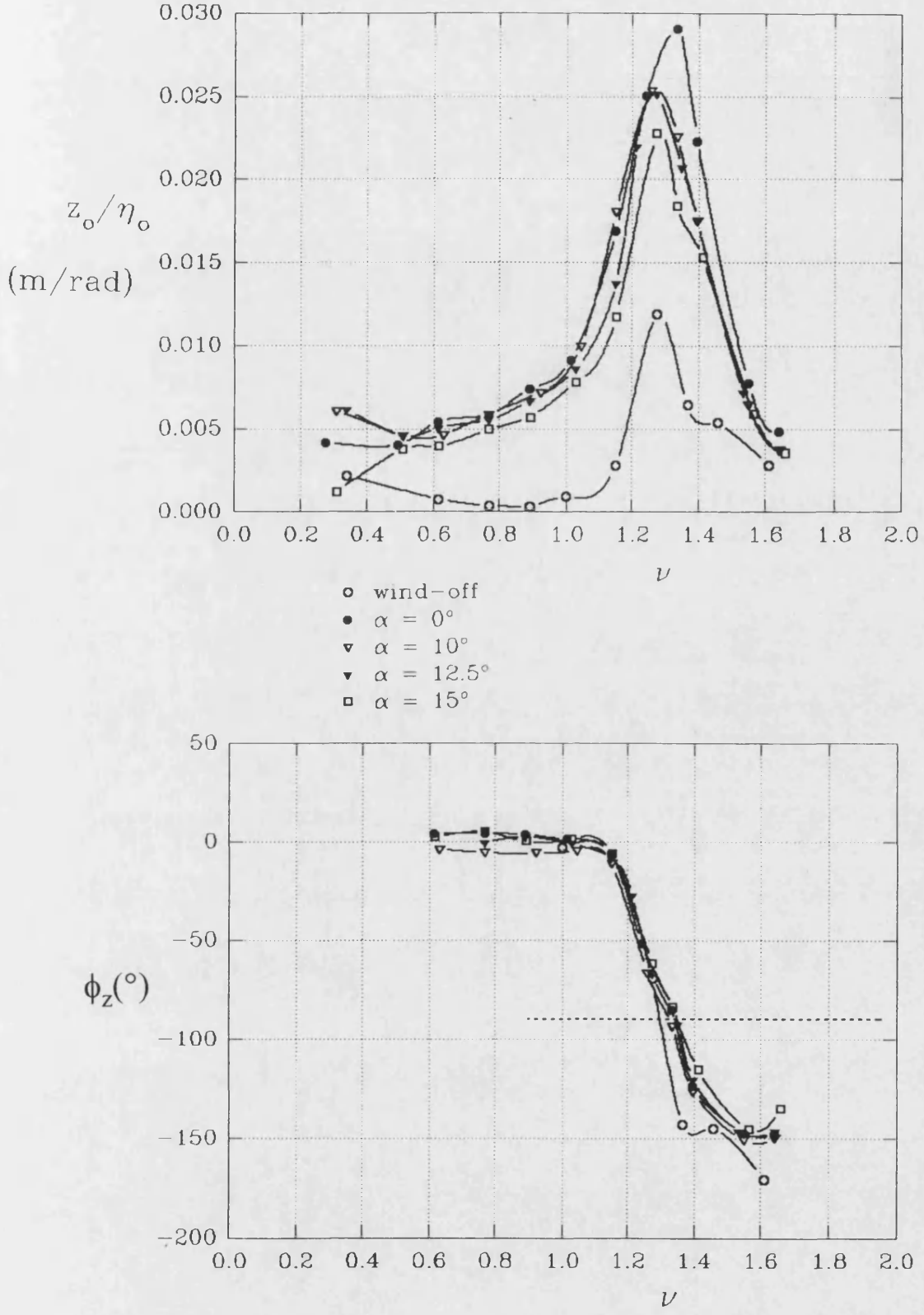

Fig. 8.4 - Wingtip response to elevon oscillations, wing natural frequency at ν=1.35

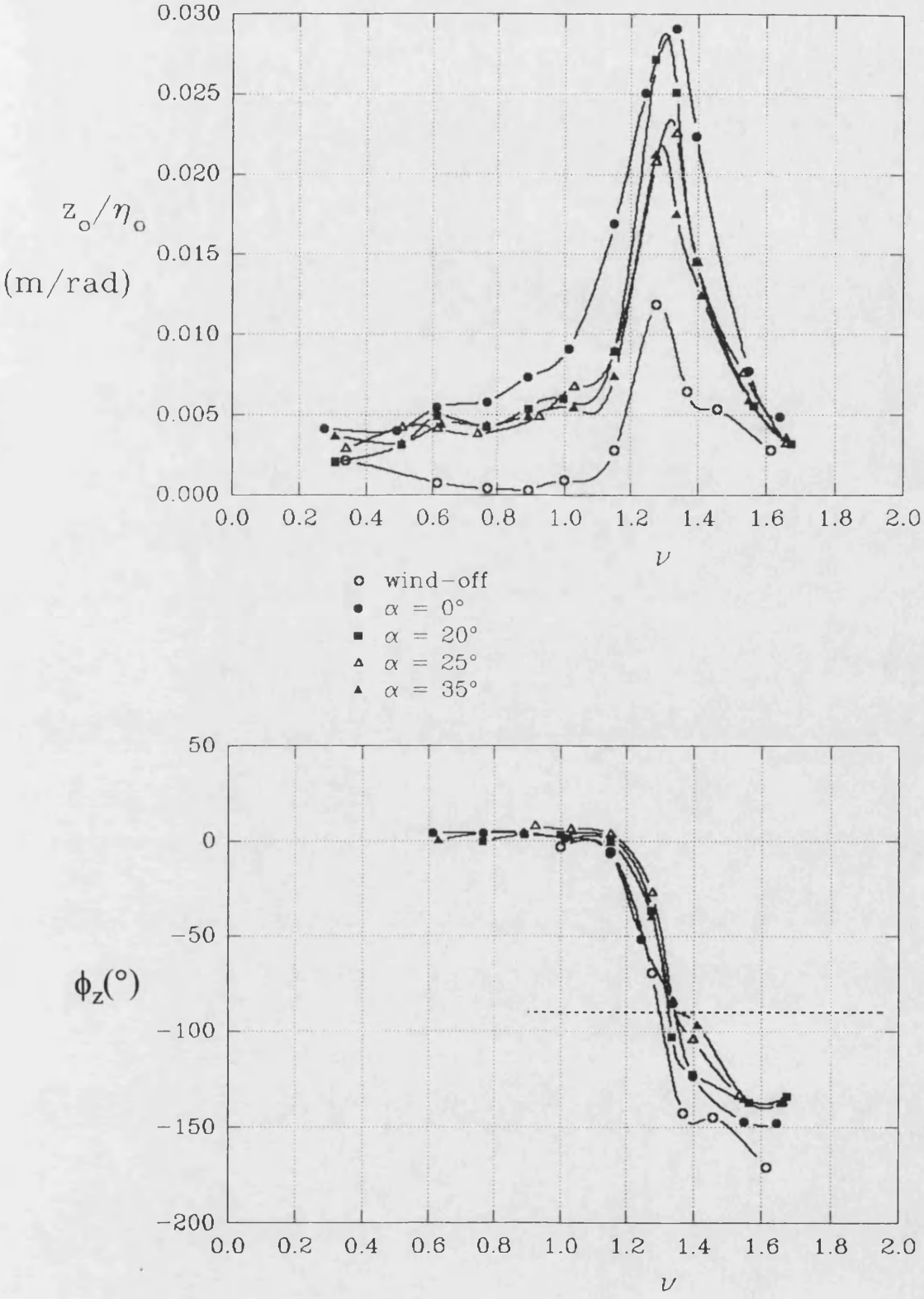

Fig. 8.5 - Wingtip response to elevon oscillations, wing natural frequency at ν=1.35

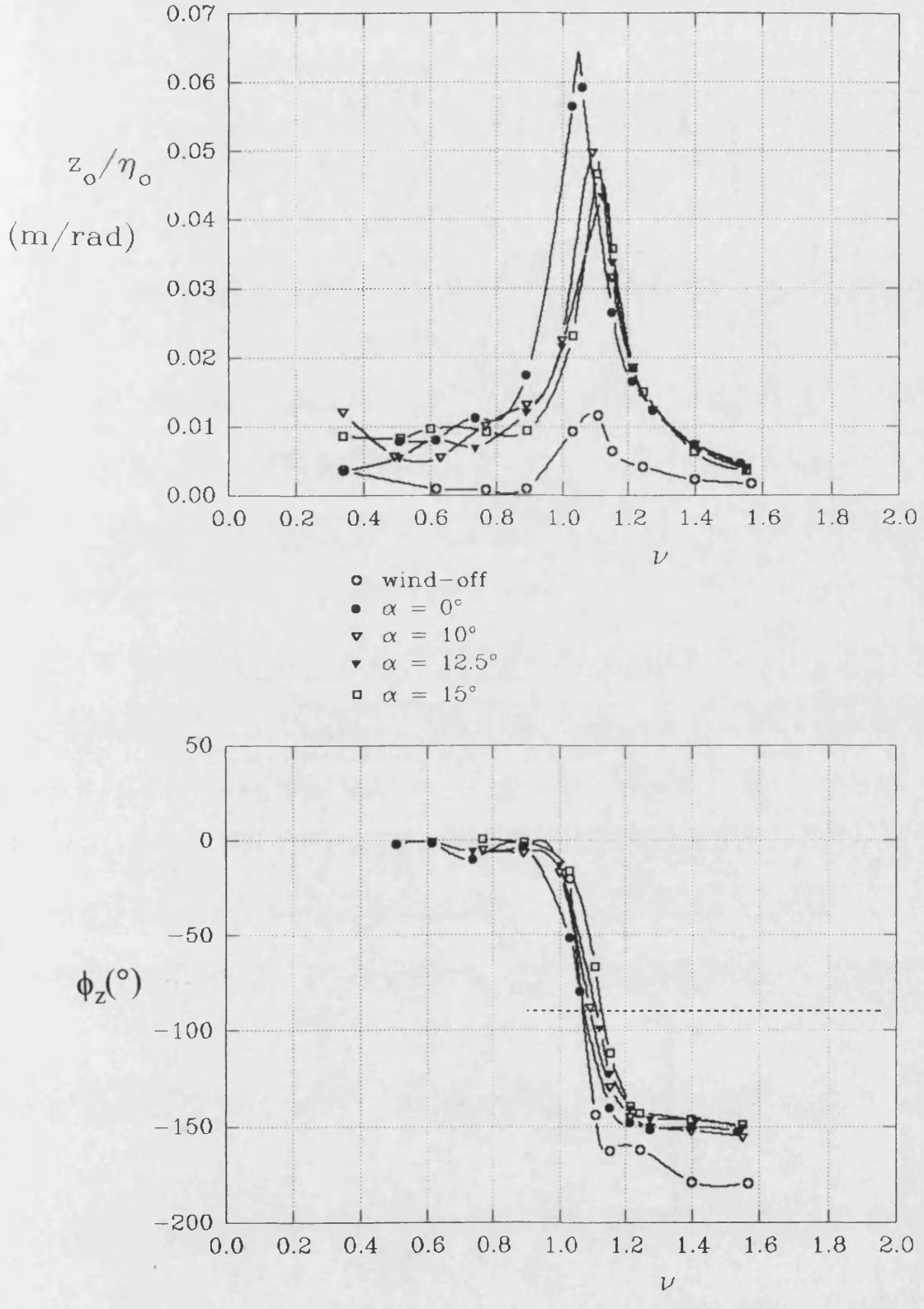

Fig. 8.6 - Wingtip response to elevon oscillations, wing natural frequency at ν=1.07

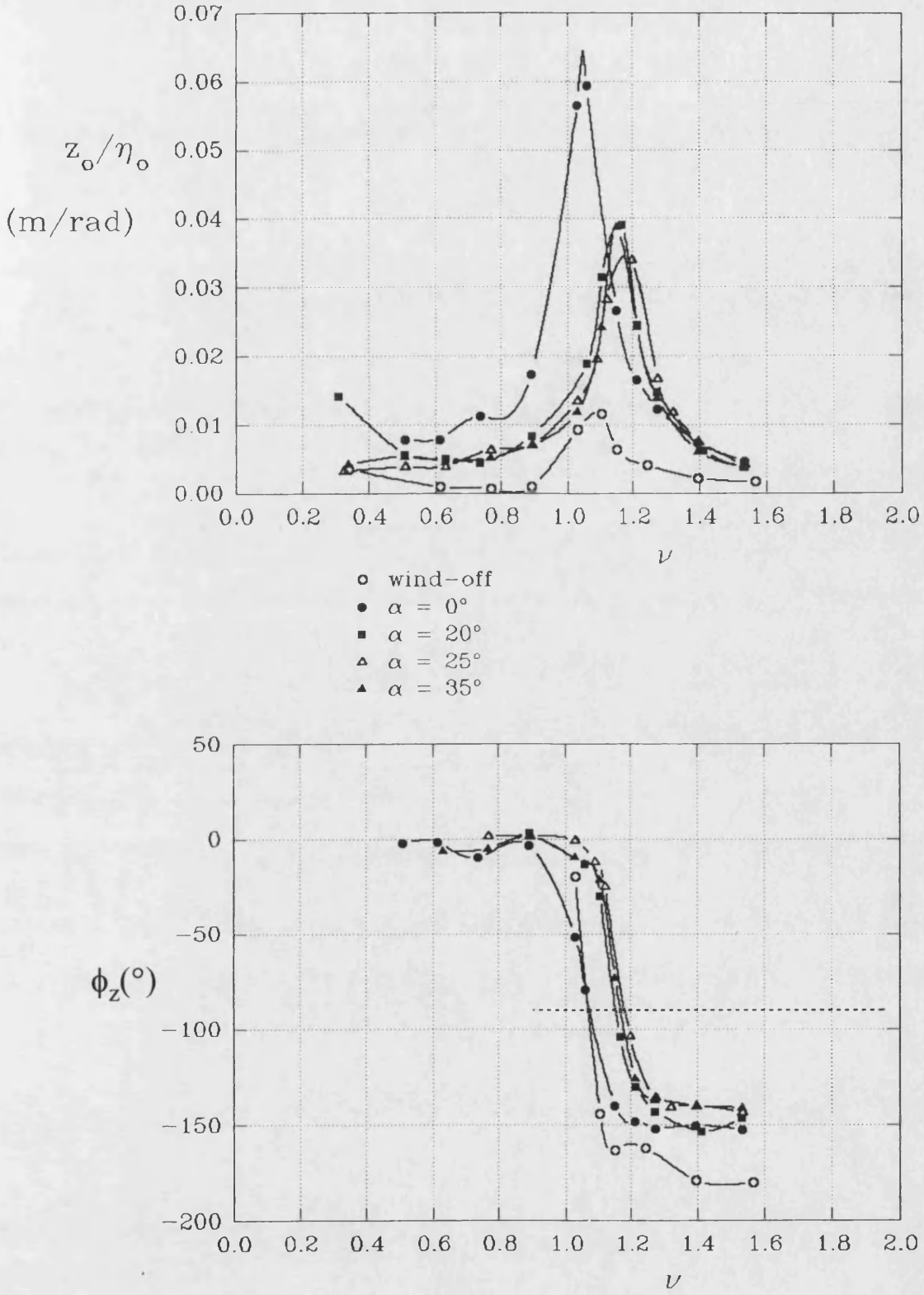

Fig. 8.7 - Wingtip response to elevon oscillations, wing natural frequency at ν=1.07

9. CONCLUSIONS.

9.1 Steady Aerodynamics.

As angle-of-attack, α, increases, a weak vortex forms above the wing. The vortex breakdown point appears on the wing for $\alpha>10°$ and reaches the apex at $\alpha=27.5°$. Beyond this incidence, the flow breaks down to the type formed behind a bluff body.

Increasing the outboard, trailing edge, control angle increases the strength of the vortex suction peak and is thought to increase the strength of the vortex and reduce the height of the core above the surface. Increasing elevon angle also moves the burst point further aft, while reducing the dynamic pressure on the lower surface around the control hinge line.

About a zero mean elevon angle, $\bar{\eta}=0°$, the control power due to the upper surface reduces with α whilst the lower surface contribution remains constant. This gives a total control effectiveness that decreases by 50% for normal force and 35% for pitching moment (about the aerodynamic centre) between $\alpha=10°$ and the stall incidence of $\alpha=27.5°$.

As the mean elevon angle, $\bar{\eta}$, about which the control effectiveness is considered increases, so the incremental pressures on the upper surface increase. The effect on the vortex is greater than at lower mean angles, though this difference reduces as α increases. The lower surface increments reduce as $\bar{\eta}$ increases due to the lower dynamic pressure around the hinge at higher mean angles. Combining the two surfaces, the control effectiveness does not alter greatly with $\bar{\eta}$.

9.2 Unsteady Aerodynamics.

The amplitude of response of the vortex reduces rapidly with both α and elevon oscillation frequency. The vortex change lags the elevon motion. This lag increases with frequency as does the phase difference between apex and hinge line. The reduction of vortex response is even greater over the elevon itself. Here, the excitation of the attached flow increases with frequency until it reaches a level similar to that found on the lower surface, in this region of the wing. This attached flow response leads the elevon motion. The unsteady

normal force, pitching moment (about aerodynamic centre) and hinge moment derivatives for the upper surface all reduce with α, though they are nearly constant with ν at each incidence. These forces and moments have an increasing phase angle with ν, and the amplitudes agree with the steady derivatives at low frequency, except for pitching moment which are lower due to the change in phase angle of the responses in the longitudinal direction. These upper surface unsteady characteristics are repeated at all $\bar{\eta}$ tested.

The lower surface unsteady pressure response is mainly around the hinge line. The amplitude of the response is nearly constant with frequency, and increases slightly with α, especially over the elevon. The pressures on the elevon have an increasing lead with frequency, though they are similar for all α. The control effectiveness in terms of normal force again agrees with the steady values, whilst the pitching moment amplitudes are lower due to the longitudinal phase changes, though it is a smaller phase difference between apex and hinge line than for the upper surface. These trends are repeated for all $\bar{\eta}$ tested.

The unsteady control effects for the complete wing are almost constant with frequency whilst having an increasing phase lead. The normal force and hinge moment values are similar to the steady derivatives. The unsteady pitching moments are also constant with frequency, but are lower than the steady values.

There is no evidence of resonance within the flow due to the control motion. The natural unsteadiness within the vortex is not excited by the oscillation. The results suggest that the attached flow response on both the upper and lower surfaces plays an important part in determining the overall unsteady responses.

The amplitude and phase results, particularly in the overall control derivatives, are easily represented within a Flight Control System and apart from the pitching moments, the steady values can be used, thus simplifying the initial FCS design process. The reduction in pitching moment amplitude, however, is important to the manoeuvrability of the aircraft at high angles-of-attack, and its form must be known, or an allowance made for control surface gain in pitch.

The agreement between the lower surface unsteady pressures at all α and those measured on a 2-d section at low α suggests it may be possible to use these simpler tests as a basis for the phase trends with frequency, and that a simple computational solution for fully attached flow would give an indication of the phase/amplitude changes with frequency of the

forces and moments.

9.3 Root bending mode

Although it was not possible to measure the unsteady pressures resulting from a root bending mode, the tests for a model with both a flexible root bending structural mode and elevon rotation mode present did not produce any large amplitude motions when the control was oscillated. The structural motion was greatest at $\alpha=0°$ and in general reduced as α increased. It was concluded that the damping associated with the root bending mode is high. The need for an increased control gain within the FCS at high-α for pitching, however, increases the potential for larger structural excitation.

10. FURTHER WORK

Although the results suggest that a steady elevon deflection changes the strength and position of the vortex above the wing, it is not possible to determine the actual effects from the measured surface pressures. An initial investigation using a Laser Doppler Velocimetry (LDV) system to measure the off-surface flow field showed that it would be possible to measure the vortex variation with elevon angle. This LDV work needs to be extended to cover a larger portion of the flow field. Improved knowledge of the vortex response to steady elevon deflections would give a greater insight into the unsteady pressure responses. Ideally, the use of an unsteady LDV system during elevon oscillations would potentially lead to an even better understanding of the interactions that occur.

The research programme was centred around a 55° leading edge sweep wing geometry. This wing was found to produce only a weak vortex that bursts over the wing at a relatively low incidence. Repeating the tests for a larger sweep angle, and hence stronger vortex, would determine whether the responses are the same and would lead to a useful design database of unsteady control surface aerodynamics for this form of wing geometry.

The importance of the attached flow response to elevon oscillations suggests it would be useful to conduct further comparisons with existing 2-dimensional attached flow experiments and with numerical solutions for a delta wing geometry. If the results proved to be similar to those presented in this report, such codes could then prove useful in the initial Flight Control System design by giving at least an indication of the unsteady amplitude and phase variations of each mode with incidence and frequency.

In order to predict the likely unsteady effects of control surface motion, it will be necessary to determine the nature of the mechanisms for attached and separated flow by which the elevon oscillation affects the flow field and surface pressures. Further improved tests for Step Changes in elevon angle would be useful in determining the speed of response of the flow and hence the nature of these mechanisms and any interactions between them.

Due to the limits of the flexible wing apparatus, the two-mode system tests did not give a full indication of the likely structural response to elevon motion. By extending this work, preferably using a model specifically designed to allow for parameters such as wing inertia to be altered, it would be possible to obtain the nature of the interaction between the unsteady aerodynamics of the two modes and the wing structure. Measurement of the unsteady aerodynamics of the wing mode would also allow the damping of the mode to be determined and for a full numerical simulation of the two-mode system to be produced. This could then be used to investigate the importance of each aerodynamic term and hence the accuracy needed in obtaining the unsteady terms.

REFERENCES.

Abel, I. [1992], 'Research and Applications in Structural Dynamics and Aeroelasticity', presented at ICAS 1992, Beijing, Peoples Republic of China, ICAS-92-6.3.1.

Aerotech, A.T.E. Ltd report [1970], 'University of Bath, Virtual Axis, 6-Component Wind Tunnel Balance : Operating Instructions and Guidance Notes'.

Baldwin, B. and Lomax, H. [1978], 'Thin-Layer Approximation and Algebraic Model for Separated Turbulent Flows', AIAA, 1978.

Becker, J. and Gravelle, A. [1985], 'Some Results of Experimental and Analytical Buffeting Investigations on a Delta Wing', contribution to the International Symposium on Aeroelasticity at Aachen, April 1-3, 1985.

Becker, J. [1991], 'Aeroservoelastic Stability of Aircraft at High-Incidence', Paper 19 from AGARD CP-497, Manoeuvring Aerodynamics, Toulouse, France, 1-2 May, 1991.

Bendat, J.S., Piersol, A.G. [1971], 'Random Data: Analysis and Measurement Procedures', John Wiley and Sons Inc., Toronto, 1971.

Bergh, H. [1955], 'Experimental Determination of the Aerodynamic Forces on an Oscillating Wing with Control Surface in Incompressible Two Dimensional Flow', Amsterdam, National Luchtvaartlaboratorium, Report F.175, 1955.

Bergh, H., Tijdeman, H. [1965], 'Theoretical and Experimental Results for the Dynamic Response of Pressure Measuring Systems', Amsterdam, N.L.R. Report No. F238, 1965.

Bergh, H., Tijdeman, H. [1972], 'The Influence of Main Flow on the Transfer Function of Tube-Transducer Systems Used for Unsteady Pressure Measurements', Amsterdam, N.L.R. Report No. mp 72023u, 1972.

Boyden, R.P. [1971], 'Effects of Leading-Edge Vortex Flow on the Roll Damping of Slender Wings', Journal of Aircraft, Vol. 8, No. 7, July 1971, pp. 543-547.

Bratt, J.B., Miles, C.J.W. and Johnson, R.F. [1957], 'Measurements of the Direct Hinge-Moment Derivatives at Subsonic and Transonic Speeds for a Cropped Delta Wing with Oscillating Flap', A.R.C. R&M No. 3163, May, 1957.

Braybrook, R. [1990], 'Demonstrating Technologies for Enhanced Fighter Manoeuvrability : The Rockwell/MBB X-31', Air International, Key Publishing, June 1990.

Brenner, M.J. [1993], 'Actuator and Aerodynamic Modeling for High-Angle-of-Attack Aeroservoelasticity', AIAA, 1993.

Broadbent, E.G. [1954], 'The Elementary Theory of Aero-Elasticity', Bunhill Publications Ltd., Holburn, 1954.

Caldwell, B. [1994], 'The FCS-Structural Coupling Problem and its Solution', AGARD conference on Active Control Technologies, May, 1994, to be published.

Chapra, S.C., Canale, R.P. [1987], 'Numerical Methods for Engineers with Personal Computer Applications', McGraw-Hill,1987.

Coe, P.L. [1974], 'A Vortex Entrainment Model Applied to Slender Delta Wings', AIAA Journal, Vol. 12, No. 1, Jan. 1974, pp.110-112.

Earnshaw, P.B. and Lawford, J.A. [1964], 'Low-Speed Wind-Tunnel Experiments on a Series of Sharp-Edged Delta Wings', A.R.C. R&M No. 3424, March, 1964.

Er-El, J. and Yitzhak, Z. [1988], 'Experimental Examination of the Leading-Edge Suction Analogy', Journal of Aircraft, Vol. 25, No. 3, March 1988, pp. 195-199.

Ericsson, L.E. and Reding, J.P. [1975], 'Unsteady Aerodynamics of Slender Delta Wings at Large Angles of Attack', Journal of Aircraft, Vol. 12, No. 9, Sept. 1975, pp. 721-729.

Ericsson, L.E. and Reding, J.P. [1977], 'Approximate Nonlinear Slender Wing Aerodynamics', Journal of Aircraft, Vol. 14, No. 12, Dec. 1977, pp. 1197-1204.

Ericsson, L.E. and Reding, J.P. [1978], 'Effect of Angle of Attack and Mach Number on Slender-Wing Unsteady Aerodynamics', Journal of Aircraft, Vol. 15, No. 6, June 1978, pp. 358-365.

ESDU Data Sheet 93034, 'Normal Force of Low Aspect Ratio Cropped-Delta Wings at Pre-Stall Angles of Attack and Subsonic Speeds', issued Dec. 1993.

Felt, L.R., Huttsell, L.J., Noll, T.E. and Cooley, D.E. [1978], 'Close Encounters of the Aeroservoelastic Kind', AIAA Paper 78-1298, 1978.

Flight International [1993] (author unknown), 'MATV attains 115° angles of attack', Flight International, Reed Business Publications, 6-12 Oct., 1993.

Försching, H. [1981], 'Some Remarks on the Unsteady Airloads on Oscillating Control Surfaces in Subsonic Flow', Paper 10 from AGARD CP-296, Boundary Layer Effects on Unsteady Airloads, 1981.

Försching, H. [1976], 'Wind Tunnel Test Techniques for the Measurement of Unsteady Airloads on Oscillating Lifting Systems and Full-Span Models', Paper 4, AGARD-R-645, Unsteady Aerodynamics, 1976.

Foster, J.V., Ross, H.M. and Ashley, P.A. [1993], 'Investigation of High-α Lateral-Directional Control Power Requirements for High-Performance Aircraft', AIAA Paper 93-3647, 1993.

Fujii, K. and Kutler, P. [1980], 'Numerical Simulations of teh Viscous Flow Fields Over Three-Dimensional Complicated Geometries', AIAA, 1980.

Gad-el-Hak, H. and Blackwelder, R.F. [1985], 'Discrete Vortices from a Delta Wing', Technical Note, AIAA Journal, Vol. 23, No. 6, pp. 961-962.

Geissler, W. [1981], 'Investigation of Unsteady Airloads on Wings with Oscillating Control for Active Control Purposes', AGARD Report R-699.

Gordnier, R.E. and Visbal, M.R. [1994], 'Unsteady Vortex Structure over a Delta Wing', Journal of Aircraft, Vol. 31, No. 1, Jan-Feb 1994, pp. 243-248.

Greenwell, D.I., Bean, D.E. and Wood, N.J. [1992], 'Calibration of the High Speed Working Section of the 7' * 5' Wind Tunnel', University of Bath, School of Mechanical Engineering Report 49/1992, July 1992.

Greenwell, D.I. and Wood, N.J. [1992], 'Determination of Vortex Burst Location on Delta Wings from Surface Pressure Measurements', AIAA Journal, Vol. 30, No. 11, November, 1992, pp. 2736-2739.

Greenwell, D.I. and Wood, N.J. [1994], 'Some Observations on the Dynamic Response of the Vortex Burst Phenomenon to Wing Motion', Journal of Royal Aeronautical Society, Feb. 1994.

Gursul, I. and Ho, C.M. [1993], 'Vortex Breakdown over Delta Wings in Unsteady Free Stream', AIAA Paper No. 93-0555, 1993.

Gursul. I. [1994], 'Unsteady Flow Phenomena over Delta Wings at High Angle of Attack', AIAA Journal, Vol. 32, No. 2, Feb. 1994, pp. 225-231.

Guyett, P.R. and Curran, J.K. [1961], 'Aerodynamic Derivative Measurements on a Wing with a Horn-Balanced Control Surface', A.R.C. R&M No. 3307, March, 1961.

Hall, M.G. [1972], 'Vortex Breakdown', Journal of Fluid Mechanics, Annual Review of Fluid Mechanics, 1972, pp. 195-218.

Herbst, W.B. [1983], 'Supermanoeuvrability', DGLR Paper No. 83-106, Munich, Germany, 7th Oct., 1983.

Huang, X.Z. and Hanff, E.S. [1993], 'Prediction of Normal Force on a Delta Wing Rolling at High Incidence', AIAA 93-3686, presented at AIAA Atmospheric Flight Mechanics Conference, Aug 9-11, 1993, Monterey, CA.

Hummel, D. [1967], 'Zur Umströmung scharfkantiger schlanker Deltaflügen bel grossen Anstellwinkeln', Zeitschrift fuer Flugwiss, Volume 15, 1967, pp. 376-385.

Hummel, D. [1973], 'Study of the Flow Around Sharp-Edged Slender Delta Wings with Large Angles of Attack', NASA TTF-15, 107, Sept. 1973.

Hummel, D. [1988], 'Documentation of Separated Flows for Computational Fluid Dynamics Validation', Paper 15 from AGARD CP-437, Validation of Computational Fluid Dynamics, 1988.

Jones, W.P. [1943], 'Theoretical Air-Load and Derivative Coefficients for Rectangular Wings', A.R.C. R&M No. 2142, Feb. 1943.

Jones, W.P. [1948], 'Aerofoil Oscillations at High Mean Incidences', A.R.C. R&M No. 2654, April 1948.

Jumper, E.J., Nelson, R.C. and Cheung, K. [1993], 'A Simple Criterion for Vortex Breakdown', AIAA Paper 93-0866, presented at 31st Aerospace Sciences Meeting and Exhibit, Jan. 11-14, 1993, Reno, NV.

Kienappel, K. and Round, D.F. [1980], 'Analysis of Unsteady Pressure Measurements on an Aerofoil Section with an Harmonically Oscillating, Slotted Flap', DFVLR-FB 80-22, Sept. 1980.

Küssner, H.G. and Schwarz, L. [1940], 'Der Schwingende Flügel mit Aerodynamisch ausgeglichemen Ruder', Luftfahrtforschung, Vol. 17, p. 377, 1940.

Küssner, H.G. [1940], 'Allgemeine Tragflächentheorie', Luftfahrtforschung, Vol. 17, p.370, 1940. (translated in NACA Tech. MEMO. 979).

Lambourne, N.C. and Bryer, D.W. [1962], 'The Bursting of Leading-Edge Vortices - Some Observations and Discussion of the Phenomenon', A.R.C. R&M No. 3282, 1962.

Lan, C.E. [1974], 'A Quasi-Vortex-Lattice Method in Thin Wing Theory', Journal of Aircraft, Vol. 11, No. 9, Sept. 1974, pp. 518-527.

Lan, C.E. [1979], 'The Unsteady Quasi-Vortex-Lattice Method with Applications to Animal Propulsion', Journal of Fluid Mechanics, Vol. 93, part 4, pp. 747-765.

Lang, J.D. and Francis, M.S. [1985], 'Unsteady Aerodynamics and Dynamic Maneuverability', Paper 29 from AGARD CP 386, Unsteady Aerodynamics - Fundamentals and Applications to Aircraft Dynamics, 1985.

Lowson, M.V. [1988], 'The Three Dimensional Vortex Sheet Structure on Delta Wings', Fluid Dynamics of Three-Dimensional Turbulent Shear Flows and Transition, AGARD CP-438, 1988.

Mabey, D.G., McOwat, D.M. and Welsh, B.L. [1979], 'Aerodynamic Characteristics of Moving Trailing-Edge Controls at Subsonic and Transonic Speeds', Paper 20 from AGARD CP-262, Aerodynamic Characteristics of Controls, 1979.

Mabey, D.G. [1983], 'Experimental Methods to Determine Control Effectiveness in Wind Tunnels', Paper 5, AGARD-R-711, Special Course on Aerodynamic Characteristics of Controls, 1983.

Marchbank, W.R. [1978], 'Evaluation of Pressure Distribution on Thin Wings with Distorted Control Surfaces Oscillating Harmonically in Linearised Compressible Subsonic Flow', A.R.C. R&M No. 3738, 1978.

Medina, M., Naman, R.A. and Kagan, E. [1992], 'Feasibility Study for an Active Aeroelastic Control System for the F-16 Aircraft', Paper ICAS-92-6.3.2, presented at the 18th International Congress of Aerospace Sciences, Beijing, Peoples Republic of China, 1992.

Moore, A.W. [1969], 'Scale Effects on Oscillatory Control-Surface Derivatives', A.R.C., C.P. No. 1151, July 1969.

Noll, T., et al [1989], 'Aeroservoelastic Wind-Tunnel Investigations Using the Active Flexible Wing Model - Status and Recent Accomplishments', AIAA paper no. 89-1168, 1989.

Norris, G. [1992], 'Breaking the Stall Barrier', Flight International, Reed Business Publishing, U.K., 11-17 November, 1992,

Orlik-Rückemann, K.J. [1982], 'Unsteady Aerodynamics and Dynamic Stability at High Angles of Attack', lecture 8 from AGARD LS-121, High angle-of-attack Aerodynamics, 1982.

Parker, A.G. [1976], 'Aerodynamic Characteristics of Slender Wings with Sharp Leading Edges - A Review', Journal of Aircraft, Volume 15, No. 3, pp 161-168, March, 1976.

Payne, F.M., Ng, T.T., Nelson, R.C. and Schiff, L.B. [1986], 'Visualisation and Flow Surveys of teh Leading Edge Vortex Structure on Delta Wing Planforms', AIAA 86-0330, Jan. 1986.

Payne, F.M., Ng, T.T., Nelson, R.C. and Schiff, L.B. [1988], 'Visualization and Wake Surveys of Vortical Flow over a Delta Wing', AIAA Journal, Vol. 26, No. 2, Feb. 1988, pp. 137-143.

Pendleton, E., Lee, M. and Wasserman, L. [1992], 'Application of Active Flexible Wing Technology to the Agile Falcon', Journal of Aircraft, Vol. 29, No. 3, May-June 1992, pp. 444-451.

Polhamus, E.C. [1966], 'A Concept of the Vortex Lift of Sharp-Edge Delta Wings Based on Leading-edge Suction Analogy', TN D-3767, Dec. 1966, NASA.

Polhamus, E.C. [1971], 'Predictions of Vortex-Lift Characteristics by a Leading-Edge Suction Analogy', Journal of Aircraft, Vol. 8, No. 4, April 1971, pp.193-199.

Press, W.H., Flannery, B.P., Teukolsky, S.A., Vetterling, W.T. [1986], 'Numerical Recioes in 'C' -the Art of Scientific Computing', Cambridge University Press, Cambridge, 1986.

Reynolds, G.A. and Abtahi [1989], 'Three-Dimensional Vortex Development, Breakdown, and Control', AIAA-89-0998, 1989.

Ross, A.J. and Thomas, H.H.B.M. [1979], 'A survey of Experimental Data on the Aerodynamics of Controls, in the Light of Future Needs', AGARD CP-262, Aerodynamic Characteristics of Controls, 1979.

Ross, A.J. [1981], 'Control Derivatives', AGARD LS-114, Dynamic Stability Parameters, 1981.

Ross, H. [1991], 'X-31 Enhancement of Aerodynamics for Maneuvering Beyond Stall', Paper 2 from AGARD CP-497, Manoeuvring Aerodynamics, 1991.

Sinnott, C.S. [1953], 'Hinge-Moment Derivatives for an Oscillating Control', A.R.C. R&M No. 2923, Sept. 1953.

Strganac, T.W.and Mook, D.T. [1990], 'Numerical Model of Unsteady Subsonic Aeroelastic Behavior', AIAA Journal, Vol. 28, No. 5, May 1990, pp. 903-909.

Strganac, T.W.and Mook, D.T. [1986], 'Application of the Unsteady Vortex-Lattice Method to the Nonlinear Two-Degree-of-Freedom Aeroelastic Equations', AIAA Paper 86-0867, 1986.

Squire, L.C. [1961], 'An Experimental Investigation of the Characteristics of Some Plane and Cambered 65° Delta Wings at Mach Numbers from 0.7 to 2.0', A.R.C. R&M No. 3305, July 1961.

Theodorsen, T. [1935], 'General Theory of Aerodynamic Instability and the Mechanism of Flutter', NACA Rep. 496, 1935.

Thomas, J.L., Taylor, S.L. and Anderson, W.K. [1987], 'Navier-Stokes Computations of Vortical Flows Over Low Aspect Ratio Wings', AIAA, 1987.

Visser, K.D. and Nelson, R.C. [1993], 'Measurements of Circulation in the Leading-Edge Vortex of a Delta Wing', AIAA Journal, Vol. 31, No. 1, Jan. 1993, pp. 104-111.

Von Kàrmàn, TH. and Sears, W.R. [1938], 'Airfoil Theory for Non-Uniform Motion', Journal of the Aeronautical Sciences, Vol. 5, No. 10, Aug. 1938, pp. 379-390.

Warsop, C. [1987], 'The Aerodynamic Loading on an Oscillating Control', University of Bath, PhD Thesis, 1987.

Washburn, A.E. and Visser, K.D. [1994], 'Evolution of Vortical Structures in the Shear Layer of Delta Wings', presented at the 25th AIAA Fluid Dynamics Conference, June 20-23, 1994, Colorado Springs, CO.

Zohar, Y. and Er-El, J. [1988], 'Influence of the Aspect Ratio on the Aerodynamics of the Delta Wing at High Angle of Attack', Journal of Aircraft, Vol. 25, No. 3, March 1988, pp. 200-205.

Zwaan, R.J. [1968], 'On a Kernel-Function Method for the Calculation of the Pressure Distribution on a Two-Dimensional Wing with Harmonically Oscillating Control Surface in Subsonic Flow', Report NLR-TR F.261, 1968.

APPENDIX 1 - General analysis program, ANAL_STY

```
#include<stdio.h>
#include<stdlib.h>
#include<alloc.h>
#include<float.h>
#include<math.h>
#include<dos.h>
#include "c:\press_no\unsteady\anal_sty.h"

#define PLAC(a,b) ((((a)-1)*5)+(b))
#define CUB(a) ((a)*(a)*(a))
#define LAST 32
#define SQR(a) ((a)*(a))

/* GLOBAL VARIABLES */

int no_channels, last_port_no;
float sample_freq_per_channel, actual_total_freq, frequency_step;
double mean_tube_press, velocity, air_temperature;

float expected_speed = 500.0;  /* for use when averaging speeds to allow for
 manometer zeroing */
int peak_value_locations[6]; /* for the FFT peaks from the function */
float peak_value[6];
float peak_value_freqs[6];

float amplitude_ratio[158][5];
float phase_effect[158][5];


float trans_func_freq;          /* these are the results from the tf func. */
float magnitude_tf, phase_tf;
float elevon_osc_amplitude;

int port_number;

/* File pointers */
FILE *fp1, *fp2, *fp3, *fp4, *fp5, *fp6, *fp7;


/* FUNCTION PROTOTYPES */

extern float *vector(int nl, int nh);
extern int *vector_int(int nl, int nh);
extern void free_vector(float *v, int nl, int nh);
extern void free_vector_int(int *v, int nl, int nh);
void peak_values(float fft[]);
extern void tube_function(int tap_location, float fft[]);
void tf(int a, float b, float c, float d[]);
void results_into_file(int k);
extern void fourier_analysis(float data1[], float data2[], float fft1[], flo
at fft2[]);
extern void four1(float data[], int n, int isign);
float average_data(float data[], int n);
```

```
void fft_to_file(int port, int signal, float fft[]);
float average_speed(float data[], int n);
void filter_data(int cut_off_posn, float fft[], float time_shift, int channe
l_no);

/*    ************************************************************
      * MAIN PROGRAM FOR THE DATA ANALYSIS.                        *
      *          CALCS. - MEANS                                    *
      *                 - CALCS TRANSFER FUNCTIONS                 *
      *                 - CALCS FOURIER TRANSFORMS                 *
      *                                                            *
      * NOTE : USES THE DATA AS SAVED USING "ACQU.C"               *
      *                                                            *
      * AUTHOR : D.J. PILKINGTON                                   *
      * DATE : 14/6/93                                             *
      ************************************************************ */

/* ************************************************************ */
/* ALTERATIONS MADE 9/11/93 :                                   */
/*                                                              */
/* CHANGED TO BINARY DATA FILE - SO THAT CAN WRITE COMPLETE     */
/* ARRAY TO FILE DURING THE ACQUISITION PROG.                   */
/* CAN ALSO SAVE THE RESULTS IN BINARY FORM - ALLOWS RANDOM     */
/* ACCESS OF THE RESULTS FROM THE POST-POST-PROCESSING ROUTINES */
/* ************************************************************ */
/* ALTERATIONS 12/11/93                                         */
/* ADDED SECTION TO PRODUCE A 'FILTERED' SIGNAL TRANSFORMED     */
/* BACK INTO THE TIME DOMAIN                                    */
/* ************************************************************ */



main(int argc, char *argv[])
{

/* local variable declarations */
int i,j,k,l,m,p, selection, signal, total_points, tap_location;
double mean_q;
float dynamic_press;
float air_pressure;
float temp_amp, temp_phase;
int cut_off_position;
float time_shift;
int data_temp[8];

float mean_elevon, mean_data1, mean_data2, mean_data3, mean_data4,
        mean_data5, mean_speed, mean_elevon_req;
float wind_off_data1, wind_off_data2, wind_off_data3, wind_off_data4,
        wind_off_data5;
float mean_data_coeff[7];

int elevon_osc_freq_loc;
float elevon_real, elevon_imag;
```

```
/* Tunnel correction for static pressure deficiency */
float tunnel_static_correc = 0.365;

/* declaration of the calibration constants for elevon and pressures */
float elevon_reqa = 1.625, elevon_reqb = -8.125e-4;
float calib_p1 = 1.56047, calib_p2 = 1.15054, calib_p3 = 1.53375, calib_p4 =
 1.51992,
                calib_p5 = -1.559;
float elevon_a = -10.6255857, elevon_b = .008469535, elevon_c = -2.279941331
e-6,
                elevon_d = 2.143775351e-10;



float *elevon, *data1, *data2, *data3, *data4, *data5,
                        *speed, *elevon_req;
float *fft1, *fft2, *fft_elevon;



/* Open the files given on the command line as the raw data file and results
 file */

if(argc < 9)
        {
        printf(" You must enter the data file, means file, unsteady, lengths
, fft, mot, tim files, expected speed \n");
        exit(0);
        }

if((fp1=fopen(argv[1], "rb")) == NULL)
        {
        printf(" Unable to open the data file %s \n", argv[1]);
        exit(0);
        }

if((fp2=fopen(argv[2], "wb")) == NULL)  /* means file */
        {
        printf(" Unable to create the results file %s \n", argv[2]);
        exit(1);
        }

if((fp3=fopen(argv[3], "wb")) == NULL)  /* fft results file */
        {
        printf(" Unable to create the results file %s \n", argv[3]);
        exit(0);
        }

if((fp4=fopen(argv[4], "r")) == NULL)  /* lengths file */
        {
        printf(" Unable to open lengths file \n");
        exit(0);
```

```
        }

if((fp5=fopen(argv[5], "wb")) == NULL)  /* fft file */
        {
        printf(" Unable to open fft results file \n");
        exit(0);
        }

if((fp6=fopen(argv[6], "wb")) == NULL)  /* motor results */
        {
        printf(" Unable to open motor results file \n");
        exit(0);
        }

if((fp7=fopen(argv[7], "wb")) == NULL)  /* filtered time signals results */
        {
        printf(" Unable to open time results file \n");
        exit(0);
        }


expected_speed = atof(argv[8]);

printf(" ANALYSIS PROGRAM  \n");
printf(" ---------------- \n\n");

/* Load the header line from the results file */
fread(&air_pressure, sizeof(float), 1, fp1);
fread(&air_temperature, sizeof(float), 1, fp1);
fread(&no_channels, sizeof(int), 1, fp1);
fread(&last_port_no, sizeof(int), 1, fp1);
fread(&actual_total_freq, sizeof(float), 1, fp1);

/* Need to load the data from the data file into defined arrays */
/* Defining arrays - one for each channel and two for the FFTs */

total_points = no_channels * N;

elevon = vector(1,N);
data1 = vector(1,N);
data2 = vector(1,N);
data3 = vector(1,N);
data4 = vector(1,N);
data5 = vector(1,N);
speed = vector(1,N);
elevon_req = vector(1,N);

fft_elevon = vector(1,N2);  /* so that can keep the elevon FFT results -
                               necessary for frequency sweep tests */
fft1 = vector(1,N2);
fft2 = vector(1,N2);
```

```
m = 1;
/* Load the data to give the phase and amplitude tube effects */
do
        {
        fscanf(fp4,"%f,%f,%f,%f", &amplitude_ratio[m][1],&amplitude_ratio[m]
[2],
                &amplitude_ratio[m][3],&amplitude_ratio[m][4]);
        fscanf(fp4,"%f,%f,%f,%f", &phase_effect[m][1],&phase_effect[m][2],
                &phase_effect[m][3], &phase_effect[m][4]);

        m=m+1;
        } while(!feof(fp4));


/* Calculate the frequency step for use by the tube calibration function */
frequency_step = actual_total_freq/(((float)no_channels)*N);

cut_off_position = (int)(2*CUTOFF/(frequency_step));



/* NEXT SECTION IS A LOOP WHICH LOADS THE DATA IN TURN AND ANALISES IT
   ------------------------------------------------------------------ */
j = 0;

for(j=0;j<=LAST;j++)              /* while not end of the file */
        {
        /* READ THE PORT NUMBER - IS ONLY IN THE FILE AT THE START OF EACH
                BLOCK OF ACQUIRED DATA                                    */
        fread(&port_number, sizeof(int), 1, fp1);

        /* this will now load each */
        /* set of port data */
        printf(" N = %i\n",N);
        for(i=1;i<=N;i++)
                {
        fread(data_temp, no_channels*sizeof(int), 1, fp1); /* reads all data
 for this port */

                /* splits the data up into the separate signals */
                elevon[i] = data_temp[0];
                data1[i] = data_temp[1];
                data2[i] = data_temp[2];
                data3[i] = data_temp[3];
                data4[i] = data_temp[4];
                data5[i] = data_temp[5];
                speed[i] = data_temp[6];
                elevon_req[i] = data_temp[7];


                /* need to apply the calibrations to the signals at this sta
ge
```

```
                    ------------------------------------------------------
-- */

                elevon[i] = elevon_a + (elevon_b*elevon[i]) + (elevon_c*(SQR
(elevon[i]))) +
                                (elevon_d*(CUB(elevon[i])));
                data1[i] = data1[i]*calib_p1;
                data2[i] = data2[i]*calib_p2;
                data3[i] = data3[i]*calib_p3;
                data4[i] = data4[i]*calib_p4;
                data5[i] = data5[i]*calib_p5;
                speed[i] = (speed[i] - 2048)*10.343*100.0*(10.0/2048);
                elevon_req[i] = elevon_reqa + (elevon_reqb*elevon_req[i]);

                }
                printf(" The data has been loaded, port no. %i \n", port_num
ber);
        j = port_number;
        mean_elevon = average_data(elevon, N);
        mean_data1 = average_data(data1, N);
        mean_data2 = average_data(data2, N);
        mean_data3 = average_data(data3, N);
        mean_data4 = average_data(data4, N);
        mean_data5 = average_data(data5, N);
        mean_speed = average_speed(speed, N);
        mean_elevon_req = average_data(elevon_req, N);

printf(" The means have been calculated \n");
            /* SETTING THE WIND OFF VALUES TO THE ABOVE MEANS */

        if(port_number == 0)
                {
                wind_off_data1 = mean_data1;
                wind_off_data2 = mean_data2;
                wind_off_data3 = mean_data3;
                wind_off_data4 = mean_data4;
                wind_off_data5 = mean_data5;

                printf("\n\n Set the wind-off values for the transducers \n"
);
                }


        if(port_number > 0)
                {
                /* if is not the wind-off port (port 0 - home port) then
                        can continue with the analysis */


                /* subtract the wind-off-values and convert to Cp values */
                dynamic_press = mean_speed;

                mean_q = mean_speed;
```

```
                velocity = sqrt((2.0*mean_q)/1.225);

                mean_data_coeff[0] = port_number;
                mean_data_coeff[1] = ((mean_data1 - wind_off_data1)/dynamic_
press) + tunnel_static_correc;
                mean_data_coeff[2] = ((mean_data2 - wind_off_data2)/dynamic_
press) + tunnel_static_correc;
                mean_data_coeff[3] = ((mean_data3 - wind_off_data3)/dynamic_
press) + tunnel_static_correc;
                mean_data_coeff[4] = ((mean_data4 - wind_off_data4)/dynamic_
press) + tunnel_static_correc;
                mean_data_coeff[5] = ((mean_data5 - wind_off_data5)/dynamic_
press) + tunnel_static_correc;
                mean_data_coeff[6] = mean_elevon;


                /* write the means to the results file */
                fwrite(mean_data_coeff, sizeof(mean_data_coeff), 1, fp2);


                /* Now need to subtract the means from the raw signals and
non-dim.
                before calculating the FFT's and TF's */

                for(i=1;i<=N;i++)
                        {
                        elevon[i] = (elevon[i] - mean_elevon);
                        data1[i] = (data1[i] - mean_data1)/dynamic_press;
                        data2[i] = (data2[i] - mean_data2)/dynamic_press;
                        data3[i] = (data3[i] - mean_data3)/dynamic_press;
                        data4[i] = (data4[i] - mean_data4)/dynamic_press;
                        data5[i] = (data5[i] - mean_data5)/dynamic_press;
                        elevon_req[i] = (elevon_req[i] - mean_elevon_req);
                        }


                /* Apply the Fourier Analysis to the signals 2 at a time
                   ---------------------------------------------------- */
                /* NOTE : The FFT routines ALTER the data signals, hence
                each one can only be analysed once, hence why the routine is
                written in the following way, i.e. treating each one separat
ely */


                /* Begin with the elevon signal and the first data signal */
                fourier_analysis(elevon, data1, fft1, fft2);

                /* find the peak frequency from the elevon motion (for TF an
alysis) */

                /* Because cant find the phase shift until found peak, but s
till
                        really want to have filtered the signal first, will
```

```
filter
                        it now, without going to the filter routine */
                for(p=1;p<=N2;p++)
                        {
                        if(p>cut_off_position) fft1[p] = 0;
                        }

                peak_values(fft1);
                elevon_osc_freq_loc = peak_value_locations[1];
                printf(" elevon osc. loc. = %i \n",elevon_osc_freq_loc);

                /* now filter the signal - and make allowance for acquisitio
n shift */
                time_shift = atan2(fft1[elevon_osc_freq_loc+1],
                                fft1[elevon_osc_freq_loc])/(2*PI*frequency_s
tep
                                                        *((elevon_osc_freq_l
oc-1)/2));
        printf(" Cutoff posn = %i",cut_off_position);
                filter_data(cut_off_position, fft1, time_shift,0);
                for(l=1;l<=N2;l++)
                        {
                        fft_elevon[l] = fft1[l]; /* so can do an inverse to
get back to time */
                        }


                /* having now altered the elevon signal to get into sink, ca
n find the
                                real and imaginary parts (imaginary should b
e 0) */

                elevon_real = fft_elevon[elevon_osc_freq_loc];
                elevon_imag = fft_elevon[elevon_osc_freq_loc + 1];
printf(" Elevon fft results %g %g\n",elevon_real, elevon_imag);
                elevon_osc_amplitude = sqrt((SQR(elevon_real))+(SQR(elevon_i
mag)));
printf(" Elevon amplitude %f\n",elevon_osc_amplitude);


                /* NEED TO APPLY THE SCANIVALVE TUBING SYSTEM TRANSFER FUNCT
ION
                   CHARACTERISTICS TO THE RESULTS FROM THE FFT TO CORRECT FO
R THE
                   SYSTEM
 */

                mean_tube_press = air_pressure + (mean_data_coeff[1]*dynamic
_press)
                                - (mean_speed*tunnel_static_correc);  /* for
 tube prog */
                tap_location = PLAC(port_number, 1);
                tube_function(tap_location, fft2);
```

```
                /* now look at the first data signal for which the FFT has b
een found */
                filter_data(cut_off_position, fft2, time_shift,1);
                peak_values(fft2);

                /* Calculate transfer function */
                tf(elevon_osc_freq_loc, elevon_real, elevon_imag,
                                        fft2);

                /* Next, can finally print the results to the FFT file */
                results_into_file(1);
                fft_to_file(port_number, 1, fft2);

                /* now reform time signal */
                four1(fft1, N, -1);
                four1(fft2, N, -1);
                fwrite(fft1, N*sizeof(float),1,fp7);
                fwrite(fft2, N*sizeof(float), 1, fp7);

                /* This is now repeated for the other signals */

                fourier_analysis(data2, data3, fft1, fft2);   /* analysis fo
r 2,3 */
printf(" data2 results before tube %g %g \n",fft1[elevon_osc_freq_loc],
                        fft1[elevon_osc_freq_loc+1]);

                mean_tube_press = air_pressure + (mean_data_coeff[2]*dynamic
_press)
                                        - (mean_speed*tunnel_static_correc);

                tap_location = PLAC(port_number, 2);
                tube_function(tap_location, fft1);

printf(" data2 results after tube %g %g \n",fft1[elevon_osc_freq_loc],
                        fft1[elevon_osc_freq_loc+1]);

                filter_data(cut_off_position, fft1, time_shift,2);
                peak_values(fft1);


                tf(elevon_osc_freq_loc, elevon_real, elevon_imag,
                                        fft1);
                results_into_file(2);
                fft_to_file(port_number, 2, fft1);

                mean_tube_press = air_pressure + (mean_data_coeff[3]*dynamic
_press)
                                        - (mean_speed*tunnel_static_correc);

                if(j<LAST)
                {
                tap_location = PLAC(port_number , 3);
```

```
                tube_function(tap_location, fft2);
                filter_data(cut_off_position, fft2, time_shift,3);

                peak_values(fft2);
                tf(elevon_osc_freq_loc, elevon_real, elevon_imag,
                                        fft2);
                results_into_file(3);
                fft_to_file(port_number, 3, fft2);

                /* now reform time signal */
                four1(fft1, N, -1);
                four1(fft2, N, -1);
                fwrite(fft1, N*sizeof(float),1,fp7);
                fwrite(fft2, N*sizeof(float), 1, fp7);

                fourier_analysis(data4, data5, fft1, fft2);    /* analysis o
f 4 & 5 */
                mean_tube_press = air_pressure + (mean_data_coeff[4]*dynamic
_press)
                                        - (mean_speed*tunnel_static_correc);

                tap_location = PLAC(port_number, 4);
                tube_function(tap_location, fft1);
                filter_data(cut_off_position, fft1, time_shift,4);

                peak_values(fft1);


                tf(elevon_osc_freq_loc, elevon_real, elevon_imag,
                                        fft1);
                results_into_file(4);
                fft_to_file(port_number, 4, fft1);
                mean_tube_press = air_pressure + (mean_data_coeff[5]*dynamic
_press)
                                        - (mean_speed*tunnel_static_correc);

                tap_location = PLAC(port_number, 5);
                tube_function(tap_location, fft2);
                filter_data(cut_off_position, fft2, time_shift,5);

                peak_values(fft2);
                tf(elevon_osc_freq_loc, elevon_real, elevon_imag,
                                        fft2);
                results_into_file(5);
                fft_to_file(port_number, 5, fft2);

                /* now reform time signal */
                four1(fft1, N, -1);
                four1(fft2, N, -1);
                fwrite(fft1, N*sizeof(float),1,fp7);
                fwrite(fft2, N*sizeof(float), 1, fp7);
                }
```

```
                /* NOW ANALYSES THE MOTOR I.E. T.F BETWEEN HALL EFFECT
                                AND THE MOTOR ENCODER  */
                fourier_analysis(elevon, elevon_req, fft1, fft2);
                filter_data(cut_off_position, fft2, time_shift,7);
                tf(elevon_osc_freq_loc, elevon_real, elevon_imag, fft2);
                fwrite(&trans_func_freq, sizeof(float), 1, fp6);
                fwrite(&magnitude_tf, sizeof(float), 1, fp6);
                fwrite(&phase_tf, sizeof(float), 1, fp6);



                printf(" End of Analysis for port %i \n\n\n",port_number);

                } /* END OF THE IF STATEMENT - I.E. END OF ANALYSIS FOR THE
PORT */
        if(feof(fp1) != 0) printf(" is end of data file \n");

        } /* END OF THE WHILE NOT END OF FILE LOOP */


free_vector(fft2,1,N2);
free_vector(fft1,1,N2);
free_vector(fft_elevon,1,N2);
free_vector(speed,1,N);
free_vector(data5,1,N);
free_vector(data4,1,N);
free_vector(data3,1,N);
free_vector(data2,1,N);
free_vector(data1,1,N);
free_vector(elevon,1,N);



} /* end of the function main */







/* Routine to print the Fourier Analysis results to the correct file
   ---------------------------------------------------------------- */
void results_into_file(int k)
        {
        int place;
        float place_f;

        place = PLAC(port_number,k);
        place_f = place;

        fwrite(&place_f, sizeof(float), 1, fp3);
```

```
        fwrite(peak_value_freqs, sizeof(peak_value_freqs), 1, fp3);
        fwrite(peak_value, sizeof(peak_value), 1, fp3); /* NOTE BOTH THESE H
AVE 6 ELEMENTS */
        fwrite(&trans_func_freq, sizeof(float), 1, fp3);
        fwrite(&magnitude_tf, sizeof(float), 1, fp3);
        fwrite(&phase_tf, sizeof(float), 1, fp3);
        fwrite(&elevon_osc_amplitude, sizeof(float), 1, fp3);


        }




/* Find the mean of the data
   ------------------------  */

float average_data(float data[], int n)
        {
        int a;
        float mean, total = 0;

        for(a=1; a<=n; a++)
                {
                total = total + data[a];
                }
        mean = total/n;

        return mean;
        }


/* Find the mean of the speed
   ------------------------  */

float average_speed(float data[], int n)
        {
        int a, actual_points;
        float mean, total = 0;

        actual_points = 0;
        for(a=1; a<=n; a++)
                {
                if ((data[a] < (expected_speed*1.1)) && (data[a] > (expected
_speed*0.9)))
                        {
                        total = total + data[a];
                        actual_points = actual_points + 1;
                        }
                }
        if(total>expected_speed)
                {
```

```
                mean = total/actual_points;
                }
        else mean = expected_speed;

        return mean;
        }


/* To find the 5 greatest FFT values */
/* --------------------------------- */

void peak_values(float fft[])
        {
        int m, n,i, flag, flag2, how_close = 16;
        double temp1, temp2, result;

        /* need to re-zero the peak_values, before starting  */
        for(m=1; m<=5; m++)
                {
                peak_value[m] = 0;
                peak_value_locations[m] = 0;
                peak_value_freqs[m] = 0;
                }

        for(m=9; m<N; m=m+2)      /* step through the fft freq by freq */
                {                 /* starts at the first non-zero freq (3) */
                flag = 0;         /* only looks at half as is symmetric */
                flag2 = 5;
                temp1 = fft[m];
                temp2 = fft[m+1];
                result = sqrt((SQR(temp1)) + (SQR(temp2)));

                for(i=5;i>=1;i--)
                        {
                        if(m < (peak_value_locations[i]+how_close)) flag2 =
i;
                        /* sets flag2 if freq within same range */

                        if(result > peak_value[i]) flag = i;
                        /* finds the place according to magnitude */
                        }


                if(flag > 0)    /* if new value is > one of the old ones */
                        {

                        for(n=flag2; n>flag; n--)  /* swap down to same freq
 */
                                {        /* if is less than same freq dont s
wap */

                                        /* move the necessary values */
                                peak_value[n] = peak_value[n-1];
```

```
                                peak_value_freqs[n] = peak_value_freqs[n-1];
                                peak_value_locations[n] = peak_value_locatio
ns[n-1];
                                }

                        if(flag2 >= flag)     /* doesnt enter new value if is
 less than old */
                                {              /* one at same freq i.e. if fl
ag2 < flag */
                                peak_value[flag] = result;  /* enter new val
ues */
                                peak_value_freqs[flag] = frequency_step*((m-
1)/2.0);
                                peak_value_locations[flag] = m;
                                }

                        }  /* end of if flag > 0 */
                } /* end of check for this freq. (end of for loop) */

        } /* end of this function */




/* Function to calculate the Transfer Function for each data
   ---------------------------------------------------------- */

void tf(int neta_loc, float neta_real, float neta_imag,
                                float fft[])
        {
        float neta_frequency, correction_factor;
        double mag_fft, phase_fft;
        double temp1,temp2,temp3,temp4;
        double real_cross_spec, imag_cross_spec;


        neta_frequency = frequency_step *((neta_loc - 1)/2.0);
        trans_func_freq = neta_frequency;

        /* correction factor must be re-applied to fft results to then calc.
                the transfer function correctly (see Bendat and Piersol) */
        correction_factor = ((1/0.875)*2.0/N);

        temp1 = neta_real/correction_factor;
        temp2 = neta_imag/correction_factor;
        temp3 = fft[neta_loc]/correction_factor;
        temp4 = fft[neta_loc+1]/correction_factor;

        real_cross_spec = (temp1*temp3) + (temp2*temp4);
        imag_cross_spec = (temp1*temp4) - (temp2*temp3);

        printf(" Transfer cross spec results %g %g \n",real_cross_spec, imag
```

```
_cross_spec);

        magnitude_tf = (sqrt((SQR(real_cross_spec)) + (SQR(imag_cross_spec))
))
                                /((SQR(temp1)) + (SQR(temp2)));

        /* Note : A phase lag is considered a negative angle, where as the
                  fft routine seems to do the opposite   */
        phase_tf =  (atan2(imag_cross_spec, real_cross_spec));
        phase_tf = phase_tf*(180/PI);

        }  /* end of the transfer function routine */




/* Function to put the processed fft results into a file so can be
   ------------------------------------------------------------------
   looked at later if required
   ---------------------------                                        */

void fft_to_file(int port, int signal, float fft[])
        {
        int a, place;
        float freq;
        float magnitude_fft;

        place = PLAC(port, signal);

        fwrite(fft, N2*no_channels*sizeof(float), 1, fp5);

        }




/* Function to filter the data and non-dimensionalise with elevon amp. */
/* ------------------------------------------------------------------- */
/* Also allows for the error due to acquisition */
/* -------------------------------------------- */

void filter_data(int cut_off_position, float fft[], float time_shift, int si
gnal_no)
        {

        float fft_amp, fft_phase, phase_correction, frequency, time_error;
        int i,j;


        /* first loop from 1 to N2 in fft */
```

```
        for(i=1;i<=N2;i=i+2)
                {

                frequency = (i-1)*frequency_step/2.0;

                /* decide if is to be filtered out or not and deal with
                                accordingly    */
                if(i<cut_off_position)
                        {
                        fft_amp = sqrt((SQR(fft[i])) + (SQR(fft[i+1])));
                        fft_phase = atan2(fft[i+1], fft[i]);

                        /* calculation of the phase error due to acquisition
 */
                        time_error = signal_no / actual_total_freq;

                        phase_correction = (time_shift+time_error)*2*PI*freq
uency;

                        fft_phase = fft_phase - phase_correction;

                        /* reconvert to real and imaginary */
                        fft[i] = fft_amp*cos(fft_phase);
                        fft[i+1] = fft_amp*sin(fft_phase);
                        }
                else
                        {
                        fft[i] = 0;
                        fft[i+1] = 0;
                        }

                }  /* end of loop for this value */

        } /* end of function */
```

APPENDIX 2 - Fast Fourier Transform Algorithm, FFT_BIN

```
#include<stdio.h>
#include<stdlib.h>
#include<alloc.h>
#include<float.h>
#include<math.h>
#include "c:\press_no\unsteady\anal_sty.h"



/* FUNCTION PROTOTYPES */
void fourier_analysis(float data1[], float data2[], float fft1[], float fft2
[]);
/* this is the main function called from analysis */

void twofft(float data1[], float data2[], float fft1[], float fft2[], int n)
;
void four1(float data[], int a, int b);
float *vector(int nl, int nh);
int *vector_int(int nl, int nh);
void free_vector(float *v, int nl, int nh);
void free_vector_int(int *v, int nl, int nh);




/* ************************************************************
   * PROGRAM TO ANALISE THE RESULTS FROM OSCILLATION TESTS    *
   * A SERIES OF 'MODULES' WHICH BUILD UP INTO THE FULL SET   *
   ************************************************************ */


void fourier_analysis(float data1[], float data2[], float fft1[], float fft2
[])
{
int isign;
int i;
float no_samples, t, test;
double result;


/* Need to use a cosine taper on the data to aid the frequency smoothing */
/* will be applied over t/10 at both ends(N/10), must then * answer of FFT b
y
   1/0.875 to obtain correct result    */

/* for the start of the sample */
no_samples = N;
i = 1;
t = 0.0;
while( i<= (N/10))
        {
        data1[i] = data1[i]*0.5*(1 - (cos(PI*10.0*t/no_samples)));
        data2[i] = data2[i]*0.5*(1 - (cos(PI*10.0*t/no_samples)));
```

```
        i++ ;
        t = t + 1.0;
        }

/* for the end of the sample */


t = (9.0*N)/10.0 + 1.0;
i = (int) t;
t = (float) i;

while( i<=N)
        {
        data1[i] = data1[i]*0.5*
                ((cos(PI*10.0*(t-(9.0*no_samples/10.0))/no_samples))+1.0);
        data2[i] = data2[i]*0.5*
                ((cos(PI*10.0*(t-(9.0*no_samples/10.0))/no_samples))+1.0);
        i++ ;
        t = t + 1.0;
        }


/* Obtain the transform for the two signals - produces fft1 and fft2 which
   are the complex transforms for the two signals     */

twofft(data1,data2,fft1,fft2,N);

/* Must now correct for the windowing of the original data */


test = (1.0/0.875)*2.0/N;

for(i=1;i<=N2;i++)
        {
        fft1[i] = fft1[i]*test;
        fft2[i] = fft2[i]*test;
        }

/* to change the imaginary part so that a lag becomes a neagative phase
                - the FFT routine seems to thik a lag should be +ve !!! */
for(i=2;i<=N2;i=i+2)
        {
        fft1[i] = -fft1[i];
        fft2[i] = -fft2[i];
        }



} /* end of this function - has created the fft results */
```

```
/* Fast Fourier Transform for TWO data signals simultaneously
   ----------------------------==-------------------------------

   Note : Uses four1 (given below) and splits the two complex
   transforms up using the symmetry of the analysis            */

void twofft(float data1[], float data2[], float fft1[], float fft2[], int n)
        {
        int nn3, nn2, jj, j;
        float rep, rem, aip, aim;
        void four1();


        nn3 = 1 +(nn2=2+n+n);

        /* now packs the two data signals into the one array to
           then perform the fft on using four1    */

        for (j=1, jj=2; j<=n; j++, jj+=2)
                {
                fft1[jj-1]=data1[j];
                fft1[jj]=data2[j];
                }

        /* transforms the data using four1  */
        four1(fft1,n,1);

        fft2[1]=fft1[2];
        fft1[2]=fft2[2]=0.0;

        /* separate the two complex transforms using symmetries  */
        for(j=3;j<=n+1; j+=2)
                {
                rep = 0.5*(fft1[j]+fft1[nn2-j]);
                rem = 0.5*(fft1[j]-fft1[nn2-j]);
                aip = 0.5*(fft1[j+1]+fft1[nn3-j]);
                aim = 0.5*(fft1[j+1]-fft1[nn3-j]);

                /* split into the two transforms */
                fft1[j]=rep;
                fft1[j+1]=aim;
                fft1[nn2-j]=rep;
                fft1[nn3-j]= -aim;
                fft2[j]=aip;
                fft2[j+1] = -rem;
                fft2[nn2-j] = aip;
                fft2[nn3-j]=rem;
                }
        }
```

```
/* Fast Fourier Transform from Numerical Recipes for 'C' (four1)
   ------------------------------------------------------------ */
/*  Note : This is the basic building block for the transfer functions etc.
*/
/* isign = 1 - fft (otherwise gives the inverse
   data[]  = complex data array of length nn
   Note : the routine starts from 1 in the array indexing          */

void four1(float data[], int nn, int isign)
        {
        int n, mmax, j, istep, i, m;
        float wtemp, wr, wpr, wpi, wi, theta;
        float tempr, tempi;

        n=nn << 1;
        j = 1;

        /* bit reversal section */
        for(i=1; i<n;i+=2)
                {

                if(j > i)
                        {
                        SWAP(data[j], data[i]);
                        SWAP(data[j+1], data[i+1]);
                        }
                m=n >> 1;
                while(m >=2 && j > m)
                        {
                        j -= m;
                        m >>= 1;
                        }
                j += m;
                }

        /* the Danielson-Lanczos secton of the routine */
        mmax = 2;

        while(n > mmax)
                {
                istep = 2*mmax;
                theta = 6.28318530717959/(isign*mmax);
                wtemp = sin(0.5*theta);
                wpr = -2.0*wtemp*wtemp;
                wpi = sin(theta);
                wr = 1.0;
                wi = 0.0;
```

```
                for (m=1; m<mmax; m+=2)
                        {

                        for (i=m;i<=n;i+=istep)
                                {
                                j = i + mmax;

                                tempr=wr*data[j] - wi*data[j+1];
                                tempi = wr*data[j+1] +wi*data[j];
                                data[j] = data[i] - tempr;
                                data[j+1]=data[i+1] - tempi;
                                data[i] += tempr;
                                data[i+1] += tempi;
                                }

                        wr=(wtemp=wr)*wpr-wi*wpi+wr;
                        wi=wi*wpr+wtemp*wpi+wi;
                        }
                mmax = istep;
                }
        }


/* Routine to allocate a vector for the fft - float
   ------------------------------------------------  */

float *vector( int nl, int nh)
        {
        float *v;

        v= (float *)malloc((unsigned) (nh-nl+1)*sizeof(float));
        if (v == NULL)
                {
                printf("Problem with memory allocation\n");
                exit(0);
                }
        return v-nl;
        }




/* Routines to free the vectors memory allocation - float
   ------------------------------------------------------  */

void free_vector(float *v, int nl, int nh)
        {
        free((char*) (v+nl));
        }
```

```
/* Routine to allocate a vector for the fft - integer array
   ------------------------------------------------------  */

int *vector_int( int nl, int nh)
        {
        int *v;

        v= (int *)malloc((unsigned) (nh-nl+1)*sizeof(int));
        if (v == NULL)
                {
                printf("Problem with memory allocation - int \n");
                exit(0);
                }
        return v-nl;
        }



/* Routines to free the vectors memory allocation
   ---------------------------------------------  */

void free_vector_int(int *v, int nl, int nh)
        {
        free((char*) (v+nl));
        }
```